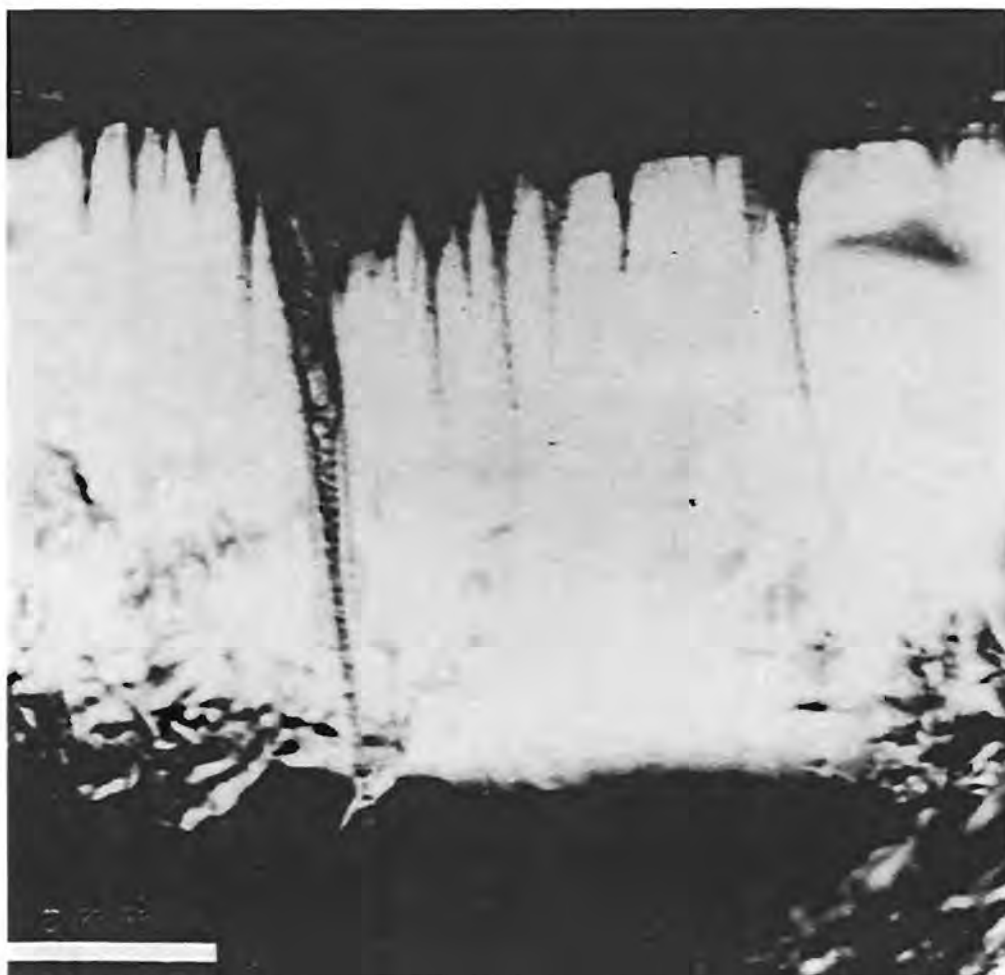


# WORKSHOP ON PARTICLE CAPTURE, RECOVERY, AND VELOCITY/TRAJECTORY MEASUREMENT TECHNOLOGIES



LPI Technical Report Number 94-05

Lunar and Planetary Institute 3600 Bay Area Boulevard Houston TX 77058-1113  
LPI/TR--94-05



**WORKSHOP ON  
PARTICLE CAPTURE, RECOVERY, AND  
VELOCITY/TRAJECTORY MEASUREMENT TECHNOLOGIES**

Edited by  
M. E. Zolensky

Held at  
Houston, Texas  
September 27–28, 1993

Sponsored by  
Lunar and Planetary Institute

Lunar and Planetary Institute 3600 Bay Area Boulevard Houston TX 77058-1113

LPI Technical Report Number 94-05  
LPI/TR--94-05

Compiled in 1994 by  
LUNAR AND PLANETARY INSTITUTE

The Institute is operated by the University Space Research Association under Contract No. NASW-4574 with the National Aeronautics and Space Administration.

Material in this volume may be copied without restraint for library, abstract service, education, or personal research purposes; however, republication of any paper or portion thereof requires the written permission of the authors as well as the appropriate acknowledgment of this publication.

This report may be cited as

Zolensky M. E., ed. (1994) *Workshop on Particle Capture, Recovery, and Velocity/Trajectory Measurement Technologies*. LPI Tech. Rpt. 94-05, Lunar and Planetary Institute, Houston. 102 pp.

This report is distributed by

ORDER DEPARTMENT  
Lunar and Planetary Institute  
3600 Bay Area Boulevard  
Houston TX 77058-1113

*Mail order requestors will be invoiced for the cost of shipping and handling.  
Please refer to the LPI Technical Report number when ordering.*

---

Cover: Tracks bored into low-density silica aerogel (0.04 g/cc) by olivine grains traveling at a velocity of 6.4 km/s in a laboratory simulation experiment (see abstract by Zolensky et al. in this report).



# Program

---

*Monday, September 27, 1993*

**7:30 a.m.** Registration

**8:15 a.m.** Welcome/Opening Remarks/Logistics

**8:30 a.m.–10:00 a.m.**

## **PARENT-DAUGHTER ORBIT DIVERGENCE**

**Chair: H. Zook**

*IRAS Observations Show that the Earth is Embedded in a Solar Ring of Asteroidal Dust Particles in Resonant Lock with the Planet*

S. F. Dermott, S. Jayaraman, Y.-L. Xu, and J.-C. Liou

*Some Considerations on Velocity Vector Accuracy in Dust Trajectory Analysis*

A. A. Jackson and H. A. Zook

*Velocity Distribution of Earth-crossing Asteroid Grains*

J. C. Liou and S. F. Dermott

**10:00 a.m.–12:00 noon**

## **TRAJECTORY SENSING**

**Chair: S. Auer**

*Plasma Produced by Impacts of Fast Dust Particles on a Thin Film*

S. Auer

*PVDF Flux/Mass/Velocity/Trajectory Systems and Their Applications in Space*

A. J. Tuzzolino

*Charge Collection During Hypervelocity Penetrations of Thin Foils*

R. Peterson

*The Status of Measurement Technologies Concerning Micrometer and Submicrometer Space Particulate Matter Capture, Recovery, Velocity, and Trajectory*

W. M. Alexander, W. G. Tanner, R. A. McDonald, G. E. Schaub, S. L. Stephenson,  
J. A. M. McDonnell, and C. R. Maag

**1:30 p.m.–5:30 p.m.**

**CAPTURE MEDIUM DEVELOPMENT: LABORATORY EXPERIMENTS**

**Chairs: D. E. Brownlee and M. E. Zolensky**

*Physics of Spacecraft-based Interplanetary Dust Collection by Impact Into Low-Density Media*

W. W. Anderson and T. J. Ahrens

*The Physics of Intact Capture*

P. Tsou, D. J. Griffiths, and A. L. Albee

*Laboratory Simulation of Intact Capture of Cometary and Asteroidal Dust Particles in ISAS*

A. Fujiwara, A. Nakamura, and T. Kadono

*High-Purity Aerogel: Manufacture and Verification of Quality and Performance*

D. J. Mendez

*The Use of Silica Aerogel to Capture Interplanetary Dust in Space*

M. E. Zolensky, R. A. Barrett, and F. Hörz

*The Intact Capture of Hypervelocity Dust Particles Using Underdense Foams*

C. R. Maag, J. Borg, W. G. Tanner, T. J. Stevenson, and J.-P. Bibring

*Penetration of Multiple Thin Films in Micrometeorite Capture Cells*

C. G. Simon

*Cratering and Penetration Experiments in Aluminum and Teflon Targets of*

*Widely Variable Thickness*

F. Hörz, M. Cintala, R. P. Bernhard, and T. H. See

**5:30 p.m.–7:00 p.m.**

**POSTER SESSION AND RECEPTION**

**Tuesday, September 28, 1993**

**8:30 a.m.–12:00 noon**

**CAPTURE MEDIUM DEVELOPMENT:  
IN SITU COLLECTIONS AND REQUIREMENTS**

**Chairs: C. G. Simon and R. M. Walker**

*Ion Microprobe Studies of LDEF Impacts on Capture Cells and Flat Plates*

R. M. Walker

*LDEF Flux Directionality*

H. Zook

*LDEF Mineralogy and Composition Summary*

D. E. Brownlee

*EURECA: Preliminary Observations*

W. G. Tanner

*Shuttle Instruments and Observations*

P. Tsou

*Intact Capture of Hypervelocity Dust Particles Using Underdense Foams*

C. R. Maag, J. Borg, W. G. Tanner, T. J. Stevenson, and J.-P. Bibring

*Collection Requirements for Trace-Element Analyses of Extraterrestrial Samples*

G. J. Flynn and S. R. Sutton

*Shock Stability of Amino Acids*

T. Bunch

*Techniques for In Situ Collection and Measurement of Volatiles Released During Hypervelocity Impact*

R. A. Heppner, W. Niu, and C. R. Maag

*Scientific Objectives of the Primitive Body Sample Return Missions—An Approach from the Light-induced Effect on Water Vapor*

M. Shimizu

**1:00 p.m.–4:00 p.m.****FUTURE FLIGHT OPPORTUNITIES****Chair: F. Hörz***SOCER: Comet Coma Sample Return Mission*

K. Uesugi

*SPICE: An Innovative, Flexible Instrument Concept*

K. Nishioka, D. Cauffman, B. Jurcevich, D. Mendez, and J. Ryder

*Future Investigations of the Near-Earth Environment*

W. H. Kinard

*MIR Plans*

K. Nishioka, C. Maag, and F. Hörz

**DISCUSSION: THE FUTURE OF COSMIC DUST INSTRUMENTS**



# Contents

---

Summary of Technical Sessions .....	1
Abstracts .....	5
Comet Coma Sample Return Instrument <i>A. L. Albee, D. E. Brownlee, D. S. Burnett, P. Tsou, and K. T. Uesugi</i> .....	5
SOCER—Comet Coma Sample Return Mission <i>A. L. Albee, K. T. Uesugi, and P. Tsou</i> .....	7
The Status of Measurement Technologies Concerning Micrometer and Submicrometer Space Articulate Matter Capture, Recovery, Velocity, and Trajectory <i>W. M. Alexander, W. G. Tanner, R. A. McDonald, G. E. Schaub, S. L. Stephenson,     J. A. M. McDonnell, and C. R. Maag</i> .....	11
Physics of Spacecraft-based Interplanetary Dust Collection by Impact into Low-Density Media <i>W. W. Anderson and T. J. Ahrens</i> .....	16
Plasma Produced by Impacts of Fast Dust Particles on a Thin Film <i>S. Auer</i> .....	21
Highly Transparent and Rugged Sensor for Velocity Determinations of Cosmic Dust Particles <i>S. Auer and F. O. von Bun</i> .....	25
Main Characteristics of the COMET/COMRADE Experiments <i>J. Borg, J-P. Bibring, and C. Maag</i> .....	29
The Hypervelocity Impact Facilities at the University of Kent at Canterbury, UK <i>M. Burchell, J. A. M. McDonnell, M. J. Cole, and P. R. Ratcliff</i> .....	32
IRAS Observations Show that the Earth is Embedded in a Solar Ring of Asteroidal Dust Particles in Resonant Lock with the Planet <i>S. F. Dermott, S. Jayaraman, Y.-L. Xu, and J.-C. Liou</i> .....	35
Collection Requirements for Trace-Element Analyses of Extraterrestrial Samples <i>G. J. Flynn and S. R. Sutton</i> .....	36
Laboratory Simulation of Intact Capture of Cometary and Asteroidal Dust Particles in ISAS <i>A. Fujiwara, A. Nakamura, and T. Kadono</i> .....	38

Techniques for In Situ Collection and Measurement of Volatiles Released During Hypervelocity Impact <i>R. A. Heppner, W. Niu, and C. R. Maag</i> .....	39
Penetration Experiments in Aluminum and Teflon Targets of Widely Variable Thickness <i>F. Hörz, M. Cintala, R. P. Bernhard, and T. H. See</i> .....	42
Some Considerations on Velocity Vector Accuracy in Dust Trajectory Analysis <i>A. A. Jackson and H. A. Zook</i> .....	48
Velocity Distribution of Earth-crossing Asteroid Grains <i>J. C. Liou and S. F. Dermott</i> .....	54
The Intact Capture of Hypervelocity Dust Particles Using Underdense Foams <i>C. R. Maag, J. Borg, W. G. Tanner, T. J. Stevenson, and J.-P. Bibring</i> .....	56
SPICE: An Innovative, Flexible Instrument Concept <i>K. Nishioka, D. P. Cauffman, B. Jurcevich, D. J. Mendez, and J. T. Ryder</i> .....	61
Charge Collection During Hypervelocity Penetrations of Thin Foils <i>R. Peterson</i> .....	64
Scientific Objectives of the Primitive Body Sample Return Missions—An Approach from the Light-induced Effect on Water Vapor <i>M. Shimizu</i> .....	76
Penetration of Multiple Thin Films in Micrometeorite Capture Cells <i>C. G. Simon</i> .....	77
Assessment of Velocity/Trajectory Measurement Technologies During a Particle Capture Event <i>W. G. Tanner, C. R. Maag, W. M. Alexander, and S. Stephenson</i> .....	79
Nondestructive Time-of-Capture, Location, and Velocity Sensing in Intact Capture <i>P. Tsou</i> .....	84
The Physics of Intact Capture <i>P. Tsou, D. J. Griffiths, and A. L. Albee</i> .....	85
PVDF Flux/Mass/Velocity/Trajectory Systems and Their Applications in Space <i>A. J. Tuzzolino</i> .....	89
The Use of Silica Aerogel to Collect Interplanetary Dust in Space <i>M. E. Zolensky, R. A. Barrett, and F. Hörz</i> .....	94
List of Workshop Participants .....	99



## Summary of Technical Sessions

**Introduction:** Planetary scientists have long recognized that a tremendous advance in the understanding of the early history of the solar system and its evolution will be possible when asteroidal and cometary dust grains can be captured at the Earth in a state permitting laboratory analysis, with accurate velocity and trajectory information on each grain to reveal its origin. This truly significant goal was made manifest by the selection of the Cosmic Dust Collection Facility (CDCF) to be one of the initial two Facility Class attached payloads for the space station. The recent redesign of the space station led to cancellation of CDCF, which in turn caused considerable uncertainty regarding ongoing instrument development. Accordingly, the current workshop was organized, at the request of NASA Headquarters, Solar System Exploration Division Code SL, to address the following three questions:

1. What are the state-of-the-art technologies for the least destructive capture of hypervelocity particles in space and for the measurement of their velocities and trajectories?
2. Where should resources be invested to advance immature technologies?
3. To what specific spacecraft mission(s) can these technologies be applied and which flight opportunities are scientifically justified?

This workshop assembled most of the individuals and/or teams currently developing the technology, at the subsystem level, for successful particle recovery and trajectory sensor development, including theoretical efforts to understand the orbital evolution of small asteroidal and cometary particles. Most of the 45 attendees were participants in the development of CDCF and/or the analysis of LDEF surfaces. Some DOD and DOE interests were represented as well. Attendees were given the opportunity to present the latest results from both laboratory simulations and actual spaceflight experience. Each participant presented detailed results, indicated the current limits of specific technologies, and made suggestions regarding the targeting of future resources toward immature technologies. They then listed the specific planned or proposed missions to which the particular technology was applicable. To facilitate this last discussion, presentations were made concerning the following potential missions: SOCCER, LDEF II, EURECA II, MIR attachments, and space shuttle payloads. The workshop was divided into four broad topics, as they appear below. Important workshop conclusions and recommendations appear in boldface.

**Parent-Daughter Orbit Divergence:** S. Dermott, A. Jackson, and J. Liou presented the results of particulate orbital evolution calculations, which are necessary to determine particular sources from velocity/trajectory measurement. The speakers agreed that most cometary particles should be distinguishable from most asteroidal particles since the

former will generally encounter the Earth with significantly higher relative velocities and orbital eccentricities. Some particles may evolve into orbits that may be compatible with either asteroids or cometary sources. These theoretical insights into the orbit divergence of small particles and their massive parent objects represent substantial progress in the scientific justification of Earth-orbiting flight instruments. **These calculations demonstrate that extraterrestrial materials from known astrophysical sources may indeed be collected in Earth orbit. However, in order to make these distinctions for the majority of particles, particle velocity must be measured to 10% accuracy and angular resolution to some 5°. Distinction of individual, collisionally produced asteroid families is possible as well, yet trajectory sensing must be better than 1% and 1°.** The former requirements ( $<10\%$  and  $<10^\circ$ ) seem readily attainable with current technology, yet the  $<1\%$  and  $<1^\circ$  requirements mandate state-of-the-art technology and substantial electronic system development, while technically attainable, substantial cost impacts are expected for the high-resolution instrument.

Predictions differed concerning the relative contribution of cometary vs. asteroidal particles to be encountered in Earth orbit. Dermott and Liou predicted 70% cometary particles, while Jackson and Zook predicted 30%. Both groups agreed that future calculations need to take the gravitational focusing of the Earth into account, while both also agreed that this effect would be too minor to resolve their differences. Dermott reported evidence indicating that the Earth shares its orbit with a permanent ring of small ( $<100\ \mu\text{m}$ ) asteroidal particles, which are concentrated directly behind the Earth. Calculations indicate that this particle concentration is closest to the Earth in September, suggesting that **there might be a temporal variation in the number of asteroidal particles collected at the Earth.**

**Velocity/Trajectory Measurements:** Three major approaches to measure the trajectory of individual particles were summarized. S. Auer proposed measuring the passage of naturally charged particles through a series of biased wires of known, three-dimensional geometry. In principle, this is the only trajectory sensor that does not physically disturb and interact with the particle to be measured, although a working model may require some sort of plasma shielding that could disrupt particles. Auer tested various subsystems at the Heidelberg Van de Graaff accelerator and performed drop-tests at low velocities. Experiment and theory agree remarkably well. The major recognized problems with this approach relate to the expected measurement of small induced charges, possibly as small as  $10^{-16}\ \text{C}$ , in an environment of poorly defined electrical noise levels; however, state-of-the-art amplifiers may solve this problem.

T. Tuzzolino reported on his latest polyvinylidene fluoride (PVDF) sensor. PVDF is a foil material that is polarized during manufacture; rearrangement or physical loss of dipoles during impact results in measurable change of the total polarity. The detector principle has been extensively tested at Heidelberg and in the Munich Plasma Drag Gun. There seem to be few technology problems with this sensor type, and there is flight experience with it, but the polarized foil is relatively thick (2–6  $\mu\text{m}$ ), and this sensor therefore seems best suited for large projectiles, typically  $>100 \mu\text{m}$  (smaller particles will not survive impact into the foil).

R. Peterson summarized the plasma sensor development at the Johnson Space Center (JSC), largely based on experiments with a 5-mm light gas gun and some preliminary tests conducted at the Van de Graaffs of the Max-Planck-Institute (MPI) in Heidelberg and the Los Alamos National Laboratory (LANL). The biased wire detectors collect the impact-triggered plasma. Velocity measurement to  $<1\%$  precision seems achievable, and positioning sensitivity to some 1 cm was achieved by the current design. However, the total charge collected is highly variable due to secondary charges generated when crater ejecta (neutral vapor, melts, or solids) impinge on the collector wire; these secondary effects can dominate the entire signal.

W. Tanner summarized plasma collection experiments at the University of Kent (Canterbury, UK) Van de Graaff accelerator that yielded similar results to those of Auer and Peterson. Emphasis of Tanner's presentation was on the conceptual design of a flight instrument, which differs, however, in signal amplification and processing from those proposed by Auer and Peterson.

An important component of velocity/trajectory sensor development is the ground testing in existing hypervelocity facilities. Testing of reasonable projectiles at velocities up to approximately 7 km/s is readily available, but C. Simon identified the facility at Auburn University as attaining velocities up to 13 km/s. Continued ground testing of sensor devices at these higher velocities is clearly desirable before flight.

Each of the trajectory sensor designs is considered to be relatively mature and ready for flight development. It seems inefficient and costly, however, to advance three detector concepts simultaneously, although each has its specific benefits and drawbacks. As the charged particle detector appears now to be scientifically the most superior, it should be developed to the state where meaningful tests regarding its sensitivity limits can be performed in orbit. Such tests could be at the subsystem level and may not require a complete detector. The space shuttle is a good vehicle to perform such tests (on gas cans or the manipulator arm). If these tests disqualify the charged particle detector concept, then the alternate design can be tested.

As both charged particle and plasma detectors rely on the measurement of very small charges, there is substantial over-

lap in the area of signal acquisition and associated electronic design. Development of the charged particle sensor will, therefore, invariably include substantial advancements in the plasma detector as well. The charged particle detector is the more demanding device, and if it tests unsuccessfully in Earth orbit, the plasma sensor may substitute readily.

**Capture Media Development:** Numerous investigators presented results of laboratory and flight testing of particulate capture media. Two capture philosophies currently predominate. The first involves low-density, high-porosity media (underdense,  $<<1 \text{ g/cc}$ ), with the leading contenders being aerogels and plastic foams. Plastic foams (such as polystyrene and polyethylene) are very stable for handling purposes, can be made at low densities, and cell sizes and wall thicknesses can be easily tailored (see the papers by P. Tsou and C. Maag). These materials are also relatively strong. However, shortcomings of plastic foam include extreme difficulty in locating captured particles and organic contamination of the particle residues. **Although some degree of organic contamination is probably inevitable from these materials, it may be possible to develop a reliable technique for the removal of captured particle residues.**

Aerogels have finer microstructures ( $\sim 50 \text{ \AA}$ ) than plastic foams, and can be made in exceedingly low densities ( $<0.001 \text{ g/cc}$ ). They are more fragile than plastic foams, but can be rendered essentially organic free, and their transparency makes particle residue removal straightforward (see the papers by Zolensky et al. and Tsou). Most development has centered on silica aerogels, which is unfortunate because these have relatively strong intragranular bonding, making the particle capture process more abrasive (see the paper by W. Anderson). L. Hrubesh and D. Mendez pointed out that **other aerogel compositions might offer superior properties, and these leads should be actively pursued.** It should be noted that all reasonable particle analog materials used in aerogel impact tests to date were significantly fractured, shocked, and/or melted during capture. However, **critical chemical, mineralogical, and physical information can be extracted from the particle residues, with proper effect.** Ideally, these foamed materials would sit at the bottom of capture cells, with the incoming particles first passing through transparent velocity/trajectory sensors.

The second capture medium philosophy involves thin films. The main problem with thin films is that the particles are not preserved as well as they are with foamed media. However, for some analytical investigations this is not a severe problem (see papers by R. Walker and C. Simon). Also, these designs can be easily integrated with the velocity/trajectory measurement devices requiring thin-film penetrations. Thin-film designs feature either (1) single foils, covering a capture cell where the particle eventually impacts a flat plate, or (2) stacked foils to gradually decelerate a particle. The first design is preferred over the underdense media by some workers interested in isotopes because most of



the information they require can be extracted from vapor deposits, and the sample is ideally situated for analysis (see paper by R. Walker). A. Fujiwara presented results of impact experiments into gas-filled capture cells, where the gas facilitates the deceleration of the particles.

Workshop participants recognized that no current capture medium can capture silicate particles at reasonable velocities ( $>5$  km/s) in completely unbroken (intact) state. Nevertheless, it is now known that the important measurements can successfully be made on the broken remnants for velocities exceeding 7 km/s. Experiments yet to be performed will demonstrate the upper velocity cutoff for this capability. However, at some (still undefined) higher velocities significant loss of scientific information is inevitable if only vaporized residues are available; in this case capture cells employing thin films may be superior to highly porous materials (in terms of providing easily analyzable substrates). **Accordingly, investigation of both capture cells employing porous materials and those with thin films should continue.**

Numerous investigators presented the results of actual flights of capture cells on LDEF (R. Walker, H. Zook, D. Brownlee), the space shuttle (P. Tsou, C. Maag), and the European Recoverable Carrier (EURECA) (W. Tanner). The impact residues from LDEF are only now, after considerable effort, beginning to provide useful information concerning the nature of particulates encountering Earth. The experience gained during this work will be valuable in second-generation LDEF II particle capture cells. Unfortunately, no underdense media were flown on LDEF, only flat plates and single or multiple foils. Silica aerogels have repeatedly been flown on the space shuttle and EURECA, and impacting particles have been captured; however, these have yet to be analyzed. EURECA results were too preliminary to be considered here, but it was recognized that EURECA should provide a wealth of information on the operation of thin-film and silica aerogel capture cells. **A general conclusion of the workshop was that any flight opportunity for particle capture cells should be pursued, provided it is properly justified on scientific or engineering grounds, and followed by complete analysis of the captured particle residues preparatory to succeeding flights.**

R. Walker made the important point that the continued development of new analytical technologies makes possible new and better measurements, and given these advances (which, however, cannot be assumed), **all past flight experi-**

**ments (in particular the LDEF) will be a resource for the future.**

**Future Flight Opportunities:** The final portion of the formal workshop program involved the description of future flight opportunities. This information is critical since future proposals to NASA for funding of capture cell velocity/trajectory sensor development may need to be tied explicitly to specific missions.

K. Uesugi (ISAS) discussed the possibilities for the Sample of Comet Coma for Earth Return (SOCCER) mission, which would return dust samples from a comet following a flyby at 7–10 km/s. Uesugi and Shimizu **underscored the need for laboratory verification of the concept of recovery of significant particle residues at impact velocities of at least 10 km/s. These tests should be performed as soon as practical.** This laboratory verification must precede approval of the SOCCER mission by ISAS. At the present time, laboratory experiments using reasonable projectiles have only been performed at velocities up to  $\sim 7$  km/s (Zolensky et al.). The space shuttle should not be considered an optimum testing platform due to limited collection periods (of up to two weeks per flight), but its continuous use can still make it attractive for device testing. K. Nishioka and C. Maag presented scenarios for flying collection cells on MIR. M. Zolensky discussed the preliminary concept for LDEF II, which is presently planned to be a smaller version of the original LDEF, with mainly cosmic ray and solar energetic particle detectors, although there would be ample opportunity for particle collection cells. LDEF II may be proposed as a Discovery mission. Other potential flight opportunities identified were space shuttle and EURECA II (whose prospects are unknown, as for LDEF II). The planned U.S. space station (ALPHA, currently) remains a viable platform and suitable utility ports are part of the redesign; also, the Japanese and European habitat modules have exterior payload capability.

The recent cancellation of the Cosmic Dust Collection Facility has had the unfortunate result of removing the framework that successfully set scientific standards for developing dust capture media, sensors, and cells, and monitored their progress. As a result, **there is a need for future meetings or workshops (such as this one) to permit economical and efficient further development of these technologies. Organization of a successor committee to the CDCF Working Group may be desirable if continued coordination of the instrument is a truly desirable goal.**



## Abstracts

**COMET COMA SAMPLE RETURN INSTRUMENT.** A. L. Albee<sup>1</sup>, D. E. Brownlee<sup>2</sup>, D. S. Burnett<sup>1</sup>, P. Tsou<sup>3</sup>, and K. T. Uesugi<sup>4</sup>, <sup>1</sup>California Institute of Technology, Pasadena CA 91109, USA, <sup>2</sup>University of Washington, Seattle WA 98195, USA, <sup>3</sup>Jet Propulsion Laboratory, Pasadena CA, USA, <sup>4</sup>Institute of Space and Astronautical Science, Sagami-hara, Japan.

**Introduction:** Comets have preserved volatiles and refractory materials that were in the outer regions of the solar nebula. The study of comets and, more especially, of material from them provides an understanding of the physical, chemical, and mineralogical processes operative in the formation and earliest development of the solar system. Bringing samples back from within the zone of parent molecules of a known comet will provide valuable information on comets, will serve as a rosetta stone for the analytical studies of interplanetary dust particles for the last two decades, and will provide much needed samples for the analysis community. The intact capture and return of cometary coma material, both dust and volatiles, has an advantage over orbiter and rendezvous missions in that the captured material can be made available to all complex, sophisticated laboratories here on Earth. Samples, if properly stored and preserved, can also be examined by analytical techniques, presently unknown but almost surely to be developed in the future.

**Sample Return Science:** The scientific goals of this Flyby Sample Return are to return coma dust and volatile samples from a known comet source, which will permit accurate elemental and isotopic measurements for thousands of individual solid particles and volatiles, detailed analysis of the dust structure, morphology, and mineralogy of the intact samples, and identification of the biogenic elements or compounds in the solid and volatile samples. Having these intact samples, morphologic, petrographic, and phase structural features can be determined. Information on dust particle size, shape, and density can be ascertained by analyzing penetration holes and tracks in the capture medium. Time and spatial data of dust capture will provide understanding of the flux dynamics of the coma and the jets. Additional information will include the identification of cosmic ray tracks in the cometary grains, which can provide a particle's process history and perhaps even the age of the comet.

The measurements will be made with the same equipment used for studying micrometeorites for decades past; hence, the results can be directly compared without extrapolation or modification. The data will provide a powerful and direct technique for comparing the cometary samples with all known types of meteorites and interplanetary dust. This sample collection system will provide the first sample return from a specifically identified primitive body and will allow, for the first time, a direct method of matching meteoritic materials captured on Earth with known parent bodies.

It is important to target SOCCER to within 100 km of the comet nucleus in order to ensure that sample collection takes place within the zone of parent molecules. While water molecules will resist photodissociation out to great distances, more fragile molecules like CS will be dissociated at distances of the order of a few hundred kilometers from the comet nucleus, for an encounter distance of 1 AU from the Sun.

**Sample Collection Technology:** Cometary coma sample collection makes use of distinct and different techniques for solid

particles and volatiles. The fundamental technology for capturing hypervelocity solid dust particles intact has been under development at JPL since 1984. Today, submicrometer particles can be captured intact at speeds up to 10 km/s. Experiments, conducted in 1987, have also demonstrated the efficacy of physisorption of noble gases on passive foil under cometary encounter conditions.

**Dust collection technology.** The development of cometary flyby sample return technology was triggered by the Halley Sample Return Mission (HSR) [1]. Due to the 70-km/s encounter speed with Comet Halley, only an atomized sample return was considered for HSR. The need for and the value of capturing dust intact was made apparent by subsequent validation of atomized sample collection [2]. The capture of solid dust particles is rooted in intact capture technology—the ability to capture solid particles, intact, at hypervelocities. At first, hypervelocity “intact” capture was thought to be impossible. Since the demonstration of intact capture [3], a wide range of capture media has been systematically explored [4], finding that passive underdense media in the form of certain foams perform the best [5].

Microcellular underdense polymer foams can capture solid 1.6-mm Al projectiles with 95% of the original mass recovered intact and unmelted at 6 km/s [4]. Glass spheres 5–50  $\mu$ m in diameter have been similarly recovered intact in the 6-km/s speed range [6]. Iron grains have been captured intact in the submicrometer range to beyond 10 km/s [7]. Transparent and ultramicrocellular aerogel was introduced for optical visibility of micrometer-sized captured particles [6]. The effect of the capture medium's mesostructure on intact capture is being investigated and analyzed [8,9]. Clearly, the technology of intact capture of hypervelocity projectiles by passive underdense media has been proven.

The capability to fabricate clear aerogel in 10 cm  $\times$  10 cm  $\times$  1 cm cell size has been developed at JPL. Since no number of laboratory simulations can substitute for a realistic space environment, concerted efforts have been made to gain space test opportunities. An intact capture experiment with aerogel capture cells has been flown on STS 47 and STS 57 in September 1992 and June 1993 respectively, with 20–30 mg/ml density aerogel cells made at JPL.

**Volatiles collection technology.** Two approaches have been conceptualized for volatile capture: physisorption and chemisorption. Initial experiments of physisorption of noble gas under a simulated cometary flyby encounter environment proved surprisingly successful [10]. A simple device for capturing volatile species consists of a getter freshly deposited by electroevaporation just before the coma flythrough, with a second, sealant surface deposited over the collected volatiles at the end of the collection period. A similar technique is used in the energetic particle composition and interstellar gas experiment (GAS) on board Ulysses. The surface area for each type of volatile will be about 100 cm, allowing for some damage by dust impact.

Other techniques commonly used to collect volatiles in the Earth's environment can be adapted for cometary sample collection. For example, there are adsorbents already known to serve the physisorption of organic compounds. Examples of such adsorbents are silica gel, alumina, and activated C. On the other hand, chemisorption makes use of absorbent compounds to react with selected volatiles. An example is NaOH used to detect Co and CO<sub>2</sub>.



**Instrument Concept:** The comet coma sample return instrument serves a dual function, science and engineering, in that the sample instrument will serve as a dust shield for the entire spacecraft system during encounter.

**Sample collection system.** The current collection concept for SOCCER [11] has evolved through a sequence of previous studies: HSR [12], Planetary Explorer, Comet Intercept Sample Return [13], ESA/NASA Giotto II [14], Comet Dust Intact Capture Explorer [15]; space station attached payloads experiments: Intact Particle Capture Experiment [15], Cosmic Dust Intact Capture Experiment [16], Interstellar Dust Intact Capture Experiment [17], Exobiology Intact Capture Experiment [18], Second Generation Space Station Cosmic Dust Collection Concept Development, and finally, the Shuttle Get-Away Special Sample Return Experiment [19]. The sample collection system consists of designated regions for dust collectors and volatiles collectors. An artist's rendition of the sample collection system, during encounter is shown, not to scale, in Fig. 1. Many of the engineering details have yet to be defined, but the sketch provides an overall perspective of the collection system. All collector regions will be modular in design. Dust collectors must allow for depth of penetration and so will be cubic in shape, whereas volatile collectors and fine dust impactors will be flat surfaces.

**Sample collection system goals.** Most dust particles will be very small grains, but the large particles will contribute the greatest mass. Thus, for sample collectors, the large particles will be of the greatest scientific value. The goals of the sample collection system are stated quantitatively as follows: (1) to collect intact at least 10 large dust particles (0.5–1 mm in diameter); (2) to collect intact at least 100 medium dust particles (10–100  $\mu\text{m}$  in diameter); (3) to collect intact at least 10,000 small dust particles (0.1–5  $\mu\text{m}$  in diameter); and (4) to collect at least 10 fluence molecules/cm of volatiles.

These goals are to be achieved under a set of desired constraints: (1) to minimize contamination among collected samples; (2) to permit temporal and spatial identification of the samples collected; (3) to maintain an environment for preserving the condition of the samples at the time of capture; (4) to allow significant depth in all intact collection media so as not to preclude large dust particle capture; and (5) to protect against impact damage to the spacecraft and collection system mechanisms.

**Dust sample collection.** The size and location of the dust collectors are allocated according to the expected flux of samples, the collection goals stated above, and the validated capture efficiency of the collection media. A portion of the surface area is reserved for novel collector concepts, as yet not fully validated. Silica aerogel at 20–30 mg/ml density is the primary candidate underdense medium for dust collection. Modular collection cells of 10 cm  $\times$  10 cm  $\times$

10 cm cube facilitate fabrication, handling, and replacements. The dust collection cubes are placed on top of a gridded polyvinylidene fluoride film to provide a nondestructive acoustic capture signal recording the time and location of the capture. Information of the temporal and spatial distribution of captured particles will enable the reconstruction of jetting dynamics relative to dust flux profiles. In order to maintain cleanliness, the collectors are kept covered and sealed, before and after the encounter, with purge gas to maintain a fixed partial pressure within the collector compartment.

The flux of large particles is expected to be low; however, since the science value of large particles is immensely greater, the depth of the dust collection cells will be dictated by the desire to capture large particles. The very small particles will have very high flux; consequently, ultrafine-mesostructure capture media dedicated to fine particles need only have a small surface area. Although sample fragmentation is expected for solid soft metal collection surfaces, for very fine dust, less than a micrometer, embedded fragments will be concentrated and offer easier analysis.

For a very close encounter with a comet nucleus of about 10 km, there is a possibility of capturing trapped nonvolatilized organics or interstitial frozen volatiles embedded within conglomerated particles; thus, some portion of the collection region will be refrigerated to a temperature of 140 K. In this cool environment, volatiles generated during capture or captured volatiles can be best preserved. This temperature can be maintained by placing these collectors in double-walled compartments. The outer compartments are maintained at 200 K and 300 K, respectively, by passive radiators. Due to the excellent insulation properties of underdense media, active refrigeration by means of a cooler is necessary only after Earth insertion, during aerobraking, and Earth descent; fortunately power will be plentiful at 1 AU.

**Volatiles sample collection.** The area allocated for physisorption of volatiles will be determined by the capture efficiencies of the capture media and the expected gas flux to be captured. Due to the need to maintain ultrapure getters for physisorption, each capture surface will be freshly deposited, just before encounter, by electro-vaporization of an ultrapure filament on ultrapure semiconductor grade Si or Ge (see Fig. 2). After the encounter, a sealer will be vapor deposited to prevent escape of trapped volatiles and to prevent external contamination. Since the flux of volatiles will be quite high, the total surface area allocated to the collection of volatiles will be small (hundreds of centimeters). For active volatile species, chemisorption will be used as the capture mode. These active capture cells will be uncovered during encounter and sealed afterward to prevent further reactions or contaminations. Capturing molecular volatiles may not be possible due to the capture energy being greater than the molecular binding energy, but this is under study. The collection surface requires a field of view along the ram direction during collection. A second field of view for a radiator for cooling the getter surface will also be required.

**Summary:** As was stated in the Solar System Exploration Committee's report of 1983, the next step in cometary exploration following the flyby missions to Comet Halley should be a rendezvous and sample return with a short-period comet. Without Mariner Mark II Comet Rendezvous and Asteroid Flyby Mission, it is all the more critical to the achievement of the goals of the Solar System Exploration Committee that a comet coma sample return be accomplished. Through a joint effort with ISAS, it is cost effective for both NASA and ISAS to acquire thousands of samples from a known

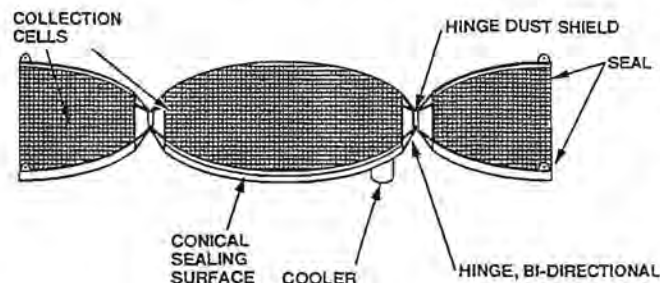


Fig. 1. Dust collector at encounter phase.

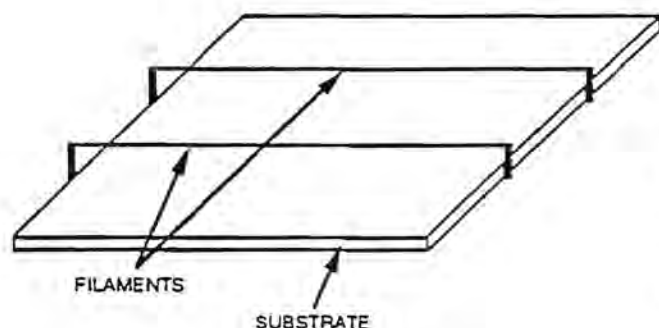


Fig. 2. Physisorption.

comet and thousands of images of a comet nucleus and dynamics of that comet coma at half the cost for each agency. This instrument will make available for analysis not only the only extraterrestrial samples from a known source since the Apollo missions, but specifically cometary material captured in the zone of parent molecules. Such material rates highest among all solar system objects for study of the planetary evolution and that of compounds and phases containing the biogenic elements.

**References:** [1] JPL (1991) *JPL 715-140*. [2] Tsou P. et al. (1983) *International Conference on Cometary Exploration, Vol. II*, 215–224. [3] Tsou P. et al. (1984) *LPS XV*, 866–867. [4] Tsou P. et al. (1989) *LPS XX*, 1132–1133. [5] Tsou P. et al. (1987) *LPS XVIII*, 1026–1027. [6] Tsou P. et al. (1988) *LPS XIX*, 1205–1206. [7] Tsou P. et al. (1992) *LPS XXIII*. [8] Tsou P. et al. (1991) *LPSC XXII*. [9] Griffiths D. J. et al. (1991) *J. Appl. Phys.*, 70, 4790–4796. [10] Tsou P. et al. (1987) *LPS XVIII*, 1024–1025. [11] Tsou P. (1990) *JPL D-7777*. [12] Tsou P. et al. (1983) *LPS XIV*, 794–795. [13] Tsou P. et al. (1983) *JPL D-1153*. [14] Tsou P. et al. (1985) *AIAA-85-0465*. [15] Brownlee D. E. (1988) *Proposal to The Small-Class Explorer Program*. [16] Brownlee D. E. (1969) *Proposal to Space Station Attached Payload Program*. [17] Brownlee D. E. (1989) *Proposal to Space Station Attached Payload Program*. [18] Carle G. (1989) *Proposal to Space Station Attached Payload Program*. [19] Tsou P. et al. (1993) *LPS XXIV*.

#### SOCCKER—COMET COMA SAMPLE RETURN MISSION.

A. L. Albee<sup>1</sup>, K. T. Uesugi<sup>2</sup>, and P. Tsou<sup>3</sup>, <sup>1</sup>California Institute of Technology, Pasadena CA 91109, USA, <sup>2</sup>Institute of Space and Astronautical Science, Sagami-hara, Japan, <sup>3</sup>Jet Propulsion Laboratory, Pasadena CA, USA.

Comets, being considered the most primitive bodies in the solar system, command the highest priority among solar system objects for studying solar nebula evolution and the evolution of life through biogenic elements and compounds. Sample Of Comet Coma Earth Return (SOCCKER), a joint effort between NASA and the Institute of Space and Astronautical Science (ISAS) in Japan, has two primary science objectives: (1) the imaging of the comet nucleus and (2) the return to Earth of samples of volatile species and intact dust. This effort makes use of the unique strengths and capabilities of both countries in realizing this important quest for the return of samples from a comet. Science from this mission will far exceed the Atomized Comet Sample Return Mission, a NASA Core Program of

Planetary Exploration Through Year 2000 [1]. Without the Comet Rendezvous and Asteroid Flyby (CRAF) mission, it is all the more critical to realize SOCCKER.

**Introduction:** The intact capture and return of cometary coma material, both dust and volatiles, has an advantage over orbiter and rendezvous missions in that the captured material can be made available to all complex, sophisticated laboratories here on Earth. Samples, if properly stored and preserved, can also be examined by analytical techniques, presently unknown but almost surely to be developed in the future. Lander- or rendezvous-type of sample return missions require rather complex spacecraft, intricate operations, and costly propulsion systems. By contrast, it is possible to take a highly simplified approach for sample capture and return in the case of a comet. This can be accomplished by an Earth free-return trajectory to the comet, in which passive collectors intercept dust and volatiles from the cometary coma. Bringing samples back from within the zone of parent molecules of a known comet will provide valuable information on comets, will serve as a rosetta stone for the analytical studies of interplanetary dust particles for the last two decades, and will provide much needed samples for the analysis community.

The Halley Sample Return (HSR) Mission was the first comet coma sample return mission studied by the Jet Propulsion Laboratory (JPL) in 1981. SOCCKER was initiated with this proposal team associated with the National Aeronautics and Space Administration (NASA) and the Institute of Space and Astronautical Science (ISAS) in Japan. This effort makes use of the unique strengths and capabilities of both countries in realizing this important quest for the return of samples from a comet, and in sharing the cost and the science findings. SOCCKER has two primary science objectives: nucleus imaging and dust and volatiles sample return. SOCCKER can achieve first-class science by being the first mission to bring back samples from a known comet, and by obtaining high-quality close-up images of a comet nucleus. Science from this mission will far exceed the Atomized Comet Sample Return Mission, a NASA Core Program of Planetary Exploration Through Year 2000 [1].

**Comet Coma Sample Return Background:** Interest in cometary missions began in the early 1970s. The first JPL mission proposed was the Halley Flyby with a Probe and Tempel Rendezvous (HFPTR) mission [2]. The development of cometary flyby sample return technology was triggered by the JPL's HSR mission [3]. Due to the 70-km/s encounter speed with Comet Halley, atomized sample return rather than intact sample return was considered for HSR. The first comet coma sample return mission with intact capture was jointly proposed with Goddard Space Flight Center (GSFC) as a NASA mission for the Planetary Observer Program and proposed direct reentry via a Discoverer Capsule [4]. Mission costs from GSFC and JPL were compared [5]. Using the spare Giotto spacecraft, JPL proposed Giotto II jointly with the European Space Agency (ESA) [6]. Based upon the Giotto II concept, an ESA Comet Atmosphere Encounter and Sample Return (CAESAR) was studied in 1986 [7]. Since 1987, low-cost flyby sample return missions to comets, SOCCKER, have been jointly studied in U.S. and Japan [8].

**SOCCKER mission.** NASA's interest in comets has been reflected in four major JPL efforts beginning with the HFPTR, Halley Intercept Mission, HSR, and finally the recently canceled Mariner Mark II Comet Rendezvous and Asteroid Flyby (CRAF) mission [9]. The high percentage of comets with Japanese surnames clearly indicates the interest of the Japanese in comets. For some time now,



ISAS has demonstrated its unique ability to develop low-cost spacecraft for a variety of missions (SUISEI and SAKIGAKE to Halley, HITEN to the Moon, GEOTAIL to the distant geomagnetic tail). The dominant video and camera industries in Japan give ISAS a strong basis for developing an imaging camera system. Since 1981, JPL has developed the enabling technology for flyby sample return-intact capture of hypervelocity particles [10], and validated techniques for the capture of volatiles [11]. NASA has an operational shuttle capable of retrieving objects in low Earth orbits, and its Deep Space Network (DSN) can track deep-space signals around the clock. JPL has mounted sophisticated missions throughout the solar system. Consequently, both NASA and ISAS have common interests in exploring comets and unique capabilities, and SOCCER has been conceived as a joint mission taking advantage of each agencies' strengths. In a tight funding environment, the total cost of a comet flyby sample return mission can be shared, making the acceptance of such a mission easier for both countries.

**SOCCER joint working group.** The first meeting of this current NASA/ISAS proposal team was held in Japan [12]. The team was formally installed as a joint study group [13], subsequently promoted to a joint working group, and met again at ISAS [14]. The second working group meeting was held jointly with the Japan-U.S. Workshop on Missions to Near-Earth Objects [15], and the third working group's meeting was held in May 1992 [16].

The working division of responsibility between NASA and ISAS follows designated capabilities. The imaging system and radio science will be provided by ISAS; NASA will provide the sample collection system. The spacecraft will be designed and built by ISAS, and launched by an ISAS M-V, three-stage solid propellant rocket with a NASA medium-expendable launch vehicle (MELV) as backup. The returned samples will be retrieved by the shuttle. Operations will be led by ISAS, supported by NASA, for launch, cruise, tracking, navigation, encounter, Earth insertion, and aerobraking.

**SOCCER Science Payloads:** Each part of the SOCCER science payload serves a dual function, science and engineering: The imaging camera will perform navigation for comet locating and encounter targeting; the sample collector will serve as a dust shield for the spacecraft during encounter; and, of course, the radio transponders will serve for spacecraft communication as well as for radio science.

**SOCCER imaging system.** The closest image of a nucleus was obtained by Giotto, a spin-stabilized spacecraft. There is a need for images of much higher resolution. The world's first high-resolution imaging of the comet nucleus can be achieved by SOCCER using a three-axis stabilized platform. A charge-coupled-device (CCD) camera can achieve fine resolution of the dynamics of the comet nucleus surface in both the pre- and postperihelion stages. The goals of the SOCCER imaging system are the following: (1) obtain nucleus surface images at the closest distance with the greatest resolution; (2) obtain observatory, wide coverage of large-scale dynamic coma phenomena; and (3) obtain pre- and postperihelion images of the comet coma development at regular and frequent intervals beginning several months before encounter and extending several months after encounter.

The SOCCER camera will be an improved version of a solid-state camera designed for several ongoing ISAS flight programs. These include the Planet B mission to be launched to Mars in 1996, and the LUNAR-A mission to the Moon in 1997. The camera's

resolution will be specified to be 10  $\mu$ rad or better, with images being focused on a CCD having a field of at least  $1024 \times 1024$  pixels. Keeping the CCD cooled to approximately 200 K will ensure a large signal-to-noise ratio. With filter wheels, this CCD camera can capture both color imaging and surface spectral data. With the high-gain antenna oriented toward Earth, selected images can be transmitted in real time. To facilitate both pre- and postencounter imaging, wide-angle, as well as narrow-angle optics will be used.

**SOCCER sample return collection system.** The current collection concept for SOCCER [17] has evolved through a sequence of previous studies: HSR [18], Planetary Explorer, Comet Intercept Sample Return [18], ESA/NASA Giotto II [20], space station attached payloads experiments: Intact Particle Capture Experiment [21], Cosmic Dust Intact Capture Experiment [22], Interstellar Dust Intact Capture Experiment [23], Exobiology Intact Capture Experiment [24], Second Generation Space Station Cosmic Dust Collection Concept Development [25], and finally, the Shuttle Get-Away Special Sample Return Experiment [26]. The sample collection system consists of designated regions for dust collectors and volatiles collectors. Many of the engineering details have yet to be defined but the sketch provides an overall perspective of the collection system. All collector regions will be modular in sign. Dust collectors must allow for depth of penetration and so will be cubic in shape, whereas volatile collectors and fine dust impactors will be flat surfaces.

**Engineering Flight System:** The engineering system includes the spacecraft, dust shield, and an aerobrake cone to enable matching of the shuttle retrieval circular orbit from a highly elliptical Earth insertion orbit. The spacecraft and launch vehicle will be designed and fabricated by ISAS. ISAS has demonstrated the technique of aerobraking, having utilized it for HITEN's cislunar aerobraking in 1991. Sample return requires close targeting, which dictates the need for optical navigation in addition to ephemeris tracking. SOCCER's navigation capacity is examined below.

**SOCCER spacecraft description.** The SOCCER spacecraft is built around an octagonal bus as illustrated in Fig. 1. The sample collection system is mounted on one end of the bus with the aerobrake drag cone mounted on the other. Since the dust collector serves as the dust shield during the encounter, no part of the spacecraft will be within  $5^\circ$  from the edge of the collector. 250 W of power come

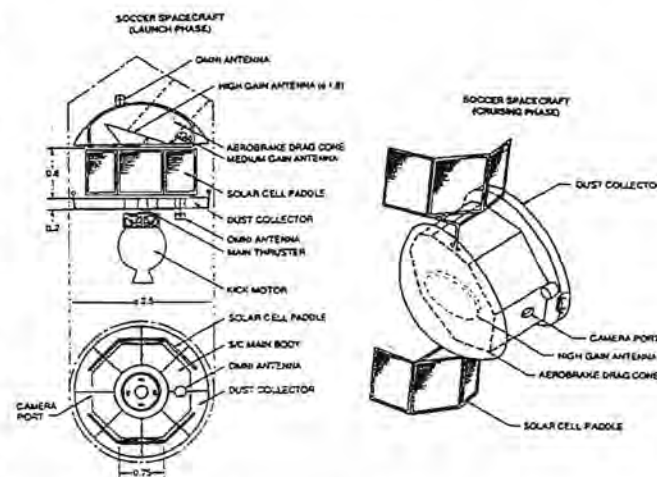


Fig. 1. SOCCER spacecraft.

from two articulated solar paddles that are wrapped about six flat faces of the bus during launch and encounter phases. The solar cells face outward to permit power generation during encounter and aerobraking phases. The articulated 1.8-m high-gain antenna, as well as the fixed medium- and low-gain antennae are mounted under the aerobrake cone shown in Fig. 1. The aerobrake cone will be composed of  $\text{SiO}_2$ , which is transparent to radio frequency transmission. On one of the uncovered bus faces, a camera port provides side field of view during encounter. A mirror to facilitate encounter imaging of the nucleus is under study. S- and X-band transponders, having 10 W and 25 W power, respectively, will provide uplink and downlink communications. At 2 AU, the data rate at X-band is about 32 kbps and 3 kbps at S-band with the 64-m antenna at Usuda. All midcourse trajectory correction maneuvers (TCMs) and Earth insertion burns will be accomplished by a bipropellant propulsion system with the main thruster mounted in the bus. Attitude control and spin control thrusters are mounted on the edge of the bus, between the bus and the aerobraking cone. The sample collection system will be separated for shuttle retrieval and placed in a cooled sample collector container aboard the shuttle. A standard shuttle grapple is mounted below and at the center of the aerobrake cone to facilitate spacecraft stabilization for sample collector removal.

**SOC CER launch system.** SOCCER will be launched by ISAS's newly designed M-V vehicle. In late 1994, the MUSES B mission will be the first launch to use this system. M-V is a three-stage solid propulsion rocket, 2.51 m in diameter and 31.4 m long. The vehicle can carry a two-ton payload to low Earth orbit. With a fourth stage kick motor, interplanetary missions can be accomplished.

**SOC CER navigation.** Reliance upon comet ephemeris alone will not suffice to achieve a targeting of the cometary nucleus better than 100 km. The uncertainties of cometary trajectories at successive apparitions are due to gravitational perturbations, as well as nongravitational effects arising from jetting, which generates the coma in the first place. With favorable orientation conditions of Earth, comet, and Sun, groundtracking of the comet can reduce the ephemeris error. It is more likely, however, that sample return targeting will require optical navigation. A prime determinant of the accuracy achievable by optical navigation is the camera's pixel size. Using a 9- $\mu\text{m}$ -sized pixel in a frame CCD camera, with an assumed ephemeris error of 750 km, and with TCM 1 and TCM 2 executed 10 days and 1 day before encounter, respectively, a delivery accuracy of 20 km can be achieved for a 10 km/s flyby speed. Figure 2 shows the delivery accuracy with respect to the time for the last TCM. Given this accuracy, the uncertainty in locating the nucleus within the coma will also need to be considered in specifying a flyby distance. For a very close flyby distance, less than 10 km, a pathfinder spacecraft would enhance the confidence; otherwise, a pathfinder would not be necessary.

**SOC CER Mission Description:** Important considerations in designing a free-return trajectory for SOCCER are a low encounter speed to enhance intact capture of dust samples, the restricted launch vehicle capability of ISAS's M-V rocket, and the need for a dependable trajectory of the targeted comet. Based upon these three considerations, the 2002 perihelion encounter with Comet Finlay has been selected as the baseline comet. A plot of this baseline trajectory to Finlay is shown in Fig. 3. The encounter speed for this trajectory is 7.98 km/s, which is within the range of speeds for which successful intact capture has been demonstrated (i.e., up to speeds of 13 km/s).

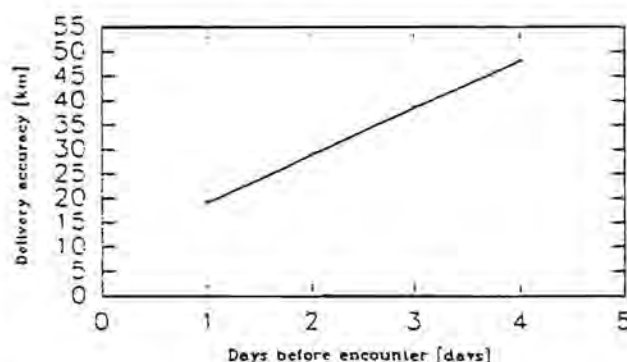


Fig. 2. Delivery accuracy (10 km/s flyby).

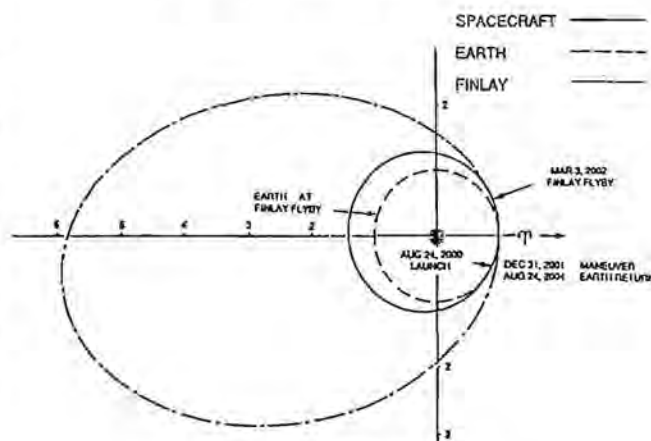


Fig. 3. SOCCER baseline trajectory.

**Cometary candidate.** Possible comet candidates for SOCCER in the 2000 time frame include Churyumov-Gerasimenko (2002), Wirtanen (2002), DuToit-Hartley (2003), Kopff (2003), and Finlay (2002). For this proposal Finlay, has been chosen as a baseline comet. Comet Finlay, known since 1886 and observed at 11 apparitions, has a well-determined and relatively stable orbit with perihelion just outside the Earth's orbit (near 1.1 AU) and a revolution period of slightly less than seven years. Since 1953, the comet has been observed at every return to the Sun with its orbital motion having been subjected to modest and somewhat variable nongravitational perturbations. However, the comet has a history of at least one major orbital anomaly, this occurring either late in the 19th century or early in this century [27].

Comparison of P/Finlay's lightcurve in 1960 (the only apparition since 1953 from which adequate information is available on the comet's brightness) with the lightcurves in and before 1926 indicates that the object's intrinsic fading has been dramatic, the peak normalized magnitude being 10 in 1960, compared with 6.5 in 1906, and 8 in 1886 and 1893. Brightness fluctuations with an amplitude of about one magnitude were reported during one week of intense observing shortly after perihelion in 1960, which suggests that the production was quite variable on a timescale of days. Still, this comet is considered to be a good candidate for particle collection.

**Mission scenario.** Ground and space telescopes would begin the tracking phase to acquire Comet Finlay before launch and continue



after launch to refine Finlay's orbit. After payload integration and tests, SOCCER will be launched by M-V on August 24, 2000, at Kagoshima Space Center. The kick motor will be ignited after the ejection of the third-stage motor of the M-V and will insert SOCCER into the heliocentric trajectory needed to encounter comet Finlay. During the pre-encounter cruise phase the solar cell paddles will be deployed and the spacecraft placed into spin stabilized mode. During cruise, the covers of the sample collectors will be kept closed. For the pre-encounter observation phase, the spacecraft will be despun for three-axis stabilization by the use of a momentum wheel and to initiate pre-encounter observation imaging science and optical navigation imaging to aid in precise orbit determination. A deterministic maneuver of 139 m/s will be performed on December 31, 2001. A week before encounter, the covers of the sample collection system will be opened. Final targeting from optical navigation update will be performed one day before the encounter. Before the encounter phase, which lasts for approximately one hour, volatiles capture getters will be deposited, solar paddles will be retracted, and the spacecraft will be poised for the encounter phase. A summary is shown in Fig. 4.

SOCCER's two primary science systems require a very close encounter with the comet nucleus to achieve good close-up imaging and to capture cometary samples with minimum processing. A target encounter distance of 10 km from the comet nucleus is highly desirable. Detailed study, involving orbit determination simulations (including the effect of center-finding error) and assessment of the coma environment, is necessary to determine the minimum feasible encounter distance. During the final encounter, nucleus images will be acquired at the maximum rate. The acoustic counter data along with some selected, compressed images will be processed and transmitted in real time. After the sealer getters are deposited and the mission begins the post-encounter observation phase, the sample collector covers will be closed. The solar paddles will be redeployed and observatory imaging will resume. The spacecraft will then commence the trip back to Earth. After having completed three orbits around the Sun in four years, the spacecraft returns to Earth on August 24, 2004.

After a final trajectory correction maneuver, a 660-m/s Earth insertion burn is performed, bringing the SOCCER spacecraft into a highly elliptical orbit. Aerobraking is subsequently used to circularize the orbit at an altitude low enough to allow rendezvous with the shuttle. Before aerobraking is initiated (with a 20 m/s maneuver reducing perigee to 120 km), the spacecraft loiters in order to allow its orbit to precess until the spacecraft's spin axis is normal to the

Sun line. This assures the availability of full power during aerobraking. About 20 apogee maneuvers are needed to navigate the spacecraft during aerobraking, totaling less than 10 m/s of  $\Delta V$ . After sighting SOCCER, the shuttle will make final adjustment for an extravehicular activity to attach the Remote Manipulator System to the grapple. After grapple attachment, the sample collection system will be separated from the spacecraft and placed into a refrigerated container for Earth return. On reaching the ground, the entire container will be moved into the laboratory for deintegration, sample examination, and sample distribution.

All flight hardware handled by the shuttle is subject to stringent safety requirements. Since SOCCER is not launched by the shuttle, and is not designed to meet shuttle launch requirements, the shuttle cannot retrieve it. Furthermore, the retrieval of a spacecraft into the bay of the shuttle after the craft has been in deep space for four years would have severe safety and, thus, cost implications. Consequently, it is cost effective for the shuttle to retrieve the sample collection system only.

**Mission Operations:** The spacecraft and instruments will be integrated at ISAS, Sagami-hara, Kanagawa Prefecture. The mission operations will be performed at ISAS by its operational staff with the support of JPL's engineering teams from sample collection systems, navigation, and tracking. At the time of shuttle retrieval, the ISAS spacecraft team will support the NASA shuttle retrieval team. Thus, operations, as much as possible, will be handled by ISAS. The typical ISAS operations team is small and very efficient, making low costs possible; uplink sequences will be designed by ISAS with participation from the sample collection team. Uplink data are transmitted in S-band and downlinked in both S- and X-bands. Imaging data and dust capture data are downlinked with minimal processing.

**Summary:** As was stated in the Solar System Exploration Committee's report of 1983, the next step in cometary exploration following the flyby missions to Comet Halley should be a rendezvous and sample return with a short-period comet. Without CRAFT, it is all the more critical to the achievement of the goals of the Solar System Exploration Committee that SOCCER be accomplished. Through a joint effort with ISAS, it is cost effective to acquire thousands of samples from a known comet and thousands of images of a comet nucleus and dynamics of that comet coma at half the cost for each agency. During development, SOCCER extends participation to NASA and ISAS facilities, and more than one university. With returned samples, many analysis laboratories throughout the world will be involved. SOCCER will make available for analysis not only the only extraterrestrial samples from a known source since the Apollo missions, but specifically cometary material captured in the zone of parent molecules. Such material rates highest among all solar system objects for study of the planetary evolution and that of compounds and phases containing the biogenic elements.

**References:** [1] SSEC (1983) NASA. [2] Atkins K. L. (1979) *AIAA 79-2066*. [3] JPL (1991) *JPL 715-140*. [4] Tsou P. et al. (1983) *International Conference on Cometary Exploration, Vol. II*, 215-224. [5] Tsou P. et al. (1985) *AIAA-85-0465*. [6] Albee A. L. (1985) *Giotto II Workshop*, Caltech. [7] ESA (1986) *ESA SCI 86, 3*. [8] Uesugi K. T. et al. (1987) *ISAS*. [9] Neugebauer M. et al. (1989) *EOS*, 70, 633. [10] Tsou P. et al. (1984) *LPS XV*, 866-867. [11] Tsou P. et al. (1987) *LPS XVIII*, 1024-1025. [12] ISAS (1987) *ISAS*. [13] ISAS (1988) *Proceedings of ISAS/NASA Joint Study Group Meeting*. [14] ISAS (1988) *Proceedings of ISAS/NASA Joint Work-*

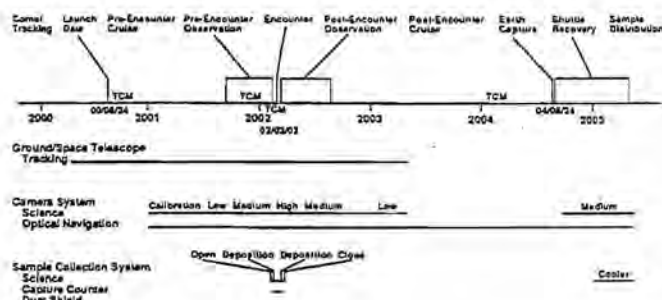


Fig. 4. SOCCER Mission Scenario.



ing Group Meeting. [15] *ISAS(1991) Proceedings*. [16] *ISAS(1992) Proceedings of 3rd ISAS/NASA Joint Working Group Meeting*. [17] Tsou P. (1990) *JPL D-7777*. [18] Tsou P. (1983) *JPL D-797*. [19] Tsou P. et al. (1983) *JPL D-1153*. [20] Tsou P. et al. (1985) *JBIS*, 38, 232-239. [21] Brownlee D. E. (1988) *Proposal to The Small-Class Explorer Program*. [22] Brownlee D. E. (1989) *Proposal to Space Station Attached Payload Program*. [23] Brownlee D. E. (1989) *Proposal to Space Station Attached Payload Program*. [24] Carle G. (1989) *Proposal to Space Station Attached Payload Program*. [25] Tsou P. (1989) *Proposal to Space Station Attached Payload Program*. [26] Tsou P. et al. (1993) *LPSXXIV*. [27] Sekanina Z. (1993) *Astron. Astrophys.*, 271, 630-644.

**THE STATUS OF MEASUREMENT TECHNOLOGIES CONCERNING MICROMETER AND SUBMICROMETER SPACE ARTICULATE MATTER CAPTURE, RECOVERY, VELOCITY, AND TRAJECTORY.** W. M. Alexander<sup>1</sup>, W. G. Tanner<sup>1</sup>, R. A. McDonald<sup>1</sup>, G. E. Schaub<sup>1</sup>, S. L. Stephenson<sup>1</sup>, J. A. M. McDonnell<sup>2</sup>, and C. R. Maag<sup>3</sup>, <sup>1</sup>Baylor University, Waco TX 76798, USA, <sup>2</sup>University of Kent at Canterbury, UK, <sup>3</sup>Science Applications International Corporation, Glendora CA 91740, USA.

**Overview:** The return of a pristine sample from a comet would lead to greater understanding of cometary structures, as well as offering insights into exobiology. The paper presented at the Discovery Program Workshop [3] outlined a set of measurements for what was identified as a SOCCER-like interplanetary mission. Several experiments comprised the total instrumentation. This paper presents a summary of CCSR with an overview of three of the four major instruments [4,9,11]. Details of the major dust dynamics experiment including trajectory are given in this paper. The instrument proposed here offers the opportunity for the return of cometary dust particles gathered *in situ*. The capture process has been employed aboard the space shuttle with successful results in returning samples to Earth for laboratory analysis. In addition, the sensors will measure the charge, mass, velocity, and size of cometary dust grains during the encounter. This data will help our understanding of dusty plasmas.

**Introduction:** Remote observation from Earth up to this time has provided everything we know regarding objects beyond our solar system and, in fact, most of what we know about the solar system itself. However, experience has shown that when we move from remote observations of cosmic objects to detailed laboratory studies on Earth of cosmic materials, we achieve far more than merely extending the perception of systems. Indeed, our complete outlook may change and place us on a higher plateau of understanding from which hitherto undiscovered pathways may lead. These statements are paraphrased from the 1987 report "Rosetta: The Comet Nucleus Sample Return Mission" [1]. The issuance of the letter of invitation from W. T. Huntress to participate in a workshop to evaluate concepts for consideration of Discovery missions presented the opportunity to consider a comet coma sample return mission, whose basic background comes out of these prior studies and workshops. The invitation letter also encouraged "participation in larger international missions in which the SSED costs do not exceed Discovery guidelines and are also within the scope of the program." Therefore, elements from the SOCCER [2] workshops

that provide spacecraft data in some detail, coupled with very specific analysis capabilities and appropriate experience with specific curator needs in both the USA and Europe, provided the basis for proposing a Comet Coma Sample Return [3] mission to be considered for the Discovery missions with SOCCER mission capabilities.

**Scientific Goals and Objectives:** The primary goal of understanding the origin of the solar system and more especially the origin of life, will not be adequately addressed until primitive bodies, e.g., comets, have been sampled. In establishing the core program, the SSEC of NASA Advisory Council has argued cogently for the inclusion of a comet sample return mission, which will "... provide a detailed elemental and isotopic composition analysis of gases and dust from the coma of a comet, data complementary to that acquired by a Comet Rendezvous mission. Ideally, the material will be returned to terrestrial laboratories from the same comet observed by the rendezvous spacecraft" (*Planetary Exploration Through Year 2000, A Core Program*, Washington DC, 1983). Unfortunately, the nonhomogeneity of comets may not allow one to assess from the sample of two or even three comets at perihelion, the primordial nature of the solar system. The most often repeated scientific question arising from the investigations of primitive bodies remains: What is the nature of the material that composed the early solar system and can that material be sampled in an unaltered state, and if so where? The primary advantage in utilizing comets as the source for samples occurs for those short-period comets that pass near the orbit of the Earth in six or fewer years.

Comets are made up of a wide variety of substances believed to have been abundant during the origin of our solar system. Composed of frozen gases, refractory grains, silicates, and carbonaceous compounds, comets are generally believed to be unaltered bodies condensed in the early stages of solar system formation. Near perihelion, the frozen gases in the outer layers of a comet sublime to form the distinctive coma. Unlocked from the nucleus, neutral gases stream from the illuminated surfaces entraining cometary dust grains embedded in the frozen composite matrix. SOCCER-like missions will be scheduled to coincide with perihelion, in principle the time when the nucleus will be most active and when gas and dust released from the nucleus will be maximum. Capture of the largest newly released grains will require a very close approach to the nucleus. In addition, the spacecraft should fly by the cometary nucleus on the Sunward side (subsolar point) to increase the probability of sampling "jets," which emanate material that had not been extensively exposed to the inner solar system environment.

Cometary samples should provide insights into the early history of the solar system and are assumed to have been altered little since the origin of the solar system. Returning even a small sample from a selected comet would provide a means to identify the properties of cometary grains. In principle, the percent of cometary materials present in our current collection of meteorites and dust is uncertain since the processes that led to the recovery of these samples has homogenized them. Cometary samples examination in terrestrial laboratories, along with subsequent identification of cometary constituents, would allow differentiation of cometary from the asteroidal particles.

The return of samples of captured intact cometary dust and volatiles drives the design of the device used to capture and maintain the intact grains. The major concern remains the deceleration of the clusters of ices and minerals. The key design features for the system

must be (1) conduction of heat away from the "burn" track where the grain has come to rest and (2) conduction of heat must be maintained once the grain has embedded in the micropore foam.

**Collect cometary dust samples: Comet Coma Sample Return (CCSR) experimental package.** Capture intact dust and organic grains in a micropore polyfoam maintained at low temperature. Locate the entry point for each captured grain by means of active trajectory system data. Upon return to terrestrial laboratories investigators will perform an examination of the returned samples recovered from micropore polyfoams and maintain the recovery unit at a low temperature to ensure the curation of the unexamined samples.

When samples are returned to Earth from the cometary environment it will be necessary to have laboratories for their analysis. Planning for the establishment of curatorial facilities for returned cometary dust particles will be an integral part of the mission. This facility needs to be capable of simulating certain conditions of the comet coma from which the samples were collected. Existing analytical tools will be adapted to operate in these conditions and new techniques for the curation and analysis will be developed to ensure that the most efficient and conservatory methods are used. Expanded discussion of the analyses associated with the specific instrumentations under discussion are presented in this workshop by C. Maag et al. [4].

However, from the comet P/Halley probe, we have learned that cometary grains also contain semivolatile organic compounds and, possibly, icy volatile inclusions. Of special and unique interest are the organic grains that were observed in the coma of Comet P/Halley, the CHON particles. If we assume that these grains are common among comets, as observational evidence suggests [5], the groundbased laboratory must have instrumentation that allows for the identification, separation, and sophisticated analyses of the individual CHON grains (micrometer to submicrometer sizes) for an overall chemical and physical characterization. The survival of organic molecules in the grains returned after a hypervelocity impact should strengthen theoretical assertions concerning the possible role of comets in the genesis of life. Therefore, biological and chemical contamination issues are of extreme importance so that the purity of the comet samples can be ensured. Based on the P/Halley experiences, the characterization of organic grains is an area that is expected to have considerable impact on laboratory activity.

**Investigate dust environment in the comet coma.** Establishing the charge, mass, and velocity vector of cometary dust, the flux of cometary grains on the capture cells will be determined so that one may delineate the major components of the total dust grain size and mass distribution for the particulates in the comet's coma and use the knowledge of the dust grain size distribution associated with the region of space near the nucleus of a comet to compare with the "jet" structures of the active comet.

A scientific objective of the proposed experimental package is the investigation of a comet's dust environment to establish the electrostatic charge, mass, and speed of cometary dust. With a measure of these parameters an upper and lower bound on the density of cometary dust grains can be established. Analysis of the dust grain data will reveal the flux profile for cometary dust grains emanating from the comet nucleus and will provide an assessment of the dust size distribution associated with the variations in cometary activity.

The flyby of Halley's comet by the Giotto probe has provided a unique opportunity to increase our knowledge of cometary structure.

Several cometary models [6] developed prior to the *in situ* measurements had predicted that the dust flux would have a simple inverse square of the distance to the comet nucleus dependence. For most of the Halley encounter this was an accurate model. However, five deviations or anomalies were found by DIDSY during the flyby. Two of these occurred before closest approach and the remaining three were noted after closest approach. This indicated an *in situ* derived example of dust/plasma interaction [7].

Utilizing cometary dust detection data and data provided by a plasma experiment, an investigation of the interactions between dust and plasma in the development of cometary structures of comets is strongly desired. Since a knowledge of the plasma environment is necessary for an understanding of any type of dust behavior, observations will both complement and be complemented by experiments that characterize the plasma and energetic particle regimes from *in situ* data. CCSR can very well provide important information on the collective effects of interactions in dusty plasmas.

**Investigations of dusty plasma environment.** Utilizing cometary dust detection, capture, and plasma data, the interactions between dust and plasma in the development of cometary structures of comets will be analyzed to study the dynamical affects on the motion of charged dust grains embedded in the plasma sheet of the cometary coma and to investigate the question of whether the number of charges on dust grains embedded in the plasma of a cometary coma may be a function of the separation distance between neighboring dust grains.

The physics of dusty plasmas is an emerging field of research with broad implications for the understanding of comets and the evolution of the early solar system protoplanetary disk. Many subtle and often surprising effects have been discovered theoretically [8], but very little experimental work has been done. Previous measurements of dust in the vicinity of planets and comets have been limited by their low sensitivity and lack of ability to measure grain velocities, charges, and masses. An *in situ* determination of all these quantities is crucial before further progress in the understanding of dusty plasmas can be made. All these quantities will be measured by the Dust Particle Dynamics and Environment Experiment (DPDEE).

**Comet targets.** The primary comet target can be Kopff in 2002; additional targets to be considered are Finlay in 2002, Wirtanen in 2002, and Churyumov-Gerasimenko in 2002. The selection of comet targets will be made based on the activity of the comet, the quality of Earth viewing for a particular perihelion passage, as well as the best estimate of the dust-to-gas ratio.

**Instrument Descriptions and Requirements: Gas Capture Cell (GCC).** Upon impact, a particle (carbonaceous chondrite or icy grain) traveling with hypervelocity speed is vaporized. In order to assess, collect, and retain the evolved gases we propose to include a unique gas capture cell. The cell will consist of numerous devices or sensors that have been tested in the space environment singly, but heretofore, not as a collective group. The gas capture cell will consist of a cryoplate, which will be maintained at approximately 150 K for the duration of the mission, i.e., from just prior to the flyby of the proposed target comet through retrieval and return of the instrument to the laboratory and subsequent data reduction. Approximately 10 cm above this plate an ultrathin film ( $t_f < 500$  Å) will be placed to act as both a primary sensing element and a thermal radiation barrier.



Attached to the cryoplate will be an array of Ge Attenuated Total Reflectance (ATR) crystals. These crystals will be maintained at 150 K by thermal conduction. Attached to the cell will be a quadrupole mass spectrometer capable of measuring from 1 to 50 AMU. The mass spectrometer will be a slightly modified version of the instrument flown four times on the space shuttle Induced Environment Contamination Monitor (IECM) [9].

**Organic Foam Capture Cell (OFCC):** Intact capture of a cosmic dust particle will be accomplished by the use of micropore foams. The principal objectives of the original program were to develop techniques that would provide the size distribution of  $\text{Al}_2\text{O}_3$  particles (AOS) expelled from a solid rocket motor (SRM). Polymeric foams, with and without deceleration films, were extensively used to capture AOS intact. Aerogel materials were also used as a capture material. Commercial organic polymer foams were initially used. Based on testing in light gas gun facilities, it was determined that the ability of these foams to retain particles impacting at hypervelocities was marginal at best. These tests found that the more complex polymers had better stopping ability. Accordingly, it was also determined that the polymers that had extremely small cell sizes, higher latent heats of fusion, and very low densities (e.g.,  $0.02\text{--}0.7\text{ g/cm}^3$ ) had the highest probability of providing intact

capture. In ground tests, the foams have been successfully tested between 1 and 11 km/s. One of the more interesting highlights of this program was the intact capture and retention of materials with a much lower density and material strength than AOS. Since the initial program other materials have been tested successfully, most notably foams of silicones, polyimides, and fluorocarbons. For this activity, foams of the aforementioned polymers will be developed and used that have both gradients in axial density, typically  $0.006\text{--}0.09\text{ g/cm}^3$ , and imbedded sensors to sense impact parameters as the particle decelerates in the foam (Fig. 1) [4]. Figures 2–4 show three conditions of particles captured intact using organic foam capture

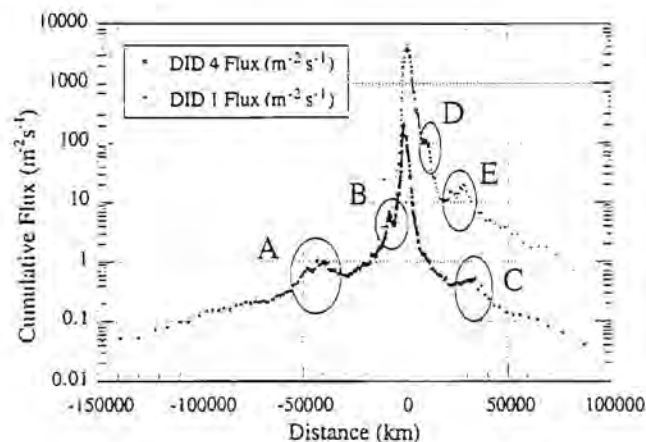


Fig. 1. Halley Giotto-DIDSY dust flux data—DID 1 and 4.

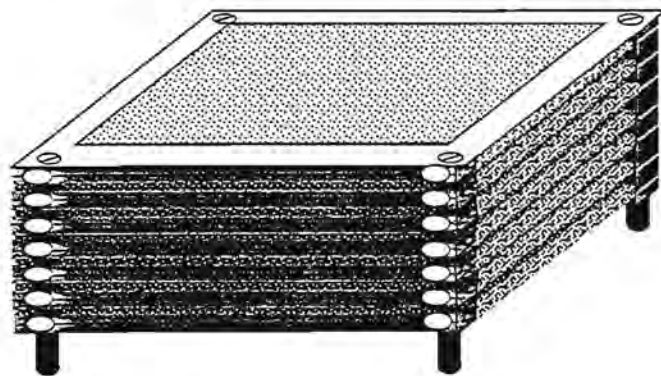
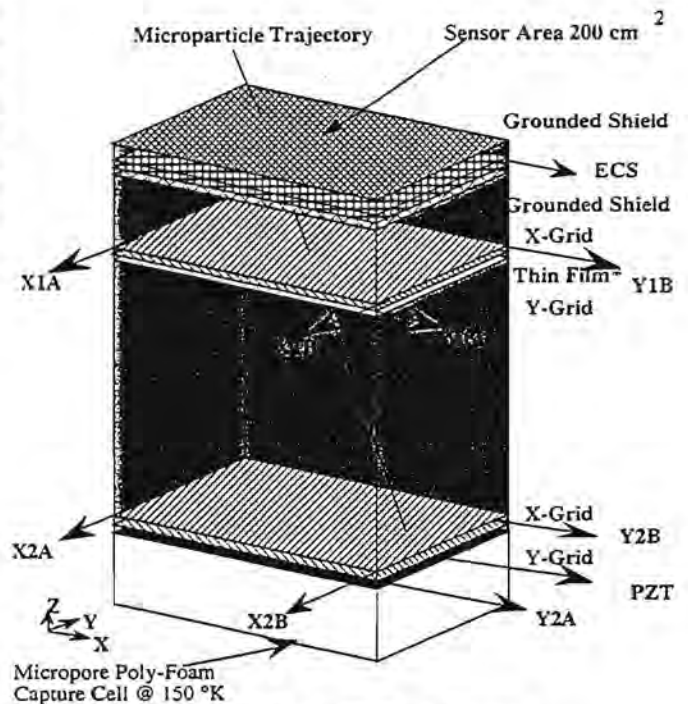


Fig. 2. A collection of cells of multiple thin films.



Cutaway 3-D view of the BUSSL dust sensor:  
A) 1 electrostatic charge sensor (voltage amplifier),  
B) 4 Charge sensitive amplifiers for TOF and location, and  
C) 1 PZT sensor at the impact plate.

Fig. 3. Dust particle dynamics and environment experiment.

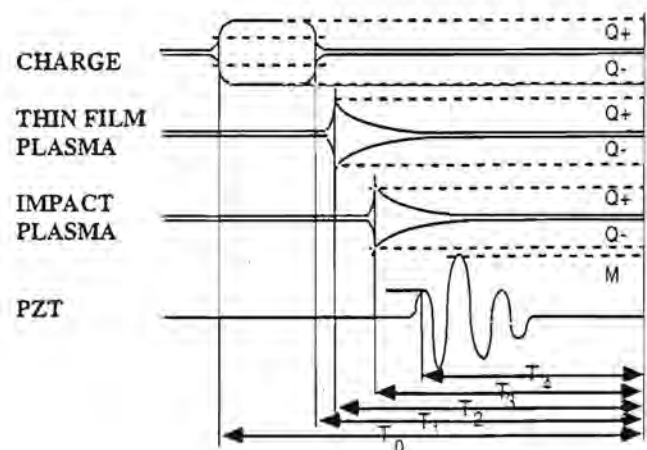


Fig. 4. Signals from the sensors used in this proposal.

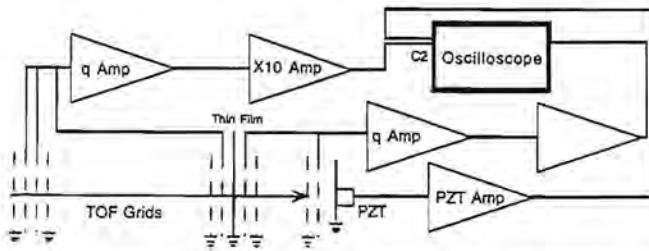


Fig. 5. Schematic of the system enclosed in the 2' x 2' x 6' central housing.

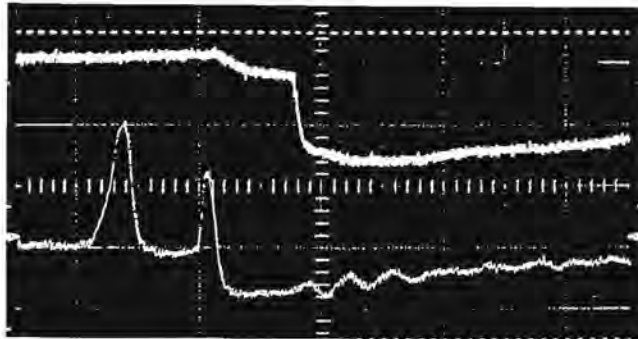


Fig. 6. Shows the detection of an induced electrostatic charge from the approaching charged particle, the plasma generated as the particle penetrates a 500-Å thin film and strikes an impact plate with the resulting PZT signal from the impact plate.

cells on shuttle STS 61-B and STS 41-D. Figure 2 depicts an interplanetary particle from STS 61-B. Figure 3 shows an AOS particle captured intact in the organic foam cell, and then in Fig. 4 the same AOS cell after the pyrolyzed foam has been removed using a low-molecular concentration of HCl. Figure 5 shows a particle captured using aerogel.

**Multiple Thin Film Array Capture Device (MTFA):** Cometary dust grains impacting on a very thin film will experience a pressure transient; however, when the thickness of the film is very much less than the diameter of the grain, the duration of the transient is extremely short with the destructive effect being greatly reduced. A succession of these films, spaced to allow nondestructive energy dissipation between impacts, significantly reduces the kinetic energy of the grain without allowing its internal energy to rise to the point of destruction of the projectile mass (Fig. 6).

**Dust Particle Dynamics and Environment Experiment (DPDEE) [10]:** Arguments were presented above for inclusion of *in situ* determination of the charge and dynamics of each of the cometary grains that impacted a collection device. The trajectory information is significant in locating the grain in the OFCC, ACC, and the MTFA capture devices. The dynamic parameters are the scientific information derived in the investigation of each captured grain and/or residue collected.

The DPDEE is a group of sensors integrated into a detection array that measures the charge possessed by the grains traversing the system, the trajectory of the grain within the system, the time of flight (TOF) of the grain within the system, and the kinetic energy of the grain.

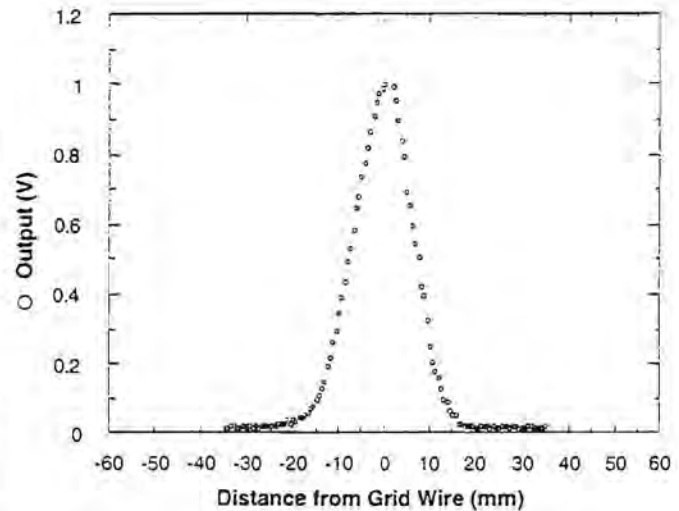


Fig. 7. ETCS experimental grid data from electronic probe.

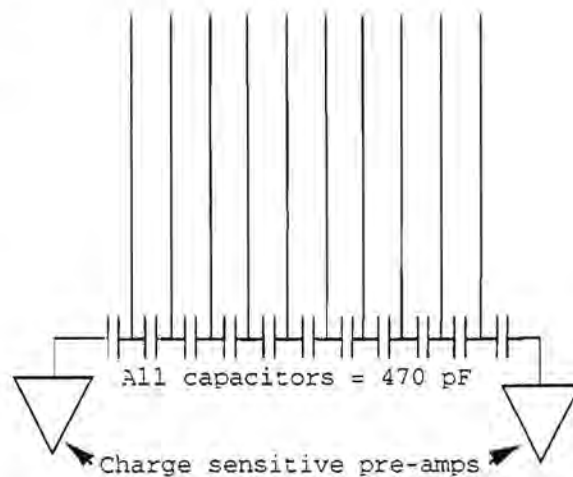


Fig. 8. ETCS grid assembly and preamplifiers.

All the sensors have been previously developed and used in some form in space. The DPDEE is depicted in Fig. 7. The system is shown coupled to an OFCC. The MTFA capture device will also couple to the DPDEE. The signals to be derived from the passage of a grain through the unit are depicted in Fig. 8. A laboratory system with these sensors (PZT impact plate instead of a capture cell) was used in a hypervelocity accelerator to demonstrate all aspects of the DPDEE with the schematic and results seen in Figs. 9 and 10. (Figure 9 shows the schematic of the system.) The bottom trace contains the charge measurement, which also yields a TOF. The top trace shows charge/plasma associated with the particles' passage through the thin film and then the sharp negative pulse from the plasma of the impact on the PZT plate. In the proposed array this last signal will come from the plasma generated as the particle impacts the capture cells. TOF and position data are obtained from the two plasma pulses while kinetic energy is derived from the second plasma pulse.

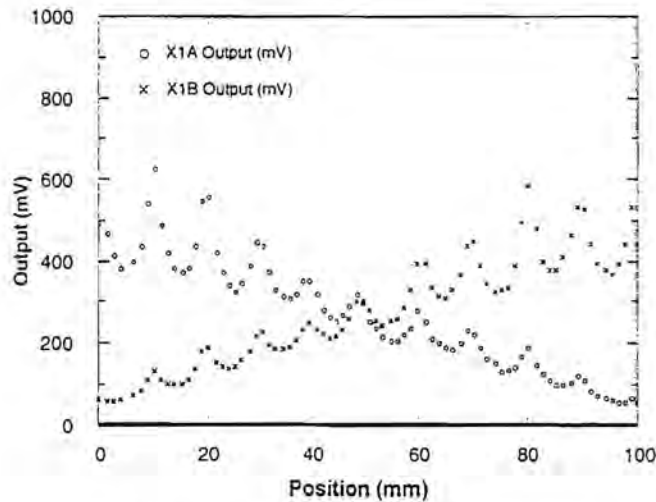


Fig. 9. Normalized signal outputs from ETCS grid system.

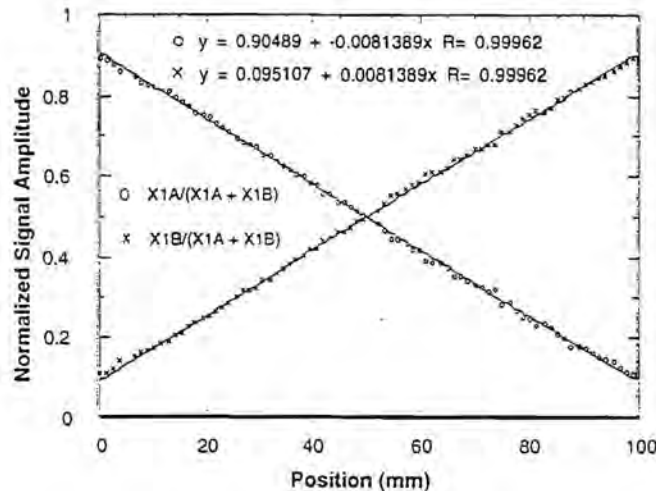


Fig. 10. Normalized signal outputs from ETCS grid system.

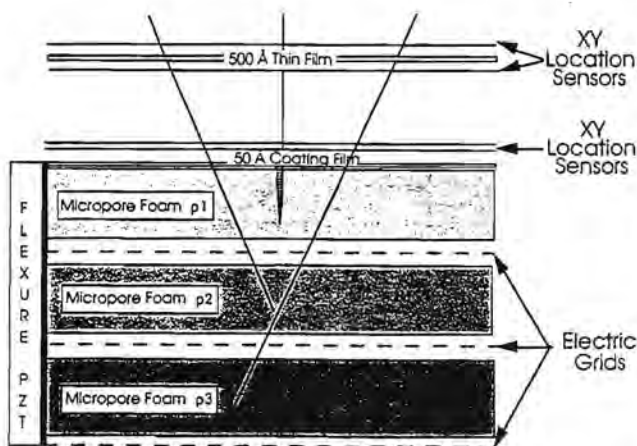


Fig. 11. Normalized signal outputs from ETCS grid system.

Electrostatic charge and trajectory information about an interplanetary micrometer-sized dust particle is retrieved from two grid systems (Fig. 11). Laboratory work has been conducted to optimize the sensor array designed with respect to grid spacing and separation using both signals from charged beads traversing two grid systems with induction from the electronically charged signals. Results around a single wire are seen in Fig. 12. Calibration tests of the 10-wire grid system resulted in data exhibiting considerable variation in pulse amplitudes between adjacent wires (Fig. 13). However, when the ratios of the outputs from the electronic system are summed and plotted, the information obtained makes possible the determination of quite precise particle trajectory. Figure 14 depicts the graph of position obtained from grid wires at 1-cm centers connected by a capacitor divider as shown in Fig. 11. Resulting "fits" to the data are shown in Fig. 14. These were obtained using linear regression techniques, having a correlation coefficient of 0.99962 and indicat-

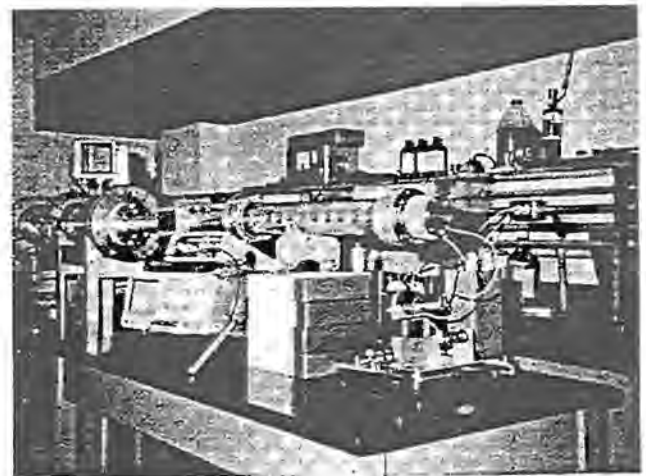


Fig. 12. The Low Velocity Dust Accelerator Facility at the Space Science Laboratory of Baylor University.

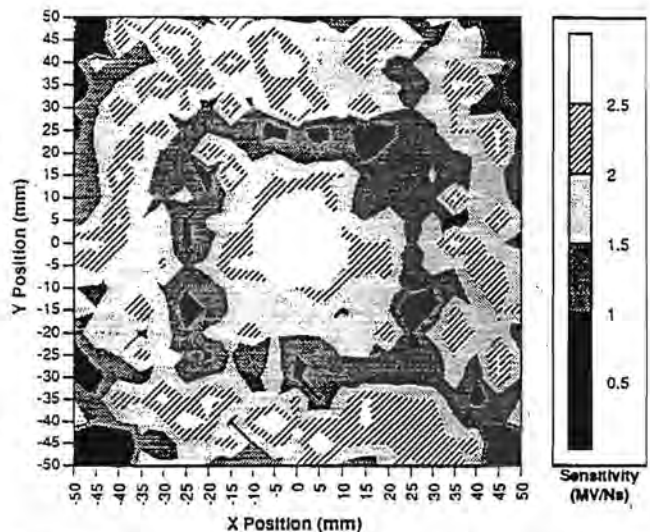


Fig. 13. Momentum sensitivity contour map of center-mounted PZT IIS sensor.



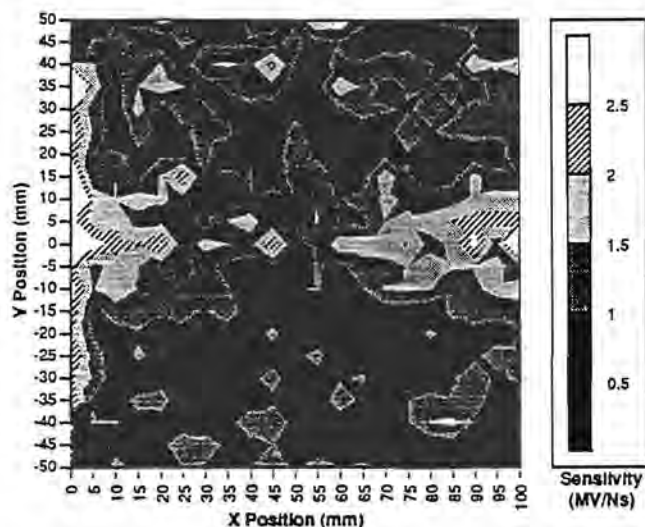


Fig. 14. Momentum sensitivity contour map of edge-mounted PZT-IIS sensor.

ing a standard deviation of less than  $\pm 0.8$  mm. This equates to an angular resolution of better than  $\pm 2^\circ$  as for particles entering the sensor array with 2 grid system detection units.

**Detection of Ion and Electron Components of Plasma Within Cometary Coma (IECCC):** The charge on the cometary grain is an important measurement. The charge primarily results from photoelectric effect and plasma interaction. Therefore, a measurement of the magnitude of the plasma prior to comet intercept and throughout passage into the coma will be provided by standard and ion electron spectrometers.

**Benefits to the Discovery Program and Solar System Exploration:** The proposed mission is designed to meet the requirements for a Discovery-class mission. The proven success of the capture materials in Low Earth Orbit combined with the support of the space science community in Japan offers a clear chance to launch an inexpensive mission to achieve the capture of cometary material in a pristine state, which has long been one of the objectives of workers in the field of solar system exploration.

**Utilization and Benefits to University, Industry, and NASA Community:** In the workshop proposal [3], the CCSR mission is an example of an international consortium whose domestic partners include NASA (JSC), industry (SAIC, Perkin-Elmer), nonprofit (SWRI), and university (Baylor, Johns Hopkins, APL). International cooperation includes the University of Kent at Canterbury (UKC) in England and the Institute of Space and Astronautical Science (ISAS) in Japan. All of these groups have extensive experience in cometary research.

**Relationship to Past and Future Planetary Missions:** Giotto Halley, Giotto Grigg-Skjellerup, Vegas, Sagisake, and Sushiam cometary missions produced a wealth of data concerning the make-up of comets. However, the compositions of the diverse materials that were intercepted by these extremely high encounter velocity spacecraft could better be unraveled if material similar to that intercepted could be analyzed in terrestrial laboratories. The sample return nature of CCSR will allow the first investigation of newly released material from an active comet, which can be analyzed in terrestrial laboratories. The CCSR mission could examine material

released from a comet that would be or had been the target of a proposed rendezvous mission to the same comet. The knowledge gained from the samples returned coupled with data gleaned from the flyby missions could set the stage for a large-scale international rendezvous and sample return mission like the ESA/NASA proposed Rosetta mission.

The many questions raised concerning the nature of primordial material by previous flyby missions, analysis of stratospheric collected IDPs, and remote sensing of primitive bodies could be answered by analysis of intact captured cometary grains *in situ* and in terrestrial laboratories. Benefits derived from comparative analysis between material detected during the outer planet missions, i.e., Galileo, Ulysses, Cassini, and that collected by CCSR could help define the nature of metamorphizing mechanisms acting on the material in the solar system.

**Major Accomplishments and Public Perceptions of the Mission:** A CCSR-type mission will return data on the composition of the comet nucleus and the grains ejected into the coma during the high activity of the perihelion passage. It will allow the determination of the basic properties of the nucleus: the size distribution of material ejected from the active areas, "jets," and the structures arising from the interaction between the plasma and the fine dust grains that may be analyzed later in terrestrial laboratories.

Cometary apparitions, once a portent of an impending cataclysm, now stimulate the imaginations of the public to wonder about the make-up of these ancient objects. As Earth-launched spacecraft glide through the icy sheets of a comet's coma, the scientific experiments link us with the encounter. Now that material from these prodigious objects can be harvested and returned to Earth, the final demystification of the ominous nature of comets can reveal the reality of the solar system's early formation and construction. For these reasons the CCSR mission would engender the highest measure of public support and interest.

**References:** [1] Wood J. A. (1987) *ESA SP-278*. [2] Uesugi K. et al. (1991) *Japan-U.S. Joint Workshop on Missions to Near-Earth Objects*. [3] Alexander W. M. et al. (1992) *Discovery Program Workshop*. [4] Maag C., this volume. [5] Huebner W. F. (1988) *Advances in Space Science Research*. [6] Gambosi T. I. et al., *Rev. Geophys.*, 24. [7] Alexander W. M. et al. (1987) *GCHP-BUSSL Research Report*, 007. [8] Huebner W. F. et al. (1988) *Icarus*, 76. [9] Heppner M., this volume. [10] Alexander W. M. et al. (1992) *BUSL Research Report*, 82992. [11] Tanner W. G. et al., this volume.

**PHYSICS OF SPACECRAFT-BASED INTERPLANETARY DUST COLLECTION BY IMPACT INTO LOW-DENSITY MEDIA.** W. W. Anderson and T. J. Ahrens, Seismological Laboratory, California Institute of Technology, Pasadena CA 91125, USA.

**Introduction:** A spacecraft encountering an interplanetary dust particle (IDP) at a relative velocity of several kilometers per second may be used to capture that particle for *in situ* analysis or for analysis upon Earth return. In this paper we study the impact of a dust particle into a low-density medium (i.e., a foam) such that the foam dissipates the kinetic energy of impact over a sufficient distance to stop the particle without destroying it.

**Theoretical Treatment:** In this study, we will specifically

consider polystyrene foams but the model is applicable to other materials as well. There are three regimes into which a particle-collector combination may be placed, based on the size of the IDP relative to the characteristic microstructural lengthscales of the foam. If  $d_w$  is the thickness of a cell wall in the foam,  $d_f$  is the diameter of a cell, and  $d_p$  is the IDP diameter, the three regimes may be defined as follows: (1)  $d_p \leq d_w$ ; (2)  $d_w < d_p \leq d_f$ ; and (3)  $d_p > d_f$ . Particles in regimes 1 and 2 will behave as if the cell walls were solid blocks of the material from which the foam is made. Particles in regime 3 will see the foam as a continuum. We will restrict the present discussion to regime 3.

Because particles in regime 3 see the foam as a very-low-density continuum, the processes involved can be described by fluid mechanics. The particle will be preceded by a bow shock wave (Fig. 1), behind which is a flow of shocked foam around the particle. A viscous boundary layer exists at the surface of the particle. At some point, the flow will separate, isolating the surface of the particle from the shocked material. The primary processes are drag, ablation, and fragmentation.

**Drag.** Development of a model for the drag experienced by an IDP must begin with the shock wave, which precedes the particle. The change in conditions across a steady, normal, planar shock wave is constrained by the Rankine-Hugoniot conservation equations

$$U_s \rho_0 = (U_s - u_p) \rho_H \quad (1)$$

$$P_H = U_s u_p \rho_0 + P_0 \quad (2)$$

$$E_H = E_0 + 1/2 (P_0 + P_H) (V_0 - V_H) = 1/2 u_p^2 \quad (3)$$

where  $U_s$  and  $u_p$  are the shock wave velocity and postshock material velocity respectively (both in the rest frame of the unshocked material),  $\rho$  is the mass density,  $P$  is pressure,  $V$  is specific volume,  $E$  is specific internal energy, and the subscripts 0 and H refer to the unshocked and shocked (Hugoniot) states respectively. Often,  $U_s$  is written as a polynomial function of  $u_p$ , which we take to second order for the present study

$$U_s = C_0 + s u_p + s' u_p^2 \quad (4)$$

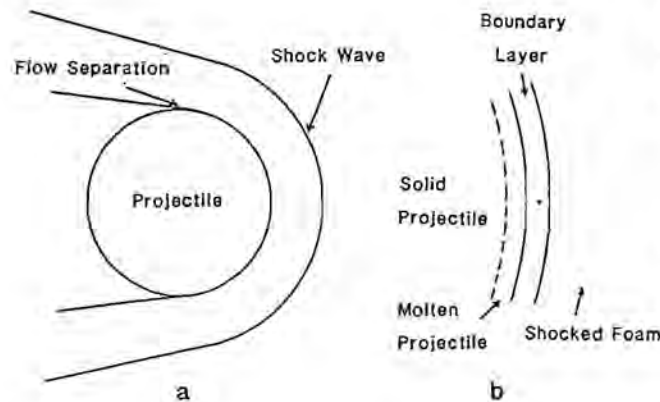


Fig. 1. Conceptual model for a particle passing through a low-density foam at high velocity.

Table I gives the values of  $C_0$ ,  $s$ , and  $s'$  for polystyrene foams with the initial densities considered in this study.

TABLE I. Hugoniot parameters for polystyrene foams.

$\rho_0$ (kg/m <sup>3</sup> )	$C_0$ (m/s)	$s$	$s'$ (s/m)
32.1	334.7	0.9104	$5.076 \times 10^{-5}$
28.5	335.1	0.9093	$5.092 \times 10^{-5}$
20.0	336.0	0.9073	$5.124 \times 10^{-5}$
10.0	336.7	0.9058	$5.147 \times 10^{-5}$

Generally, the bulk sound speed of a material defines the lower limit on the velocity of a steady shock wave. A wave traveling at the bulk sound speed  $C_b$  of the solid polymer must travel around the cells rather than directly across them. Even for highly distended foams, however, this only increases the path by a factor of  $\sim p/2$ . Thus, the effective bulk sound speed  $C_f$  of the foam, which we take as a lower limit on  $U_s$  is  $C_f \approx 2C_b/p$ . For nonporous polystyrene, the bulk sound speed is  $C_b = 1898$  m/s [2], so the effective bulk sound speed of polystyrene foams is  $C_f \approx 1203$  m/s. For IDP velocities  $u > C_f$ , decelerating forces arise from two sources: the pressure difference across the particle and the viscous stresses set up in the boundary layer. Let us begin by considering the pressure effects.

The "ambient" pressure  $P_H$  of the shocked foam is, taking  $P_0 = 0$  in equation (2) and setting  $U_s$  equal to the velocity  $u$  of the IDP (required for the shock wave to remain steady)

$$P_H = \rho_0 u^2 p \quad (5)$$

Using equation (4) we can get  $P_H$  solely as a function of  $u$ . In addition, to this "ambient" shock pressure, the forward-facing surface of the IDP experiences a dynamic pressure  $P_D$ , which for a surface element whose normal makes an angle  $\theta$  with the velocity vector of the IDP is

$$P_D = 1/2 \rho_H (u - u_p)^2 \cos^2 \theta \quad (6)$$

By definition, the pressure exerted on the IDP by the foam must vanish where the flow separates. The pressure gradient that gives rise to this phenomenon exists because of the requirement to accelerate the shocked foam, which comes to rest against the surface of the IDP, around the particle. We will assume that separation occurs at  $\theta = \pi/2$ . Since there is already a gradient built into  $P_D$ , we satisfy the requirement that the surface pressure  $P_H'$  associated with  $P_H$  decrease to zero at  $\theta = \pi/2$  by approximating  $P_H'$  as

$$P_H' = P_H \cos \theta \quad (7)$$

To get the component of pressure acting parallel to the velocity vector of the IDP, we must further multiply  $P_H'$  and  $P_D$  by  $\cos \theta$ , obtaining the total pressure force acting to decelerate the IDP from the surface integral

$$F = \int (P_H \cos^2 \theta + P_D \cos \theta) ds \quad (8)$$

The viscous shear stress  $\tau_s$  in the boundary layer is given by

$$\tau_s = \eta (ds/dt) \quad (9)$$

where  $\eta$  is the absolute viscosity and  $\epsilon$  is shear strain. We assume that

$$d\epsilon/dt = (u - u_p)/\delta \quad (10)$$

where  $\delta$  is the characteristic thickness of the boundary layer. To estimate  $\eta$  for organic polymers, we use [3]

$$\eta \sim (\rho T/M)^n (d\epsilon/dt)^{-n} \quad (11)$$

where  $M$  is the average molecular weight of a polymer chain and  $n \approx 1/2$ . For the present study, we take the quantity  $M/T$  constant to approximate the effect of bond breakage, thus making  $\eta$  independent of both  $M$  and  $T$ . We take  $\eta$  as

$$\eta = \eta_0 (\rho \delta)^{1/2} (u - u_p)^{-1/2} \quad (12)$$

where  $\eta_0$  is empirically determined. Now,  $\delta \sim d_p / \text{Re}^{1/2}$ , where  $\text{Re}$  is the Reynolds number of the fluid flow [4], given by

$$\text{Re} = \rho d_p (u - u_p) / \eta \quad (13)$$

Combining equations (12) and (13) and solving for  $d$ , we get

$$\delta = \delta_0 (d_p^2 \eta_0^2 / \rho)^{1/3} (u - u_p)^{-1} \quad (14)$$

where  $\delta_0$  is an empirical scaling factor.

Unlike  $P$ ,  $\tau_s$  acts parallel to the surface, so the stress acting directly to decelerate the IDP goes as  $\tau_s \sin \theta$ . Additional energy is dissipated moving this viscous fluid laterally, so that the actual total force is simply  $\tau_s A$ , where  $A$  is the frontal surface area of the IDP. We must account for the spherical geometry of the system in our model by multiplying by  $(1 + \delta/r)^2$ , where  $r$  is the radius of curvature of the surface. Thus, the viscous force acting to decelerate the IDP is

$$F = \tau_s (1 + \delta/r)^2 A \quad (15)$$

The total deceleration, then, is

$$du/dt = -[P_H \cos^2 \theta + P_D \cos \theta + \tau_s (1 + \delta/r)^2] ds/m \quad (16)$$

where  $m$  is the mass of the IDP.

At velocities  $u < C_f$ , the foregoing treatment is invalid because there is no shock wave and the properties of the material surrounding the IDP are very different from those of the shocked foam. Under these circumstances, the IDP is decelerated by overcoming the crushing strength,  $S_T$ , of the foam. The available data [5] show that  $S_T$  is typically proportional to  $u$  for polymer foams. Expecting  $S_T$  to also be proportional to the foam initial density, we model  $S_T$  as

$$S_T = S_{Tr} (\rho_0 / \rho_r) u \quad (17)$$

where the reference value  $S_{Tr}$  for density  $\rho_r$  is determined from data. This strength is expected to operate over some finite radius of deformation  $r_d$ , which we take to be the cell size  $d_r$ , so that the IDP has an effective cross-sectional area,  $A_{eff}$ , which is given by

$$A_{eff} = 1/4 \pi (d_p + 2r_d)^2 \quad (18)$$

One important note is in order. When the IDP itself is small compared to  $d_r$ , then  $r_d$  should decrease rapidly with decreasing particle diameter. This is very important for the extrapolation of laboratory data to the proper size regimes for IDPs. In the present model, we assume the limiting case of  $r_d = 0$  when  $d_p < r_d$ . The deceleration resulting from  $S_T$  is

$$du/dt = S_T u A_{eff} / m \quad (19)$$

At very low velocities, the discrete nature of the foam becomes important, with single cell walls acting as barriers with finite strength even at  $u = 0$ .

**Ablation.** At high velocities, the IDP may lose mass by thermal ablation as it passes through the foam. This is limited by the rate of supply of the effective heat of ablation,  $H_{eff}$ , to the particle

$$dm/dt = -Q A_{ab} / H_{eff} \quad (20)$$

where  $Q$  is the heat flux at the IDP surface and  $A_{ab}$  is the surface area being ablated. The heat that drives the ablation comes from two sources. First is the energy deposited in the foam by passage of the shock wave [e.g., equation (3)]. The second source of heat is the viscous dissipation of kinetic energy in the boundary layer. The heat from this second source is generated and deposited directly at the surface, but the heat from the "ambient" shocked foam is not, so that we must consider the transport phenomena involved.

The diffusive heat flux across a boundary layer of thickness  $\delta$  is [5]

$$Q_D = K(1 + \delta/r)(T_f - T_a)/\delta \quad (21)$$

where  $K$  is the thermal conductivity,  $r$  is the radius of curvature of the surface, and  $T_f$  and  $T_a$  are the temperature of the shocked foam and the ablating surface respectively. We approximate  $K$  by the following expression, which is derived from the Debye model for conduction

$$K = K_0 (Pp)^{1/2} / T \quad (22)$$

where  $K_0$  is chosen to fit laboratory impact data.

Heat transfer also occurs by radiative transport, although this phenomenon is important only at the highest velocities we will be considering. The radiative flux at the particle surface is

$$Q_r = \sigma \epsilon [T_f^4 (1 + \tau_f/r)^2 - T_a^4] \quad (23)$$

where  $\tau_f$  is the photon mean free path,  $\epsilon$  is the emissivity (assumed to be frequency independent), and  $\sigma$  is the Stefan-Boltzmann constant.

**Calculation of  $T_f$ .** Equations (21) and (23) require the calculation of  $T_f$ . Normally, this is fairly simple. Because of the nature of the material making up the foam, however, we expect that chemical reactions, namely decomposition, could have a significant effect on the value of  $T_f$ . We model these reactions using a unimolecular decomposition model in which the kinetic timescale for bond breakage is the bond vibration frequency of the lowest energy bond in the system. This model approximates  $T_f$  by

$$T_f = T_0 + (1/2 u_p^2 - f E_{eq}) / C_{p0} \quad (24)$$



$$f = \exp[(u_p - u)hN_A \exp(E_b/RT_f)/(d_p E_b)] \quad (25)$$

where  $E_{eq}$  is the energy difference between the intact polymer and its decomposition products at equilibrium at  $T_f$ ,  $E_b$  is the energy of the weakest bond in the system, the quantity  $(u-u_p)/d_p$  is the timescale for the shocked foam to be in contact with the IDP,  $N_A$  is Avogadro's number,  $h$  is Planck's constant, and  $C_{p0}$  is the STP constant pressure molar heat capacity of the polymer.

**Fragmentation.** An IDP may fragment by one or both of two mechanisms during impact with and passage through the foam. First, the initial shock experienced upon impact with the foam may produce stresses that exceed the dynamic crushing strength of the IDP. Second, the nonhydrostatic stresses due to the differential pressure across the particle may cause the particle to undergo tensile fracture. The main effect of fragmentation is to produce smaller particles, which behave as any other particle of comparable size. Because the stresses are greatest immediately upon the initial impact, that is the point at which an IDP is most likely to break up. Many single solid mineral grains may be strong enough that they will not fragment. Fluffy aggregates of the type often collected by high-altitude aircraft, on the other hand, probably will fragment, breaking up into their component grains.

**Model Results:** We now present results of calculations using our model in comparison with existing experimental data and make specific predictions concerning interplanetary dust collection. We assume that the impacting dust particle is spherical and that its spatial orientation is constant, so that the same side is always in contact with the shocked foam. We also assume that the rate of mass loss varies linearly from a maximum at  $\theta = 0$  to 0 at  $\theta = \pi/2$  to account for variation of  $\delta$  with  $\theta$ . We have also included the effects of the transient shock wave that is generated upon the initial impact with the foam. The primary effect of this shock wave is to slow the particle slightly.

**Comparison with Experimental Data:** Several equations in the model contain empirical constants. Specifically, these are  $\eta_0$  in equation (12),  $\delta_0$  in equation (14),  $S_{Tr}$  in equation (17),  $r_d$  in equation (18), and  $K_0$  in equation (22). We use experimental data [6–8] to constrain these constants.  $S_{Tr}$  and  $r_d$  can be obtained independent of the other parameters by integrating equation (19) to get the stopping distances measured in experiments in which the impact velocity is lower than  $C_f$ . These values are then held constant while  $\eta_0$ ,  $\delta_0$ , and  $K_0$  are constrained simultaneously from the high-impact velocity data with equations (14) and (20). Table 2 lists all the values used for polystyrene in the present study, based on the experimental data. Table 3 lists properties assumed for the impacting particles.

Most of the experimental data are for foam densities near 30 kg/m<sup>3</sup>. The calculations for comparison were performed for densities of 32.1 kg/m<sup>3</sup> and 28.5 kg/m<sup>3</sup>. Figure 2 shows the results of the calculations for Al projectiles, along with experimental data. The data are best modeled by using  $T_a \approx 1200$  K, with the corresponding  $H_{eff}$  being the enthalpy difference for Al between  $T_a$  and 298 K. Aluminum melts at 933 K and vaporizes at 2791 K [9]. The intermediate value of  $T_a$  is best explained by requiring the viscosity of the liquid to drop to a certain threshold value before the flow of shocked foam around the particle can strip the melted material away from the surface.

**Calculation for Interplanetary Dust:** For hypothetical dust particles, we consider four different materials: iron metal, troilite (FeS), olivine (Mg<sub>2</sub>SiO<sub>4</sub>), and organic material, which we assume

TABLE 2. Foam properties used in the present study.

Property	Value	Units
$\eta_0$	1000	kg <sup>1/2</sup> m <sup>1/2</sup> s <sup>-1/2</sup>
$\delta_0$	50	s <sup>-2/3</sup>
$S_{Tr}$	6558	Pa × s/m
$r_d$	$2.24 \times 10^{-4}$	m
$K_0$	100	m <sup>3</sup> /s <sup>2</sup>
$\rho_f$	28.5	kg/m <sup>3</sup>

TABLE 3. Properties of materials assumed for impacting particles.

Material	$\rho$ (kg/m <sup>3</sup> )	$C_0$ (m/s)	$s$	$T_a$ (K)	$H_{eff}$ (MJ/kg)	References
Aluminum	2750	5330	1.34	1200	1.38	[2,9]
Iron	7850	3995	1.58	3133	8.65	[2,13]
Troilite	4602	2947	1.578	3133	8.00	[2,14,15]
Forsterite	3200	6285*	0.565*	3662	19.52	[2,9,15]
Organics	1046	2233	1.636	550	1.00	[2,16]

\*Hugoniot parameters for enstatite are used.

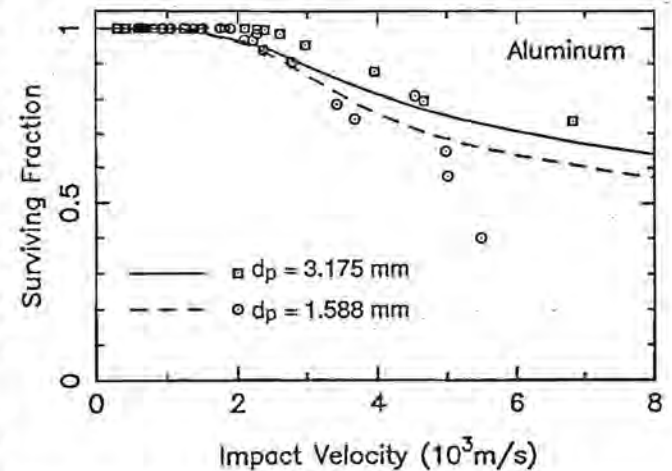


Fig. 2. Calculation results for survival of Al spheres impacting 28.5 kg/m<sup>3</sup> polystyrene foam. The results are compared with the experimental data of [6] and [7].

has the properties of polystyrene. Table 3 gives the properties of these materials. It should be noted that  $T_a$  for all of these materials is the vaporization temperature, with  $H_{eff}$  being the corresponding enthalpy difference from 298 K. The reason that we use the vaporization temperature is that the absolute viscosities of the liquid phases of these materials never drop to the value for Al at 1200 K, so we assume that, even though the materials have melted, they cannot be stripped away by the flow of shocked foam around the particle. The value of  $H_{eff}$  for organic material is the depolymerization enthalpy of polystyrene, with an extra term for a limited amount for further decomposition. It should be considered as very uncertain.

We have considered only single solid grains, rather than aggregates of smaller grains. This is based on the assumption that particles that are aggregates of smaller grains will break up because of the initial shock experienced upon impact.

Figure 3 shows the effects of particle composition on the survival of particles during impacts, with organic particles being significantly ablated for impact velocities in excess of 4–5 km/s.

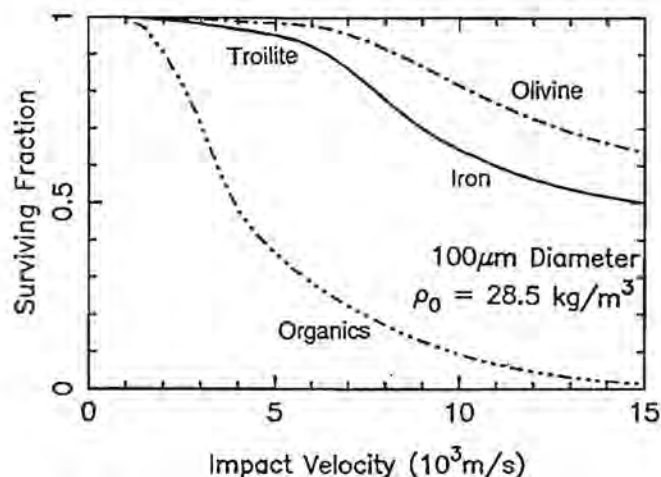


Fig. 3. Results for survival of 100- $\mu\text{m}$ -diameter dust particles impacting 28.5 kg/m<sup>3</sup> polystyrene foam.

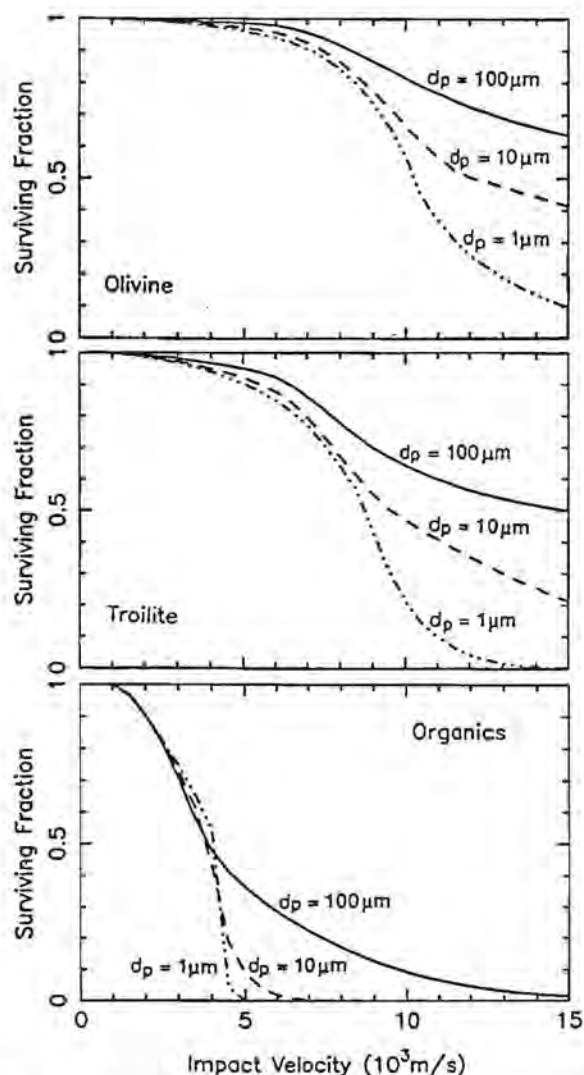


Fig. 4. Results for troilite, olivine, and organic particles of different diameters impacting 28.5 kg/m<sup>3</sup> polystyrene.

Inorganic particles, on the other hand, survive to considerably higher impact velocities.

The results in Fig. 3 are for 100- $\mu\text{m}$ -diameter particles, which are relatively large. Figure 4 shows the effects of decreasing the particle size for troilite, olivine, and organic materials. We see that the threshold impact velocity for significant survival becomes more sharply defined for smaller particles, but remains at about the same values for a given particle composition. For organic particles with  $d_p < 100 \mu\text{m}$ , recovery drops to <10% of the initial mass at impact velocities greater than 4–5 km/s. This represents a threshold velocity for recovery. For metals, sulfides, and silicates this threshold increases to 8–15 km/s. Since organic chemistry is an important aspect of interplanetary dust studies, this result is a very strong constraint. Encounters in excess of 5 km/s may preclude the useful collection of most organic material for study.

Figure 5 shows the result of varying the density of the foam. While foam density has an effect on the survival of an impacting particle, this effect is <10% of the initial mass. This is because of the similarity between different Hugoniot curves for different densities and the density scaling of the viscous dissipation in the boundary layer.

**Discussion:** The limit of 4–5 km/s for useful recovery of organic materials is reasonable, as is a limit of 8–15 km/s for metals, sulfides, and silicates. Recovery of these materials from organic polymer foams would in principle be straightforward, but cosmogenic organic materials may be difficult to distinguish from the final decomposition products of such foams. Inorganic collector materials might be necessary for this application. It should also be remembered that the properties of the materials that actually exist in interplanetary dust may vary widely.  $H_{\text{eff}}$ , for instance, may vary by a factor of several, depending on the materials involved.

The present study has concentrated on organic collector materials because of the wealth of data for such materials, although the same physical arguments should be applicable to inorganic foams as well. The most attractive inorganic collector materials identified to date are the silica aerogels [10, 11]. Although we do not directly treat these materials in this study, we can make some qualitative assessments of these materials based on this model. Data for the shock Hugoniot curves of aerogels are sparse, but the data that do exist

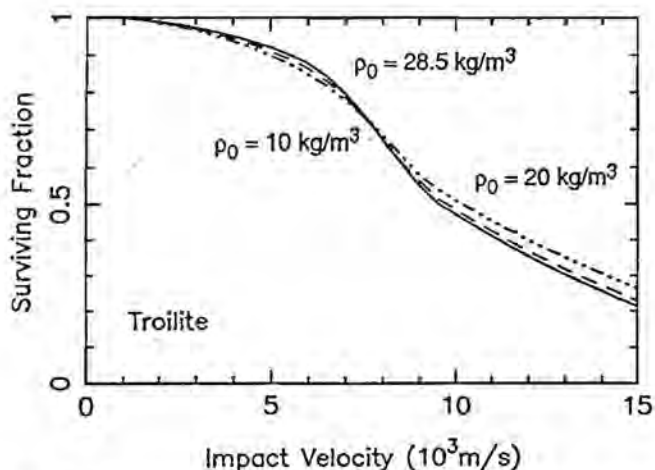


Fig. 5. Results for 10- $\mu\text{m}$ -diameter troilite particles impacting foams of different densities.

suggest that, for mass densities similar to those considered in this study,  $C_0 \approx -560$  m/s,  $s \approx 1.14$ , and  $s' = 0$ . The most significant differences between the silica aerogels and organic polymer foams are the viscosities and expected shock temperatures.  $\text{SiO}_2$  is very viscous, even at high strain rates and very high temperatures. Thus, we expect the viscous drag term in the deceleration to be very important in the deceleration process. The high viscosity also suggests that the shocked aerogel will not readily flow around the dust particle, but will build up in front of the particle. The formation of this viscous "cap" has two effects. First it increases the effective mass and cross-sectional area of the particle, with consequent effects on the pressure drag. Second, it dramatically increases the boundary layer thickness, possibly substantially decreasing the diffusion in heat across the boundary layer. This second effect is offset somewhat by the high temperature of the molten  $\text{SiO}_2$  in the cap. The other difference expected between aerogel and polymer foams is in the shocked foam temperature  $T_f$ .  $\text{SiO}_2$  lacks the abundance of relatively easily broken bonds found in organic polymers. These bonds serve to buffer the temperature in the shocked foams, so we can expect aerogels to subject the impacting dust particle to higher temperatures than encountered in polymer foams. These observations are supported by data that have recently become available for impacts of nonspherical monomineralic dust grains into silica aerogels [11]. Up to the maximum impact velocity investigated ( $\sim 7$  km/s), silicate and sulfide particles can be successfully collected, although substantially ablated and often thermally altered. The particles are usually found encased in melted aerogel after coming to rest, attesting to the formation of the viscous cap in front of the particle.

While we have not attempted to quantify the effects of the ratio of the dust particle diameter  $d_p$  to the foam cell diameter  $d_f$ , we do expect this ratio to have an effect on the survival of a particle during impact, especially as  $d_f$  approaches  $d_p$ . Available data [12] show that decreasing  $d_p/d_f$  from 6 to 3 significantly decreases the recovery of Al spheres impacting polystyrene foams. We suggest that the present model may be a limiting case for large  $d_p/d_f$ .

A number of recommendations are suggested by the calculations and by the equations presented. These recommendations apply to the areas of collector materials development, mission planning/spacecraft design, and further experiments. In the area of materials development, both inorganic and organic foams should be developed, with very small cells (ideally  $d_f < 1 \mu\text{m}$ ). The best materials would be characterized by a large number of low-energy covalent bonds and a high specific heat to minimize the value of  $T_f$ .

To maximize the scientific return of a collection mission, a variety of collector materials, including both organic and inorganic foams, should be used. Encounter velocities should not exceed 5 km/s if recovery of organic materials is to be attempted, but this constraint relaxes to velocities of 8–15 km/s if only inorganic materials are to be collected. Also, methods need to be developed to minimize and account for contamination of spacecraft instruments by decomposition products from the foams.

Experiments should be continued with a variety of collector materials, with projectiles of various compositions and structures, and with very small ( $d_p \leq 100 \mu\text{m}$ ) particles.

**Acknowledgments:** We would like to thank P. Tsou for much helpful discussion and for his willingness to share his experimental data with us. This work was supported by NASA grants NSG-7129 and NGL-05-002-105. Contribution number 5330 of the Division of

Geological and Planetary Sciences, California Institute of Technology.

**References:** [1] Zel'dovich Ya. B. and Raizer Y. P. (1967) *Physics of Shock Waves and High-Temperature Hydrodynamic Phenomena*, Vol. 2, Academic, New York, 452 pp. [2] Marsh S. P. (1980) *LASL Shock Hugoniot Data*, Univ. of California, Los Angeles, 658 pp. [3] Bueche F. (1962) *Physical Properties of Polymers*, Wiley, New York, 354 pp. [4] Landau L. D. and Lifshitz E. M. (1959) *Fluid Mechanics*, Pergamon, New York, 536 pp. [5] Carslaw H. S. and Jaeger J. C. (1959) *Conduction of Heat in Solids*, 2nd edition, Clarendon, Oxford, 510 pp. [6] Tsou P. et al. (1988) *LPI Tech. Rpt. 88-01*, 47–48. [7] Peng S. T. J. et al. (1988) *LPI Tech. Rpt. 88-01*, 47–48. [8] Tsou P., personal communication. [9] Chase M. W. et al. (1985) *J. Phys. Chem. Ref. Data*, 14, Suppl. 1, 1856 pp. [10] Tsou P. et al. (1989) *LPS XX*, 1132–1133. [11] Barrett R. A. et al. (1992) *Proc. LPS*, Vol. 22, 203–212. [12] Griffiths D. J. et al. (1991) *J. Appl. Phys.*, 70, 4790–4796. [13] Brown J. M. and McQueen R. G. (1986) *JGR*, 91, 7485–7494. [14] Brown J. M. et al. (1984) *JGR*, 89, 6041–6048. [15] Weast R. C. ed. (1977) *CRC Handbook of Chemistry and Physics*, 58th edition, CRC Press, Cleveland. [16] Van Krevelen D. W. (1972) *Properties of Polymers; Correlations with Chemical Structure*, Elsevier, New York, 427 pp.

**PLASMA PRODUCED BY IMPACTS OF FAST DUST PARTICLES ON A THIN FILM.** S. Auer, A & M Associates, 1906 Paris Court, Bowie MD 20716, USA.

A 100-nm Al film was subjected to impacts by submicrometer iron particles having speeds of  $v = 10 \dots 90$  km/s. Electrons and ions of the plasma produced by the impact on the film were collected with a special arrangement designed to suppress the plasma produced by secondary impacts on neighboring walls. The charges (in C) of electrons and ions fit the formulae  $Q^- = 5 \times 10^{-9} \text{ m}v^{6.2}$  and  $Q^+ = 2 \times 10^{-9} \text{ m}v^{6.2}$ , respectively, where  $m$  = particle mass (in g).

**Introduction:** The thin-film impact plasma detector was pioneered by Berg [1] for detecting small cosmic dust particles and measuring their approximate velocities in a time-of-flight configuration. While Berg's device was highly successful in establishing the flux of interplanetary dust, the accuracy of measuring the velocities of individual particles was a moderate 18% in magnitude and  $27^\circ$  in angle. A much greater accuracy of  $\leq 1\%$  in determining the velocity components appears desirable in order to associate a particle with its parent body [2]. In order to meet that need, research was initiated to determine if a thin-film detector can be designed to provide such accurate velocity measurements.

Previous laboratory investigations of the impact plasma uncovered two difficulties: (1) Solid or liquid spray is ejected from a primary impact crater and strikes neighboring walls where it produces secondary impact craters and plasma clouds; as a result, both quantity and time of detection of the plasma can vary significantly with the experiment configuration [e.g., 3]. (2) Particles from an accelerator rarely have speeds  $v \geq 10$ –15 km/s, while cosmic dust particles typically impact at  $v = 10$ –72 km/s.

The purpose of the tests discussed in this paper was to resolve the two difficulties mentioned. That is, the experiment configuration was designed to reduce the contribution of plasma from secondary impacts. In addition, most particles with  $v \leq 25$  km/s and all particles with  $v \leq 10$  km/s were eliminated from the beam.



**Experiment Configuration:** The experiments were performed on the 2-MV electrostatic dust accelerator [4] of the Max-Planck-Institut für Kernphysik at Heidelberg. The accelerator provides positively charged particles at a rate of about 1–10/s. Each particle passes through two cylindrical Faraday cups, inducing a charge equal to its own charge  $q$ . The duration  $\tau_1$  of this charge signal corresponds to the time the particle is inside the Faraday cup, therefore  $v \sim 1/\tau_1$ . Based upon these data, a particle selection unit (PSU) selects particles whose  $q$  and  $v$  are within preprogrammed limits. The PSU controls a particle filter [5] that electrically deflects and thus eliminates all unselected particles. As a result, only selected particles proceed to the experiment chamber.

Each selected particle passes through another charge/speed detector, as depicted in Fig. 1, where it induces a charge signal. Then it enters the experiment chamber and strikes a 100-nm-thick Al film. During the impact on the film, plasma is ejected from both front and back of the film. With the voltages shown in Fig. 1, the negative ions and the electrons are separated from the plasma plume and drawn to the charge collector, while the positive ions are repelled and leave the cage. A low-noise amplifier senses the collected charge. Both signals, from the last charge/speed detector and from the charge collector, are fed into a digital storage oscilloscope and displayed. Each signal is visually examined and characteristic features, such as rise time and amplitude, are noted.

**Selection of Fast Particles:** Most accelerated particles had velocities of  $v \approx 2$ –6 km/s; however, the accelerator also provided some fast particles. Figure 2, in the upper righthand corner, shows the  $m, v$  distribution of the particles used for this work (the penetration limits, also shown in Fig. 2, will be discussed later). As can be seen, the fastest particles were the smallest (roughly  $m \sim v^{-3.7}$  or  $d \sim v^{-1.2}$ ). For example, the fastest particle with  $v = 90$  km/s (see Fig. 2) had only a charge of  $q = 2$  fC and a mass of 1 fg, whereas another particle with  $v = 10$  km/s had  $q = 55$  fC and  $m = 2.2$  pg. In addition, they were very rare, since the dust supply in use was not supposed to contain very small particles.

The PSU was programmed to select all particles having  $v \geq 25$  km/s. Their rate was about 1 particle every 10–30 min. In addition, for a short time, all particles with  $v \geq 10$  km/s were admitted. Their rate was about 1 particle every few minutes.

Since the fastest dust particles were also the smallest, they carried small charges and were generally hard to detect in the presence of electrical interference and amplifier noise. Because of

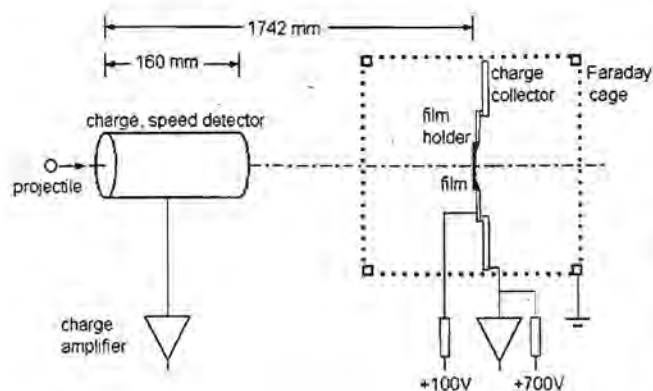


Fig. 1. Experiment schematics.

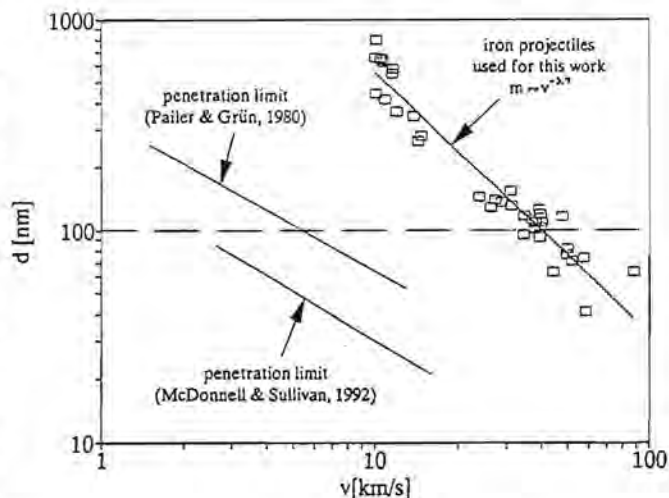


Fig. 2. Distribution of diameter  $d$  vs. speed  $v$  of the projectiles used in the experiment. Note the horizontal dashed line indicating particle diameter = film thickness. Also shown are film penetration limits calculated [8,9] for Fe projectiles striking a 100-nm Al film at normal incidence.

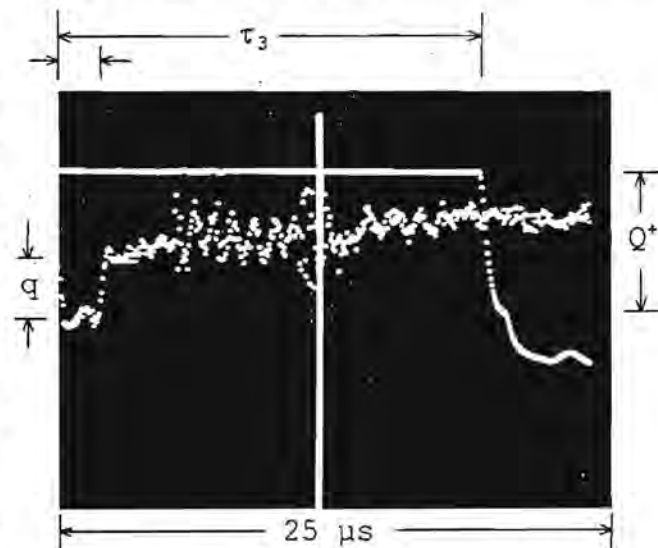


Fig. 3. Oscilloscope display of the signals from the detection and impact of the particle with  $v = 90$  km/s. Lower trace: signal from the charge detector; amplitude  $q = 2$  fC, duration  $\tau_2 = 1.9$   $\mu$ s; upper trace: signal from the charge collector; amplitude  $Q^+ = 253$  fC, delay  $\tau_3 = 19.8$   $\mu$ s. The width of the entire display corresponds to 25  $\mu$ s.

this difficulty, we will discuss in more detail the methods used to detect small signals in a noisy environment.

Figure 3 is an oscilloscope picture of signals from the detection and impact of the 90-km/s particle. The lower trace shows, near the left-hand edge of the picture, the negative-going induced charge signal from the charge/speed detector with typical steep leading and trailing edges and a flat level in between. Added to it are high-frequency interference, especially near the center of the picture, at a frequency of about 1 MHz and amplitudes (peak-to-peak) equivalent to 0.5–2.0 fC, and amplifier noise with a high-frequency component equivalent to about 0.02–0.05 fC (rms).

To make sure that  $v$  was correct, a particle's speed was measured or verified and documented four-fold: (1) The PSU measured and stored  $v$  in memory. (2) From  $v$ , the PSU calculated the time when it expected the particle to enter the charge detector (Fig. 1) and generated a signal when that time had arrived; the signal was used to trigger the oscilloscope display. The fact that the particle was detected entering at the very time that the PSU had calculated verifies the correct measurement of  $v$ . (3)  $v = 160 \text{ mm} \div \tau_2$ , with  $\tau_2$  being the duration of the signal from the charge detector and 160 mm being its length (see Fig. 1). (4)  $v = 1742 \text{ mm} \div \tau_3$ , with  $\tau_3$  being the time between the charge/speed detector signal and the impact on the film and 1741 mm being the corresponding distance (see Fig. 1). We considered this to be the most accurate measurement of  $v$ .

In these experiments the particle's charge was recorded only once (by the last charge detector, as mentioned) since the PSU is not designed to accurately measure  $Q$  when a charge signal has both small amplitude and short duration. In future experiments, however, we intend to measure  $Q$  redundantly.

**Reduction of the Effect of Secondary Impacts:** In order to reduce the collection of plasma from secondary (and tertiary) impacts, we (1) used a large test chamber and placed the film near its center; (2) mounted the charge collector sideways to the film; (3) generated a potential well around the charge collector, trapping the charges to be collected; (4) placed a highly transparent Faraday cage around both film and charge collector and connected it to signal ground; and (5) recorded only the charge that was collected within 0.3–1.0  $\mu\text{s}$  after the impact. In the following, we briefly discuss each item in some detail.

The large test chamber (inside dimensions  $1.2 \times 0.8 \times 0.5 \text{ m}$ ) and the central mounting of the film had the effect of separating the secondary impacts of spray particles on the chamber walls from the primary impact of the original particle on the thin film in both space and time. As a result, such secondary impacts occurred typically 20–100  $\mu\text{s}$  after the primary impact. In addition, the secondary plasma expanded into a large and essentially field-free space; thus, only a minute portion could ever reach the charge collector.

The charge collector was mounted on the side of the film (see Fig. 2) such that spray particles, traveling in straight lines from the impact crater, could not strike it. Thus, only ions or electrons could reach it, on curved paths, following the pull by the electric field.

A potential well for negative ions and electrons was generated by applying voltages of +100 V and +700 V to the film and collector respectively. As a result, the charges were trapped inside the cage and were drawn to the collector. Secondary electron emission at the charge collector is assumed to be negligible for the energy (600 eV) and materials used (mostly Al). Positive ions were pushed out of the cage, leaving it with an energy of 100 eV.

For collecting positive ions and rejecting negative charges, the polarities of both applied voltages were reversed, i.e., the film was at –100 V and the collector at –700 V.

The Faraday cage consisted of a cubical frame, 254 mm wide, made of Al, with 229-mm-wide square openings in each face. 0.1-mm-thick parallel W wires, separated by 5 mm, were stretched across the six openings, providing continuous electrical shielding. While the transparency of the openings was 98%, the transparency of the cage, including the frame, was about 80% on average.

One function of the Faraday cage was to shield the charge collector from undesirable electric ac fields inside the chamber [voltages, measured between opposite sides of the chamber, were

typically 0.1 V (peak-to-peak) at frequencies from 50 Hz to several megahertz]. Another function was to contain the potential well within the volume of the cage, such that plasma produced by secondary impacts outside the cage would not be drawn toward the charge collector.

**Results:** The charge measured at the collector varied from approximately  $5 \times 10^{-15} \text{ C}$  to  $5 \times 10^{-13} \text{ C}$ . Negative charges were generally higher than positive charges by about a factor of 2.5. In most previous simple impact plasma experiments like this one it has been found that the measured charge  $Q$  is roughly proportional to the mass of the impacting material [e.g., 6]. Therefore, we present the data in the form charge normalized to particle mass,  $Q/m$ , vs. speed  $v$ . The results are shown in Fig. 4 for negative charges and in Fig. 5 for positive charges. The charge-to-mass ratio is a strong function of particle speed. The highest values are reached at the highest impact speed. Least-squares fitting yielded the following formulae

$$\log(Q^-/m) = (-8.3 \pm 0.3) + (6.2 \pm 0.3)\log v \text{ (with } r^2 = 0.97)$$

or

$$Q^-/m = 5 \times 10^{-9} v^{6.2}$$

for negative charges, and

$$\log(Q^+/m) = (-8.7 \pm 0.4) + (6.2 \pm 0.4)\log v \text{ (with } r^2 = 0.96)$$

or

$$Q^+/m = 2 \times 10^{-9} v^{6.2}$$

for positive charges.

**Discussion:** The value  $Q^+/m = 243 \text{ C/g}$  for the particle having  $v = 90 \text{ km/s}$  falls below the solid line in Fig. 5 by a factor of 10. This is not surprising considering the fact that an Fe atom at this high speed has a kinetic energy of 2.4 keV. The temperature of the plasma from this impact was very high (probably in excess of  $10^6 \text{ K}$  according to Eichhorn [7]) with the bulk of ions having kinetic energies in the kiloelectron volt range; thus, a voltage difference between film and charge collector of 600 V was able to draw only a small portion of the ions, the least energetic ones, to the charge collector.

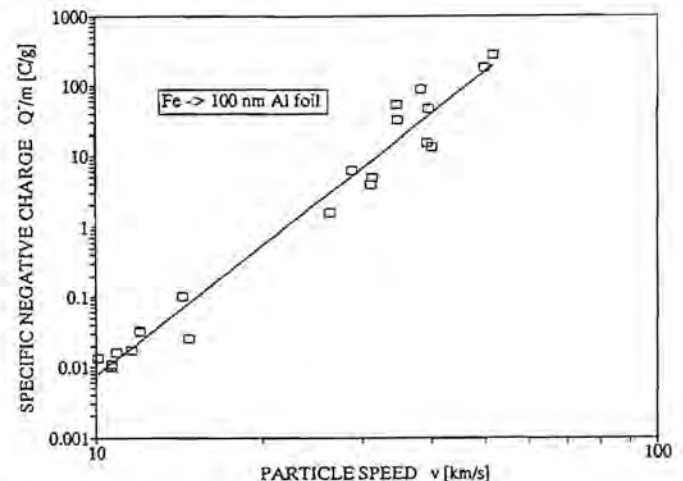


Fig. 4. Specific negative charge vs. particle speed. The solid line indicates the least-squares fit  $Q^-/m = 5 \times 10^{-9} v^{6.2}$ .

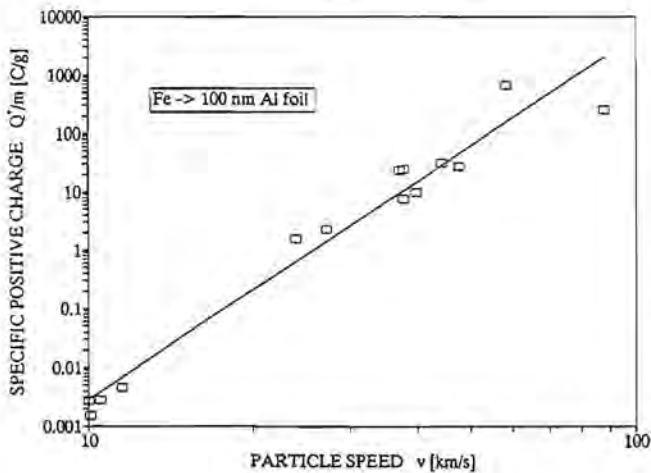


Fig. 5. Specific positive charge vs. particle speed. The solid line indicates the least-squares fit  $Q^+/m = 2 \times 10^{-9} v^{6.2}$ .

According to our results, a thin-film detector can readily sense the impact of a cosmic dust particle having, for instance, a diameter of 10  $\mu\text{m}$ , a density of  $\rho = 1 \text{ g cm}^{-3}$ , and speed  $v \geq 10 \text{ km/s}$ . Even with a film as thin as 30 nm, one can expect the charge signal to be at least 2 orders of magnitude above the noise level of a low-noise amplifier.

As is evident from Fig. 2, there is a strong correlation ( $r^2 = 0.93$ ) between  $m$  (or  $d$ ) and  $v$  of the particles from the Heidelberg dust accelerator. This means that  $m$  and  $v$  are largely dependent variables. Therefore, the dependence of  $Q$  vs.  $m$  at fixed  $v$  should be specifically measured in future tests using the very small and also some bigger particles, e.g., those available from the plasma drag accelerator in Munich.

Fig. 2 also shows the penetration limit for a 100 nm Al film according to a formula by Pailer and Grün [8] and a formula by McDonnell and Sullivan [9]. It can be seen that the particles used in our experiments are only a factor of about 10 bigger than particles that are barely able to penetrate. It is very likely that the particles used here were destroyed by the impact. Therefore, future tests should include thinner films and bigger particles, as mentioned.

The production of negative charges using Fe microparticles was also measured on the thin film of the Helios micrometeoroid analyzer. Results for  $2.5 \leq v \leq 9.2 \text{ km/s}$  [10] are shown in Fig. 6. Results for  $1.4 \leq v \leq 4 \text{ km/s}$  [11] are similar but not shown. Also presented in Fig. 6 are the results of this experiment. It can be seen that near  $v = 10 \text{ km/s}$  the Helios film produced about five times as much plasma ( $Q^-/m = 0.04 \text{ C/g}$ ) as the 100 nm Al film ( $Q^-/m = 0.008 \text{ C/g}$ ).

Two reasons for this difference appear obvious. (1) The Helios film consisted of 300 nm Parylene with a 75 nm Al layer, the areal density being  $59 \mu\text{g cm}^{-2}$ , while the density of the 100 nm Al film was only  $27 \mu\text{g cm}^{-2}$ . This can explain a factor of 2.2 if we assume the plasma production to be roughly proportional to the areal density of the film. (2) In addition, when testing the Helios film, the measured charges included contributions from secondary impacts, whereas we suppressed them. This can account for the remaining factor of 2–3.

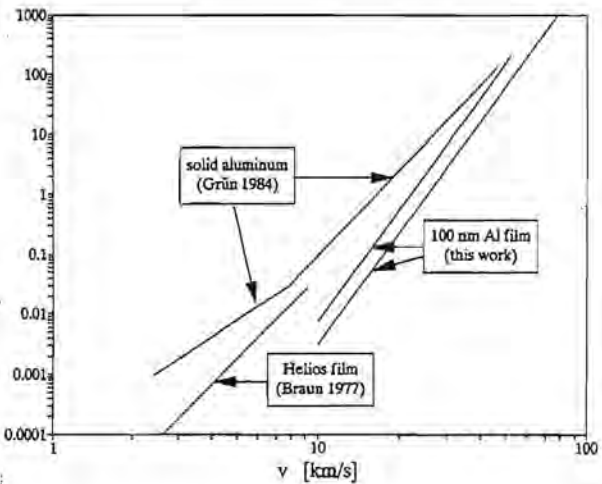


Fig. 6. Specific negative charge  $Q^-/m$  produced on the Helios film [10], solid aluminum [12], and in this experiment (upper line for  $Q^-/m$ , lower line for  $Q^+/m$ ). All experiments in this figure were performed with Fe projectiles from the Heidelberg dust accelerator.

For solid Al as a target, the production of negative charges was measured by Grün [12] and is shown in Fig. 6. As expected, these charges are significantly higher than for the thin film. However, at higher speed the curves converge. Notice in Fig. 2 that at the highest speed, the particle diameter is less than the film thickness. Apparently, for the smallest and fastest particles the "thin film" and the solid target present similar obstacles.

Future tests of the thin-film impact plasma detector should also include particles with lower densities and should investigate the response to oblique impact.

**Conclusions:** The production of plasma increases strongly with the speed of the particle,  $\sim v^{6.2}$ , in the speed range from 10 to 90 km/s. Negative charges are more abundant ( $>2.5$ ) than positive charges. The charge signals are strong enough, even when extrapolated to a 30-nm film, to assure the reliable detection of a 10- $\mu\text{m}$  dust particle (at  $v \geq 10 \text{ km/s}$  and  $\rho \geq 1 \text{ g cm}^{-3}$ ).

Secondary plasma was suppressed by a combination of spatial and temporal separation from the primary plasma.

The results are compatible with previous measurements of particle impacts on a thin film and on solid Al.

**Acknowledgments:** The Max-Planck-Institut für Kernphysik, Heidelberg, Germany (E. Grün) generously provided time on the dust accelerator while the author was on sabbatical leave from Applied Research Corporation, Landover, Maryland. The CDCF project (F. Hörz) of the Johnson Space Center, Houston, Texas, supported the analysis of the data under Purchase Order No. T-8495S.

**References:** [1] Berg O. E. et al. (1973) *Space Res. XIII*, 1057–1062. [2] Zook H. A. (1985) *LPI Tech. Rpt. 86-05*, 97–99. [3] Slattery J. C. (1972) *Tech. Rpt. Under Contract NASW-2246 for NASA HQ*, TRW Systems Group. [4] Fechtig H. et al. (1978) *Cosmic Dust* (J. A. M. McDonnell, ed.), Wiley, 607. [5] Rudolph V. (1966) *Z. Naturforsch.*, 14a, 1993–1996. [6] Grün E. (1981) *ESA SP-155*, 81. [7] Eichhorn G. (1976) *Planet. Space Sci.*, 24, 771–781. [8] Pailer N. and Grün E. (1980) *Planet. Space Sci.*, 28, 321–331. [9] McDonnell J. A. M. and Sullivan K. (1992) *Workshop on Hypervelocity Impacts in Space*, Univ. of Kent. [10] Braun G. (1977)



*Diplomarbeit*, Universität Heidelberg. [11] Pailer N. (1978) *Doktorarbeit*, Universität Heidelberg. [12] Grün E. (1984) ESA SP-224, 39-41.

**HIGHLY TRANSPARENT AND RUGGED SENSOR FOR VELOCITY DETERMINATIONS OF COSMIC DUST PARTICLES.** S. Auer and F. O. von Bun, A & M Associates, 1906 Paris Court, Bowie MD 20716, USA.

A sensor for naturally charged cosmic dust particles is discussed. Two models of the sensor were tested, one with a free-falling steel ball and the other with particles accelerated to high speed. Analytic expressions of the sensor signals are presented and compared with the test results. The errors in speed and angle were estimated to be about 0.3% and 0.2° respectively.

**Introduction:** In order to understand the evolution of interplanetary dust, numerous dust particles have been collected and analyzed. An analysis of the composition often provides information on the particle's origin. So does its orbit. Composition and orbit data complement each other and should be determined together.

If the last orbit of a particle can be determined, its orbital history can often be calculated backward in time and associated with its parent body. To determine the last orbit, the velocity needs to be measured before the particle is collected. The precision required in determining the velocity components relative to the spacecraft should be 1% or better [1].

The thin-film impact plasma detector is one of two methods under investigation to meet that need; the charged-particle detector is the other. While the charged-particle detector is totally non-destructive and can, at least in principle, achieve unlimited precision, it is sensitive to solar UV radiation. In addition, shielding from external plasma and electrical interferences is mandatory but feasible. On the other hand, the thin-film impact plasma detector is much less sensitive to external interference by UV, plasma, or electric fields, but tends to damage the particle during the impact and also to alter the velocity components that are to be measured. Obviously, for measuring low-density (especially "fluffy") dust particles, which are easily damaged by any thin-film penetration, a charged-particle detector must be used, whereas for the measurement of dense particles, especially in the presence of UV, a thin-film detector may be adequate. Also, the thin-film detector is more sensitive to fast particles, while the charged-particle detector is more sensitive to slow particles. Thus, the two methods complement each other.

The charged-particle detector relies on the fact that a charged dust particle passing next to a conducting rod induces a charge signal in the rod (or wire or grid). Based on this fact, two sensors for position and velocity have previously been designed, built, and tested with fast particles from an electrostatic dust accelerator [2]. A third sensor combines the wide field of view of the first and the sensitivity of the second sensor with a new feature, ruggedness. In this paper we discuss the construction and some test results of this "rod sensor" version of the charged-particle detector.

**Brief Sensor Description:** Figure 1 shows a schematic cross section (not to scale) of the sensor. Each of grids  $G_1$  and  $G_2$  consists of thin (0.1 mm) tungsten wires stretched across an aluminum frame (mesh size 5 mm). These grids are grounded. Each of rod assemblies  $R_1$  through  $R_4$  consists of 12 thin (1 mm), parallel, equidistant,

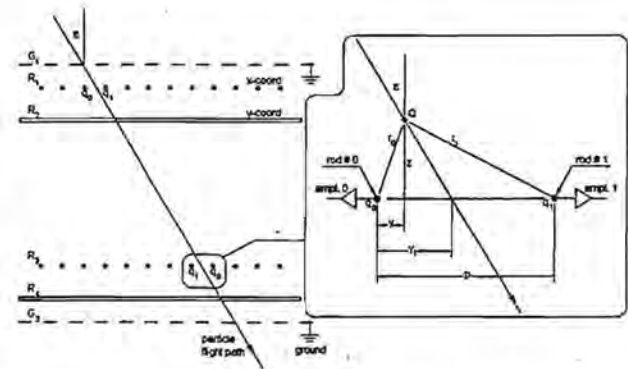


Fig. 1. Schematic cross section of rod sensor.

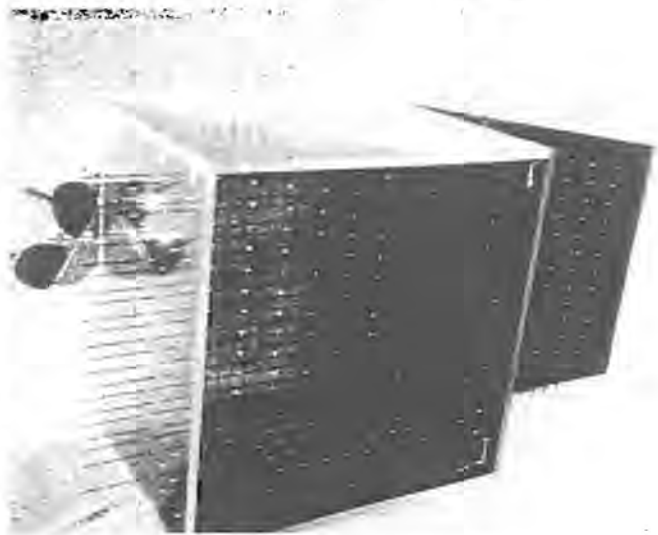


Fig. 2. Photograph of first test model.

conductive rods mounted on an insulating frame. Each rod consists of a carbon fiber-vinylester composite and is either connected to a charge amplifier or grounded.

Two sensor models have been built, one with a single rod assembly, tested in the laboratory with a free-falling steel ball, and a second one with five rod assemblies, tested on the Heidelberg dust accelerator.

Figure 2 is a photograph of the first model that we used for drop tests in the laboratory. Figure 3 is a photograph of the second model, mounted in the experiment chamber of the dust accelerator.

**Sensor Tests:** A charged steel ball, free-falling into the first model was used to simulate a moving dust particle in space. Figure 4 shows a schematic cross section of the model. The ball (diameter 2 mm) carried a charge of about  $10^{-12}$  C and moved at a speed of about 6 m/s.

Figure 5 is an oscilloscope display of the charge signals induced in the two rods that were closest to the path of the steel ball. In Fig. 6 we have plotted how the signals of Fig. 5 should look according to our theory (to be discussed later). Note the similarity of Figs. 5 and 6. Figure 7 depicts the measured ( $^{\circ}$ ) charge  $q_0$  of rod #0 for  $z = 0$  as a function of distance  $y$  (see also Figs. 1 and 4). The crosses show the  $q_0$  values as computed using equation (2). Note the very good agreement between theory and measurement.

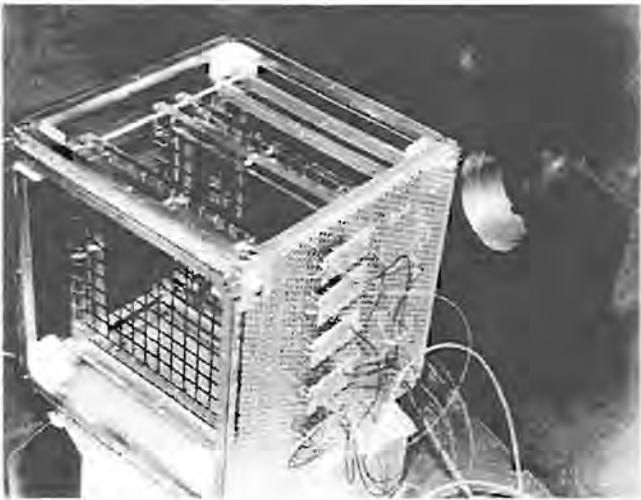


Fig. 3. Photograph of second test model while in the test chamber of the Heidelberg dust accelerator. The dust beam enters the chamber through the opening that can be seen on the right.

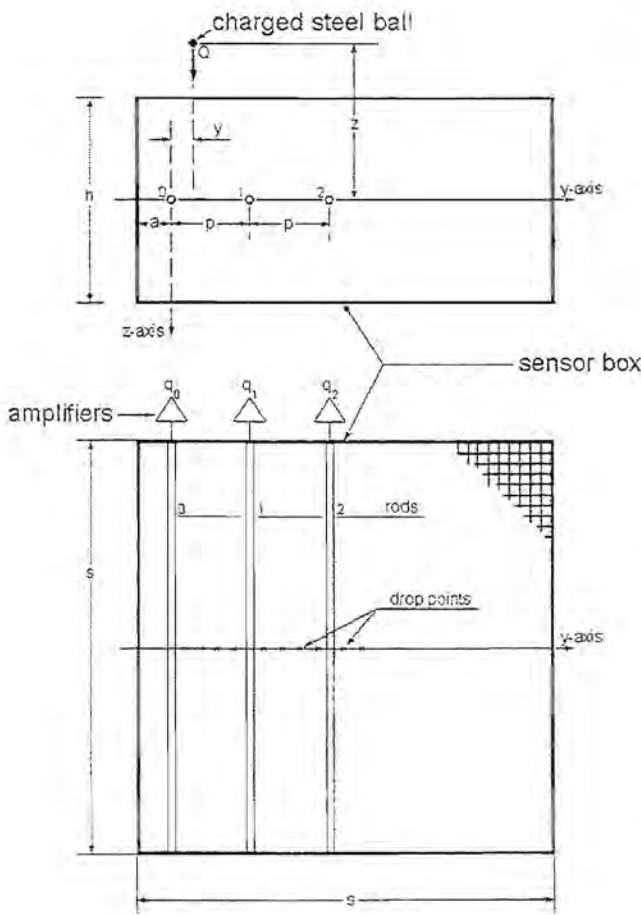


Fig. 4. Schematic cross sections of first test model.

Measured Rod Signals

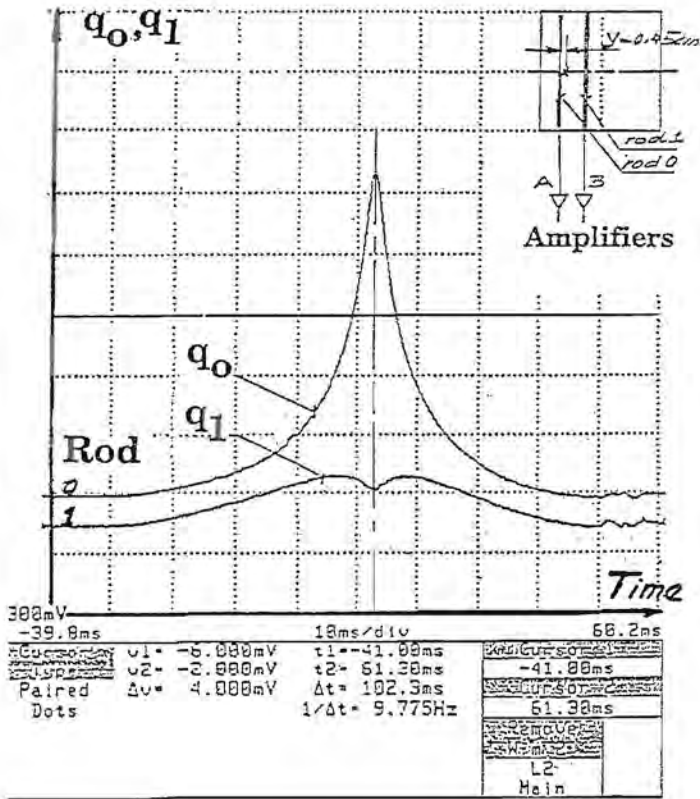


Fig. 5. Oscilloscope display of rod signals induced by falling ball.

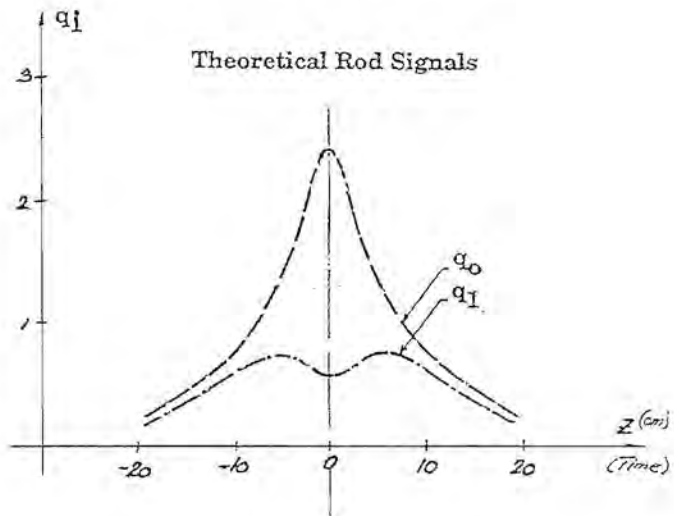


Fig. 6. Theoretical rod signals of charges induced by falling ball.



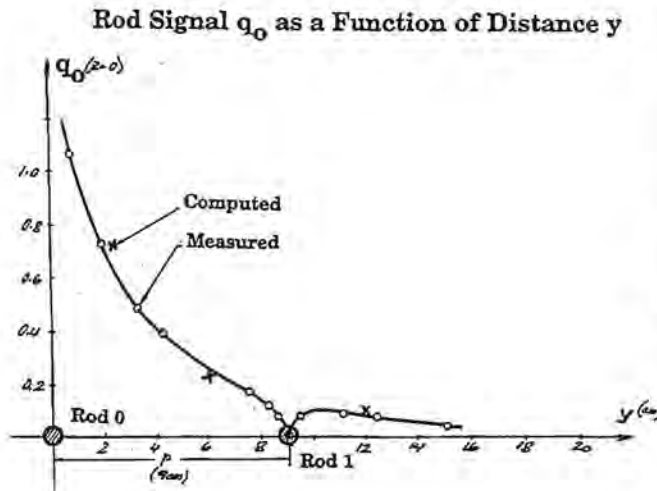


Fig. 7. Measured and calculated amplitude of rod signal induced by falling ball as a function of rod distance  $y$ .

The second model of the rod sensor was tested on the Heidelberg dust accelerator [3]. This machine accelerates iron microspheres to speeds of about 1–30 km/s. The particles' charges range from about  $10^{-15}$  to  $10^{-12}$  C and their diameters vary from about 0.1  $\mu\text{m}$  to 10  $\mu\text{m}$ . The sensor model was placed inside a test chamber at the output of the particle accelerator. The chamber provided both shielding from external electrical interferences and the vacuum required to form a dust beam.

The charge-sensitive amplifiers used had an equivalent RMS noise of about 300 electrons or  $5 \times 10^{-17}$  C. Figure 8 is an example of an oscilloscope display of amplified induced charges. Note the similarity of these signals with the theoretical signals of Fig. 5.

**Analytic Expressions for the Induced Charges:** The charge  $Q$  on a spherical particle with diameter  $d$  and surface potential  $\phi$  is known to be

$$Q = 2\pi\epsilon_0\delta\phi \quad (1)$$

The charge induced on rod  $i$  (in the first approximation [4]) is

$$q_i = (Q/r_i) / \sum (1/r_j) \quad (2)$$

where  $r_i$  is the perpendicular distance between the particle and rod  $i$  and the sum is taken over all rods  $j$  of the sensor.

From the geometry in Fig. 1 one obtains for  $r_i$  as a function of time  $t$

$$r_i = \{(ip - y_0)[(ip - y_0) + 2vts\sin\epsilon] + (vt)^2\}^{1/2} \quad (3)$$

where  $t = 0$  and  $y = y_1$  at  $z = 0$  (rod plane),  $\epsilon$  is the angle of incidence, and  $v$  is the magnitude of the velocity. Similar relations can be derived for the distances  $r_i$  to other rods in the same rod plane or to the rods in other rod planes.

Because the induced signals are also affected by conducting walls and grids, especially when the particle is close to one, and because of the finite length of the rods, the higher-order approximations for  $q_i$  are more complex than given in equation (2). We plan to present them in a future paper.

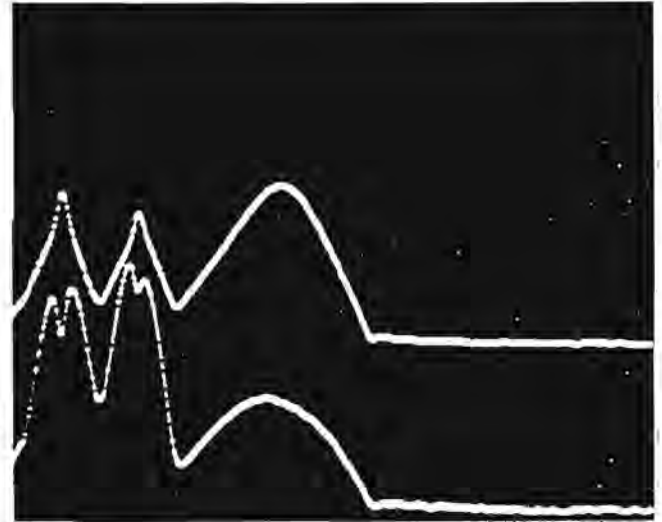


Fig. 8. Oscilloscope display of rod signals induced by particles from Heidelberg dust accelerator. The particle's speed is about 2 km/s and its charge 0.1 pC.

**Filtering of Noisy Signals:** By using the above equations we demonstrated that, with a signal-to-noise ratio (SNR) of 2.5, we were able to extract a value  $y_1 = 120$  mm with an error of about  $\pm 1$  mm. This corresponds to an angular path error of about  $\pm 0.2^\circ$  over an assumed flight distance of 300 mm. Using similar considerations, we estimated the error in  $v$  to be about  $\pm 0.3\%$ .

In order to perform our computer study, we assumed a rod/path configuration as shown in Fig. 9. As a specific example we used  $p = 50$  mm,  $y_1 = 120$  mm,  $\epsilon = 40^\circ$ ,  $v = 5$  km/s, and  $t = -40$  to  $+40$   $\mu\text{s}$ . The signal shapes ( $Q = 1$  for simplicity) as a function of time  $t$  are shown in Figs. 10–13. The darker line represents the theoretical signal as given by equation (2) above.

For our test we needed a more realistic signal, that is, a signal disturbed by noise as it will be in real life. We thus superimposed onto the theoretical signal white noise with a Gaussian amplitude distribution, equivalent to a SNR of 2.5. After we had thus "distorted" our signal we extracted the original signal. The extraction process is in essence the same as we plan to use for the "real" signals received by our sensor on the spacecraft.

The extracted signals are also shown in Figs. 10–13 (light lines). In the extraction process, we started by assuming an arbitrary path, i.e., arbitrary values for  $y_1$ ,  $\epsilon$ ,  $v$ ,  $\epsilon$ , and  $t$ , and computed the four theoretical rod signals resulting from that path. We then compared these signals with the "real" signals by computing the sum of the squares of the deviations, point by point, i.e., by least-squares fitting. The entire procedure was repeated, in essence, with all possible paths. We considered the signal with the minimum sum as the "filtered" or "extracted" signal and the corresponding path as the solution.

By studying the shapes of the signals  $q_i$  one can actually infer a lot about a particle's path without any analysis. Obviously, if the induced signal is large at a certain time compared to the others, it means the particle passed close to that rod. At oblique incidence, the signals peak at different times, depending on the angle of incidence.

**Conclusions:** Two simple test models have been built and tested in the laboratory and on a dust accelerator. The sensor operation is well understood, both practically and theoretically, and the tests support the theoretical calculations.

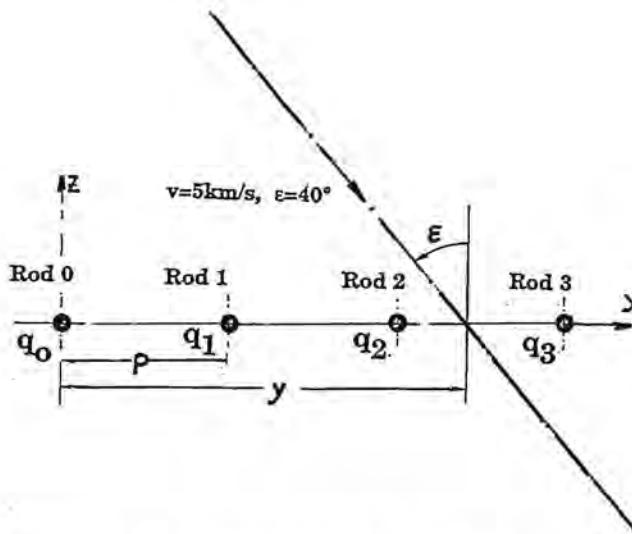
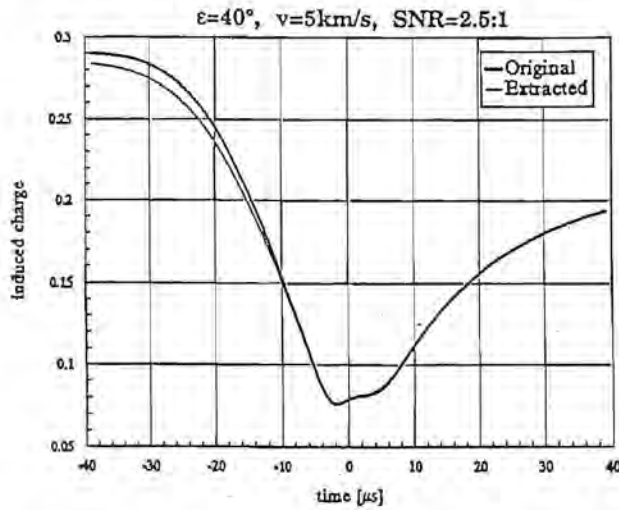
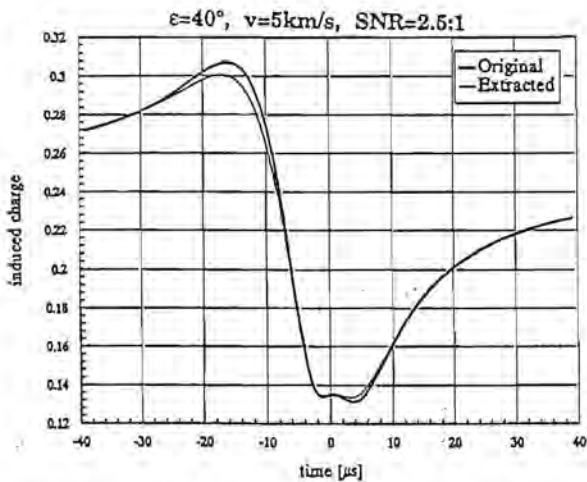
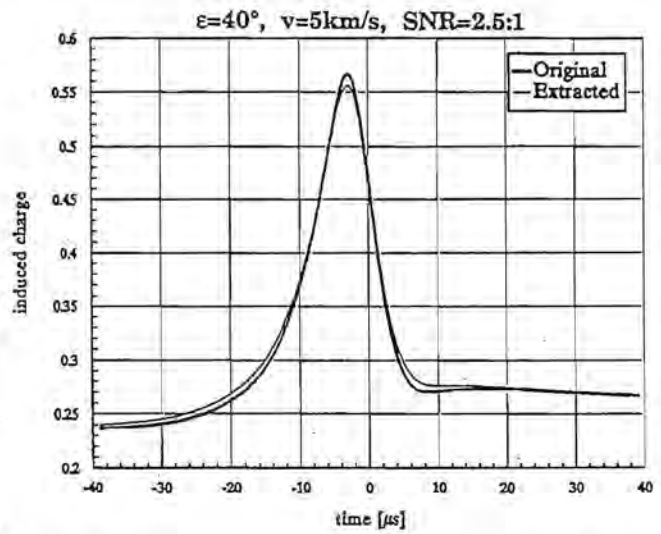
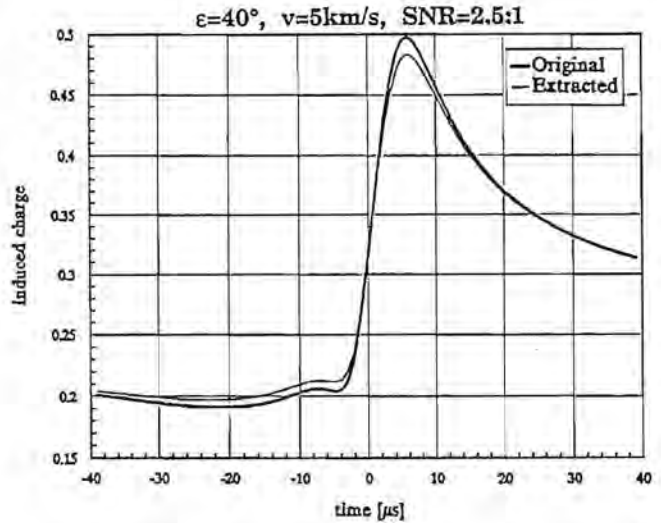


Fig. 9. Rod/path configuration assumed for the signal extraction test.

Fig. 10. Rod charge  $q_0 = f(t)$  for  $\epsilon = 40^\circ$ ,  $v = 5 \text{ km/s}$ ,  $\text{SNR} = 2.5$ .Fig. 11. Rod charge  $q_1 = f(t)$  for  $\epsilon = 40^\circ$ ,  $v = 5 \text{ km/s}$ ,  $\text{SNR} = 2.5$ .Fig. 12. Rod charge  $q_2 = f(t)$  for  $\epsilon = 40^\circ$ ,  $v = 5 \text{ km/s}$ ,  $\text{SNR} = 2.5$ .Fig. 13. Rod charge  $q_3 = f(t)$  for  $\epsilon = 40^\circ$ ,  $v = 5 \text{ km/s}$ ,  $\text{SNR} = 2.5$ .

The rod sensor is simple and rugged, and thus well suited for use on the space station or a free flyer. The required precision of  $\leq 1\%$  for the velocity components is satisfied. The probability of non-destructively sensing particles is very high (70–80%).

It should be noted that our sensor can readily be combined with a particle capture device or with an *in situ* dust composition analyzer.

**Acknowledgments:** This work was supported by the CDCF project (F. Hörz) of the Johnson Space Center, Houston, Texas,

under contract NAS9-18368. The Max-Planck-Institut für Kernphysik, Heidelberg, Germany (E. Grün), generously provided time on the dust accelerator. R. Auer developed the computer programs, assisted with the laboratory experiments, and performed the signal extraction tests.

**References:** [1] Zook H. A. (1985) *LPI Tech. Rpt.* 86-05, 97-99. [2] Auer S. (1975) *Rev. Sci. Instrum.*, 46, 127-135. [3] Fechtig H. et al. (1978) *Cosmic Dust* (J.A.M. McDonnell, ed.), 607, Wiley. [4] Auer S. and von Bun F. O. (1990) *Phase I Report to NASA/JSC NAS9-18304*, 21-23.

**MAIN CHARACTERISTICS OF THE COMET/COMRADE EXPERIMENTS.** J. Borg<sup>1</sup>, J-P. Bibring<sup>1</sup>, and C. Maag<sup>2</sup>, <sup>1</sup>Institut d'Astrophysique Spatiale, Bat. 121, 91405 Orsay Cedex, France, <sup>2</sup>Science Applications International Corporation, Glendora CA 91740, USA.

**Introduction:** Both the COMET (Collection en Orbite de Matière ExtraTerrestre) and the COMRADE (Collection of Micrometeorites, Residue and Debris Ejecta) programs are devoted to the collection and analysis of the particles of various origins orbiting around the Earth at low altitudes (between ~300 and ~500 km).

These particles can be roughly divided into categories of orbital debris resulting from manmade effects and extraterrestrial particles. The goal is to collect the extraterrestrial particles before they are processed by the Earth's atmosphere, which can cause severe alteration. The main interest in their study is because some of these particles contain information on the origin of the solar system. In particular, cometary material is likely to be the most primitive material accessible for analysis. It is thought that grains once present in the cometary nuclei and now present as individual grains in interplanetary space are the best candidates for still having properties they acquired before or during the condensation of planetary objects. A second minor component is also present, originating from the asteroidal belt. The smaller size fraction (grains less than 10  $\mu\text{m}$  in diameter) is supposed to be enriched in grains of cometary origin [1]. The grains we analyze are thus of various origins from inside the solar cavity and should reflect in their elemental, isotopic, molecular, and mineralogic composition the variety of components of the primary solar nebula. In addition, they have been subject, inside the past and present solar cavity, to various kinds of irradiations. It is now well known that these different irradiations of grains can result in different physical, chemical, or isotopic properties [2]. Also present is orbital debris with velocities of the same order and resulting from manmade activities (paint flakes, aluminium oxide spheres, etc.). The small-sized grains are the most frequent ones orbiting around the Earth, manmade debris having, for all sizes, much larger fluences than extraterrestrial grains.

The COMET experiment is more specifically designed to be flown for a short period of time (a few days), in concordance with a meteor stream crossing the Earth. Thus, it results in a considerable enrichment in the collection of grains related to a given comet.

The COMRADE experiment has been selected as a proposal for long-duration flights (a few months), in order to gain information on all sizes of particles present on low Earth orbits, including submicrometer grains. It has been accepted by ESA authorities for use on the EURECA 2 platform.

We are concerned simultaneously, for the future exposure of

both experiments, with a destructive capture of orbiting grains, using metallic collectors, improved since the COMET-1 experiment [3] and a nondestructive capture, using new low-density targets in which the impacting grains are slowed down and stopped, practically intact. The advantage of the first type of capture is twofold: It allows us to gain information on the smallest size fraction and to detect the presence of light elements such as C. The interest of the second type of capture is to allow the extensive study of intact IDPs. Up to now, this technique has only been applied to short flights of the NASA space shuttle for studies of orbital debris [4]. Grains a few micrometers in size can be stopped in those low-density materials and recovered for further studies.

The objectives of these studies are multiple. The use of passive detectors gives access to the chemical and isotopic properties of the grains in the micrometer size range, by analyzing either the particle remnant mixed with the target material, or the intact particle captured in a specific low-density material. The particle remnants of the micrometer-sized extraterrestrial grains, having impacted on purposely designed metallic collectors, are identified for complete and detailed chemical, isotopic, and organic analysis, thereby determining grain composition as well as the existence of organic and inorganic molecules, to be related with the possible cometary origin of the grains. Micrometer/submicrometer dust grains are also captured in a manner that ensures minimal particle degradation. The captured intact particles are returned to Earth for complete and detailed chemical, isotopic, spectral, mineralogical, and organic analysis.

These investigations, which will collect micrometer/submicrometer particles or their remnants, can at the same time measure the dynamic particle parameters (determination of its mass, velocity, trajectory, and, for some, charge) with a high degree of confidence, if active detectors are exposed in parallel with the collecting passive detectors. This part of the investigation is more adequately meant to be part of the COMRADE program, as long-term *in situ* dynamic measurements of these particles, in this spatial region, do not exist reliably and are of great importance by themselves, since detailed trajectory information is currently needed to calibrate experimental laboratory measurements. Such dynamic measurements, coupled with collection analysis, will help in advancing current theories on the evolution of the universe and the solar system.

**COMET Experiment:** The specificity of the COMET experiment is to expose collectors only during the encounter of the Earth with a given meteor stream, so that the collection is enriched in grains of a known origin, related to a specific comet. For this purpose, the collectors are installed in boxes that can be automatically closed and opened by the astronauts from inside the station.

Such a grain collection on low Earth orbit has started with the COMET 1 experiment that was designed to allow the collection of grain remnants by impacts on targets installed outside Salyut 7 station, orbiting at 350 km altitude [5]. The collectors were exposed to space in October 1985, while the Salyut 7 station was crossing the Draconides meteor stream, in order to study the chemical properties of grains originating from the Giacobini-Zinner comet. The collectors consisted of high-purity Au and Ni modules, of 2  $\text{cm}^2$  area, covered by an ultrathin (100 nm) Au film, having two main functions: (1) protection against contamination and (2) identification of impact positions. Modules with a total collecting area of 1152  $\text{cm}^2$  were allocated in four boxes. The boxes were opened and closed through an electronic unit from inside the station by the cosmonauts.



The collectors, after their exposure in space, are brought back in the sealed boxes to the clean rooms of the lab. There, they are opened and a first optical scanning is performed in order to identify the impact positions of the larger grains. The impact positions of the micrometer-sized grains are identified directly on the surface of the metallic collectors: After contaminant removal, the various metallic targets are thoroughly scanned, using a JEOL 840 scanning electron microscope (SEM) at 750 $\times$  magnification, in order to select events showing typical hypervelocity crater features (round circular habits, ridge). Such a magnification allows the identification of crater features down to diameters of  $\sim 0.5 \mu\text{m}$ . We can thus analyze the size distribution of the impacting particles, down to these sizes, allowing the evaluation of the incident microparticle flux in the near-Earth environment.

In a second step, it is possible to determine the chemical composition of the impacting particles. The JEOL SEM is equipped with an EDS analysis TRACOR system, allowing semiquantitative analysis down to Na, and qualitative detection down to C. Such a chemical identification can be followed by a high-resolution analytical protocol including instruments such as Field Emission Scanning Electron Microscope (FESEM) for high-resolution imagery of the impacting events, Laser Induced Mass Spectroscopy (LIMS) for molecular identification of the carbon compounds, or Secondary Ion Mass Spectroscopy (SIMS) for isotopic identification, for a complete characterization of the impacting particles.

The main results obtained up to now from the COMET 1 experiment are very encouraging. By counting the number of holes in the protective films and of impact craters on the bars of the grids holding the films and directly exposed to space, it is possible to estimate the flux distribution of particles at the moment of exposure. The correlations between hole and crater diameter and particle size were determined from simulation experiments that took place at the Dust Accelerator of the Max-Planck-Institut in Heidelberg.

We found for the number of impacting particles smaller than  $10 \mu\text{m}$  in diameter a cumulative flux of  $\sim 8 \times 10^{-2} \text{m}^{-2} \text{s}^{-1}$ , consisting of  $\sim 90\%$  orbital debris, as confirmed by chemical analysis. This value induces a large enhancement as compared with the known estimations of the micrometeoroid particle mass distribution [6]. We attribute this enhancement to the fact that the collection occurred during the encounter of the Giacobini-Zinner meteor stream. The extraterrestrial particles, supposed to be mainly of cometary origin, show various proportions of the following elements: Na, Al, Mg, Si, S, Ca, and Fe, associated in most cases with various proportions of C and O. For some extraterrestrial particles, C and O are found alone. The systematic presence of low Z elements, either exclusively or associated with other elements whose abundances reflect a chondritic-type composition, can be compared to results obtained by the PUMA and PIA experiments that analyzed the grains in the close environment of the Halley nucleus [7] or with chemical identifications on extraterrestrial particles from the stratospheric collections [8].

After the COMET 1 collection, we proceeded to improve the collectors: The protective 100-nm film has been eliminated and the collectors are now clean, flat metallic surfaces, either of Au or Ni, on which 50 nm of Au is evaporated in order to "decorate" and enlarge the impacting positions.

Also, collectors have been conceived to recover intact grains, whatever their density and size, as the return of extraterrestrial material to the laboratory is a primary goal of future investigations.

Such collectors are made of very-low-density material, either foam or silica aerogel, that would provide a unique means to slow down all the grains with minimal destruction and thus allow their further analysis, not only for elemental and isotopic composition, but also their molecular composition and mineralogical and physical properties.

In order both to visualize the impact hole of intact particles at the surface of the low-density material and thermally protect the material, the surface of the collectors will be covered by 50 nm of a highly reflective metal (either Al or Au) and 200 nm of evaporated silicon oxide. An optical survey of the surface allows the identification of the impact positions. By following the track inside the foam, the particle can be reached, picked up with a clean needle, and recovered on a golden microscope grid for future analysis [9]. A quick EDS identification can indicate whether the particle is an IDP (chondritic elements: Mg, Fe, Si, . . .) or orbital debris (Al, Ti, Zn, . . .). The same high-resolution analysis protocol (FESEM, LIMS, SIMS, . . .) as for grain remnants can be applied to the intact particles for their further identification.

An improved version of the COMET instrument has been designed, manufactured, and tested. It will hopefully be installed in the near future onboard one of the two last automatic spacecraft to be docked to the Russian MIR station. The results already obtained with the COMET 1 experiment show that such an instrument can constitute an important step toward the analysis of cometary material and the understanding of the early evolution of the solar system.

**COMRADE Experiment:** As an extension of the COMET program, and taking into account the future possibilities of long-duration flights, we proposed in 1991 to ESA the COMRADE program, which was to be integrated as a program to be flown on the EURECA 2 carrier, devoted to the determination of the main properties of the particles on LEO. Therefore, it includes a more complete set of detectors, both passive and active, in order to gain the maximum information on the impacting particles [10].

The concept underlying the proposed investigation is to conduct a long-term investigation into micrometer/submicrometer charged dust grains in near Earth orbit. During this investigation, the proposed experiment will capture intact dust grains/particles and ejecta as well as remnant particles for chemical analysis and at the same time conduct state-of-the-art *in situ* measurements of the fundamental grain parameters (trajectory, velocity, mass, and charge).

The specific concepts/methods underlying the various parts of the integrated instrument are quite similar to what has been described for the COMET experiment, concerning the passive detectors, except that it is proposed that the various collectors are exposed for the totality of the mission and thus do not have to be mounted in boxes to be opened and closed. Independent cells can be devoted to specific tasks, as the detectors are conceived as independent units that need not sit together if needed. The use of the multiuser facility ESTEF (European Science and Technology Exposure Facility) is provided on EURECA, the external faces of which could receive our experiment tray of passive detectors. The exposure geometry of EURECA is supposed to be essentially Sun pointing; this situation is such that the Earth-orbital particle population component will be randomized by opposition to the heliocentric interplanetary component. All crossing meteor streams will thus have grains impacting our collectors, enriching our collection in grains of cometary origin.

What is specific to the COMRADE experiment, as opposed to the COMET experiment, is the possibility of having access at the



same time to the measurement of the fundamental parameters of the particles.

The reliable determination of the trajectory of each individual dust particle is a high priority of the proposed investigation. Historically, particle trajectories (as well as particle time of flight) have been determined using the thin film/plasma technique. This technique is based on the fact that a cosmic dust particle that impacts an extremely thin film will create a minute plasma cloud. The collection of this plasma cloud then allows the analytic determination of dynamic particle parameters. The use of multiple thin films thereby yields a method whereby particle trajectories and time of flight can be determined.

In addition to the particle trajectory, it is vital that dynamic particle parameters also be measured with a high degree of reliability. The basic parameters that the proposed experiment could measure and/or determine are the particle's velocity, mass, and mass flux. The particle charge and time of flight can be measured by examining the thin-film/plasma technique discussed previously. Also, by examining the amplitude of the plasma pulse produced, the kinetic energy of the particle can be obtained, which in turn enables a determination of the particle's mass. Since one of the major goals of the proposed instrument is to capture the particle while causing minimum particle degradation, it is necessary that extremely thin films be used in this sensor. The thinner the foil, the smaller the plasma produced and the more difficult it is to capture the signal produced. However, the experiments previously listed, along with the production and collection of ions and electrons from current laboratory hypervelocity impact studies, have yielded the data necessary to optimize the collection ability of the proposed instrument [11]. Collection of plasma from rear-plate hypervelocity impact will imply penetration of thin films by an incident dust grain. Thus a lower bound on particle mass is set that depends on inferred density and the penetration mass limits established during calibration studies conducted using materials with various densities.

In order to determine the momentum of individual particles, piezoelectric transducers (PZT) have been used as impact impulse sensors since Explorer 1. The distinctive characteristic of any linear elastic system, like a PZT crystal, is that the maximum displacement of the system is directly proportional to the impulse imparted, and the displacement of the crystal produces a proportional potential. Through calibration, a known impulse may be equated with a specific charge produced on the electrodes of the PZT crystal. With precise knowledge of the plasma collected at the PZT impact plate, and with accurate measurement of velocity vector, one can with calibration data from hypervelocity impacts on PZT plates establish an upper bound on the particle mass. The accuracy of this method depends on the composition of dust grains utilized in laboratory simulation studies.

Therefore, by coupling plasma collection after thin-film penetration and hypervelocity impact PZT measurements, one may establish a lower bound and an upper bound on the mass of the dust grain encountered. If one assumes that the incident dust grains are spherical, one can then determine the volume from the radius derived by the electrostatic charge measurement. The density of the dust grain can thus be deduced using the lower and upper bound values provided by the other sensors of the detector package.

One aspect of measurement not yet exploited is the density difference of impactors. If the density of a dust grain is less than the thin film and/or the impact plate material then the hypervelocity

impact will convert more of the dust grain into plasma than thin film or PZT impact plate material. If calibration studies are performed to characterize the plasma signature, e.g., pulse width, received from an Al thin film and a Au-coated PZT plate, then impact plasma signals collected after hypervelocity impacts of less dense material could show anomalies. With these data a greatest upper bound on particle density may be established, i.e., anomalous plasma signature with too narrow a pulse width implies low atomic number material. With an estimate of density,  $\rho$ , and with mass of the grain values,  $m_g$  (density of the grain) may be calculated and finally bounds set on the ambient potential  $V_a$ .

Independent unit cells have been designed to accommodate the myriad subexperiments needed for the determination of the various parameters described. Each unit will possess one or two thin Al films (nominal  $t_f < 50$  nm) stacked above a coated substrate. Beneath the thin films and above the substrate will be a network of collimating plates. These divisions will assure that grains whose velocity vectors make a large angle with respect to the surface normal of any film will not impinge on another cell, but will impact the witness plates of a specific cell or be stopped by a thin film.

**Conclusions:** It is in the context of the search for organic material in extraterrestrial particles down to submicrometer sizes that our proposal must be perceived, exposing our types of passive detectors (metallic collectors and low-density material) onboard the EURECA 2 flights, as well as on the MIR flight, in boxes opened for exposure only during the encounter with a given meteor stream. Any collection facility designed to identify particles of cometary origin should contain some high-purity metallic targets for chemical and isotopic identification of particles. The coupling of metallic collectors and low-density material is a unique opportunity to complete information on all sizes of grains from submicrometer sizes to a few micrometers.

All grains down to submicrometer sizes can be collected on our metallic targets. Because of their high relative velocity ( $\geq 5$  km/s), the impacting grains are physically destroyed, leaving a melted remnant that is mixed with the crater material. This process is more favorable for the smaller grains, with sizes in the micrometer size range; the larger grains can vaporize, leaving no analyzable remnant. Our previous results have shown that Au and Ni collectors are favorable for the collection and analysis of the small-sized grains orbiting around the Earth. For the less frequent larger grains, their collection is possible in the large surfaces of low-density material we will expose.

The analysis of the grains, either remnants or entire, will be performed with the high-resolution instruments we will have access to (optical microscopy, SEM, EDS, ion probe . . .). By the time the collectors will be back from space, new techniques will have been developed and accessible for our analysis, for instance, IR spectroscopy of individual grains, or double laser probe, promising techniques for eventually identifying organic molecular species present inside the grains. The possibility of recovering particles of cometary origin, in which the organic phase can be analyzed, is a very exciting one, as the comet grains remain privileged witnesses of the beginning of the solar system.

The present COMET and COMRADE proposals expand upon a program initiated a few years ago with the COMET 1 experiment. It concerns the collection of cometary dust and space debris by exposing various detectors onboard spacecraft orbiting the Earth. It takes into account not only the possibility of gaining information

during the given flights, but also, and more importantly, the fact that these experiments could fit into the general perspective of proposing a permanent collection facility.

**References:** [1] Bell J. F. (1991) *Meteoritics*, 26, 316. [2] B  nit J. and Bibring J.-P. (1990) *LPS XXI*, 65-66. [3] Bibring J.-P. et al. (1985) *LPS XVI*, 55-57. [4] Maag C. et al. (1993) *Proc. ESA Conference on Orbital Debris Ist.* [5] Borg J. et al. (1993) *Meteoritics*, in press. [6] Borg J. et al. (1993) *LDEF-69 Months in Space*, NASA Publication 3194, 347-356. [7] Langevin Y. et al. (1987) *Astron. Astrophys.*, 187, 761-766. [8] Rietmeijer F. J. M. (1992) *Asteroids, Comets, Meteors 1991*, 513-516. [9] Maag C. R. and Lindner W. K. (1992) in *Hypervelocity Impacts in Space* (McDonnell, ed.), 187-195. [10] Borg J. et al. (1993) *Proc. ESA Conference on Orbital Debris Ist.* [11] Tanner W. G. et al. (1992) in *Hypervelocity Impacts in Space* (McDonnell, ed.), 239-243.

**THE HYPERVELOCITY IMPACT FACILITIES AT THE UNIVERSITY OF KENT AT CANTERBURY, UK.** M. Burchell, J. A. M. McDonnell, M. J. Cole, and P. R. Ratcliff, Unit for Space Sciences, University of Kent, Canterbury, Kent CT2 7NR, UK.

The University of Kent at Canterbury facilities for production of hypervelocity impacts are described. Meteoroids are simulated by electrostatic acceleration of small ( $10^{-12}$ – $10^{-17}$  kg) particles using a 2-MV Van de Graaff accelerator. This machine has been operational for many years; both the machine and experimental area are currently being upgraded. Larger particles ( $10^{-10}$ – $10^{-4}$  kg) are accelerated using a more recently installed light gas gun. The status of all hardware (including experimental areas) is given, along with brief details of recent, current, and future projects making use of them.

**Introduction:** The Unit for Space Sciences at the University of Kent has an extended history of studies of micrometeoroids. The design, manufacture, and calibration of micrometeoroid detectors has been one of the group's major activities. An important tool in this process has been the laboratory simulation of hypervelocity impacts on selected target materials. Traditionally the Unit has achieved this using electrostatic acceleration of (charged) microparticles in a 2-MV Van de Graaff accelerator (operational at Kent since 1974). More recently a light gas gun has been installed, explosively accelerating larger particles. This extends the projectile mass regime from micro (order  $10^{-15}$  kg) to macro ( $10^{-4}$  kg) particle size. Details of these devices are given below, along with descriptions of their current use.

**Van de Graaff Accelerator (2 MV):** This has been operational at Kent since 1974. It is one of only two such installations that have been continuously available for microparticle acceleration over the years. The other is also a 2-MV machine, at the Max-Planck-Institut f  r Kernphysik, Heidelberg, Germany [1]. (Note also that a 6-MV machine was used at Los Alamos for similar work at the end of the 1980s [2].) The machine has been described in detail previously [3], so only brief details or new information are given here. A dust reservoir is at the high-voltage end of the machine (top terminal). This is kept at 15 kV above the 2 MV of the rest of the top terminal, and is pulsed at 1 Hz to just 1 kV above 2 MV. Charged dust is then directed onto a needle tip positioned in front of a small hole in the base plate of the top terminal. The most efficiently charged particles

arrive at the needle tip and are exposed to the potential difference between the top terminal and the earthed far end of the machine. They thus accelerate through the hole in the top terminal base plate and along a flight tube that runs the length of the machine. The 2-MV potential difference is linear along the length of the flight tube, and is maintained by 52 equally spaced ring electrodes. Between the top terminal and the first of these is a cylindrical tube maintained at a voltage set by the machine operator. The field at the entrance and exit of this cylinder serves as a focusing element for the beam. The main axis of the accelerator is horizontal, and the flight tube is approximately 2 m in length. While the flight tube is maintained under a vacuum of some  $10^{-6}$  mbar, the rest of the accelerator is filled with a dry gas (20%  $\text{CO}_2$  and 80% N, mixed with a trace of  $\text{SF}_6$ ) at 100 to 150 psi. This is to prevent sparking and breakdown of the potential.

Although the potential is 2 MV, due to the mass of the microparticles, the acceleration is totally nonrelativistic. Thus we can write that the kinetic energy is simply the energy gained by acceleration

$$0.5 \text{ mv}^2 = qV$$

where  $m$  is particle mass,  $v$  its final velocity,  $q$  its charge, and  $V$  the accelerating potential. It can thus be seen that  $v$  is a function of  $q/m$ . For fully efficient charging, the charge is a surface effect, and thus (for perfectly spherical particles of a given type)  $q/m$  is fixed at a given mass. So (with a small spread) there is only one velocity for a given mass particle, and the highest velocities are associated with the smallest masses. This is shown in Fig. 1, where data for iron particles accelerated in the machine are given. Note that for a normal dust sample (one that has not been finely graded for particle size) the bulk of the population is at high mass, and hence low velocity. Figure 1 shows that the typical mass range for iron particles is  $10^{-13}$  to  $10^{-16}$  kg, with corresponding velocities 1–25 km/s. Iron is typically used in the accelerator, but other conducting materials can be used as required. Indeed, nonconducting materials can also be used, provided they can be coated with a conducting surface.

The accelerated particles (the flux above 1 km/s is typically 5 or so per minute) leave the Van de Graaff as a beam with diameter of up to 2 cm. Some dispersion of the beam is present, and typically represents a maximum opening angle to the beam axis of  $\tan \theta = 1/250$ . In part this can be controlled by the focusing element mentioned above.

In order to improve the understanding of the machine and ensure better operator control, a new top terminal monitoring system is currently being installed (summer 1993). This consists of a programmable circuit board mounted on the top terminal. Via ADCs it can sample up to eight inputs at a frequency of 15 kHz. Since the top terminal cannot be directly linked to Earth via an electric cable, this monitor is read out via a fiber optic link connected to the base (Earth) of the machine. Circuits to convert the electrical signals to light pulses (and vice versa) are included at both ends of the cable. This permits a two-way data flow. Voltages of components inside the top terminal are to be monitored, as is the voltage of the focus element and the temperature. Control of the system is via a microcomputer used by the machine operator.

The user area consists of three main elements linked by 6-cm-diameter stainless steel tubes. Any or all of these main components may be present at one time. The first component is a stainless steel



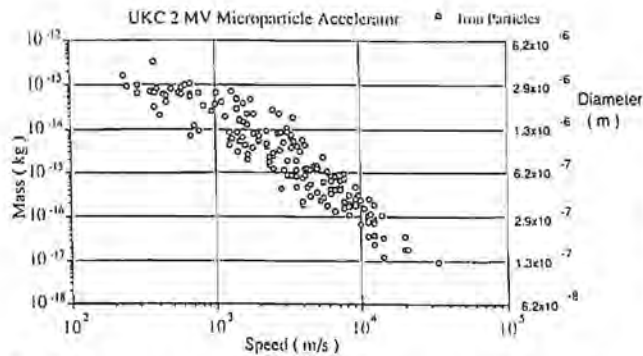


Fig. 1. Measured mass vs. velocity for iron particles accelerated in the 2-MV Van de Graaff Facility.

"pot" (a cylinder of height 50 cm and diameter 30 cm). This is equipped with high-vacuum flanges with electrical feedthroughs and view ports. It is positioned in the beam line with the cylinder's main axis vertical. It contains a stage, which can be moved vertically over a distance of 10 cm by an external crank. This is in the process of being changed, so that the new stage will be motorized, being capable of 10 cm movement vertically and 10 cm horizontally along an axis perpendicular to the beam. A motorized rotatable small stage will be mountable on the main stage if required. This system will be driven by the operator from a touch panel, and the position will be continually monitored, with the information available to the user. This should be installed and operational beyond September 1993.

The "pot" is used as close to the accelerator as possible, and is connected to it via a T-shaped beam pipe. The extra outlet from the T junction leads to an oil diffusion pump, which provides a vacuum of  $10^{-6}$  mbar in both the accelerator flight tube and the "pot."

The second main component is a velocity selection unit. This has four parts. The first is inserted in the beam pipe. It consists of three tubes positioned sequentially along the beam axis. They serve as pickups when a charged particle passes through them. The induced charge is amplified by an Ortec charge sensitive amplifier (type 142A). The first and third tubes are 10 cm apart and give signals, the leading edges of which serve to provide the timing information necessary for determining the velocity. The central tube is used to provide an accurate charge measurement (necessary when combined with the velocity to obtain the particle mass). The second element of this system is the hardwired electronics, which takes the signals, looks for a leading edge above a threshold on the first and third signals, and finds their time separation in units of 20 ns. This is then compared to a preset velocity window and a yes/no decision and the particle velocity and charge are then available on outputs. The third element is simply a 50-cm-long tube, which serves to introduce a particle flight time sufficient to permit the electronics to reach a decision. The final element is a coffin-shaped box, 165 cm long, 13 cm high, and a maximum of 56 cm wide. An oil diffusion pump is mounted on the coffin to provide an interior vacuum of  $10^{-6}$  mbar. The coffin contains two pairs of kicker plates that can be charged and discharged to deflect the beam particle. This system operates in two modes. The first is to keep the plates charged and to discharge them if the particle's velocity is acceptable (i.e., the chosen particles suffer no deflection and travel straight through the system). The second method is to charge the plates only when a particle is selected and to deflect it a fixed amount into a new, off-axis, beam line.

The final user component normally present is a large stainless steel "churn." This is a cylinder 2-m long, with a diameter of 1 m. It is positioned so that the main (2-m) axis is horizontal and perpendicular to the beam direction. It is equipped with view ports and high-vacuum flanges with electrical feedthroughs. The vacuum is supplied by an oil diffusion pump mounted directly on the churn, giving a vacuum of  $10^{-6}$  mbar. It is planned to replace this pump with a new cryopump. This will provide a vacuum of at least  $10^{-7}$  mbar, which, locally, should be free of any contaminating oil vapor. To reduce oil contamination from the rest of the system, a turbo-molecular pump will be mounted on the beam line just before the churn to provide an isolating vacuum region of at least  $10^{-8}$  mbar. The specification for the cryopump has an over-capacity on the gas compressor, so that extra cold heads can eventually be installed to replace the other oil diffusion pumps in the experimental area. Other improvements to the user area are also underway. A new, more compact velocity selection system is being designed and built. The coffin will be replaced with a tube 50 cm long, and 10 cm in diameter (slightly larger than the normal beam tubes). This will contain one pair of kicker plates 35 cm long. This is under construction. The three-element charge pickup will be replaced by a new two-element device. The central element of the previous device is removed, and the last element used to provide not only a timing signal but also the measure of the charge. Again this is under construction. A new electronic decision-making circuit is being designed and should make the system more flexible. Beam position monitors are also being installed. These consist of parallel plates followed by a conducting tube, all inserted into the beam line. In each pair of plates, one is earthed and the other read out via an Ortec charge-sensitive amplifier. The passage of a charged particle between the parallel plates produces an output signal whose magnitude is dependent on the particle's charge (measured by the tube) and its relative distance between the plates. The calibration of this is achieved by collimating the beam so that it passes along a known path between the plates, the resulting signals then being studied. This is checked by a calculation of the expected induced charge on the plates. One device, consisting of two pairs of parallel plates (the second pair rotated by  $90^\circ$  around the beam relative to the first) has already been installed and calibrated. It provides position information on the location of a particle in two axes perpendicular to the beam direction good to 1 mm. Refinements in the calibration method are hoped to improve this. Two more such devices are being constructed. One feature of these beam monitors is that the signals are read out not just on an oscilloscope, but also into an IBM-486-compatible personal computer. The data acquisition system used is a software package from National Instruments called LABVIEW [4]. This is interfaced either directly to the data (via a standard DAQ board) or to the oscilloscope (via an IEEE 488.2 standard GPIB board). The user writes his own application program using the LABVIEW software and can not only acquire the data (and store on 3.5-inch disk) but also display and analyze on line. Thus in a time of order 1 s after acquisition, the x,y coordinates are available (as is a measure of the velocity). The LABVIEW language is not a text-based system, rather it is symbolic, using icons and circuit drawing tools to permit operations upon the data similar to that which occurs in a hardwired electronic circuit.

**Experimental Programs Using the Van de Graaff Accelerator:** The Van de Graaff has been used for many years to support the activities of the Unit for Space Sciences at Kent. During

the 1980s, data from the machine was used in the calibration or interpretation of data from the space shuttle STS 3 microabrasion foil experiment, the Long Duration Exposure Facility (LDEF) microabrasion foil experiment, the Giotto Dust Impact Detector System and Particulate Impact Analyzer, and for prototype work for several other projects. The recently retrieved ESA satellite EURECA, carried an experiment (TICCE) built at Kent, the analysis of data from which will owe much to studies made using the accelerator. Indeed, the studies of thin foil penetration and crater size and depth in semi-infinite (thick) targets, which has been carried out at Kent has been widely published and used [e.g., 5].

Similar programs of work are continuing, as is work studying the impact processes themselves, and comparing the results with the predictions of calculations. In particular, plasma production, the role of ejecta, the influence of oblique angle impacts, and the energy partitioning occurring during impacts are all being studied.

Current detector work includes the design and testing of the Cosmic Dust Analyzer [6] for the Cassini/Huygens mission to Saturn and its moons, scheduled for launch in October 1997. This is an elaboration of the dust detectors on the Ulysses and Galileo missions now operational [7]. The detector is an ionization sensing device. A schematic is shown in Fig. 2. The dust enters through the grids at the top of the device. Any charge is detected as a pulse in the electronics connected to the grids. The dust particle then impacts an ionization target (a curved surface made of gold) or a chemical analyzer target (a curved surface made of rhodium). The ions liberated in the impact are attracted to an ion detector (a discrete dynode electron multiplier) mounted at the focus of the curved surfaces. Over the 3 mm just above the chemical analyzer target surface an intense field of 1 kV is applied. There is a further potential difference of 350 V between the entire target surface and the ion detector. For the chemical analyzer this combination is sufficient to make any initial ion momentum negligible, thus permitting a chemical decomposition of the ions by the time-of-flight method. After subtraction of the target contribution, the remaining chemical species present are a measure of the dust particle's composition. Due to the high field and small drift length, a fast digitization of the signal from the ion detector is required. A 100-MHz system is under separate development at the Rutherford Appleton Laboratory (UK). The incident particle velocity is found by one of several methods (listed in decreasing accuracy). If there is sufficient charge the shape of the pulse on the entrance grids yields the velocity. Next, if the particle impacts the ionization target (Fig. 2) the rise time of the pulses on the target and ion collector give the velocity. If the particle hits the chemical analyzer, the rise time of the signal is too fast to give the velocity; however, there is a broadening of the signals in the mass spectrum that can give velocity to a factor of 2. The particle mass is found from the total ion yield, since this has been shown to be proportional to mass for a given velocity [6].

That the detector design was feasible was demonstrated with a prototype used in the Van de Graaff accelerator in 1989–1990. A typical mass spectrum is shown in Fig. 3. This was for an iron particle (25 km/s) impacting on an Al target doped with Ag. Since the velocity and mass are independently measured for accelerated particles, the calibration of the detector for measuring these quantities can also be obtained. Testing and calibration of the project laboratory model of the detector was scheduled to take place during late 1993.

A new project, which will shortly start to make use of the

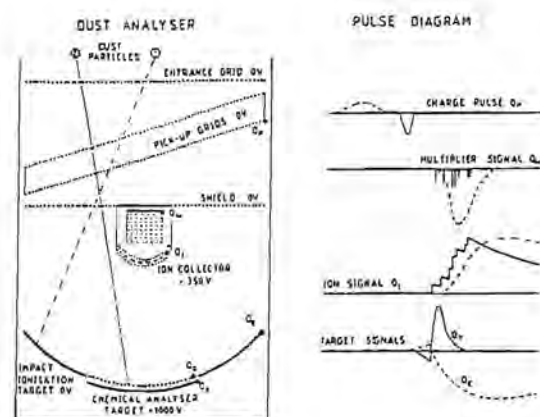


Fig. 2. Schematic of the Cassini Cosmic Dust Analyzer and representation of signals obtained [6].

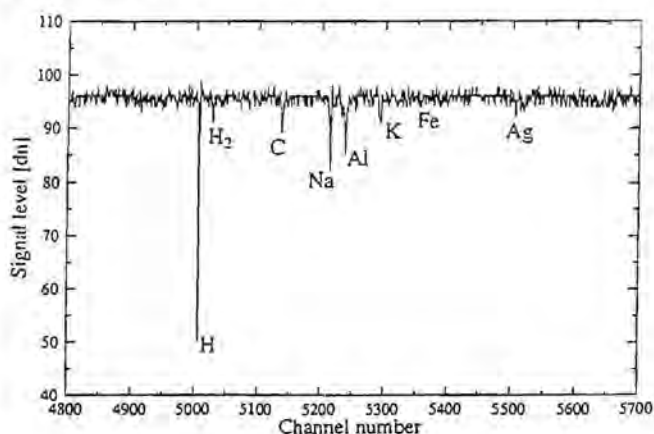


Fig. 3. Mass spectrum obtained by the Cosmic Dust Analyzer for an iron particle impacting a Ag-doped Al target at 25 km/s [6].

accelerator, is a proposal to construct a dust flux analyzer for the Pakistani satellite Badr-B. This is scheduled for launch in December 1994. It is proposed to include on the satellite a plate for detecting dust impact. This will be multiply instrumented, including PVDF coatings, which when penetrated are locally depolarized, producing a signal proportional to the incident kinetic energy. Piezoelectric zirconium titanate sensors and lead zirconate transducers will also be present, allowing both a confirmation of the impact and, by arranging several sensors on the plate, the relative timing of the signals will permit a position determination for the impact. This concept will be tested in the accelerator, making particular use of the new motor-driven stage and beam position monitors. Although, the piezoceramic sensors require a relatively large mass impact to be fully sensitive, sufficient masses can be accelerated to make calibration and testing practical.

A separate program of work is also planned to observe the degree of degradation of optical surfaces after exposure to the micrometeoroid population in Earth orbit. This will involve use of both the accelerator and the light gas gun below.

**Light Gas Gun:** The Light Gas Gun was installed at Kent in 1989, and has since undergone development. It is approximately



6 m long. At one end is a gun, firing a 32-g cartridge (diameter 2 cm). The volume of powder is typically 10–13 g. The expanding combustion gases cause a piston to advance down a shaft, compressing a chamber of hydrogen gas (initially at 40 bar). At the far end of this chamber is a pressure-sensitive disk, which ruptures when a sufficient pressure has been reached. This then permits the acceleration of a nylon sabot (a cylinder 4 mm long, 4 mm diameter, and mass of 80 mg). This can serve as the projectile and reaches velocities of up to 5.45 km/s. Alternatively it can be pre-cut and loaded with a chosen projectile. In this case, due to rifling in the barrel down, which it initially travels, plus the cuts, the sabot is discarded and flies away from the projectile leaving it free to fly to the target by itself.

During the sabot's (or projectile's) flight its velocity is measured by the time interval between its passage through two light curtains. These are from white light sources mounted perpendicular to the direction of flight, and are 50.5 cm apart. The flight through a curtain is detected from light scattered into a photomultiplier tube positioned perpendicular to the flight direction and at 90° to the light source.

The target is mounted in a target chamber at the far end of the system. A target diameter of 10 cm can be accommodated. This chamber (as is all the system after the rupture disk) is pumped by a rotary pump to a minimum vacuum of  $10^{-3}$  mbar.

**Light Gas Gun Experimental Program:** The gun is being used for a variety of programs. Chief among these are studies of crater shape (in particular ellipticity and depth variations across the crater) for oblique impacts. The distribution (in both direction and mass) of ejecta is also being studied. Both these projects use the 80-mg nylon sabot as the projectile. Recent firing of the gun for this work has consistently attained velocities of around 5 km/s, with the highest reliably recorded velocity being 5.45 km/s.

A separate project is underway where the sabot is loaded with small glass beads. The sabot has been successfully discarded in flight and a sample target bombarded with a cloud of the beads. These beads are typically around 50–200  $\mu\text{m}$  in diameter (and thus mass ranges from  $10^{-9}$  to a few  $10^{-7}$  kg). It is clear that masses greater than those obtainable in the Van de Graaff machine are being accelerated. Fine grading of the beads by size will be carried out during the full program of work to produce impacts of just a limited mass range on each target. The targets to be used correspond to materials flown on previous space flights, where interpreting the data has proved difficult due to suspect or questionable calibrations. Thus it is hoped to recalibrate the results of micrometeoroid fluxes from past experiments, to check the results, and to increase the size of usable datasets in such studies.

**Conclusion:** The hypervelocity impact (simulation) facilities of the Unit for Space Sciences at the University of Kent have been described. Their main features have been given, along with indications of their typical performance and the use to which they are put. Although the internal program of work is a vigorous one, care is taken to ensure that, where possible, time is made available to external collaborators or to groups who wish to visit. This is essential given the limited number of such facilities.

**References:** [1] Fechtig H. et al. (1972) *Naturwiss.*, 59, 151. [2] Keaton P. W. et al. (1990) *Int. J. Impact Eng.*, 10, 295–308. [3] Green S. F. et al. (1988) *J. Brit. Interplanet. Soc.*, 41, 393. [4] *LABVIEW*, a product of National Instruments. Contact the local sales office for details. [5] McDonnell J. A. M. and Sullivan K.

(1992) *Proc. Hypervelocity Impacts in Space* (J. A. M. McDonnell, ed.), 39–47, Univ. of Kent. [6] Ratcliff P. R. et al. (1992) *J. Brit. Interplanet. Soc.*, 45, 375. [7] G  ller J. R. and Gr  n E. (1989) *Planet. Space Sci.*, 37, 1197–1206.

## IRAS OBSERVATIONS SHOW THAT THE EARTH IS EMBEDDED IN A SOLAR RING OF ASTEROIDAL DUST PARTICLES IN RESONANT LOCK WITH THE PLANET.

S. F. Dermott, S. Jayaraman, Y.-L. Xu, and J.-C. Liou, University of Florida, Gainesville FL 32611, USA.

Collisions among the asteroids result in the grinding down of the asteroid belt and the production of small dust particles that spiral toward the Sun due to the action of drag forces, particularly Poynting-Robertson light drag. Numerical integrations show that a significant fraction (~23%) of these particles are temporarily trapped in corotational resonances external to the orbits of each of the terrestrial planets, particularly the Earth. The result is that the Earth is embedded in a sharply defined ring of asteroidal particles of width 0.4 A.U. There are longitudinal variations in the number density of the ring: in particular, there is a well-defined cavity that contains the planet. The action of drag introduces a phase lag into the equation of motion of these resonant particles with the result that the position of the Earth within the cavity is markedly asymmetric with the Earth closer to the edge of the cavity in the trailing orbital direction (opposite to the Earth's orbital motion) than in the leading orbital direction. We have analyzed all the infrared observations of the zodiacal cloud obtained in 1983 by the Infrared Astronomical Satellite (IRAS) and shown that when viewed at a constant elongation angle of 90°, the elliptic brightness of the cloud is systematically greater by ~3% in the trailing direction than in the leading direction. This asymmetry is observed at all times of the year and in all three of the IRAS wavebands in which the zodiacal cloud is clearly observed. The orbits of cometary particles are highly eccentric and these particles are unlikely to be trapped in corotational resonances. Thus, the IRAS observations are evidence that the Earth is embedded in a ring of asteroidal particles. Similar rings are expected to be associated with Mars and Venus. The existence of asteroidal families and their associated dust bands (also discovered by IRAS) are evidence that the asteroid belt is a significant and maybe the dominant source of dust in the zodiacal cloud. These new observations give quantitative information both on the rate of transport of asteroidal dust to the Earth and on the rate of grinding down of the asteroid belt. Without resonant trapping most dust particles spiral past the Earth without striking the planet. However, most particles trapped in resonances are released from these resonances due to close encounter with the Earth. Thus, the ring may act as a funnel through which asteroidal particles are deposited in the Earth's atmosphere. This could have implications for the efficiency of the transport of carbonaceous material from the asteroid belt to the Earth and for the origin of life on the planet. One important prediction is that the number of IDPs collected in near-Earth orbit from the ring should vary significantly with the time of the year reaching a maximum in September. Further work is needed to determine the directions and velocities of these particles when they impact the Earth. This abstract is an extended and modified version of the abstract of a paper that will be read at the DPS meeting in Boulder (October 1993). A full paper on this discovery is being prepared for

submission to *Science*. Some of our earlier work in the area of particle dynamics is described in the references.

**References:** [1] Dermott S. F. et al. (1984) *Nature*, 312, 505–509. [2] Dermott S. F. et al. (1985) *IAU Colloquium No. 85* (R. H. Giese and P. Lamy, eds.), 395–409, Reidel. [3] Dermott S. F. et al. (1986) in *Asteroids, Comets and Meteors II* (C.-I. Lagerkvist and H. Rickman, eds.), 583–594, Uppsala. [4] Dermott S. F. et al. (1988) in *Comets to Cosmology* (A. Lawrence, ed.), 3–18, Springer Verlag. [5] Dermott S. F. and Nicholson P. (1989) *Highlights of Astronomy*, 8, 259–266. [6] Sykes M. V. et al. (1989) in *Asteroids II* (R. Binzel et al. eds.), 336–367, Univ. of Arizona. [7] Dermott S. F. et al. (1990) *Adv. Space Res.*, 10, 171–180. [8] Dermott S. F. et al. (1992) *Chaos, Resonance, and Collective Dynamical Phenomena in the Solar System* (S. Ferraz-Mello, ed.), 333–347, Kluwer. [9] Dermott S. F. et al. (1992) *Asteroids, Comets and Meteors* (A. W. Harris, and E. Bowell, eds.), 153–156, LPI. [10] Durda D. D. et al. (1992) *Asteroids, Comets, Meteors 1991* (A. W. Harris and E. Bowell, eds.), 161–164, LPI. [11] Gustafson B. Å. S. et al. (1992) *Asteroids, Comets, Meteors 1991* (A. W. Harris and E. Bowell, eds.), 223–226, LPI. [12] Dermott S. F. et al. (1993) *Meteoroids and Their Parent Bodies* (J. Stohl and I. P. Williams, eds.), 357–366, Astronomical Inst., Slovak. Acad. Sci. [13] Xu Y. L. et al. (1994) *Proc. Chinese Acad. Sci.*, in press. [14] Durda D. D. and Dermott S. F. (1993) *Planet. Space Sci.*, submitted. [15] Xu Y. L. et al. (1993) *Planet Space Sci.*, submitted. [16] Dermott S. F. et al. (1993) *Science*. [17] Dermott S. F. et al., *Icarus*. [18] Dermott S. F. et al., *Icarus*. [19] Dermott S. F. et al. (1993) *Asteroids, Comets, Meteors*. [20] Dermott S. F. et al., *Icarus*. [21] Dermott S. F. et al., *Icarus*. [22] Durda D. D. et al., *Icarus*. [23] Liou J. C. and Dermott S. F., *Icarus*.

# COLLECTION REQUIREMENTS FOR TRACE-ELEMENT ANALYSES OF EXTRATERRESTRIAL SAMPLES.

G. J. Flynn<sup>1</sup> and S. R. Sutton<sup>2</sup>, <sup>1</sup>Department of Physics, State University of New York, Plattsburgh NY 12901, USA, <sup>2</sup>Department of Geophysical Sciences, University of Chicago, Chicago IL 60637, USA.

Trace-element abundances and abundance patterns in meteorites have proven to be useful indicators of (1) nebular [1] and parent body [2] fractionations, (2) formation temperatures [3], (3) thermal metamorphism [4], and (4) co-genesis [5]. Trace-element measurements on individual interplanetary dust particles have been useful in separating an "igneous" subgroup from the chondritic particles [6], identifying particles that were severely heated on atmospheric entry [7], and suggesting a possibly volatile enrichment of the interplanetary dust over the most volatile-rich type of meteorite [8].

Synchrotron X-Ray Fluorescence (SXRF) is a nondestructive trace-element analysis technique particularly useful for the analysis for small samples. In the present X-ray microprobe instrument installed on beamline X26 of the National Synchrotron Light Source (NSLS) at Brookhaven National Laboratory samples are excited with filtered, continuum synchrotron radiation from a bending magnet on a 2.5-GeV electron storage ring [9]. Flynn and Sutton [6] have demonstrated that the present SXRF microprobe at the NSLS can detect elements from Cr to Mo in concentrations down to a few parts per million in 10- to 30- $\mu$ m-diameter interplanetary dust particles (see Fig. 1).

A particular advantage of SXRF analysis is its low-energy deposition in the sample, making possible the analysis of volatile elements and even ices. The NSLS X-ray microprobe deposits approximately 10–5 cal/s into a 100- $\mu$ m cube of ice/silicate aggregate [10]. The corresponding power density is 10<sup>-6</sup> times that of a typical electron microprobe [10].

SXRF also has the potential of performing *in situ* analyses of particles imbedded in the collection medium, allowing preliminary characterization of particles prior to extraction.

**Instrument Improvements:** The commissioning of the Advanced Photon Source (APS) at the Argonne National Laboratory in 1995 will significantly improve the element analysis capability by providing a more highly focused X-ray beam of higher X-ray energy [11]. The X-ray microprobe to be installed at the Advanced Photon Source is expected to be capable of analyzing individual micrometer-sized grains with an element sensitivity better than 100 ppb [11].

The element detection limits of the present X-ray microprobe at the NSLS is compared to the expected sensitivities of X-ray microprobes installed on the APS bending magnets and wiggler magnets in Fig. 2.

**Sample Contamination Requirements:** All sample collection techniques require some contact, and possible contamination, between the sample and the collector. Even in the case of the relatively low velocity collection of interplanetary dust from the Earth's stratosphere onto impact collectors coated with silicone oil, traces of residual silicone oil (and any contaminants it contains) remain on the particle surface [12].

High-velocity collection, as proposed for in-orbit capture of interplanetary dust or flyby capture of cometary dust, has the potential for more severe particle contamination and alteration of the collected samples. For example, particles impacting into aerogel have been observed to acquire a "glassy" coating of melted aerogel material [13].

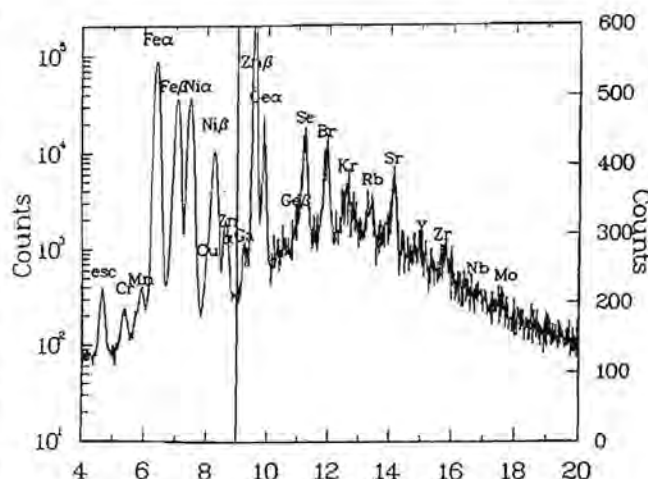


**Fig. 1.** Synchrotron X-ray fluorescence spectrum for a 30- $\mu$ m chondritic interplanetary dust particle (W7027C5) obtained during a 30-minute data acquisition at National Synchrotron Light Source beamline X26A at the Brookhaven National Laboratory. Energies less than 9 keV are plotted logarithmically while those above 9 keV are plotted linearly. The Kr fluorescence results from the air along the path from the sample to the detector. The Fe escape peak is labeled "esc."



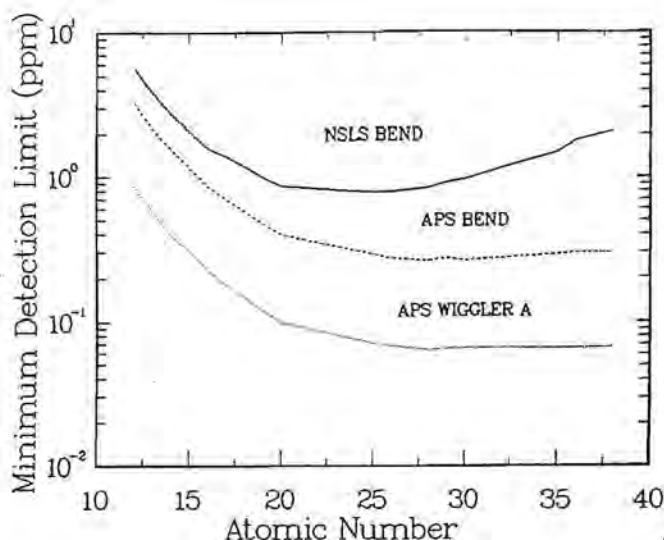


Fig 2. Estimated minimum detection limits for elements from  $Z = 12$  to 38 for a 10-mg/cm<sup>2</sup> thick ice/dust sample analyzed using three different synchrotron radiation sources: the NSLS bending magnet (currently in use), the APS bending magnet, and the APS wiggler A.

We have previously measured the content of trace elements from Cr to Rb in two aerogel samples (provided by M. Zolensky), and found those samples to be sufficiently clean to be suitable for trace-element measurements at the NSLS detection limits of particles collected at high velocities [14]. However, the abundance of Fe was distinctly different in the two samples, indicating that aerogel from different sources is likely to contain different amounts of contamination [14]. Zolensky et al. [13] measured Fe, Sn, Br, Zn, Cr, Sb, Co, and Sc in an aerogel sample produced by Henning AG, while a sample from Lawrence Livermore Laboratories contained detectable Rb, Na, Zn, Br, and Au. The importance of testing proposed flight materials for contamination must, therefore, be emphasized. In addition, the wider range of elements and increased element sensitivity that will become available using the X-ray microprobe at the Advanced Photon Source will necessitate retesting flight materials with the new instrument.

It is essential that sample collection hardware be constructed from high-purity materials, but it is equally important that the selection of these materials be given considerable thought. For example, one class of stratospheric particles has a high Al content. These particles are generally believed to be terrestrial, but Flynn et al. [15] have reported roughly chondritic Fe/Ni and Mg/Si ratios in these particles, possibly suggestive of an extraterrestrial origin. The use of Al collection material would seriously compromise the identification of material of this type.

**In Situ Characterization of Particles Imbedded in Collector Material:** Dust collection in low Earth orbit poses a particular problem of discriminating between orbital debris and interplanetary particles. Although particles of both types are inherently interesting, the experimental protocols for the subsequent study of these different types of particles are likely to differ. The X-ray penetration depths and fluorescence X-ray escape depths indicate that *in situ*

chemical analysis of particles imbedded to a depth of about 100  $\mu\text{m}$  in low-density material such as aerogel is possible. Small fluid inclusions in quartz have been analyzed to a depth of tens of micrometers by SXRF [16]. Thus SXRF should provide a technique for *in situ* classification of collected particles.

**Individual Grain Analyses:** The availability of high X-ray brightness at X-ray energies up to 40 keV using the APS undulator will allow efficient excitation of heavier elements than are accessible with the present NSLS microprobe. It is anticipated that rare earth and platinum group elements will be detectable in microparticles using the APS facility. Trace-element determinations on individual particles as small as 1  $\mu\text{m}$  in size should be possible with a detection limit of about 100 ppb.

**Computed Microtomography:** When intact samples of cometary material (ice and dust mixtures) are recovered, measurement of the spatial relationships between mineral phases, ices, and voids will be important. X-ray-computed microtomography could be used to obtain this information in a nondestructive manner with a spatial resolution better than 5  $\mu\text{m}$  (see discussion in [10]). If samples are to be cored from a cometary or asteroidal parent body, a coring technique that preserves the inherent structure of the parent body is critical.

**Conclusions:** Trace-element abundances have proven important in understanding the evolution of and interrelationships between different meteorites. Preliminary investigations of the trace-element contents of interplanetary dust particles indicate that trace-element abundances will prove equally important in distinguishing between micrometeorites of different types, comparing the interplanetary dust to the meteorites, and assessing the degree of thermal alteration experienced either on the parent body or during the collection process.

Sample collection, delivery, and curation must be accomplished in a manner to avoid contamination with even trace amounts of the elements to be analyzed. The present SXRF sensitivity for micrometeorite analysis is of order 1 femtogram, but anticipated improvements in sensitivity will require sample contamination substantially below this level. Sample collection and handling equipment should be constructed from materials selected for ultrahigh purity, and serious consideration should be given in selecting the particular set of elements from which the collection apparatus is composed so as not to compromise useful information.

**References:** [1] Larimer J. W. and Anders E. (1967) *GCA*, 31, 1239–1270. [2] Schnitzer C. C. and Philpotts J. A. (1969) in *Meteorite Research* (P. Millman, ed.), 206–216, Reidel. [3] Keays R. R. et al. (1971) *GCA*, 35, 337–363. [4] Ikramuddin M. et al. (1977) *GCA*, 42, 1247–1256. [5] Schaudy R. (1972) *Icarus*, 17, 174–192. [6] Flynn G. J. and Sutton S. R. (1990) *Proc. LPSC 20th*, 335–342. [7] Flynn G. J. and Sutton S. R. (1992) *Proc. LPS*, Vol. 22, 171–184. [8] Flynn G. J. and S. R. Sutton (1992) *LPS XXIII*, 373–374. [9] Gordon B. M. (1987) *X-Ray Microscopy II*, 56, 276–279. [10] Flynn G. J. et al. (1993) *Proceedings of Workshop on Returned Comet Nucleus Samples*, in press. [11] Sutton S. R. et al. (1988) in *Synchrotron X-Ray Sources and New Opportunities in the Earth Sciences*, Argonne National Laboratory Technical Report ANL/APS-TM-3, 93–112. [12] Sandford S. A. and Walker R. M. (1985) *Astrophys. J.*, 291, 838. [13] Zolensky M. E. (1990) *LPS XXI*, 1381–1382. [14] Flynn G. J. and Sutton S. R. (1990) *LPS XXI*, 371–372. [15] Flynn G. J. et al. (1982) *LPSC XXII* [16] Vanko D. A. et al. (1993) *Chemical Geology*, in press.

**LABORATORY SIMULATION OF INTACT CAPTURE OF COMETARY AND ASTEROIDAL DUST PARTICLES IN ISAS.** A. Fujiwara, A. Nakamura, and T. Kadono, The Institute of Space and Astronautical Science, 3-1-1 Yoshinodai, Sagami-hara, Kanagawa 229, Japan.

In order to develop a collector for intact capturing of cometary dust particles in the SOCCER mission and regolith dust particles released from asteroid surfaces by the impact of projectiles launched from a flying-by spacecraft (Fig. 1) [1], various kinds of materials as the collector candidates have been exposed to hypervelocity projectiles in our laboratory. Data based on the penetration characteristics of various materials (penetration depth, hole profile, effectiveness for intact capturing) are greatly increased. The materials tested for these simulation experiments include various kinds of low-density media and multisheet stacks; these are foamed plastics (polystyrene 0.01 g/cc), silica aerogels (0.04 g/cc), air (0.001 g/cc), liquid, and multisheet stack consisting of thin Al sheets (thickness 0.002 to 0.1 mm) or polyethylene sheets. Projectiles used are spheres or cylinders of nylon, polycarbonate, basalt, copper, iron, and volatile organics (e.g., paradichlorobenzene) of size ranging from 30  $\mu\text{m}$  to 1 cm launched by a two-stage light gas gun and a rail gun in ISAS at velocity up to about 7 km/s. Some results obtained by using nylon projectiles of velocity less than about 5 km/s have already been published elsewhere by the present authors [2-5], and two figures from these works are reproduced here; the penetration depth vs. bulk density of the collector material for several kinds of materials (Fig. 2) and the velocity at which the projectiles begin to fragment vs. material density for foamed polystyrene (Fig. 3).

Figure 3 shows that if we want to capture particles of velocity 8-10 km/s, the expected relative velocity in the SOCCER mission, the density of the collector media must be as low as 0.001 g/cc, which corresponds to almost the density of air at 1 atm. Hence deceleration and trapping by gas cells followed by low-density soft material like aerogel seems to be a possible way of intact capturing very fragile and volatile dust particles like cometary dusts. At present, efforts are being made to extend the data for wider experimental parameters (e.g., higher projectile velocity, variety of lower-density materials, etc.), and aerogels of lower density are also being developed.

**References:** [1] Fujiwara A. et al. (1990) *Proc. 12th Solar System Sci. ISAS*, 167-172 (in Japanese). [2] Fujiwara A. and T.

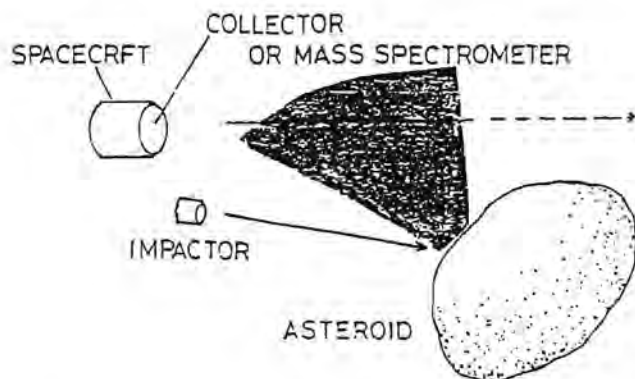


Fig. 1. Regolith dust particles released from asteroid surfaces [1].

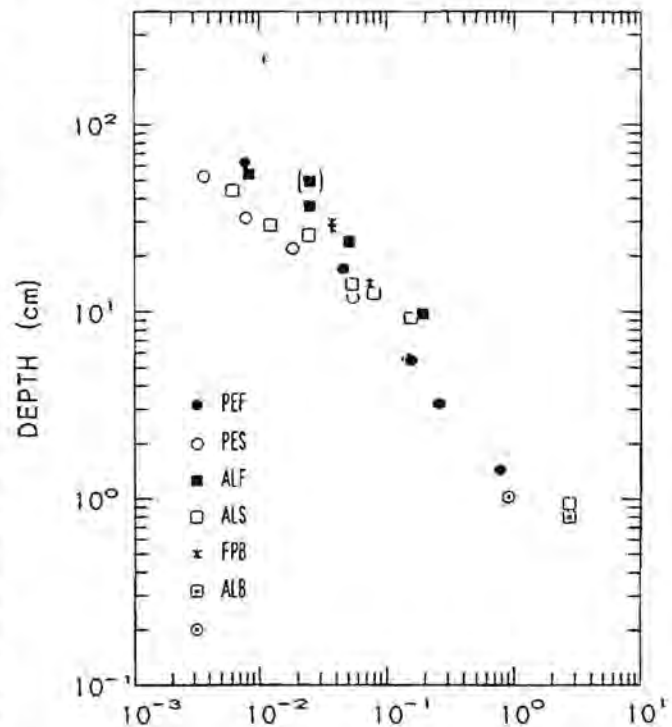


Fig. 2. The hole depth vs. the target bulk density for PEF: polyethylene film (thickness = 50  $\mu\text{m}$ ), PES: polyethylene sheet (thickness = 300  $\mu\text{m}$ ), ALF: aluminum foil (thickness = 15  $\mu\text{m}$ ), ALS: aluminum sheet (thickness = 100  $\mu\text{m}$ ), FPB: foamed polystyrene, ALB: aluminum block, and PEB: polyethylene block.

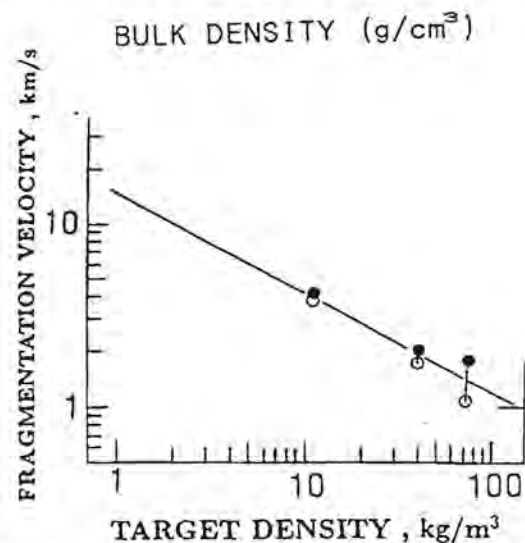


Fig. 3. Fragmentation velocities and depths vs. target densities. Solid line represents the critical fragmentation velocity  $V_c$ , where the fragmentation of projectile occurs between two impact velocities for each target density as shown by open and filled circles. Dashed line represents the fragmentation depth, where the depths corresponding to two impact velocities are indicated by open and filled rectangles respectively.



Kadono (1990) *Jpn. J. Appl. Phys.*, 29, 1620–1624. [3] Ishibashi T. et al. (1990) *Jpn. J. Appl. Phys.*, 29, 2543–2549. [4] Nakamura A. et al. (1991) *Jpn. J. Appl. Phys.*, 30, 2129–2133.

**TECHNIQUES FOR *IN SITU* COLLECTION AND MEASUREMENT OF VOLATILES RELEASED DURING HYPERVELOCITY IMPACT.** R. A. Heppner<sup>1</sup>, W. Niu<sup>1</sup>, and C. R. Maag<sup>2</sup>, <sup>1</sup>Perkin-Elmer, Applied Science Operation, Pomona CA 91767, USA, <sup>2</sup>Science Applications International Corporation, Glendora CA 91764, USA.

**Introduction:** The proposed Comet Coma Sample Return (CCSR) payload contains a variety of instrumentation for characterizing and collecting cometary dust [1]. In this suite of instruments the Gas Capture Cell (GCC) is unique in that it not only collects the vaporization products resulting from the dust particle impacts, but also provides chemical characterization information prior to return of the dust particles for analysis on Earth. The GCC provides near real-time characterization of the volatile species, such as low- and medium-molecular-weight organic compounds that evolve from dust particles on impact with metal targets. Instrument sensitivity is sufficient for analyzing the volatile impact products resulting from single, individual dust particles. This capability will enable characterization of near-pristine dust particles, including the CHON particles, to be performed at a level not previously possible.

Collection of interplanetary dust particles has been performed since the mid 1970s when U2 and ER2 flights at high altitudes were utilized for this purpose. Numerous particles were collected; however, the degree to which particle nature was changed by the relatively long residence time in the Earth's reactive upper atmosphere was unknown. Recent shuttle experiments have collected particles in space, enabling gross particle composition to be determined. However, the capability to detect the potential presence of more volatile, organic species was lost because of the nature of the hypervelocity impact. The question as to whether primordial seed material was contained on interplanetary and/or cometary dust grains could not be answered.

In the GCC experiment dust particles impact on metal targets causing all organic and significant amounts of the inorganic material to vaporize. Low-volatility inorganic elements/compounds will immediately condense on the walls of the gas collection chamber. Less volatile organic/inorganic species will condense more slowly while undergoing multiple collisions with gas collection chamber walls until finally collecting on the actively cooled surfaces within the GCC. Volatile organic/inorganic molecules resulting from the impact will not condense and are difficult, if not impossible, to transport back to Earth for study. Both the volatiles and the semivolatile species will be characterized according to their *m/z* ratios with a small mass spectrometer.

The combination of the actively cooled surfaces, the cell walls, and the targets themselves serve as carriers to return dust particle components for Earth study. These components are integrating-type collectors because material is collected over the full duration of the experiment, whereas the mass spectrometer performs near real-time analysis. The two coldplates are continuously maintained at an operating temperature of nominally 150 K by small Peltier coolers. One of the plates has Ge Internal Reflection Spectroscopy (IRS) crystals attached to its surface enabling IR analysis of the surface film of accumulated semivolatiles once the payload returns to Earth.

Both coldplates maintain sample material in the condensed phase until the examination phase under curation laboratory conditions.

**Scientific Objective:** The GCC supports the (CCSR) objective of characterizing the distribution and composition of both interplanetary and cometary dust particles. Mass spectrometer (MS) analysis of volatile material and cryoplate collection of semivolatiles will complement analytical information from other CCSR experiments that collect intact particles after hypervelocity impact. By comparing QCM profiles with mass spectral data not only can the amount of material being deposited be determined, but the chemical composition can be determined as well. Observation of vaporization products *in situ* will aid in determining the degree to which hypervelocity impact has altered amounts of volatile and semivolatile material on the dust particles that are collected by other CCSR experiments and returned to Earth for analysis. These analyses and comparisons will provide new insights into the detailed composition of gases and dust within the coma of a comet and on the makeup of interplanetary dust particles.

**Gas Collection Cell Concept: GCC configuration.** Figure 1 shows the proposed gas collection cell concept. The cell has nominal dimensions of  $10 \times 10 \times 10$  cm<sup>3</sup> to provide an expansion volume of approximately 1 liter for the vaporization products. Dust particles enter the cell by penetrating a thin (500–1000 Å) vapor-deposited Al film. The film is thin compared to particle diameter, and previous work [2] has shown that the brief particle/film encounter has very little effect on particle composition or integrity. A 90% transmission screen backs the film to provide structural support during launch and return phases of the mission. Once inside the cell, particles travel unimpeded to the target plate on the floor of the cell. The target is a polished Ni plate with a vapor-deposited Au coating to provide a clean, specular, well-characterized surface. Upon impact with the plate, volatile and semivolatile dust components are released into the cell where they are sampled by the MS and are collected on the coldplates and the temperature-controlled quartz crystal microbalance (TQCM). Two coldplates are used in order to provide redundancy and prevent loss of organic semivolatiles collected on the surfaces should one cooler fail.

The cell is protected by a door that is closed during ground, launch, and retrieval operations through a double-seal arrangement that prevents air leakage when the cell door is closed. The volume between the door and the thin film and the internal cell volume both connect to a common solenoid vent valve that opens to space. Connecting both volumes to a common vent valve prevents pressure differentials from developing that could potentially damage the thin film.

**GCC block diagram.** The block diagram for the GCC is illustrated in Fig. 2. The GCC interfaces with the spacecraft computer for instrument control and data storage. A limited set of discrete digital commands control basic system functions, such as system power, MS power, Peltier cooler/TQCM power, and door actuation.

Data acquisition and associated instrument control functions, such as scanning the MS and measurement of mass spectral peak intensities and TQCM frequency shifts, are performed through the serial bus communication interface. Monitoring of various house-keeping parameters, such as internal temperatures and power supply voltages, is also performed through this interface.

Various analog electronic modules support operation of the TQCM, the Peltier-cooled coldplates, and the MS. These modules are either controlled directly by the discrete digital lines or commu-

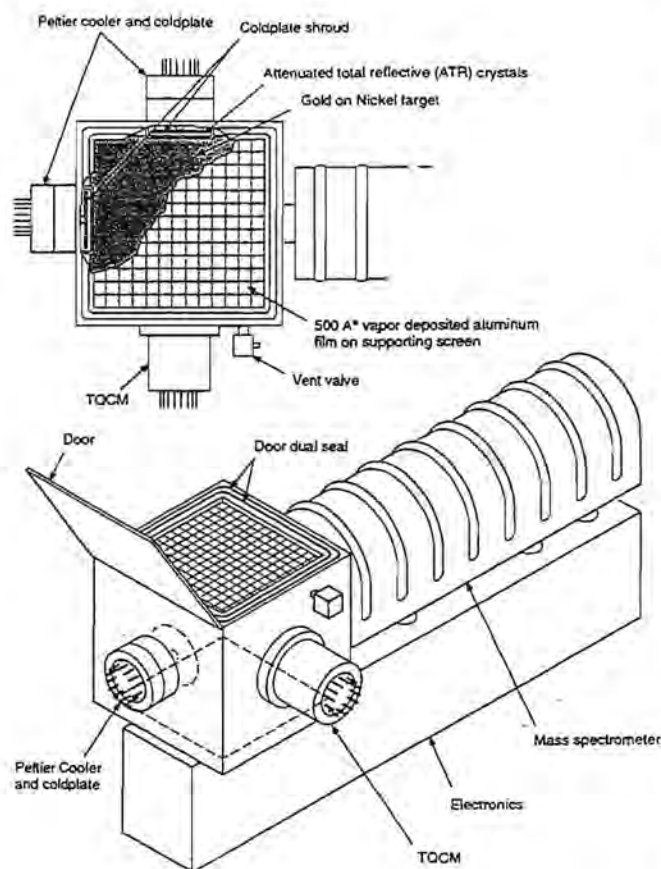


Fig. 1. Gas collection cell (GCC) concept showing the cell with the mass spectrometer for analyzing volatile impact products and the Peltier-cooled coldplates and TQCM for collection of less volatile products. All GCC components have proven flight heritage.

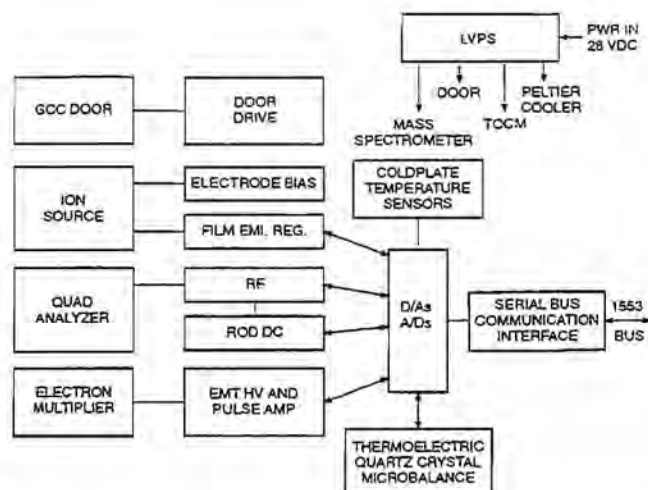


Fig. 2. Block diagram of the GCC electronic system. The spacecraft microprocessor is used for instrument control and data acquisition.

nicate with the data bus through an analog to digital converter and/or a digital to analog converter.

**GCC operational scenario.** During ground testing and prior to launch the cell door will be closed and both the internal cell volume and the space between the door and the vapor-deposited film will be evacuated and baked out through the solenoid vent valve. Once evacuated, the Peltier coolers, the TQCM, and the MS can all be exercised and their performance verified. After launch and orbital injection are complete, the vent valve and cover can be opened to enable the GCC to acquire dust samples.

The GCC can be activated at any point in the mission cycle. Although its principal purpose is the acquisition of dust samples while in the comet coma, operation at larger distances could help determine whether the features observed in the Halley Giotto dust flux data [3] have corresponding compositional variations. If necessary, power can be conserved by operating the MS intermittently, otherwise keeping it in a standby configuration. A few seconds will be required to scan the mass spectrum, depending upon the desired sensitivity. Thus scans may require a longer time period when particle fluxes and evolved gas levels are correspondingly low. At peak particle flux levels (estimated at approximately 50/s and perhaps higher), the scan time will be reduced. At mission completion and prior to CCSR retrieval, the door and vent valve will be closed to prevent accumulation of shuttle-associated contaminants. The GCC will then remain sealed, with Peltier coolers operating, until opening occurs in the controlled environment of the curation facilities. Here the semivolatile organic material trapped on the coldplates will be analyzed using a variety of spectroscopic and chromatographic techniques. Material absorbed on the IRS crystals can be directly analyzed using FT-IR spectroscopy without extensive sample preparation. Some of the dust particles trapped in the metal target plate will be extracted and examined for compositional comparison with those particles trapped in foam- and aerogel-based collection devices.

**Analysis of GCC performance.** A number of factors will affect GCC performance, such as particle size and flux, GCC cell volume, and impact magnitude. These factors will be fully considered during the conceptual design phase; however, preliminary performance estimates can be made.

A 1- $\mu\text{m}$ -diameter particle having density of 1 g/cm<sup>3</sup> has a mass of approximately 0.5 pg. This particle impacting within the GCC will cause vaporization of a number of molecules given by

$$m \times v_f \times (1/M) \times (6 \times 10^{23} \text{ molecules/mole})$$

where  $m$  = the particle mass,  $v_f$  = the vaporization factor, and  $M$  = the molar mass.

For a 0.5-pg particle with molar mass of 30, and 0.1 vaporization factor, approximately  $1 \times 10^9$  atoms/molecules are vaporized. Assuming the cell temperature is nominally 300 K, and scaling from the molar volume relation (22.4 liter at STP), the  $1 \times 10^9$  molecules will produce a pressure rise of

$$\frac{(1 \times 10^9 \text{ mol}) \times 22,400 \text{ cm}^3 \times 760 \text{ torr}}{(1000 \text{ cm}^3) \times (6 \times 10^{23} \text{ mol})} = 2.8 \times 10^{-11} \text{ torr}$$

A portion of the material contributing to this pressure rise will be nonvolatile and will immediately deposit on chamber walls; also semivolatile material will slowly be removed by the coldplates. If

10% of the material remains as volatile species, then the resultant pressure rise from a single 1- $\mu$ m particle will be  $2.8 \times 10^{-12}$  torr.

The MS sensitivity under normal operating conditions is  $5 \times 10^{-6}$  amp/torr, so the above pressure rise produces a current of  $1.4 \times 10^{-17}$  amp, which, with ion counting, corresponds to approximately 100 ions/s at the detector. The MS background count rate is typically 1 or 2 cts/s and thus 100 ions/s is detectable. If this count rate is spread over several ion masses it may be necessary to increase the sensitivity to provide sufficient signal when the mass range is scanned. Increasing the MS filament emission level by a factor of 10 provides a simple means to increase sensitivity by an order of magnitude. Since the MS only has to operate over a total time period of a month or so, high emission (which reduces filament life) could be employed, if required.

The primary conductance out of the gas cell will be the  $40 \text{ cm}^3/\text{s}$  through the MS system. This conductance provides a time response of approximately 25 s for the GCC and provides sufficient time for evolved gas to condense on cryoplate surfaces and be sampled by the MS. At high particle impact rates, near coma center, impact rates may be as high as 60/s of particles with mass of  $4 \times 10^{-10}$  g or greater. Using the assumptions made above for particle vaporization, this corresponds to a gas load into the cell of approximately  $1.3 \times 10^{-6}$  torr-liter/s. The MS pumping speed will limit the pressure rise in the cell to approximately  $3 \times 10^{-5}$  torr. In the event extremely high gas evolution rates are encountered, then the vent valve can be opened to limit the internal cell pressure rise.

The coldplates and the TQCM will remove semivolatiles from the cell by cryogenic pumping. For each 0.5-pg particle, we calculated earlier that approximately 0.045 pg would be semivolatile. If the TQCM sensor area of  $1 \text{ cm}^2$  is approximately 10% of the total cryoplate area, then it will receive approximately 4.5 fg per 0.5-pg particle. A 1-Hz frequency change from the TQCM corresponds to approximately  $1 \times 10^{-10}$  g/cm<sup>2</sup> mass change. Thus the TQCM will be capable of sensing events resulting from individual large particles ( $10^{-9}$  g). At the high particle flux rates near coma center the mass increase rate of the TQCM will be

$$60 \text{ part/s} \times (4 \times 10^{-10} \text{ g/part}) \times 0.1 (\text{vap frac}) \times 0.1 (\text{area frac}) = 2.4 \times 10^{-10} \text{ g/s}$$

Using the sensitivity factor given above, this mass deposition rate will result in a several-hertz change every second.

**Instrument Description:** The GCC system contains a number of important elements. These are described in some detail below.

**Cell and targets.** High-purity metallic surfaces will be used for collecting gaseous species and dust particles/grains on the cryoplates and targets. During impact of a high-density particle, a characteristic crater is formed with rounded edges and a depth-to-diameter ratio determined by the encountered metal and the velocity and size of the impacting particle. Typically the particle is destroyed and the remnants are mixed with target material, concentrating in the bottom of the crater or on the surrounding rim. Gold and Ni are metals suitable for such targets. A top layer composed of 50 nm of evaporated Au facilitates identification of the impacting position, as the torn film indicates impact position.

The chemical and isotopic properties of the impacting particle can be identified by analyzing the rim material. The major strength of the metallic collectors lies in the fact that analytical techniques

can be applied without modification to craters ranging from tens of nanometers up to millimeters in size, limited only by the thickness of the plate. Also, identification of C and organic material is made possible, which is essential for the study of extraterrestrial material.

A low-weight latching solenoid valve will be used for the cell vent. A stepping motor will drive the cell cover between open and closed positions.

**Vapor deposited thin film.** The basic approach to implementing an ultrathin film is shown in Fig. 3. The thin Al film of 500 Å or so is initially deposited onto a C foil over a Buckbee Mears 30-line-per-inch 90% transmissive grid [4]. After deposition, the C is removed, leaving a free-standing 500-Å Al film for particles to transit. This approach to film fabrication has already been expanded to the required  $10 \times 10 \text{ cm}^2$  entrance area of the GCC. A film of the required size was recently returned from the European Retrievable Carrier/Timeband Capture Cell Experiment, EURECA/TICCE.

**Mass spectrometer (MS).** The MS will be adapted from the Induced Environmental Contaminant Monitor (IECM) instrument design, which has flown on numerous shuttle and satellite payloads. On several of these missions it monitored ram and wake gas fluxes with equivalent pressures in the  $10^{-11}$  to  $10^{-13}$  torr range [5]. Most recently one of these instruments was refurbished and upgraded for use on the MSX Contamination Monitoring Experiment. The MS analyzer and electronics packaging is illustrated in Fig. 4. For the GCC application we will investigate the potential for reducing the rod length consistent with the resolution and mass range requirements of the GCC. The IECM electronics were also upgraded for the MSX mission and these designs will serve as the basis for the GCC MS. This upgrade replaced analog current measurement with pulse counting, which will provide high sensitivity by detecting single ion events.

**Temperature-controlled quartz crystal microbalance (TQCM).** The TQCM measures material deposited on the sensing head by detecting the frequency shift of a quartz crystal oscillator. A cross-



Fig. 3. An exploded view of the thin-film assembly. The Baylor University Space Science Laboratory has flown this assembly on three shuttle missions. Recently this approach has been used for a  $10 \times 10 \text{ cm}^2$  foil on EURECA/TICCE.



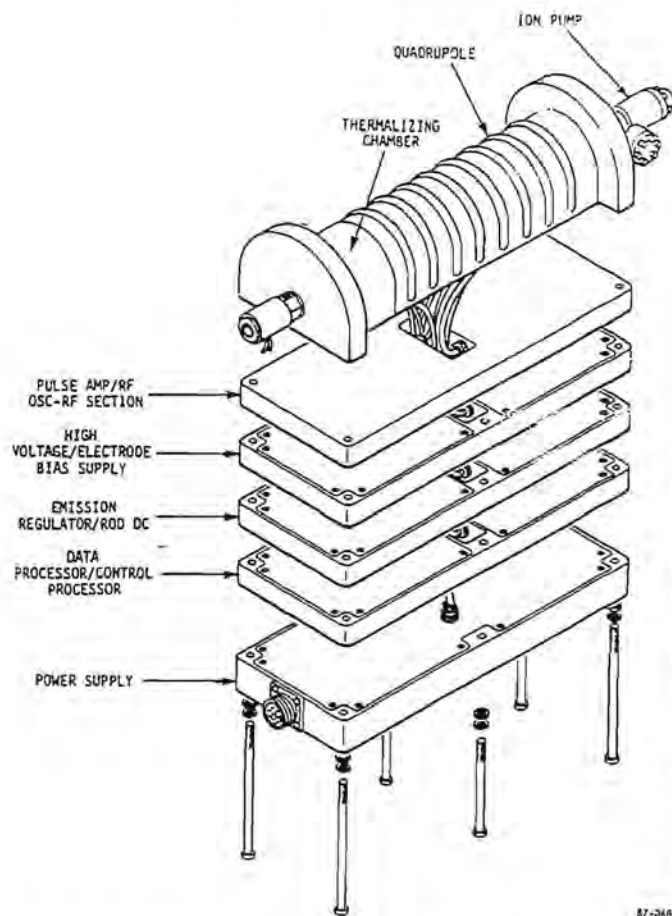


Fig. 4. Exploded view of the mass spectrometer (MS) used on the GCC experiment to monitor in real time volatile and semivolatile species resulting from dust particle collisions with the GCC target. This instrument is derived from the Induced Environmental Contaminant Monitor (IECM).

sectional view of the TQCM is shown in Fig. 5. Two matched quartz crystals, one for sensing contamination and the other operated as a reference crystal, provide a beat signal that is totally independent of temperature and power supply fluctuations, but shifts by 1 Hz for  $1 \times 10^{-10}$  g/cm<sup>2</sup> accretion of mass on the sensing crystal. A two-stage thermoelectric cooler cools the crystals to the 150 K operating temperature. A Pt temperature probe senses operating temperature.

**Cryoplate/IRS.** Witness samples will be attached to at least one of the cryoplates to facilitate identification and quantification of species that condense on the cryoplates. One potential witness sample uses a dielectric mirror consisting of a highly polished substrate (such as Ni) with an evaporated Al coating and overcoat of aluminum oxide with  $8\lambda/4$  thickness. With this plate conventional reflectance spectroscopy could be used to observe any changes in spectral or total reflectance by observing shifts and amplitude changes in reflectance maxima or minima due to the accumulation of vaporized material from particle impact. If a change occurs, it indicates an absorbing layer of another substance has been deposited on the surface.

A second witness material uses a Ge prism to aid in analysis by internal reflection spectroscopy (IRS). With IRS the optical spec-

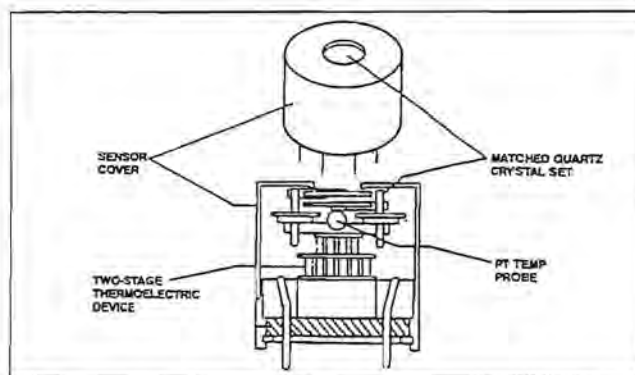


Fig. 5. Cross section of the temperature-controlled quartz crystal micro-balance (TQCM) used to monitor deposition rate of impact products from dust particle and GCC target collisions.

trum of a deposited film in contact with an optically dense but transparent medium (the Ge prism) can be obtained by launching light into the denser medium. The measured reflectivity depends upon the interaction of the evanescent wave with the sample material. One application of IRS is the measurement of material optical constants by measuring perpendicular and parallel polarization at a properly selected angle of incidence or, alternatively, using incident-polarized light and measuring reflected intensity at two angles of incidence. Once material optical constants are known, the thickness of a contaminant film can be determined from the first term of the series expansion of Fresnel's equation.

**Conclusion:** The GCC experiment has the capability to both collect particles and semivolatile species released as a result of particle impacts, and, in addition, characterize the noncollectable volatile species produced during impact. Every element of the proposed GCC experiment has gone through proof-of-concept and flight testing. Most of the equipment has considerable flight experience and provides mature, proven hardware. The GCC experiment and the other instruments in the CCSR package will permit better understanding of comet composition and dynamics, as well as help in resolving whether comets contain and distribute the primordial organic compounds necessary for life.

**References:** [1] Alexander W. M. et al., this volume. [2] Tanner W. G. et al. (1993) *Int. J. Impact Eng.*, in press. [3] Alexander W. M. et al. (1988) *Proc. LPSC 19th*. [4] Tanner W. G. et al. (1991) *Proc. Workshop on Hypervelocity Impacts in Space* (J. A. M. McDonnell, ed.), Univ. of Kent. [5] Naumann R. J. et al. (1985) *NASA TM-86509*.

## PENETRATION EXPERIMENTS IN ALUMINUM AND TEFLON TARGETS OF WIDELY VARIABLE THICKNESS.

F. Hörz<sup>1</sup>, M. Cintala<sup>1</sup>, R. P. Bernhardt<sup>2</sup>, and T. H. See<sup>2</sup>, <sup>1</sup>Solar System Exploration Division, Mail Code SN4, NASA Johnson Space Center, Houston TX 77058, USA, <sup>2</sup>Lockheed Engineering and Sciences Company, Mail Code C23, 2400 NASA Road 1, Houston TX 77058, USA.

A 5-mm light gas gun was used to fire spherical soda-lime glass projectiles from 50 to 3175  $\mu$ m in diameter ( $D_p$ ), at a nominal 6 km/s, into Al (1100 series; annealed) and Teflon (Teflon<sup>TFE</sup>) targets.



Targets ranged in thickness ( $T$ ) from infinite halfspace targets ( $T \equiv \infty$ ) to ultrathin foils ( $T \equiv \mu\text{m}$ ), yielding up to 3 orders of magnitude variation in absolute and relative ( $D_p/T$ ) target thickness. This experimental matrix simulates the wide range in  $D_p/T$  experienced by a space-exposed membrane of constant  $T$  that is being impacted by projectiles of widely varying sizes.

Penetration hole size ( $D_h$ ) decreases systematically with decreasing target thickness. Relative hole size ( $D_h/T$ ) may be used to extract projectile diameter  $D_p$  from individual penetration holes in space-exposed surfaces, provided one assumes a constant impact velocity. The condition of  $D_h = D_p$  mandates  $D_p/T > 50$  in both targets. The ballistic-limit thickness ( $T_{BL}$ ), at 6 km/s, occurs at  $D_p/T = 0.29$  for our Al, and at  $D_p/T = 0.16$  for the Teflon. While these thicknesses define the onset of physical perforation, they are not synonymous with the transition from cratering to penetration processes; this transition is gradual and occurs over a wide range of  $T$ . Consideration of the shock-pulse duration ( $t$ ) in both the projectile ( $t_p$ ) and target ( $t_t$ ) identifies the condition of  $t_p/t_t = 1$  as the real transition between cratering and penetration processes. This transition, at 6 km/s, takes place in our Al and Teflon targets at a  $D_p/T = 0.83$  and  $0.62$  respectively (i.e., at target thicknesses some factor of 2–3 thinner than the ballistic limit). Consideration of pulse duration is readily extended to impact velocities beyond those simulated in the laboratory; it may assist in understanding the velocity scaling of penetrative impact events.

**Introduction:** The morphologies and detailed dimensions of hypervelocity craters and penetration holes on space-exposed surfaces faithfully reflect the initial impact conditions. However, current understanding of this postmortem evidence and its relation to such first-order parameters as impact velocity or projectile size and mass is incomplete. While considerable progress is being made in the numerical simulation of impact events, continued impact simulations in the laboratory are needed to obtain empirical constraints and insights [e.g., 1–3]. This contribution summarizes such experiments with Al [4] and Teflon [5] targets that were carried out in order to provide a better understanding of the crater and penetration holes reported from the Solar Maximum Mission (SMM [6]) and the Long Duration Exposure Facility (LDEF [7–9]) satellites. The ultimate objective of both the impact experiments and the dimensional analysis of the space-produced impact features is to obtain reliable mass-frequencies, fluxes, and other dynamic properties of natural and man-made particles in low Earth orbit (LEO). These parameters are of significance in their own right, yet they can also relate diagnostically to properties and processes of their parent objects, such as comets or asteroids.

Figure 1 illustrates the size distribution of penetration holes in the double-walled thermal louvers of SMM, which consisted of 125- $\mu\text{m}$ -thick sheets of Al (>99% Al; 1100 series) and similar data from penetrations of thermal-control blankets exposed on LDEF, which were composed largely of Teflon ~125  $\mu\text{m}$  thick, and some additional 50–60  $\mu\text{m}$  of organic binder and thermal protective paint [7]. These surfaces rank among the most significant opportunities for detailed investigations of particle populations in LEO, with the largest holes (and projectiles?) approaching millimeter dimensions. Clearly, these SMM and LDEF opportunities motivated selection of our target materials.

It should also be obvious that Fig. 1 represents only the most energetic impacts on these surfaces (i.e., only those that were capable of perforating a target of thickness  $T$  to form a penetration

hole of diameter  $D_h$ ). Both surfaces sustained innumerable, small-scale impacts that resulted in full-grown hypervelocity craters of relatively small size, the majority of  $D_c \ll T$  [e.g., 6, 10]. As a consequence, interpretation of the complete bombardment record on most space-exposed surfaces requires a detailed understanding of both their cratering and penetration behavior [see also 11]. Therefore, we devised an experimental matrix that systematically varied target thickness from targets thick enough to sustain full-fledged cratering events, to foils so thin that the size of the penetration hole approaches typical projectile dimensions.

The above transition from cratering to penetration is traditionally characterized as the "ballistic limit" ( $T_{BL}$ ) of the target. Given specific initial impact conditions, the latter specifies a minimum particle mass that is capable of physically perforating the target. By definition, targets of thickness  $T_{BL}$  will simultaneously sustain a full fledged cratering event of some characteristic, maximum depth  $P$  ( $P < T$ ; e.g., [11,12–14]), as well as incipient penetration holes of dimensions  $D_h = 0$  ([4]). Applicable cratering and penetration formulas must yield identical particle mass for such threshold craters and penetration holes, yet analysis of the Solar Max [6] and LDEF impact features in Al targets [14, 15] revealed that current cratering [e.g., 16 and others] and penetration formulas [e.g., 17 and others] do not yield congruent results for the ballistic-limit case (see also [13] or [11]). Typically, the penetration formulas yield smaller particle masses than the cratering formulas for penetration holes at or close to the ballistic limit. Therefore, special emphasis was placed on the transition from cratering to penetration processes in this work.

**Experimental Results: Procedures and definitions.** Detailed procedures of the impact experiments employing a 5-mm light gas gun may be found in Hörz et al. [4]. All experiments were performed with spherical soda-lime-glass projectiles at normal incidence. Particles >0.5 mm were launched individually in serrated sabots; smaller projectiles were shotgunned. Velocities were measured by arrays of photodiodes that either sense the occultation of an IR-LED laser beam in the free-flight chamber (four stations), or of an impact flash at the sabot separator and the target. All experiments were equipped with massive witness plates of Al (1100 series, 3.2 or 6.4 mm thick, and 25 cm square) that were located ~10 cm to the rear of the penetrated target. We measured, using optical and scanning

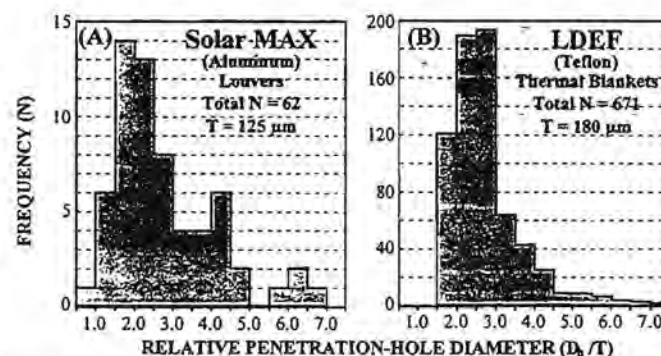


Fig. 1. The frequency distribution of penetration holes normalized to target thickness ( $D_h/T$ ) in the (a) Solar Maximum louvers [6] and (b) all penetration holes >300  $\mu\text{m}$  in diameter that were documented in the thermal-control blankets of LDEF [7].

electron microscope methods, the diameters of the crater ( $D_c$ ; intercept of cavity walls with initial target surface); of the rim ( $D_r$ ; rimcrest to rimcrest), the crater lip ( $D_l$ ; average diameter of lip periphery), the spall-zone ( $D_s$ ; average extent of the lobate area of displaced mass), hole diameters ( $D_h$ ; minimum diameter of physical opening), and spall diameter of the back surfaces ( $D_b$ ) [see 4].

**Crater Morphology:** Typical craters and penetration holes produced in Al (1100 series) and Teflon<sup>TFE</sup> targets are illustrated in Fig. 2. Target thickness varies by essentially 3 orders of magnitude, from infinite halfspace (at top of each column) to foils as thin as 0.8  $\mu\text{m}$  thick. Target thickness is given in normalized form ( $D_p/T$ ) to facilitate convenient comparison with craters and penetration holes at different dimensional scales. The Al experiments employing projectiles of various sizes demonstrate that grossly similar morphologies are obtained at equivalent experimental conditions, no matter what absolute scale. All experiments show a strong and systematic relationship between hole size and target thickness. Note that the penetration holes in massive targets have dimensions typical for actual cratering events, yet hole size diminishes with decreasing foil thickness and approaches projectile dimensions at very thin foils, typically of  $D_p/T > 50$ .

Figure 3 illustrates representative cross sections through relatively massive Al and Teflon targets, using the 3.2-mm projectiles, to specifically document the transition from pure craters to penetrative events. Although already visible in Fig. 2, these cross sections best illuminate the substantially ductile deformation behavior of Al as opposed to the brittle response of Teflon. Nevertheless, many morphologic features, not just hole size, are part of a continuum that strongly depends on target thickness, such as the substantial, yet gradual increase in the depth of Al craters as the ballistic limit (at  $D_p/T \approx 0.3$ ) is approached (Fig. 3a), or the development of connective fractures leading to spallation at the rear surface of Teflon targets (Fig. 3b), or the relative width of the crater lip or of the spall zones (Figs. 2, 3).

The dependence of most morphologic features in Figs. 2 and 3 is so systematically related to target thickness that their detailed characterization and dimensional measurement should lead to diagnostic relationships between the parameters  $D_p$ ,  $D_h$ , and  $T$ . As  $T$  is known for any space-retrieved surface, substantial information about projectile size may be extracted from the characterization of such quantities as hole diameter, relative rim width, distribution of fractures, spall zones at the target's front and rear surfaces, etc. Note, however, that the current observations apply to some limited laboratory conditions, most notably a constant impact velocity of 6 km/s. Interpretation of space-exposed surfaces requires, as a minimum, the additional understanding of the velocity dependence of these relationships, and possibly other factors, such as projectile density and/or shape.

Returning to Fig. 3, the physical perforation of both target materials is preceded by massive internal deformation and fractures close to the target's rear where reflection of the initial shock front results in a rarefaction wave and associated tensile forces [e.g., 18]. This deformation proceeds to a stage where physical removal and spallation of substantial mass takes place at the target's rear, yet still without resulting in complete perforation (e.g., at  $D_p/T = 0.29$  in Al or at 0.149 in Teflon). Physical perforation is accomplished in Al (1100 series) at  $D_p/T \approx 0.3$ , whereas equivalent Teflon targets may be almost twice as thick ( $D_p/T \approx 0.16$ ). Throughout these developments, the diameter of the crater and its rim or the extent of spall

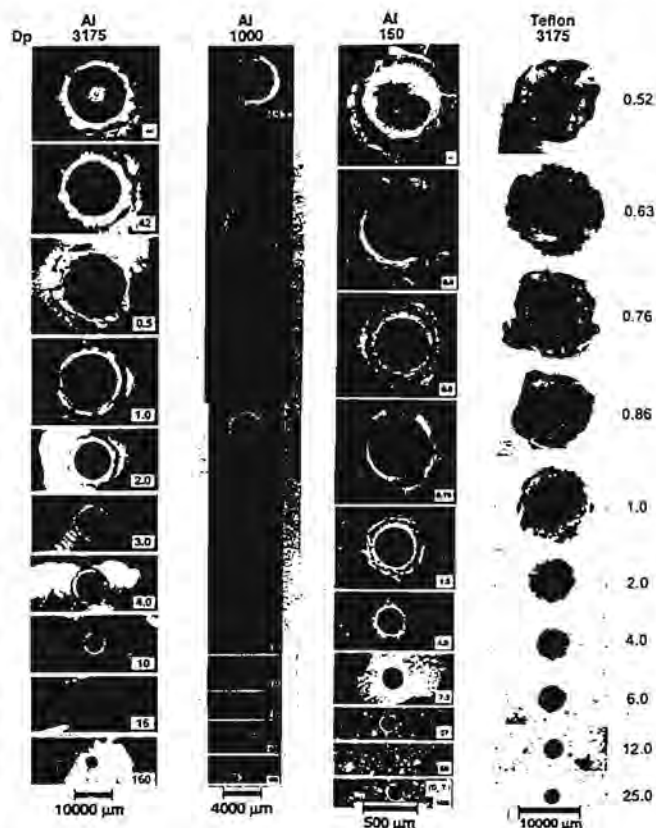


Fig. 2. Craters and penetration holes resulting from soda-lime-glass projectiles in Al and Teflon<sup>TFE</sup> targets of highly variable thickness, identified by specific  $D_p/T$ . Each column illustrates a specific series of experiments at constant projectile diameter ( $D_p$ ). Note that most holes in the thinnest foils approach the condition of  $D_h = D_p$ .

zones at the target's front side remain essentially that of the standard crater into infinite halfspace targets.

All experiments employed witness plates that monitored the evolving debris cloud towards the target's rear [see 4]. From the cross sections it seems self-evident that most debris in massive targets is dislodged from the target itself, and that the mass ratio of target and projectile residue must vary considerably as a function of  $T$  [e.g., 19, 20]. Detailed witness-plate analysis of Al experiments [4] reveals the first traces of projectile material at  $D_p/T \approx 0.6$  (at 6 km/s). This seems surprising in view of the gaping holes produced at all conditions of  $D_p/T < 0.6$ , including the most substantial penetrations of the entire Al series, none of which revealed projectile traces on their witness plates. Not coincidentally, our observations reveal that projectile residue may exit a penetrated target only if the target thickness is smaller than the depth ( $P$ ) of the associated standard crater (i.e., if the condition of  $T < P$  applies; see Fig. 3a). These observations imply that at all conditions of  $T > P$ , the projectile is totally entrained in cratering-related material flows to eventually emanate from the evolving crater cavity as uprange ejecta. It is only at conditions of  $T < P$  that the cratering-related flows [e.g., 21] are sufficiently disturbed to have parts of the crater bottoms and projectile melts exit through the target's rear. This suggests that

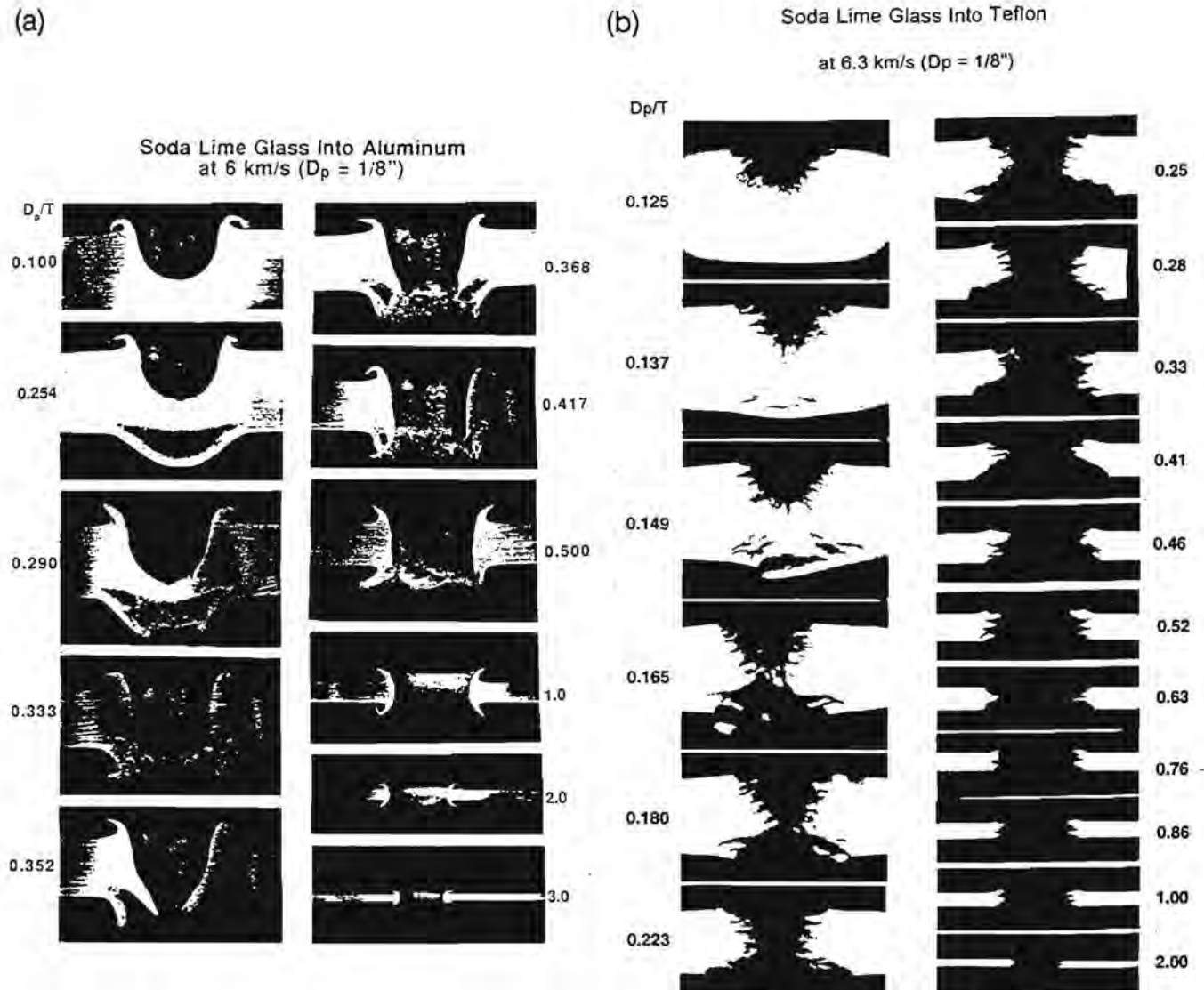


Fig. 3. (a) Cross sections of a "standard" crater in an infinite-halfspace Al target (upper left) and the transition to genuine penetrations at  $D_p/T > 2$  ( $V = 6$  km/s;  $D_p = 3175 \mu\text{m}$ ). For scale note that  $T = 3.2$  mm at  $D_p/T = 1.0$  (see text for discussion). (b) Cross sections of Teflon targets ( $V = 6.3$  km/s;  $D_p = 3175 \mu\text{m}$ ).

bona fide rim or spall phenomena at the target's front side should still resemble those of standard craters at these conditions, possibly at targets still thinner than  $P$ . Indeed, one may observe in Figs. 2 and 3 that the cavity diameter at the initial target surface ( $D_c$ ) is approximately that of the crater until  $D_p/T \approx 1$  is reached. Rim details and spallation phenomena remain grossly similar to standard craters as well. Diameters  $D_c$  and  $D_h$  start to decrease measurably and significantly only in targets thinner than  $T \approx D_p$ .

**Dimensional Measurements:** Figure 4 illustrates measurements of  $D_c$  and  $D_h$ , which are the primary diameters and features to address projectile size. Figure 4 is purposely arranged such that it may function as a "calibration" curve to solve for the unknown projectile diameter  $D_p$  on space-exposed surfaces from the readily measured parameters  $D_h$  and  $T$ . Note, however, that these curves only apply to  $\sim 6$  km/s cases, and that corresponding penetration

experiments at different velocities are needed to understand the effects of velocity.

Returning to Fig. 1 we see that most penetrations documented on the Solar Max and LDEF surface occurred at  $D_h/T < 5$ . This clustering around relatively low  $D_h/T$  values will be typical for all penetrated membranes retrieved from space, including those that are substantially thinner or thicker than a few hundred micrometers. The mass frequency of natural and man-made impactors is simply so dominated by "small" particles that all penetrated membranes will have a large population of genuine hypervelocity craters; penetrations of "massive" targets barely above the ballistic limit are the next most populous group of impact features, and the relative frequency of still larger events will rapidly decline with increasing  $D_h/T$ . The majority of penetration events will have dimensions that are truly intermediate between the genuine crater ( $D_c = nD_p$ ) and the



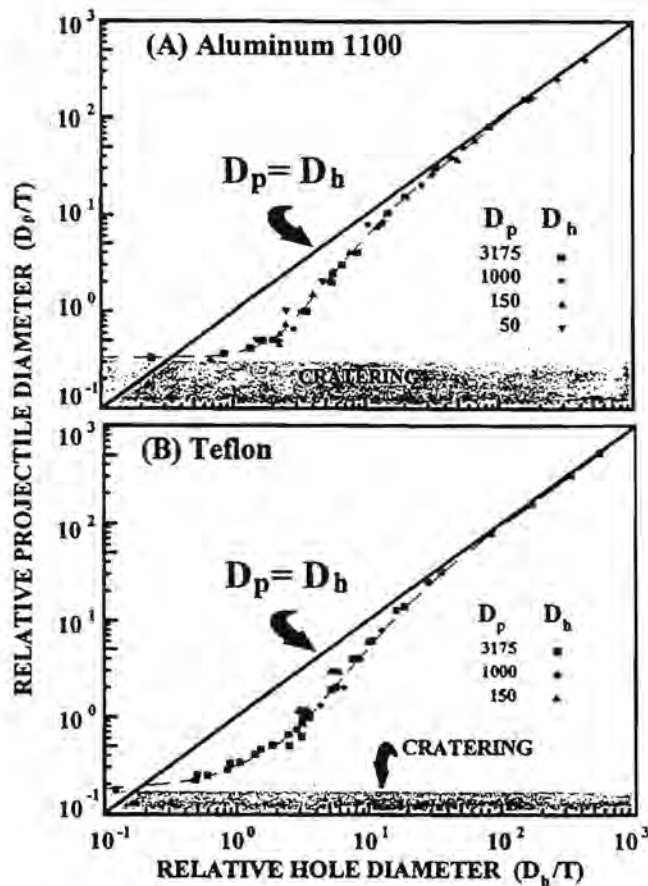


Fig. 4. Dimensional measurements of crater and penetration hole diameters for impact experiments into (a) Al and (b) Teflon targets at 6.0 and 6.3 km/s respectively. Note that substantially more experiments were conducted and analyzed than could be illustrated in this short report, and that experiments of substantially different scales conform to a single curve. Unique solutions—at some constant impact velocity—for projectile diameter seem possible for any individual penetration hole that is characterized by the measurements of  $D_h$  and  $T$ .

case of  $D_h = D_p$  in the ultrathin foil. This underscores that the transition from cratering to penetration regimes must be well understood to correctly interpret space-exposed surfaces. If 6 km/s were indeed an applicable velocity for the data illustrated in Fig. 1, the largest penetration holes would be due to impactors of  $\sim 500 \mu\text{m}$  in diameter for Solar Max and  $\sim 600 \mu\text{m}$  in diameter for LDEF surfaces.

Returning to Fig. 4 we also see that experiments conducted with a wide range of projectile sizes combine to define a single curve that has rather similar characteristics for both target materials. This validates that dimensional scaling is a suitable approach to solve for first-order projectile dimensions from the measurement of  $D_h$  and  $T$  [e.g., 22]. Hörz et al. [4] corroborate, however, that some scale-dependent behavior exists at very small projectile dimensions ( $<100 \mu\text{m}$ ) as first described by Cour-Palais [16].

We have performed various curve-fitting procedures to the data illustrated in Fig. 4 to generalize the relationships of  $T$ ,  $D_h$ , and  $D_p$ .

We found that a polynomial fit of the form

$$\log_{10} y = a_0 + a_1(\log_{10} x) + a_2(\log_{10} x)^2 + a_3(\log_{10} x)^3 + a_n(\log_{10} x)^n \quad (1)$$

best describes the experimental results with  $y = D_p/T$  and  $x = D_h/T$ .

Table 1 provides the associated coefficients for both Al and Teflon.

TABLE 1. Polynomial fit of the experimental results illustrated in Fig. 4.

	$a_0$	$a_1$	$a_2$	$a_3$	$a_4$
Al(1100)	-0.458	0.175	1.008	1.199	-1.131
Teflon (TFE)	-0.485	0.667	0.562	-0.230	0.518
	$a_5$	$a_6$	$a_7$	$a_8$	
Al(1100)	-0.800	1.152	-0.434	0.546	
Teflon (TFE)	0.021	-0.661	0.415	-0.075	

**Discussion:** Aluminum alloys are among the best-investigated materials in terms of cratering and impact behavior, due to their wide use as spacecraft materials as summarized by Carey et al. [17], Cour-Palais [16], Hermann and Wilbeck [13], Christiansen [23], and Watts et al. [11], yet we are not aware of corresponding experiments and data for Teflon targets. Consequently, our present comparison with other investigations is limited to Al. The salient results are shown in Fig. 5, where we compare our data with the penetration equations of other investigators, the latter suitably adjusted to our experimental conditions (velocity, densities, compressive strengths, etc.). We also extrapolated the equations to targets thicker than suggested and intended by the original workers, for illustrative purposes; many previous experiments were not necessarily meant to be extrapolated to very thin targets of  $D_p/T > 10$ .

The agreement among the various approaches is very good in the range of  $D_p/T$  of 0.5 to 10, in which most of the original data were gathered and for which most of the equations and applications were intended. Note, however, that we differ distinctly from all other workers at, or close to the ballistic limit. We not only observe experimentally that hole size may be very small close to  $T_{BL}$ , but we also postulated that the ballistic limit would satisfy the condition of  $D_h = 0$ . This causes a precipitous drop over a very narrow range in  $D_p/T$  of this experimental curve in Fig. 5. While Carey et al. [17] do account for decreasing hole sizes in massive targets, they did not consider  $D_h = 0$ ; this condition constitutes a major datum that totally forces and controls the curve shape over a very small interval in target thickness. Extrapolation of existing penetration formulas to the infinite halfspace case, as purposefully illustrated in Fig. 5 and as performed by Warren et al. [6] or Humes et al. [15] and others, will always lead to projectile diameters smaller than those derived from cratering formulas. The ballistic limit obviously does not reflect the transition from cratering to penetration in the context of projectile size characterization based on the measurement of penetration-hole diameters.

We have emphasized throughout this report that the target's front-side morphology is either identical to or strongly resembles that of the standard crater for targets as thin as  $D_p/T = 1$  in Al or 0.6 in Teflon (see Fig. 3). The cratering-related material flow at or close



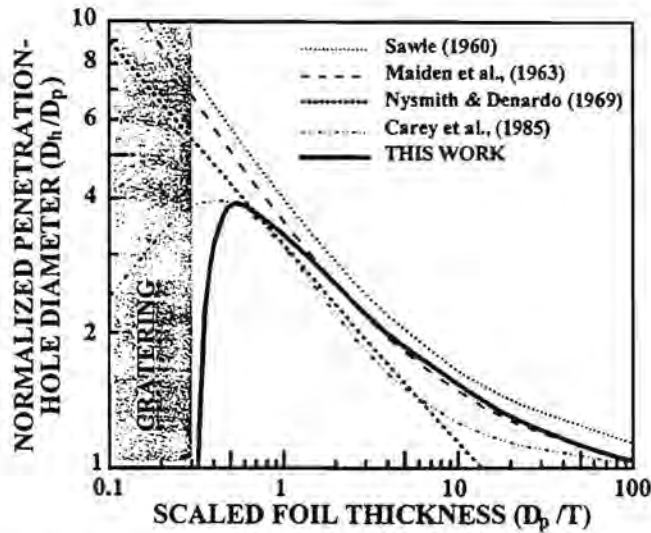


Fig. 5. Comparison of our experimental Al impacts with diverse penetration formulas suggested by previous workers for metal targets if not specifically for Al. Note the fundamental difference between this work and all previous generalizations in the vicinity of the ballistic limit.

to the target surface, as manifested by rim developments or spall zones and ultimately by a seemingly constant crater diameter  $D_c$ , does not seem to be significantly disturbed in targets thicker than these threshold thicknesses. As a consequence, penetrations of such targets must be thought of as craters when viewed (and measured) from the front side. The measurement of a hole diameter at some interior target location is incorrect and nonspecific for the derivation of the projectile diameter in such massive targets. For the purposes of projectile-size characterizations, the transition from cratering to penetration occurs in targets much thinner than those that characterize the ballistic limit. This transition occurs when the feature diameter  $D'_c$  becomes measurably and distinctly smaller than the standard crater diameter  $D_c$ .

As detailed by Hörz et al. [4], each and every one of the scaled experiments reported here is uniquely characterized in terms of absolute and relative shock-pulse duration [e.g., 18]. Pulse duration ( $t$ ) is defined as the transit time for a shock front of speed  $U$  to reach the target's rear and to return as a rarefaction wave to the projectile/target interface where it will initiate decompression of the target. Pulse duration defines how long the compressive phase of a collisional event will last. It seems obvious that the dimensionally smaller member of an impacting pair is apt to control the pulse duration, in most cases. Cratering in infinite halfspace targets will be totally controlled by the pulse duration of the projectile (i.e.,  $t_p \ll t_t$ ). As long as  $t_p < t_t$ , the total duration of the event's compressive phase is precisely that of a standard crater, and corresponding material flows will be initiated (and largely sustained) by the target. However, as target thickness decreases, the condition of  $t_p = t_t$  will be reached at some specific  $D_p/T$ ; targets thinner than this threshold value imply that  $t_p > t_t$  (i.e., that target pulse duration has become dominant). At all conditions where  $t_p > t_t$ , the material flow in the target will not be that normally associated with a standard crater.

We suggest that  $t_t = t_p$  marks the transition from genuine cratering to penetration processes when extracting projectile sizes from space-exposed surfaces. All penetrations of  $t_t < t_p$ , when inspected in plan view, must be interpreted and *measured* as craters (i. e., a  $D_c$  reading must be taken rather than a hole diameter  $D_h$ ).

The condition of  $t_t = t_p$  (and other pulse durations) is readily calculated if the equations of state (EOS) of both the projectile and target are known. Using the EOS for  $\text{SiO}_2$ , Al 2024, and Teflon<sup>TFE</sup> [23] and the numerical method of Cintala [24], we calculated the shock-wave velocities (and peak pressures) applicable to our experiments. The glass/Al impacts at 6.0 km/s resulted in a peak pressure of 56 GPa; the associated  $U_{\text{glass}} = 6.97$  km/s and  $U_{\text{aluminum}} = 8.43$  km/s. Teflon impacts at 6.3 km/s yielded 46 GPa at the projectile/target interface with an associated  $U_{\text{glass}} = 6.53$  km/s and  $U_{\text{teflon}} = 7.35$  km/s. The ratio of these velocities corresponds directly to that  $D_p/T$  at which  $t_p = t_t$  (i.e.,  $D_p/T_{\text{aluminum}} = 0.83$  and  $D_p/T_{\text{teflon}} = 0.89$ ). These relative thicknesses are in excellent agreement with the experimental evidence illustrated in Figs. 3a,b, as well as the data plotted in Figs. 4 and 5.

In principle, shock velocities  $U_p$  and  $U_t$  may be calculated for any impact velocity, provided the EOS is known for both the target and projectile materials. This led Hörz et al. [4] to calculate  $t_t/t_p = 1$  for impact velocities beyond those simulated, and to determine the associated  $D_p/T$  values, which mark the transition from cratering to penetration for any given model velocity. Example calculations are illustrated in Fig. 6 for the glass/Al pair. All impact features to the left of the  $t_p = t_t$  line must be interpreted as craters. One may use applicable cratering equations and those for the ballistic limit in Al [e.g., 16, 23] to calculate any standard crater diameter (and associated  $D_c/D_p$ ) and a ballistic limit thickness (expressed as  $D_p/T$ ) as a function of velocity. All features to the left of the ballistic-limit line are genuine craters, while the features between the ballistic-limit

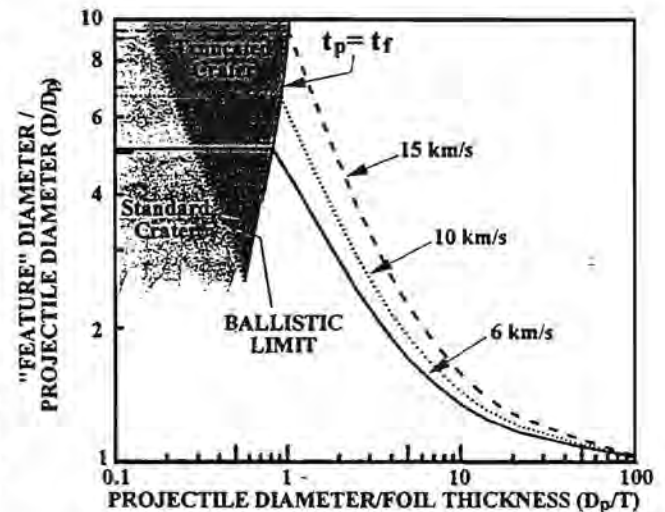


Fig. 6. Possible extrapolation of experimental penetration results in Al targets to prevalent velocities in near Earth orbit. The condition  $t_t = t_p$  represents the demarcation between cratering and penetration regimes as calculated from equations of state data and associated shock velocities. Relative crater diameters ( $D/D_p$ ) and ballistic limits were calculated from Cour-Palais [16] and Christiansen [23].

line and the pulse-duration line are actual penetrations, in part, substantial ones that must be interpreted as craters; all features of  $t_p > t_p$  must be considered genuine penetrations. The latter curves are modeled, other than the experimental data at 6 km/s. All holes will essentially decrease from crater diameter  $D_c$  to the condition of  $D_h = D_p$  at very thin foils. We assume that this is the case at  $D_p/T = 100$  (Fig. 6), and that this condition is essentially independent of velocity. Both assumptions are critical and the subject of ongoing laboratory investigations. Nevertheless, it is suggested that consideration of the shock-pulse duration may lead to an improved understanding of some velocity-dependent aspects of cratering and penetration mechanics.

We consider the agreement between the experimental evidence and the pulse duration arguments to imply that many penetrations should be viewed and measured as craters instead of penetrations. Furthermore, when interpreting space-produced penetrations, the transition from cratering to penetration formalisms may not occur at the ballistic limit, but at substantially thinner targets (i.e., where  $t_p/t_c = 1$ ).

**Acknowledgments:** We wish to acknowledge the contributions and skills of F. Cardenas, W. Davidson, G. Haynes, and J. Winkler of Lockheed Engineering and Sciences Company in conducting the impact experiments. We also appreciate the many useful discussions and exchanges with H. Zook, A. Watts, J. Warren, and M. Zolensky.

**References:** [1] Anderson C. E., ed. (1987) *Proc. 1986 Symp. Intl. J. Impact Eng.*, 5, 760 pp. [2] Anderson C. E., ed. (1990) *Proc. 1989 Symp. J. Intl. Impact Eng.*, 10, 635 pp. [3] Anderson C. E., ed. (1993) *Proc. 1992 Symp. J. Intl. Impact Eng.*, in press. [4] Hörz F. et al. (1993) *Intl. J. Impact Eng.*, in press. [5] Hörz F. et al. (1993) *Proc. HVIS Intl. J. Impact Eng.*, in press. [6] Warren J. L. et al. (1989) *Proc. LPSC 19th*, 641–657. [7] See T. H. et al. (1990) *NASA JSC Report #24608*, 561 pp. [8] Levine A. E., ed. (1992) *First Post Retrieval Symposium, NASA CP-3134*. [9] Levine A. E., ed. (1993) *LDEF—69 Months in Space. Second LDEF Post Retrieval Symposium, NASA CP-3194*. [10] McDonnell J. A. M. (1991) *Proc. LPS, Vol. 22*, 185–193. [11] Watts A. et al. (1993) *Contract Report by POD Associates*, Albuquerque, NM to Lockheed Engineering and Sciences Company, Houston, Texas, 84 pp. [12] Pailer N. and Grün E. (1980) *Planet. Space Sci.*, 28, 321–331. [13] Hermann W. and Wilbeck J. (1986) *Sandia National Laboratories Report, SAND-86-1884C*, 29 pp. [14] McDonnell J. A. M. and Sullivan K. (1992) in *Hypervelocity Impacts in Space* (J. A. M. McDonnell, ed.), 39–48, Univ. of Kent. [15] Humes D. H. (1992) in *LDEF—69 Months in Space. First Post Retrieval Symposium* (A. E. Levine, ed.), 399–419, *NASA CP-3134*. [16] Cour-Palais B. G. (1987) *Intl. J. Impact Eng.*, 5, 681–692. [17] Carey W. C. et al. (1985) in *Properties and Interactions of Interplanetary Dust* (R. H. Giese and P. Lamy, eds.), 131–136, Reidel. [18] Gehring J. W. (1970) *High-Velocity Impact Phenomena* (R. Kinslow, ed.), 105–156, Academic. [19] Pietkutowsky A. J. (1990) *Intl. J. Impact Eng.*, 10, 453–472. [20] Stip A. J. et al. (1990) *Intl. J. Impact Eng.*, 10, 543–554. [21] Maxwell D. E. (1977) in *Impact and Explosion Cratering* (D. J. Roddy et al. eds.), 1003–1008, Pergamon. [22] Holsapple K. A. and Schmidt R. M. (1990) *JGR*, 87, 1849–1870. [23] Marsh S. P., ed. (1980) *Univ. of California*, 658 pp. [24] Cintala M. J. (1992) *JGR* 97, 947–973. [25] Christiansen E. L. (1992) *AIAA Space Programs and Technologies Conference*, Huntsville, Alabama, *AIAA 92-1462*, 8 pp.

**SOME CONSIDERATIONS ON VELOCITY VECTOR ACCURACY IN DUST TRAJECTORY ANALYSIS.** A. A. Jackson<sup>1</sup> and H. A. Zook<sup>2</sup>, <sup>1</sup>Lockheed Engineering and Sciences Company, Houston TX 77058, USA, <sup>2</sup>Solar System Exploration Division, NASA Johnson Space Center, Houston TX 77058, USA.

**Introduction:** The relative contributions of comets and asteroids to the reservoir of dust in the interplanetary medium is not known. There are direct observations of dust released from comets and there is evidence to associate the IRAS dust bands with possible collisions of asteroids in the main belt [1]. A means toward sorting out the parent sources has been proposed in the establishment of a dust collector in orbit about the Earth [2]. The purpose of such a facility would be to collect not only cosmic dust particles intact but also the state vectors [3], as they arrive at the detector, the idea being that one may combine analytical laboratory analysis of the physics and chemistry of the captured particles with orbital data in order to help distinguish between bodies and identify parent bodies. The theoretical study of dust particle orbits in the solar system takes on greatly more importance if we use collected trajectory data. The orbital motion of dust when radiation and forces alone are acting is well understood [4,5]. When gravitational forces due to the planets are included, the motion can become quite complex [6–8].

In order to characterize the orbits of particles as they crossed the Earth's orbits, a study of the long-time dust orbital evolution was undertaken. We have considered various parameters associated with these dust orbits to see if one may in a general way discriminate between particles evolved from comets and asteroids.

**Preliminary Accuracy Considerations:** We proceed in this study as we have done previously [8]. That is, we considered the dust particles as ideal black bodies, of density 1 gm/cc, spherical, with radii 10–100  $\mu$ m. Particles of this size are affected by radiation forces, photon pressure, and Poynting-Robertson drag. Account was also taken of solar wind drag, which amounts to about 30% of the Poynting-Robertson drag negligible. The gravitational forces due to the planets are included, unlike in our previous study; the planetary orbits are those of true n-body interaction so that the possibility of secular resonance is included. Our method was to calculate explicitly by a numerical procedure the orbits of dust particles after they left their parent bodies. The motion is determined numerically with the implicit Runge-Kutta integrator using Gauss-Radau spacings [9].

Particles are ejected from comets or asteroids at perihelion. This will happen due to some outgassing process on the comet or meteoric impact on an asteroid. Particles then feel the immediate effect of radiation pressure and move on radiation-modified orbits that have new semimajor axis and eccentricity. Then the particle orbit was followed until it was well inside Mercury's orbit.

When the ascending or descending node of a test particle falls within the range of 0.983 to 1.017 AU from the Sun, a collision with a spacecraft in the same orbit as the Earth's becomes possible. The Earth is not a target for right now since we did not include the effects of its gravitational acceleration. Two orbital parameters proved useful for the characterization of parent body origin, orbital eccentricity  $e$ , and magnitude of relative velocity  $u$ , of intersection at the node.

For illustration we plot  $u$  vs.  $e$  in Fig. 1 for 30- $\mu$ m particles. The circles are particles from asteroids and the squares are particles from comets. As might be expected, dust from the comets retain

their high eccentricities, while asteroidal grains are of low eccentricity.

However, there is some overlap in eccentricity and velocity. Figures 2 and 3 show histograms of the magnitude of the velocity and eccentricity of the particle orbits from comets and asteroids at nodal crossing.

We considered as a measure of accuracy the following quantity

$$\text{Acc} = (\delta v_r^2 + \delta v_t^2 + \delta v_n^2)^{1/2} / |v|$$

where  $\delta v_r$  is the magnitude of the difference between the relative radial velocities of the asteroid and comet,  $\delta v_t$  is the magnitude of the difference between velocities tangential to the Earth's orbit, and  $\delta v_n$  is the magnitude of the difference between the velocities normal to the Earth's orbit. Relative here means the relative velocity between the dust particle and a hypothetical spacecraft in a circular orbit at the Earth's orbit.

Figure 4 shows the results of taking pairwise for each 30- $\mu\text{m}$  dust asteroid particle with each comet particle and keeping only the minimum value of the accuracy that results.

**Error Analysis:** We take the following as a simple model of the effect of measurement error on the determination of dust orbits by a detector. In order to make the problem tractable, take the dust detector to be in a circular heliocentric orbit with dust particles striking it. Such acceleration processes as the gravitational field of the Earth (important for a spacecraft orbiting the Earth) are not considered here.

We also take the collisions to occur with the detector spacecraft at the dust particle orbit ascending node. Let there be a coordinate system  $x, y, z$  erected at the instantaneous position of the spacecraft and the intersection point of the dust particle, where  $x$  is in the radial direction away from the Sun,  $y$  points tangent to the velocity vector of the circular spacecraft orbit, and  $z$  is along the angular momentum of the spacecraft orbit. Öpik [10] then gives the components of particles velocity vector  $u$  by the following

$$u_x^2 = (2 - a(1 - e^2) - 1/a)$$

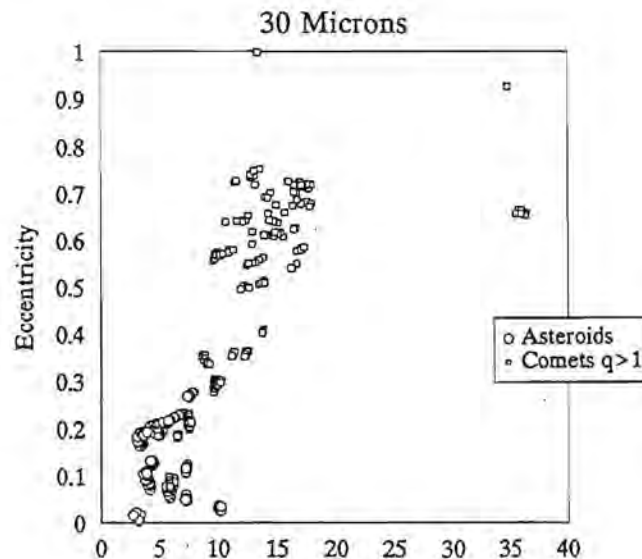


Fig. 1. Magnitude velocity at ascending node (km/s).

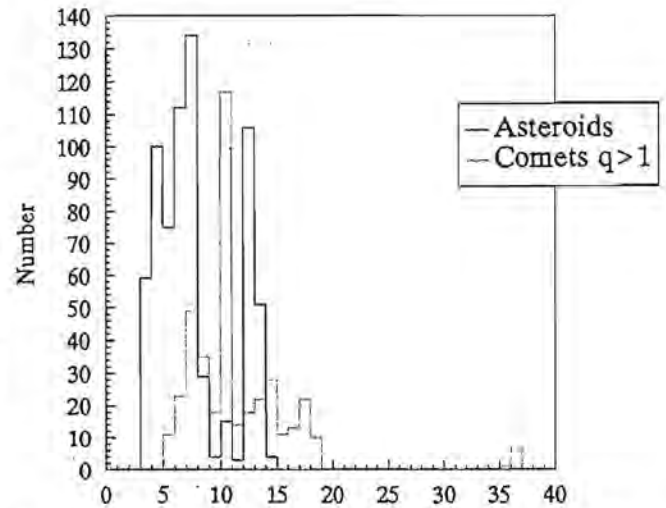


Fig. 2. Magnitude of relative velocity at ascending node (km/s) 30  $\mu\text{m}$ .

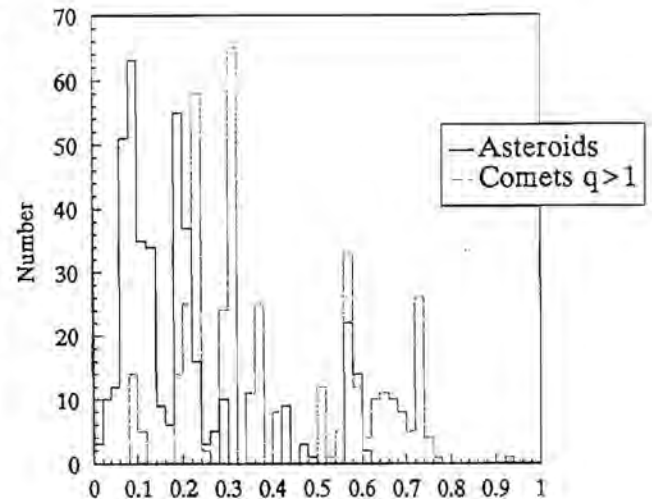


Fig. 3. Eccentricity at ascending node 30  $\mu\text{m}$ .

$$u_y = [(a(1 - e^2))]^{1/2} \cos i - 1$$

$$u_z^2 = a(1 - e^2) \sin^2 i$$

where  $a$  (in units of the spacecraft orbit semimajor axis) is the semimajor axis of the particle orbit,  $e$  is its orbital eccentricity, and  $i$  is its inclination to plane of the spacecraft's orbit.

In the above, orbital elements are computed relative to a "radiation"-modified gravitational potential. That is, if  $\beta$  = force of radiation/force of gravity, then the potential is of the form  $(1 - \beta)\mu/r$ , if  $\mu$  and  $r$  are the usual gravitational parameter distance from the Sun.

Conversely one may write

$$a = (1 - u^2 - 2u)^{-1}$$

$$1 - e^2 = (2 - a^{-1} - u_x^2)a^{-1}$$



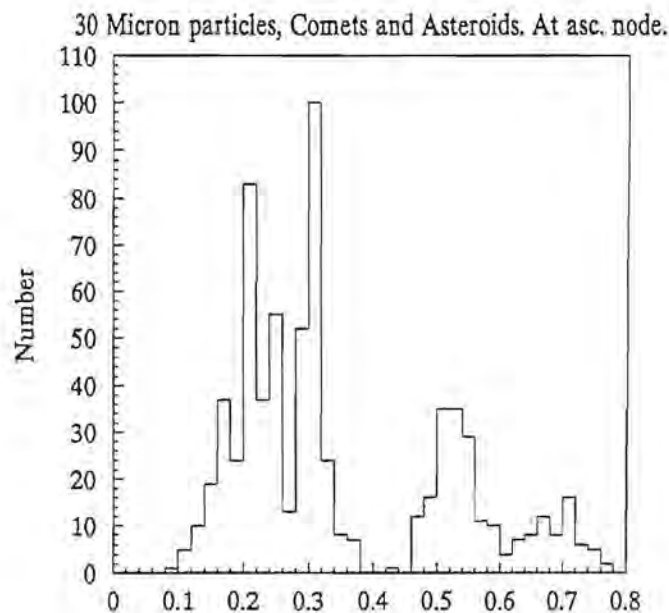


Fig. 4. Accuracy in magnitude of difference of velocities.

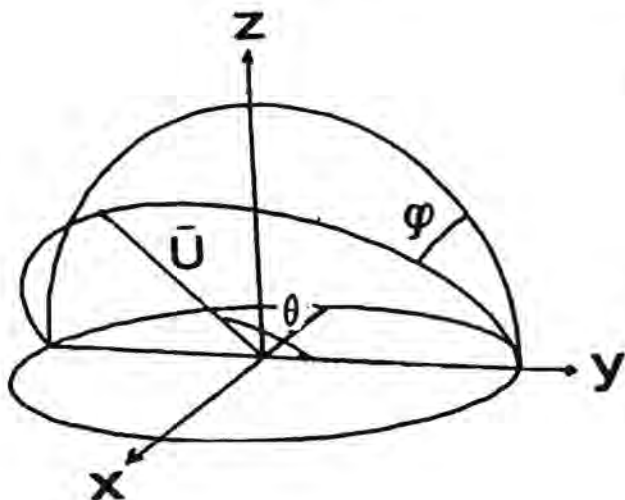


Fig. 5.

$$\tan i = u_z / (1 + u_y)$$

which give orbital elements as a function of the velocity components.

Let the detector measure the magnitude of the particle velocity and two angles,  $\theta$  the angular distance from the positive  $y$  axis and  $\phi$  the azimuth angle (see Fig. 5). Then the velocity components can be expressed as

$$u_x = u \sin \theta \sin \phi$$

$$u_y = u \cos \theta$$

$$u_z = u \sin \theta \cos \phi$$

so that

$$\cos \theta = u_y / u$$

$$\tan \phi = u_x / u_z$$

Now consider another simplification. Take the angular measurements  $\theta$  and  $\phi$  to be perfect. Let an error occur in the measurement of magnitude of the relative velocity,  $u$ . Holding  $\theta$  and  $\phi$  constant we have

$$da/du = (2u + 2du_y/du)/(1 - u^2 - 2u_y)^2 \quad (1)$$

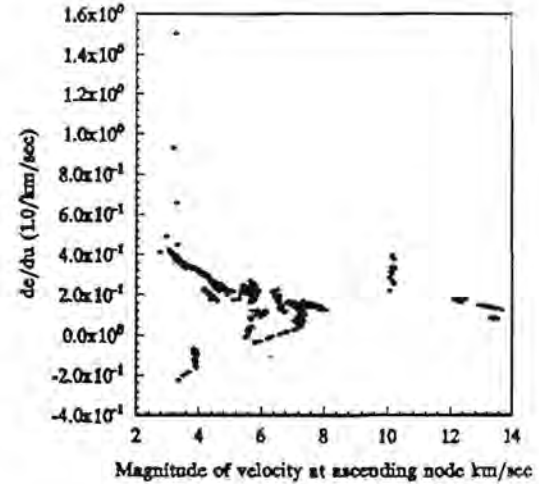
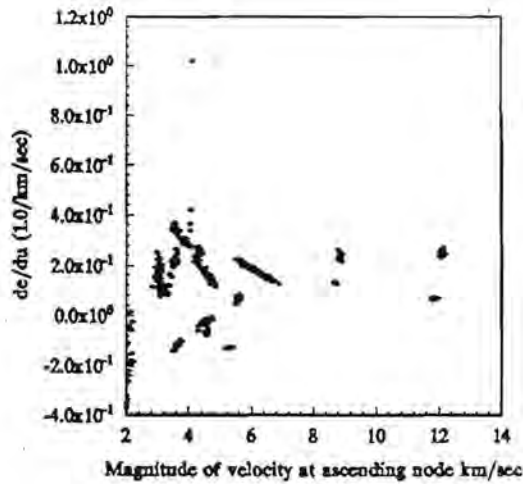
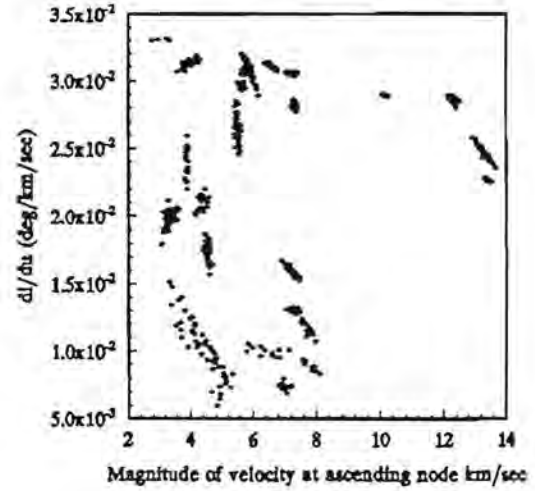
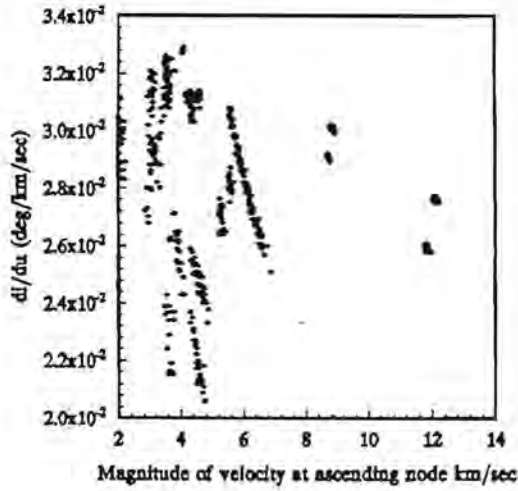
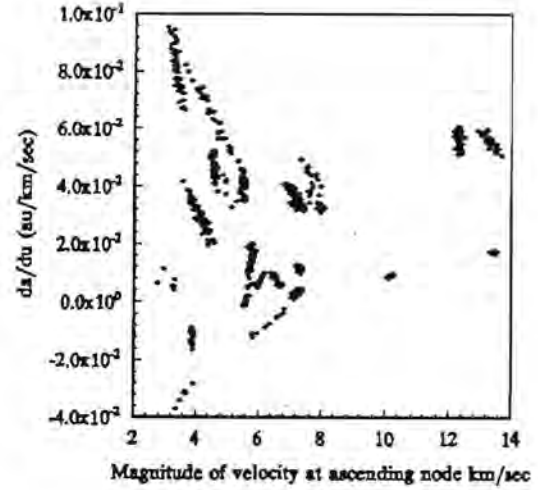
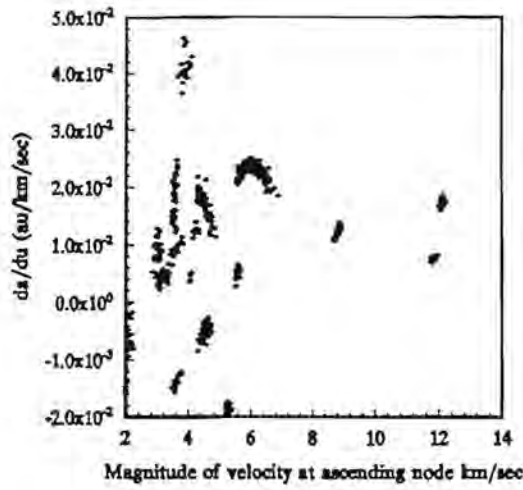
$$de/du = [(2 - a^{-1} - u_x^2)a^{-2}da/du + (a^{-2}da/du + 2u_x du_x/du)a^{-1}]/2e \quad (2)$$

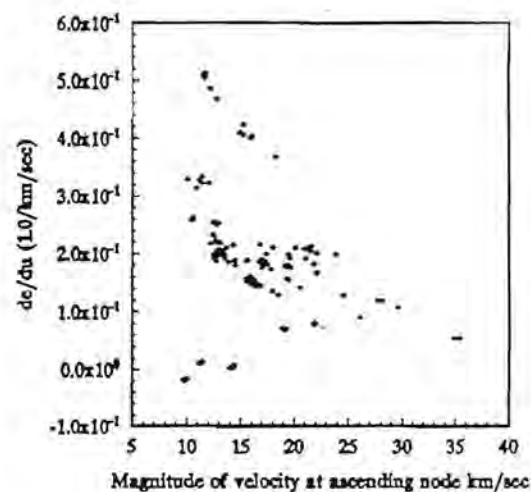
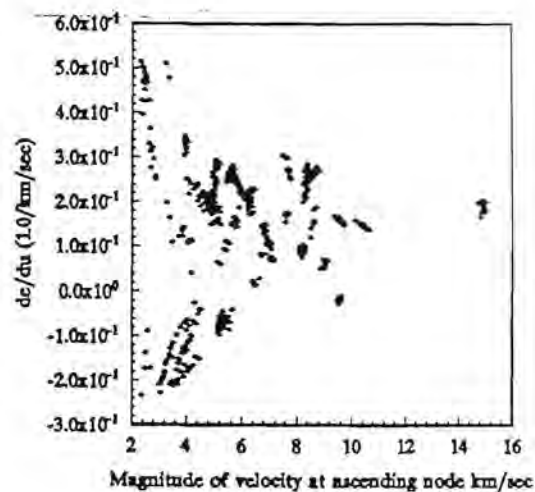
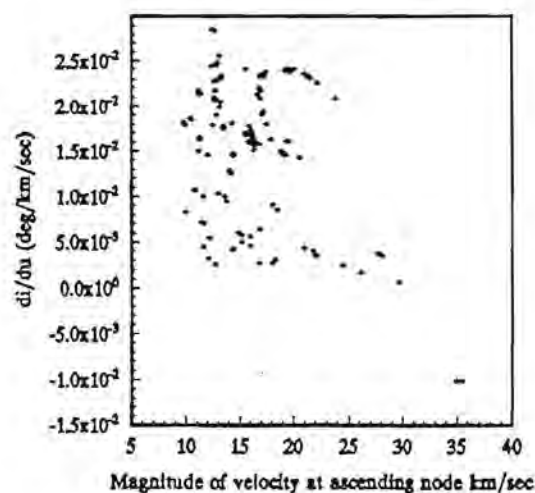
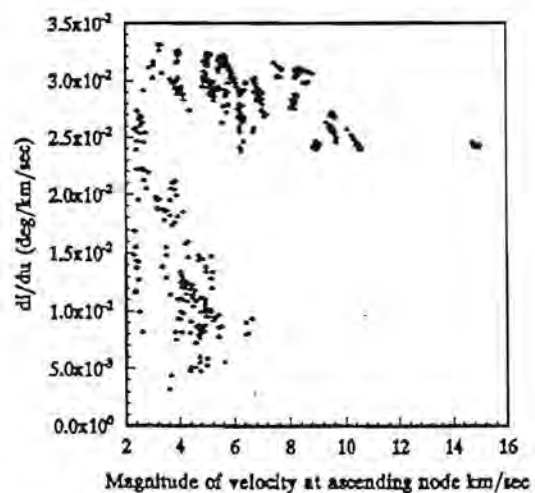
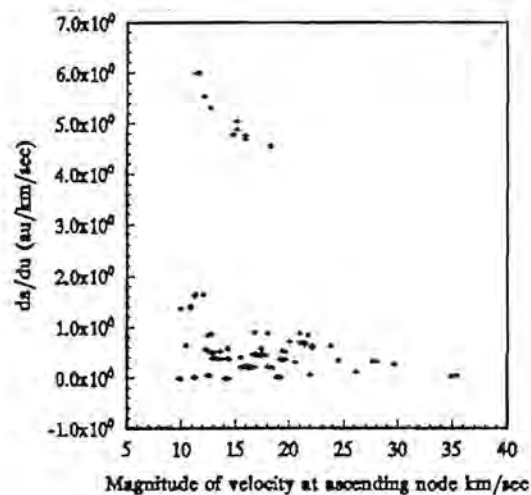
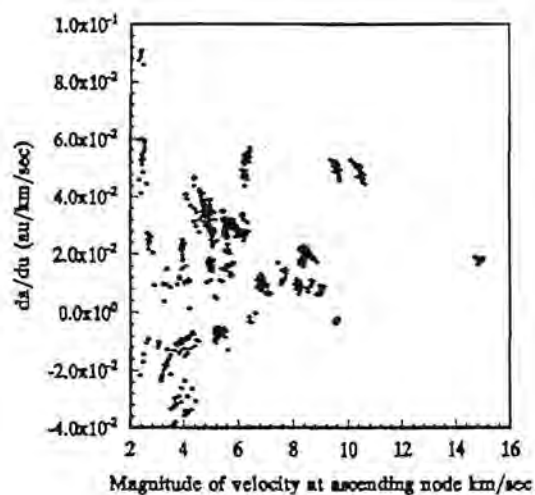
$$s^2 i \, di/du = du_z/du(1 + u_y)^{-1} - u_z du_y/du(1 + u_y)^{-2} \quad (3)$$

Taking the data given at the ascending node from the computed orbital evolution of dust particles, the dependence of  $da$ ,  $de$ , and  $di$  on  $du$  are given in Figs. 6–8 for the asteroidal particles and Figs. 9–11 for the cometary particles.

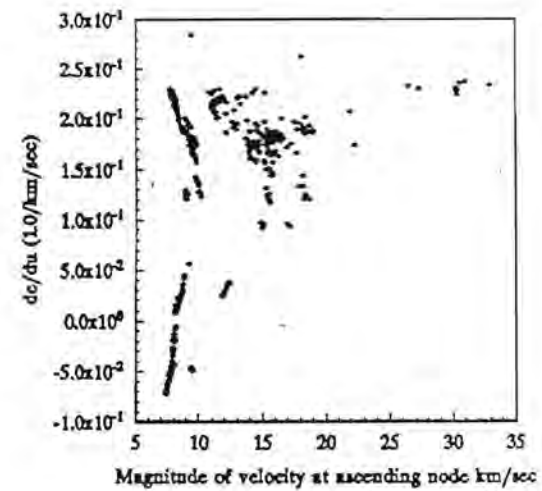
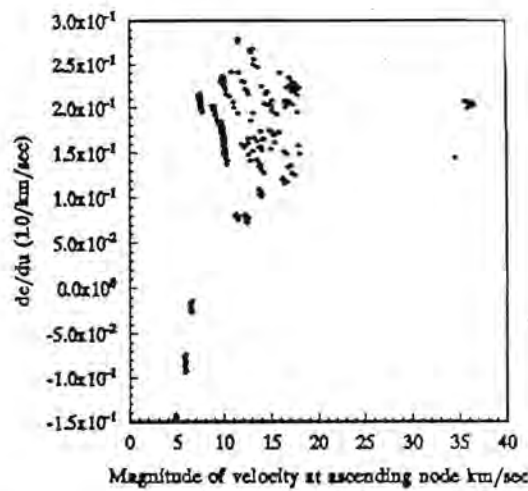
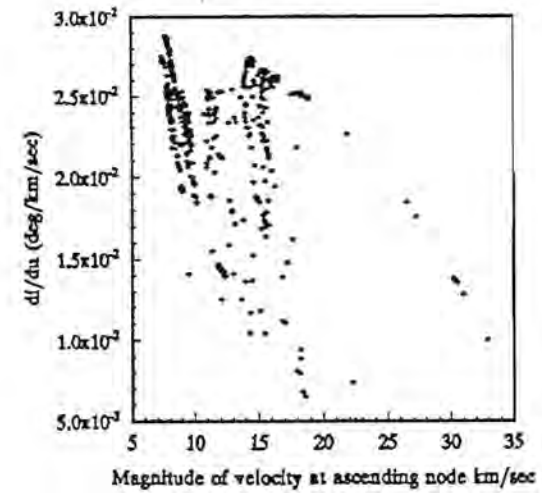
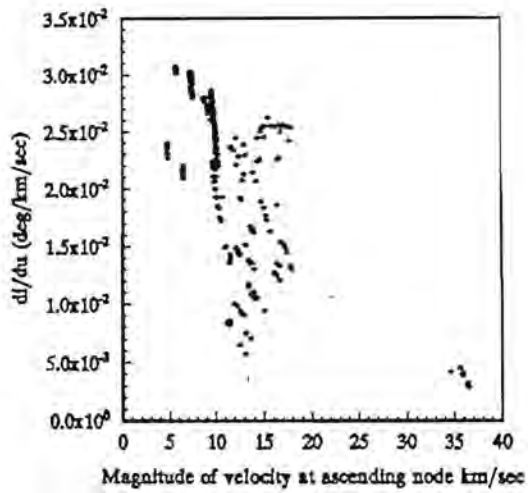
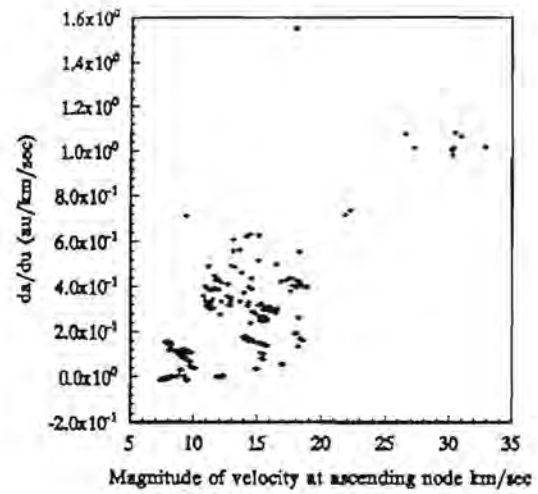
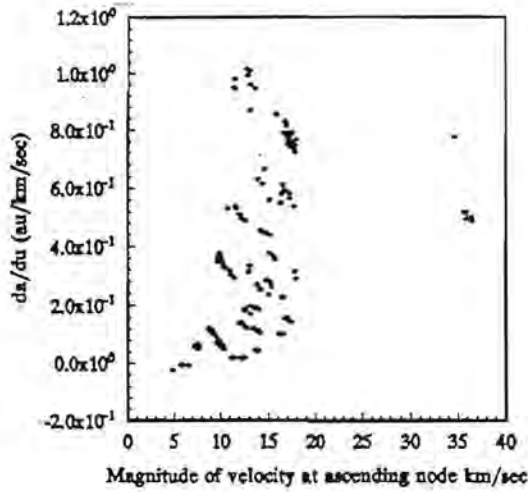
**Conclusions:** The largest error incurred in semimajor axis determination arises in the case of 10- $\mu$ m particles from comets,  $da/du \gg 6$  (see Fig. 9). This was a particle from Comet Honda-Mrkos-Pajduskova that had at the time of intercept a semi-major axis of approximately 8 AU and a eccentricity of about 0.87. One sees from equation (1), and noting that the magnitude of  $u = 3 - 2[a(1 - e^2)]^{1/2} - 1/a$ , that for large  $a$  and  $e \sim 1$  that  $da/du \sim a$ . Thus for particles captured from large  $a$  and high-eccentricity orbits the error in  $u$  can be substantial.

A value of  $de/du$  of nearly 1.5 occurs in a 30- $\mu$ m asteroidal particle from asteroid Flora (Fig. 7). In this there is nothing unusual

Fig. 6. Errors for asteroidal particles at ascending node 10  $\mu\text{m}$ .Fig. 7. Errors for asteroidal particles at ascending node 30  $\mu\text{m}$ .

Fig. 8. Errors for asteroidal particles at ascending node 100  $\mu\text{m}$ .Fig. 9. Errors for cometary particles at ascending node 10  $\mu\text{m}$ .



Fig. 10. Errors for cometary particles at ascending node 30  $\mu$ m.Fig. 11. Errors for cometary particles at ascending node 100  $\mu$ m.

about the orbital elements at arrival; however, the particle has a low azimuth angle and high elevation of nearly  $90^\circ$ . In this case  $de/du \sim u^2$ .

The errors incurred in measured orbital inclination were always smaller than those for the other orbital elements. The current error budget for CDCF has candidate value of 1% [3]. In the worst case above this would result in an error of 0.07 AU in semimajor axis determination (can be higher for bigger cometary orbits) and 0.015 in eccentricity.

We will continue study of this problem, including effects of the Earth's gravitation and errors in the measurement angles. We will present further results in a later report.

**References:** [1] Dermott S. F. et al. (1984) *Nature*, 312, 505–509. [2] Hörz F. et al. (1990) *NASA TM-102160*. [3] Zook H. A. (1986) *LPI Tech. Rpt. 86-05*. [4] Wyatt S. P. and Whipple F. L. (1950) *Astrophys. J.*, 111, 134–141. [5] Burns et al. (1979). [6] Gonzci R. et al. (1982) *Icarus*, 51, 633–654. [7] Gustafson B. Å. S. and Misconi N. Y. (1986) *Icarus*, 66, 280–287. [8] Jackson A. A. and Zook H. A. (1992) *Icarus*, 97, 70–840. [9] Everhart (1985). [10] Öpik E. (1976) *Interplanetary Encounters*, Elsevier, New York.

#### VELOCITY DISTRIBUTION OF EARTH-CROSSING ASTEROID GRAINS. J. C. Liou and S. F. Dermott, University of Florida, Gainesville FL 32611, USA.

**Introduction:** We have systematically studied the evolution of 4- and 9- $\mu\text{m}$ -diameter dust particles from three prominent asteroid families, Eos, Koronis, and Themis, until they reach the Earth. We have found that they are quite distinguishable in their  $(I \cos \Omega, I \sin \Omega)$  phase space. The different distributions in the inclination space have several important observational consequences, which can be used to identify the origins of these dust particles. We convert the orbital elements of these Earth-crossing dust grains into six position and velocity components. It is not so easy to distinguish them by using any one single velocity component. We conclude that in order to identify the origins of the Earth-crossing dust grains we need all three velocity components to get their orbital elements and find their positions in the inclination space.

**Method:** We study the orbital evolution of dust particles with two different sizes (diameters equal to 4  $\mu\text{m}$  and 9  $\mu\text{m}$ ) originating from Eos, Koronis, and Themis asteroidal families. We use the "particles in a circle" method [1] to set up the initial condition for dust particles from the same family. Figure 1 shows the distribution in the inclination space for asteroids between 2.5 and 3.5 AU. It is clear that the way we set up the initial condition is the best systematic way to study dust particles coming from a given asteroidal family. We numerically integrate hundreds of particles from each family using RADAU [2] on an IBM ES/9000. All the planetary perturbations, radiation pressure, Poynting-Robertson light drag, and corpuscular solar wind effect are included in our calculation. We record the orbital elements of all the particles while they are spiralling toward the Sun and analyze the data when they are in the Earth-crossing region.

**Results:** Figure 2 shows the positions of 4- and 9- $\mu\text{m}$  particles in  $(I \cos \Omega, I \sin \Omega)$  space when they are in the Earth-crossing region. The numbers of particles from these three families have been adjusted to the actual dust ratios produced from them (Themis : Eos :

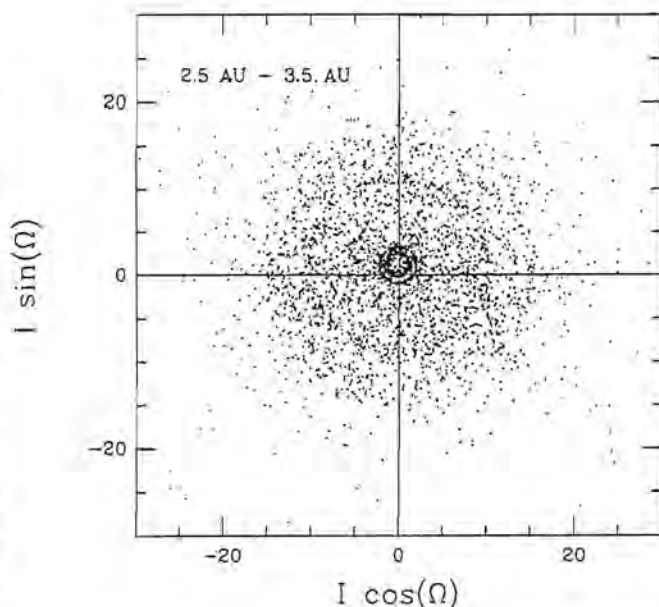


Fig. 1. Positions in  $(I \cos \Omega, I \sin \Omega)$  space of asteroids between 2.5 AU and 3.5 AU.

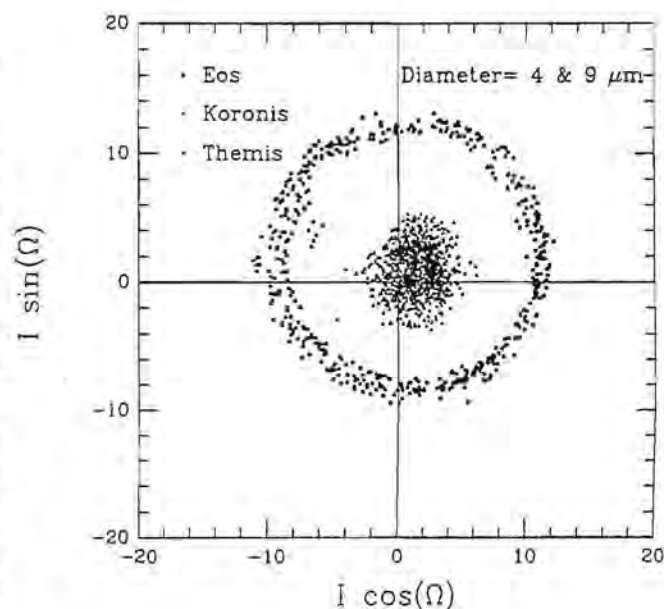


Fig. 2. Positions in  $(I \cos \Omega, I \sin \Omega)$  space of 4- and 9- $\mu\text{m}$ -diameter particles from Eos, Themis, and Koronis families when they are in the Earth-crossing region.

Koronis = 1 : 0.61 : 0.12). There are more Themis and Koronis particles in the first and fourth quadrants than in the other two. Thus, over the period of one year, when the Earth is moving around its orbit, it will encounter more Themis and Koronis particles (with ascending nodes) at the places corresponding to the first and fourth quadrants in Fig. 2. By using the distribution in the inclination

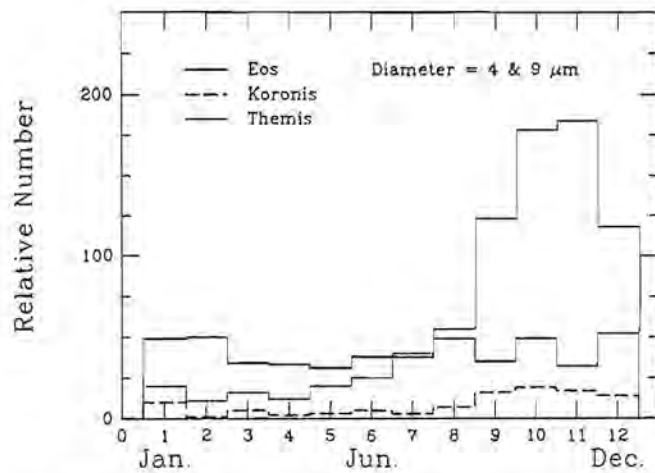


Fig. 3. A histogram showing the variation in relative number of particles as a function of different month of the year. These are 4- and 9- $\mu$ m-diameter particles at their ascending nodes.

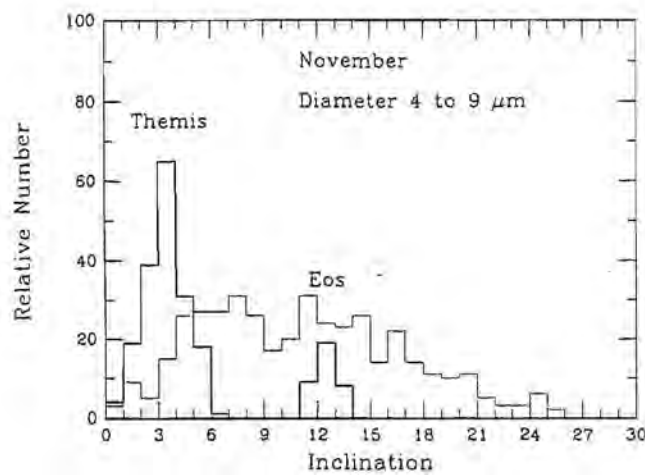


Fig. 4. Relative number of particles vs. possible inclination range from three different sources being collected at near-Earth vicinity in November. These are 4- and 9- $\mu$ m-diameter particles from Themis family (bold line), Eos family (bold line), and all-asteroid background (dotted line). The all-asteroid background does not include Eos and Themis families.

space, we calculate the relative number of particles the Earth will encounter over the course of one year (Fig. 3). The seasonal variation in terms of relative number is more than a factor of 8 for Themis particles.

We plot the relative number of particles that will encounter the Earth in November as a function of inclination in Fig. 4. Again, these are particles at their ascending nodes. We have also put the particles produced from the whole asteroidal population (excluding three families) in the diagram for a comparison. The low inclination regions (around 3°) are dominated by Themis particles while about half of 12° particles are of Eos origin.

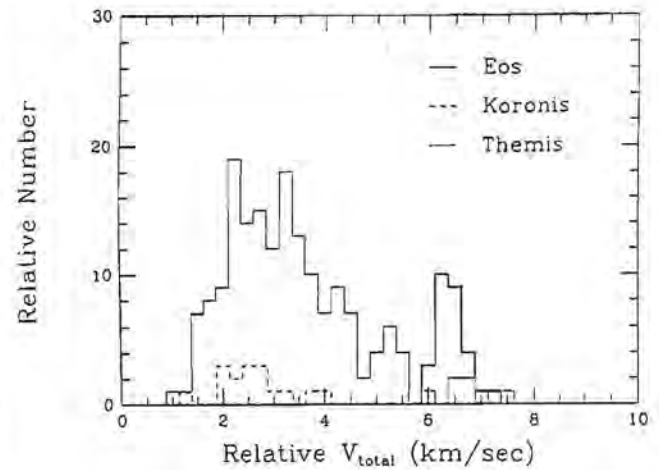


Fig. 5. Total relative encounter velocity distributions for particles from three different families in November.

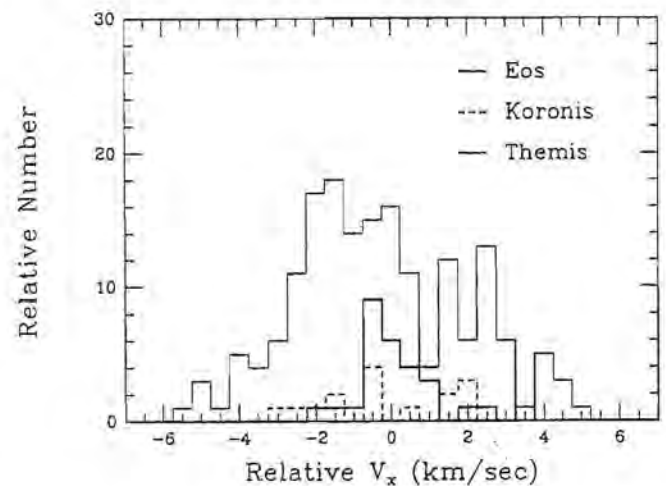


Fig. 6. Same as Fig. 5 for x velocity component.

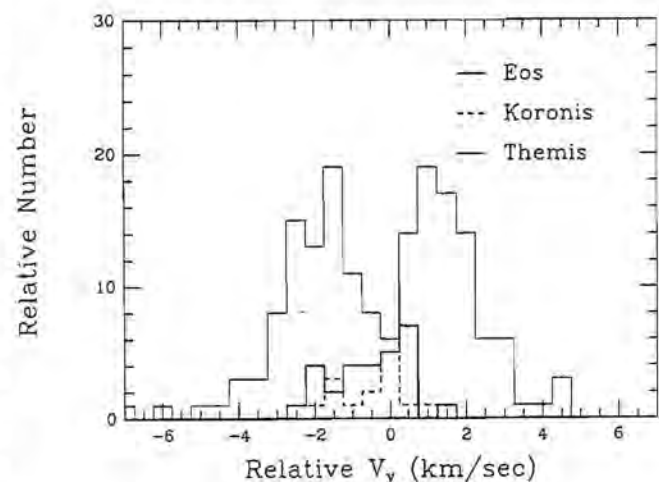


Fig. 7. Same as Fig. 5 for y velocity component.



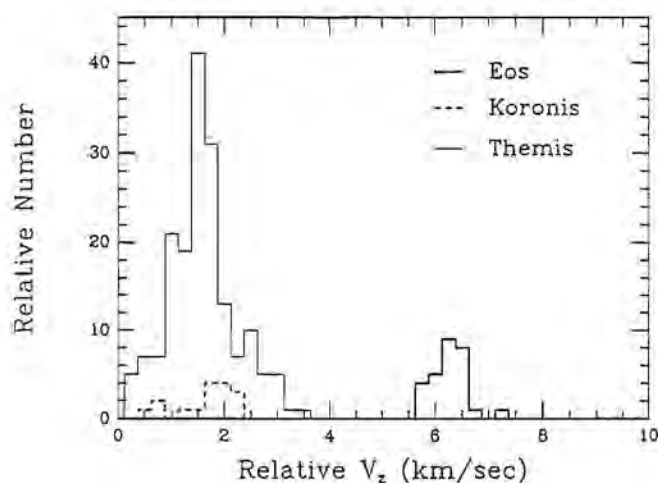


Fig. 8. Same as Fig. 5 for  $z$  velocity component.

There is an one-to-one correlation between six orbital elements and three position and three velocity components for the dust particles. We calculate the relative velocity components for particles from three families when they encounter the Earth in November. The results are shown in Figs. 5–8. The gravitational effect of the Earth is not included in our calculation. The  $x$  component is pointing towards the vernal equinox and  $y$  component is in the orbital plane of the Earth and perpendicular to the  $x$  direction. The  $z$  component is in the normal direction of the orbital plane of the Earth. In general, those particles have small encounter velocities (we have done a similar calculation for Encke-type particles; the typical encounter velocity is around 30 km/s). In the  $z$ -component diagram, Eos particles are quite distinguishable from Themis and Koronis particles. This is due to their high inclinations. In the other velocity components, as well as the total velocity diagrams, we do not see any clear difference between particles from different families.

Finally, we use the  $x$  and  $y$  velocity components of the particles to show how they approach the Earth in November (Fig. 9). ( $X$ ,  $Y$ ) is the Earth's orbital plane. The Earth is shown in its mean position in November. The relative positions of particles indicate from which directions they are going to encounter the Earth. The distances from those points to the Earth are proportional to their relative encounter velocities. From the diagram we can see that particles approach the Earth from all directions. There are no preferential directions that can be specified from the diagram.

**Discussion:** Based on our study, we conclude that it is very difficult to establish any parent-daughter relationship of near-Earth dust grains from their velocity components. It is, however, possible to find the origins of some dust particles at certain time of the year if we know their orbital elements. If we can measure all three velocity components of an Earth-crossing dust grain (of course, position vector as well), then we can find its orbital elements and place it in the inclination space. And then the task of identifying its origin will become possible.

**References:** [1] Dermott S. F. et al. (1992) in *Chaos, Resonance, and Collective Dynamical Phenomena in the Solar System* (S. Ferraz-Mello, ed.), 333–347, Kluwer. [2] Everhart E. (1985) in *Dynamics of Comets: Their Origin and Evolution* (A. Carusi and G. B. Valsecchi, eds.), 185–202, Boston.

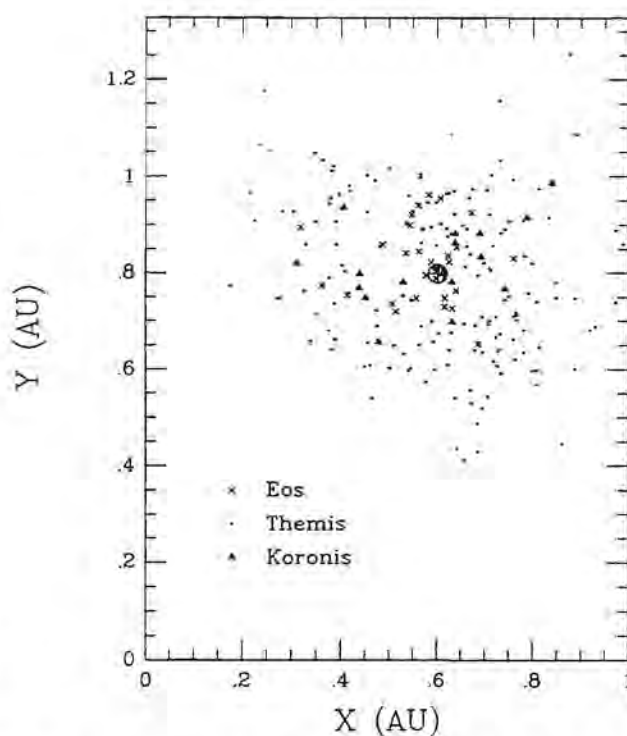


Fig. 9. Encounter geometry of the 4- and 9- $\mu$ m particles in November. The distances from the points to the Earth are proportional to their relative encounter.

#### THE INTACT CAPTURE OF HYPERVELOCITY DUST PARTICLES USING UNDERDENSE FOAMS.

C. R. Maag<sup>1</sup>, J. Borg<sup>2</sup>, W. G. Tanner<sup>3</sup>, T. J. Stevenson<sup>4</sup>, and J.-P. Bibring<sup>4</sup>,  
<sup>1</sup>Science Applications International Corporation, Glendora CA 91740, USA, <sup>2</sup>Institut d'Astrophysique Spatiale, 91405 Orsay Cedex, France, <sup>3</sup>Baylor University Space Science Laboratory, Waco TX 76798, USA, <sup>4</sup>Mare Crisium, Laurel Cottage, Silver Street, Tetsworth, Oxon OX9 7AR, UK.

**Overview:** Since the first NASA U-2 flight to collect extraterrestrial particles [1], the interest in the continued collection and analysis of these particles has increased. The main scientific interest in the analysis of extraterrestrial microparticles, more commonly called interplanetary dust particles (IDPs), is due to the fact that part of these particles could be of cometary origin and thus contain information on the origin of the solar system. Cometary material is likely to be the most primitive material accessible for analysis. It is thought that grains once present in the cometary nuclei, and now present as individual grains in interplanetary space, are still the best candidates for having properties acquired before or during condensing in the protosolar nebula. Also present in the low Earth orbit (LEO) environment are orbital debris (paint flakes, aluminum oxide spheres, etc.) with velocities of the same order as IDPs, which have resulted from the activities of man in space.

Many materials and techniques have been developed by the authors to sample the flux of particles in LEO. Through regular *in situ* sampling of the flux in LEO the materials and techniques have

produced data that complement the data now being amassed by the Long Duration Exposure Facility (LDEF) research activities. Thirteen flight experiments have been conducted on the space shuttle as part of an ongoing program to develop an understanding of the spatial density as a function of size for particles  $1 \times 10^{-6}$  cm and larger. In addition to the enumeration of particle impacts, it was also the intent that hypervelocity particles be captured and returned intact.

In addition to the shuttle payloads, an experiment was developed and flown as part of the Timeband Capture Cell Experiment (TICCE) on the EURECA 1 payload. This experiment has provided the opportunity to assess a wide range of dynamics of ejecta created by hypervelocity impacts on various substrates.

The 12 years of flight experimentation has provided the understanding and experience for the intact collection, removal, and analysis of particles in underdense materials. This experience will be used in the development of the capture cells proposed for the SOCCER-like Comet Coma Sample Return (CCSR) mission.

**Background:** A large body of experimental data exists concerning hypervelocity impacts. There are several empirical expressions relating the crater volume to the impacting particle size and mass and many previously flown experiments have examined these relationships. It is also well established that a part of the projectile mass is deposited and detectable on the inner surface of the impact crater. Despite being totally disassociated, elements detected from these sites allow coarse categorization of the impacting particle type, particularly with regard to all the important discrimination of space debris.

High-purity metallic surfaces have been used for the collection of all grains down to submicrometer sizes [2]. During the impact, a characteristic crater is formed, with rounded habits and a depth-to-diameter ratio equivalent to the velocity and size of the impacting particle and the encountered metal. During the impact, the particle is destroyed and the remnants are mixed with the target material, concentrating in the bottom of the crater and on the surrounding rims. A major strength of the metallic collectors lies in the fact that analytical techniques can be applied without modification to the craters. Also, identification of carbon and organic material is quite possible; this is essential for the study of extraterrestrial material (C, H, O, N).

The impact of a hypervelocity projectile ( $>3$  km/s) is a process that subjects both the impactor and the impacted material to a large transient pressure distribution. The resultant stresses cause a large degree of fragmentation, melting, vaporization, and ionization (for normal densities). The pressure regime magnitude, however, is directly related to the density relationship between the projectile and target materials. As a consequence, a high-density impactor on a low-density target will experience the lowest level of damage.

Historically, there have been three different approaches toward achieving the lowest possible target density. The first employs a projectile impinging on a foil or film of moderate density, but whose thickness is much less than the particle diameter. This results in the particle experiencing a pressure transient with both a short duration and a greatly reduced destructive effect. A succession of these films, spaced to allow nondestructive energy dissipation between impacts, will reduce the impactor's kinetic energy without allowing its internal energy to rise to the point where destruction of the projectile mass will occur. An added advantage to this method is that it yields the possibility of regions within the captured particle where a

minimum of thermal modification has taken place [3].

Polymer foams have been employed as the primary method of capturing particles with minimum degradation [4]. The manufacture of extremely low bulk density materials is usually achieved by the introduction of voids into the material base. It must be noted, however, that a foam structure only has a true bulk density of the mixture at sizes much larger than the cell size, since for impact processes this is of paramount importance. The scale at which the bulk density must still be close to that of the mixture is approximately equal to the impactor. When this density criterion is met, shock pressures during impact are minimized, which in turn maximizes the probability of survival for the impacting particle.

The intact capture of cosmic dust particles has been accomplished by the use of micropore foams [5]. The principal objectives of the original program were to develop techniques that would provide the size distribution of  $\text{Al}_2\text{O}_3$  particles (AOS) expelled from a solid rocket motor (SRM). Polymeric foams, with and without deceleration films, were extensively used to capture AOS intact. Aerogel materials were also used as a capture material. Commercial organic polymer foams were initially used. Based on testing in light gas gun facilities, it was determined that the ability of these foams to retain particles impacting at hypervelocities was marginal at best. These tests found that the more complex polymers had better stopping ability. Accordingly, it was also determined that the polymers that had extremely small cell sizes, higher latent heats of fusion, and very low densities (e.g.,  $0.02$ – $0.7$  g/cm<sup>3</sup>) had the highest probability of providing intact capture. In ground tests, the foams have been successfully tested between  $1$  and  $11$  km/s. One of the more interesting highlights of this program was the intact capture and retention of materials with a much lower density and material strength than AOS. Since the initial program, other materials have been tested successfully, most notably foams of silicones, polyimides, and fluorocarbons. For this activity, foams of the aforementioned polymers will be developed and used that have both gradients in axial density, typically from  $0.006$ – $0.009$  g/cm<sup>3</sup>, and imbedded sensors to sense impact parameters as the particle decelerates in the foam. Figures 1–3 show three conditions of particles captured intact



Fig. 1. IDP (C1) recovered from HVI experiment on STS 61-B.



Fig. 2. Aluminum oxide sphere, 8  $\mu\text{m}$  diameter, recovered from foam. The encrusted pyrolyzed foam is easily removed, leaving an undegraded specimen.

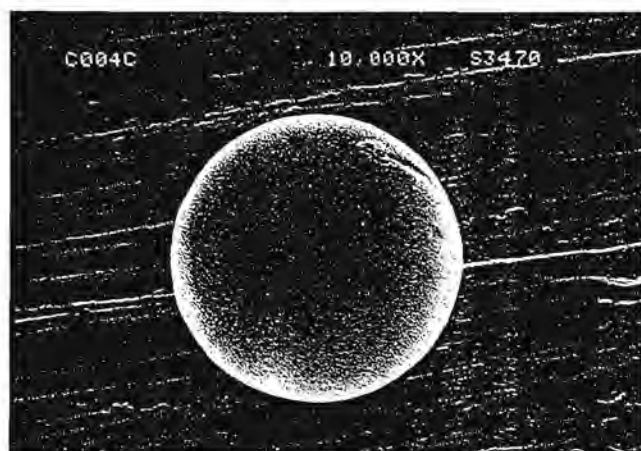


Fig. 3. AOS (ref. Fig. 2) after cleanup with HCl.

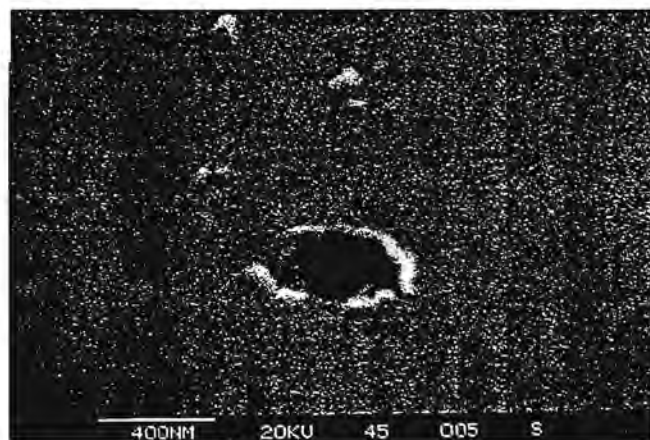


Fig. 4. Film perforation occurring during STS 32 flight.

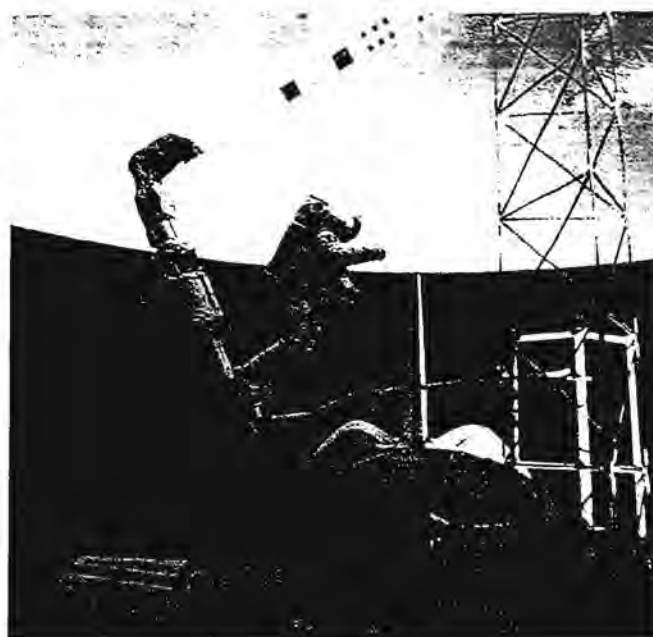


Fig. 5. Capture cell experiment flown on STS 61-B.

using organic foam capture cells on shuttles STS 61-B and STS 41-D. Figure 1 depicts an IDP recovered from the STS 61-B experiment. Figure 2 shows an AOS particle captured intact in the organic foam cell, and Fig. 3 shows the same AOS particle after the pyrolyzed foam has been removed using a low-molar concentration of HCl. Figure 2 also shows a portion of the "burn track" after the foam had been microtomed to locate the particle. Figure 4 shows a perforation through a typical 3- $\mu\text{m}$  deceleration film.

Aerogel has also been used as the capture medium in capture cells. Aerogel is particularly useful where extremely small cell sizes (150 Å) are necessary. This material in its silicon form is commonly produced for the nuclear industry Cherenkov radiator and has, in fact, been used in both space (HEOS, Ulysses) and balloon instrumentation. In comparison with polymer foams, however, the extremely low densities (0.035 g/cm<sup>3</sup>) cannot be achieved in any aerogel without producing great fragility. An aerogel capture cell was first used on shuttle mission STS 61-B. Figure 5 shows the placement on the remote manipulator system arm. While a particle was captured essentially intact, the fragility of this capture medium was demonstrated by the inability to remove the particle intact. In addition to the inherent fragility, aerogel has suffered from the effects of the space environment. Low temperatures seem to alter the shape of the "burn track"; atomic oxygen exposure erodes the surface; and it has been reported by the Centre National Etudes Spatiales (CNES) that the material embrittles after exposure to the radiation environment. Irrespective of these reported problems, experimentation with aerogel will continue.

**Shuttle Experimentation:** One of the means to test the aforementioned capture cells has been on the Interim Operational Contamination Monitor (IOCM) developed under the auspices of the U.S. Air Force/Space and Missile Systems Center. The IOCM contains an array of passive and active sensors that continuously sample three orthogonal directions in the shuttle cargo bay (Fig. 6).



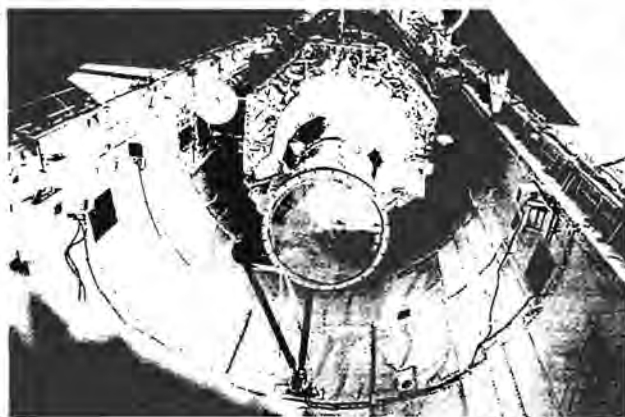


Fig. 6. The IOCM experiment as flown on STS 44.

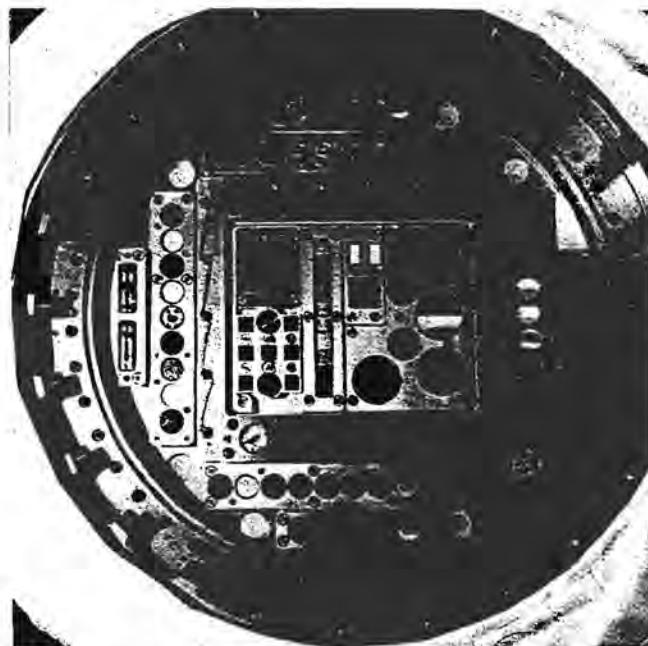


Fig. 7. The LDCE-1/HVI experiment as mounted on STS 46.

The IOCM has successfully flown on four shuttle missions, the two most recent being STS 32 and STS 44.

Although the primary objective of the IOCM on STS 32 and STS 44 was to verify the effects of the space environment on the cargo element, a secondary objective was to sample the LEO space debris and micrometeoroid complex using an array of passive sensor experiments. An additional design goal for these experiments was to test the survivability of thin-film sensors with a thickness of less than 750 Å.

The Limited Duration Space Environment (LDCE) Candidate Materials Exposure experiment was launched on STS 46. LDCE-1 and -2 were mounted in GAS canisters with door assemblies. LDCE-3 was mounted on the top of the Space Complex Autonomous

Payload (CONCAP). Figure 7 depicts the layout of the LDCE-1 exposure plate after integration into the GAS canister. The GAS canisters were located in Bay 13 of OV-104. The samples mounted on LDCE-3 were exposed for the entire duration of the mission. After the door assemblies of GAS canisters open, the samples mounted in the LDCE-1 and -2 were exposed for 40 hr. The exposure occurred toward the end of the mission, near 200 km, with a continuous payload bay attitude into the velocity vector. The LDCE experiment flew principally to understand the influence of atomic oxygen on materials. Our array of sensors was uniquely designed for the detection of hypervelocity impacts (HVI).

The LDCE-1 HVI package contained an Au foil (nominal  $T_f \sim 4.0 \mu\text{m}$ ) that covered a low-density micropore foam. Similar foams had been used on past missions to collect hypervelocity particles intact. A similar piece of Au foil covered a highly polished Al strip coated with vacuum deposited Au. This aided in the understanding of the distribution of ejecta material. Also included was a thin Al film (nominal  $T_f < 500 \text{ Å}$ ) stacked above a coated substrate. It was hoped that an estimate of the trajectory of grains within the experiment could be derived from the analysis of penetrations made in the thin film and impact sites (these data have not yet been reduced). The last group of passive sensors were high-purity metallic surfaces used for the collection of grains down to submicrometer size.

The LDCE-1 and -2 Al films, with a total surface area of  $3.24 \times 10^{-4} \text{ cm}^2$ , should have experienced 5.2 particle impacts in 10 days while in LEO. This estimate was based on Pegasus data published in 1970. Using a foil thickness of  $7.24 \times 10^{-5} \text{ cm}$ , a density of  $2.8 \text{ g/cm}^3$ , and a velocity of  $7 \text{ km/s}$ , the minimum mass that could penetrate the thin film was calculated. The thin films could be penetrated by a grain that possesses a mass greater than a picogram.

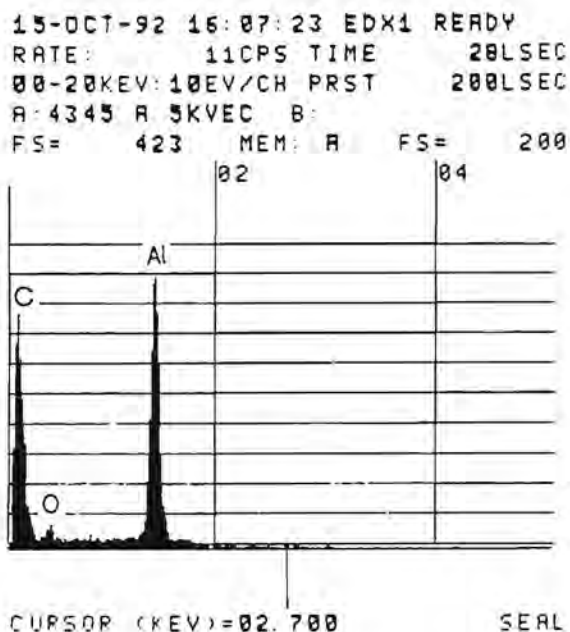
**EURECA Experimentation:** As a consequence of the experimental data developed during both recent and earlier STS missions and the data expected from this mission, the authors have produced and delivered an experiment for the European Space Agency, European Retrieval Carrier (EURECA). The HVI experiment was flown as part of the TICCE experiment. The EURECA payload was launched on OV-104 (Atlantis) on 31 July, 1992, providing a total mission exposure of nearly 11 months.

**Objectives of the TICCE/HVI Experiment:** The primary objectives of the experiment are to (1) Examine the morphology of primary and secondary hypervelocity impact craters. Primary attention will be paid to craters caused by ejecta during hypervelocity impacts on different substrates. (2) Determine the size distribution of ejecta by means of witness plates and collect fragments of ejecta from craters by means of momentum-sensitive micropore foam. (3) Assess the directionality of the flux by means of penetration-hole alignment of thin films placed above the cells. (4) Capture intact the particles that perforated the thin film and entered the cell. Capture media consisted of both previously flight-tested micropore foams and aerogel. The foams had different latent heats of fusion and, accordingly, will capture particles over a range of momenta. Aerogel was incorporated into the cells to determine the minimum diameter that can be captured intact.

**Data Analysis and Expected Results:** Primary analyses will be performed using a scanning electron microscope (SEM) outfitted with a Princeton Gamma Tech (PGT) elemental analysis system (Be window). Since each unit cell will be  $\sim 10 \text{ mm}$  square, samples will be easily prepared for viewing in the SEM. The SEM is sufficiently large to support the viewing of 5-cm substrate material.



Fig. 8. Irregularly shaped  $\text{Al}_2\text{O}_3$  captured particle (STS 44).



Count of hypervelocity impact craters on the witness plates with diameters larger than  $4\text{ }\mu\text{m}$  will be accomplished by the use of SEM photographs. Once digitized by means of a high-resolution optical scanner, these data will be analyzed using a hypervelocity impact morphology system.

Analysis of the substrate will be of particular importance. The same procedure outlined above to analyze the witness plates will be applied to the substrate. Of primary interest will be the recovery of data concerning the effects on the substrate's optical properties, which have been subjected to primary and secondary hypervelocity impacts. Also recoverable from the substrate (and perhaps the witness plates) will be data pertaining to the fragmentation of grains by the thin films.

Principal theoretical analyses will be conducted using hydrocodes to establish the limiting mass that will penetrate all, two, or only one of the thin films. Comparisons of the computational results with experimentally derived parameters will be carried out.

Based on the present knowledge of the space debris and micrometeoroid fluxes, all cells should be penetrated by grains with the properties  $m_p = 3.4 \times 10^{-13}\text{ g}$ ;  $r_p = 3.8\text{ g/cm}^3$ ;  $v_p = 7.00\text{ km/s}$ ; thus,  $r_p = 0.3\text{ }\mu\text{m}$ .

Since EURECA was in orbit for approximately one year, there should be  $\sim 50,000$  impacts/ $\text{m}^2$ ; with  $100\text{ cm}^2$  ( $1.0 \times 10^{-2}\text{ m}^2$ ), the HVI experiment should expect 3.75 impacts/cell from grains this size and larger. In addition to the 200 unit cells, the HVI contains high-purity metallic surfaces plus  $200\text{ cm}^2$  of micropore foam.

**Summary:** The experimentation on the shuttle (1983–1993), although snapshots in time, has yielded interesting data. One of the more salient results suggest that the smaller particles,  $10^{-4}$  to  $10^{-2}\text{ cm}$  diameter, have a much higher flux rate ( $\sim 2$  orders of magnitude) than previously considered. Another interesting result of the long-term study, irrespective of the high uncertainty, suggests that the growth in this size range is approximately 6% per year,



Fig. 9. Intact captured  $\text{Al}_2\text{O}_3$  particle with EDS spectra (STS 44).

whereas the growth of the  $10^{-2}$ - to  $10^{-1}\text{ cm}$ -diameter size is approximately 2% per year. LDEF, unfortunately, due to its extended stay on orbit, could not provide population growth data.

The research program also developed/modified a family of materials useful in intact capture particle studies. A reasonable number of particles (250) have been captured intact using micropore polymeric foams. Four bonafide IDPs have been captured and returned intact.



Fig. 10. A second irregularly shaped  $\text{Al}_2\text{O}_3$  particle (STS 44).

The passive space debris/micrometeoroid sensors suggest a flux of  $0.2 \times 10^2$  impacts/ $\text{m}^2$  occurred during the STS 32 mission (7 days duration). The average diameter of the perforations was  $\sim 12.5 \mu\text{m}$ . The largest perforation measured was  $65 \mu\text{m}$ .

STS 44 has proved to be one of the most interesting HVI experiments placed on the shuttle. During the course of the STS 44 mission, the space shuttle corrected its altitude by 26 km to evade a spent upper stage. The object, which was slightly outside the given collision ellipsoid, was determined to be the Kosmos 851 rocket body. Kosmos 851 was launched on 27 August, 1976, into an  $81^\circ$  inclination orbit. The results of our data suggest that a cloud of irregularly shaped particles, most of which were aluminum oxide, impacted the shuttle during the mission (Figs. 8–10). Data also suggest that the associated debris cloud caused a nearly 2-order-of-magnitude increase in flux over the background flux typically experienced.

Other major impacts on STS 44 were primarily due to low-velocity, low-density substances. Investigation of these sites revealed no hypervelocity impact features and only slight evidence of residual materials left by the impactor. Shallow and wide impressions in the films were seen immediately adjacent to the perforation sites. The morphology of these sites suggests that low-density material formed the impressions. It is thought that the impacts came from water ice dumped by the shuttle. Water and waste dumping from the orbiter have been observed contributing significant amounts of gaseous and particle contaminants. These materials and the propulsion contaminant mass remain near the orbiter for some time before they disperse.

Very preliminary data from STS 46 suggest that nine impacts and perforations occurred during the mission. One of the particles captured intact has tentatively been identified as an IDP.

**“Quick-Look” Results from EURECA:** Data from the two-dimensional computer simulations of hypervelocity impact events for the TICCE/HVI thin films conform to a high degree with the Carey, McDonnell, and Dixon (CMD) equation for all densities tested.

Early examination of the aerogel samples flown on the EURECA TICCE exhibit signs of shrinkage ( $\sim 6\%$  in both length and width). Recovery as a function of time will be monitored.

Visual impacts were observed in the deceleration films covering the polymeric foam capture cell experiments. Work is proceeding to analyze the perforations and remove the grain.

**Conclusion:** The proposed underdense foam capture cell experiment has the capability to capture intact cometary grains. More importantly, the techniques to remove the particles have been developed over 10 years of research. This experiment, when flown in concert with the other instruments in the CCSR package, will permit an in-depth understanding of cometary composition.

**References:** [1] Brownlee D. E. et al. (1976) *NASA TMX 73*, 152–168. [2] Bibring J.-P. et al. (1985) *LPS XVI*, 55–57. [3] Tanner W. G. et al. (1994) *Int. J. Impact Eng.*, in press. [4] Maag C. R. and Linder W. K. (1992) *Hypervelocity Impacts in Space* (J. A. M. McDonnell, ed.) 186–190, Univ. of Kent. [5] Maag C. R. (1987) *JPL Task 80-1547A*.

**SPICE: AN INNOVATIVE, FLEXIBLE INSTRUMENT CONCEPT.** K. Nishioka<sup>1</sup>, D. P. Cauffman<sup>2</sup>, B. Jurcevich<sup>2</sup>, D. J. Mendez<sup>2</sup>, and J. T. Ryder<sup>2</sup>, <sup>1</sup> SETI Institute, Mt. View CA 94043, USA, <sup>2</sup>LMSC, Palo Alto CA 94304, USA.

**Introduction:** Studies and plans for orbital capture of cosmic dust and interplanetary dust particles (IDPs) looked very bright with the advent of space station *Freedom* (SSF) and formal selection of Cosmic Dust Collection Facility (CDCF) as an attached payload in 1990. Unfortunately it has been downhill since its selection, culminating in CDCF being dropped as a attached payload in the SSF redesign process this year. This action was without any input from the science or cosmic dust communities. The Exobiology Intact Capture Experiment (Exo-ICE) as an experiment on CDCF was also lost. Without CDCF, no facility-class instrument for cosmic dust studies is available or planned.

When CDCF (and Exo-ICE) was selected as a SSF attached payload, an exercise called the small particle intact capture experiment (SPICE) was started for Exo-ICE to develop an understanding and early testing of the necessary expertise and technology for intact capture of cosmic dust and IDPs. This SPICE activity looks to fly small, meter square or less, collection area experiments on early orbital platforms of opportunity such as EURECA, MIR, WESTAR, and others [1], including the shuttle. Orbital stay times ranging from three to six months were shown to be adequate by a dust frequency/collection abundance analysis [1]. The necessity for uncontaminated dust samples, and particularly organically pristine samples for exobiology, is dictated by the science community. Pristine uncontaminated samples guarantee that any presence of chemicals and compounds, including organics that are detected in the captured dust particles, can be ascertained precisely. This precision in analyses of abundance and format is critical to inferring their possible contribution to the formation of the solar system or to the beginnings of life. Current sample sources from the Arctic and Antarctic glaciers, surviving meteorites, and stratospheric air capture have provided abundant samples; unfortunately all these samples suffer contamination from the Earth's atmosphere, the ice, or the capture process itself.

The SPICE activity has focused on developing techniques and



instrument concepts to capture particles intact and without inadvertent contamination. It began with a survey and screening of available capture media concepts and then focused on the development of a capture medium that can meet these requirements. Evaluation and development of the chosen capture medium, aerogel (a silicon oxide gel), has so far lived up to the expectations of meeting the requirements and is highlighted in a companion paper [2] at this workshop. Others such as McDonnell's [3] Timeband Capture Cell Experiment (TICCE) on EuReCa and Tsuo's [4] GAS-CAN lid experiments on STS 47 and 57 have flown aerogel, but without addressing the contamination issue/requirement, especially regarding organics. Hörz, Zolensky, and others [5] have studied and have also been advocates for its development. The SPICE instrument's experiment design builds on the knowledge gained from these efforts to meet the intact capture, noncontamination requirements. An overview of a possible SPICE experimental instrument concept using the MIR space station as a host platform for cosmic dust collection is provided in this paper. The SPICE concept is nonplatform-specific and can fly on any platform that provides a mode for experiment recovery.

**Science:** As stated earlier, the SPICE instrument's design requirements encompass the science requirements for the capture of intact (or nearly intact) uncontaminated space particles. An additional key science requirement has to be the early and continuing access to space and return of samples. The SPICE concept also provides this capability. Three primary science disciplines, planetary, exobiology, and space debris, have interest in orbital capture and study of dust particles and are expected to be the primary beneficiaries of the SPICE concept. Basically the planetary science discipline is interested in capturing pristine primitive space dust to determine the prehistoric cosmic chemical makeup that will perhaps help unravel the mystery of the Sun and the solar system formation, whereas the exobiology science community, as stated above, is interested in investigating primitive bodies to find fundamental data on the biogenic elements and compounds, the precursors to the formation and beginnings of life. The space debris science community's interest is the long-term detailed observations to determine the evolution of manmade space debris and to infer their impact on the space environment and the potential hazards that they signify for space operations of both manned and unmanned orbital space platforms.

**Mission/Instrument Description:** The mission/instrument conceptual design was worked out by a SETI Institute/LMSC collaboration where the objective was to assemble an instrument concept that will meet the science requirements and also meet the constraints of a typical space platform. The choice of platform for this exercise was the MIR space station. Also, it was required that the concept be low cost, technically doable, and capable of exploiting several different space platforms with a high probability of successfully capturing and recovering uncontaminated nearly intact space particles. An innovative flexible concept, the mission scenario is illustrated in Fig. 1. For this exercise, the assumptions were made that the necessary arrangements to use/fly on the MIR platform and use of the Soyuz launch capsule have been worked out, and that the space shuttle will dock with the MIR station and be available to transport the SPICE experiment back to the ground.

**Mission Description:** The SPICE instrument package/experiment will be developed and assembled by a SETI Institute-LMSC team, managed by a NASA/ARC Principal Investigator, with sci-

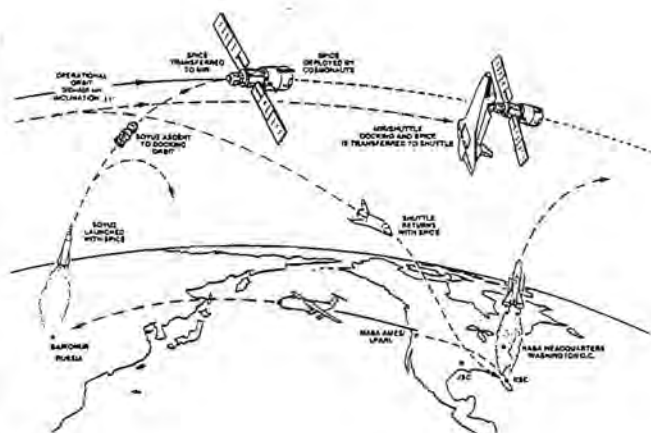


Fig. 1. Scenario.

ence collaboration and guidance from a science working group composed of scientists from, for example, ARC, JSC, industry, and the academic community under the PI's leadership. Once fabricated and flight qualified, the instrument will be transported by aircraft to Russia and integrated into the Soyuz capsule for transport to the MIR station. Upon arrival on MIR, the instrument package will be taken to the external attach point, and attached via quick connect/disconnect clamps to MIR; the external shipping container (cover) will then be removed, the capture trays manually deployed (the procedure can be automated, but for safety the initial deployment will be manual), and the electronics for the instrument activated. For three to six months the instrument will passively capture and record particulate impacts and other necessary parameters for particle identification. At the end of the exposure period the instrument will be deactivated, folded, cover emplaced, secured, the external attachment clamps released, and the instrument package transferred to the space shuttle for transport back to KSC and ultimately to the science PIs.

**Science Requirements:** The system or instrument concept design requirements used were flowed down from the following science requirements: (1) There will be no contamination of the particles during capture through laboratory recovery, analysis, and archiving; (2) particles will be captured nearly intact, which means that a major part of the particle will remain pristine and not undergo physical or chemical alteration; (3) the particles will be time- and coordinate-tagged so that each particle can be identified; (4) velocity of impact and mass of the particles will be inferred at least at the order-of-magnitude level from the acquired data; (5) where possible, the particle trajectories will be inferred via their tracks in the aerogel and other acquired data; (6) particles at velocities  $\geq 10$  km/s will be captured if possible; and (7) particles 1  $\mu\text{m}$  or larger, up to 1 mm, will be the primary capture sizes of interest. These requirements were used in concert with the space platform constraints for the conceptual design.

**Space Platform (MIR) Constraints:** The Russian MIR space station has adequate external capability to host a 1-m-square SPICE instrument. It is expected that the environment around the MIR station will be fairly high in manned contaminants. Recovery of the

instrument and analysis of the capture medium surface should provide an indication of the acceptability of samples obtained from MIR and for its hosting future particulate capture missions. Practical constraints on the use of the MIR and Soyuz infrastructure indicate that, if possible, the instrument should be self-contained for instrument control and data capture electronics, as well as for power. Physical size is limited by the Soyuz capsule hatch diameter of 75 cm, and mass must be easily handled by one astronaut. Recovery of the instrument by the Soyuz capsule is not feasible for two reasons: (1) The down-payload capability is limited and not advised and (2) Soyuz lands vertically by parachute on land and impact g's can be high, and special recovery load attenuation devices for the aerogel will be required.

**SPICE System Design Requirements:** The primary requirement is that the design be flexible so the resulting instrument will be platform friendly, low cost, and capable of accommodating improved or additional sensors. Design requirements will be (1) It will be self-contained for electrical power, instrument control, and data capture. (2) The packaged dimension of the instrument will be no larger than 70 cm in diameter and about 1 m long. (3) The mass of the integrated package will be less than 100 kg. (4) The capture media package will use aerogel of high purity [organics < 1 ppm and total carbon (TBD)] to meet the science capture requirements of noncontamination; particle capture parameters to be measured will include the time and location of impact, impact velocity, and mass to be inferred by the location sensors with the physical evidence of the particle track. In addition, the particle trajectory will be inferred by its track in the aerogel together with other collected data. (5) The instrument package during transport will be protected from contamination by use of microsieves in the cover as ambient pressure is maintained. (6) The instrument particle capture area will be about 1 m<sup>2</sup>. (7) The instrument will be capable of either manual or automated deployment and folding once attached externally to the host platform. (8) The instrument package will be designed to withstand the launch and recovery loads for the space shuttle and Soyuz launch loads. (9) The instrument design will comply with all NASA safety, reliability, and quality assurance requirements, as well as those required for Russian Soyuz/MIR payloads. The overall schedule for design, fabrication, system testing, and integration will be no more than 18 months and may be as short as 12 months. Costs will be minimized by using proven technology and space system fabrication techniques.

**Conceptual Instrument:** Figure 2 shows the overall instrument in the deployed and transport mode, folded and packaged. The transport container provides for pressure equalization, but with a microsieve to ensure that contaminants are kept out of the instrument and vice versa. As stated earlier, the instrument package for transport is 70 cm in diameter and 1 m long. It is expected that the package will be attached to the orbital platform in the folded transport configuration. When attached to the platform, the cylindrical cover can be removed by unlocking the storage latches shown and placing the latches in the stored position. The instrument contains the aerogel collection media neatly compartmentalized in 16 containers packaged 4 to a tray. The electronics for data capture and the batteries for the electronics are contained in sections in the bottom of each tray. Sensors for the time of impact and location of impact are the two dimensional grid work seen in Fig. 2. The sensor grid wires for the x and y coordinates are separated by a centimeter from each other and the wire spacings are also a centimeter apart.

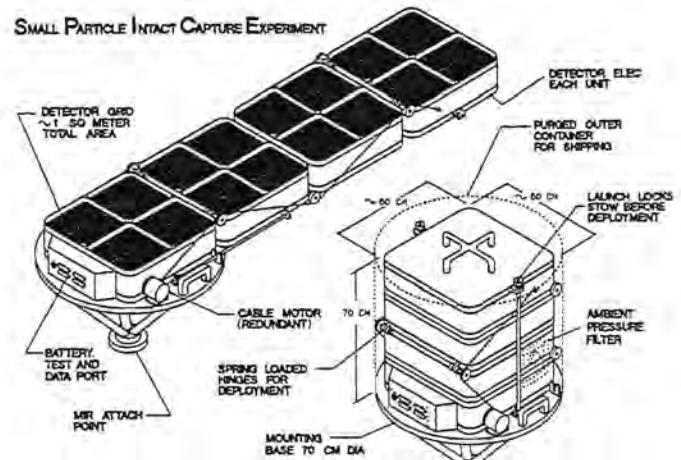


Fig. 2. SPICE instrument concept.

Other sensors such as particle trajectory and mass sensors will be integrated into the instrument as they become available. The instrument is made up of four nearly identical self-contained trays; each tray measures approximately 48 × 48 × 20 cm (provides approximately 0.25 m<sup>2</sup> of capture surface) and is divided into four sections of aerogel, 24 × 24 × 15 cm. With each tray being self-contained, quadruple redundancy effectively results for the instrument. The outer three trays are hinged as shown so that they fold neatly into a single unit on top of the fourth tray. Hinges are spring loaded so that deployment is always assured with two electric drive motors providing for the slow and gentle deployment as well as for folding the trays slowly for storage and transport back to Earth. Provisions will be made to allow for manual deployment of the trays.

All structures will be of aircraft-grade Al, probably 7075 T-6, and the electronics will be powered by surplus Galileo batteries. VLSI microelectronics [6] will be used to minimize power consumption, mass, and size of the electronics for SPICE. This will ensure that batteries will be feasible even for six-month missions.

**Schedule:** A strawman schedule to meet the development time constraint for the space shuttle/MIR docking experiment was developed and is shown in Fig. 3. This is an ambitious schedule timeline and based on conducting the design, reviews, fabrication, test, and shipment with minimum bureaucracy, and the project manager and team empowered with all decisions pertaining to the project and working as a unit. This schedule was reviewed by a team of senior managers and found to be doable. The SPICE instrument as described here is simple, and that may be the key that will allow this schedule to be met. Effectively it allows a year to design, fabricate, test, and ship the finished instrument.

**Prospective Orbital Platforms:** The near-term prospective platforms are the Russian MIR space station, Germany's EURECA free-flyer orbital platform, and the space shuttle. Space station *Freedom* is a future possibility, but it looks like it will not be available before 2000 A.D. WESTAR, a commercial orbital free-flying platform by Westinghouse Corporation, now looks doubtful.

Each of the three near-term potential platforms have issues that must be resolved before they can be used to host SPICE. MIR has two key issues associated with its utilization: (1) It is not readily

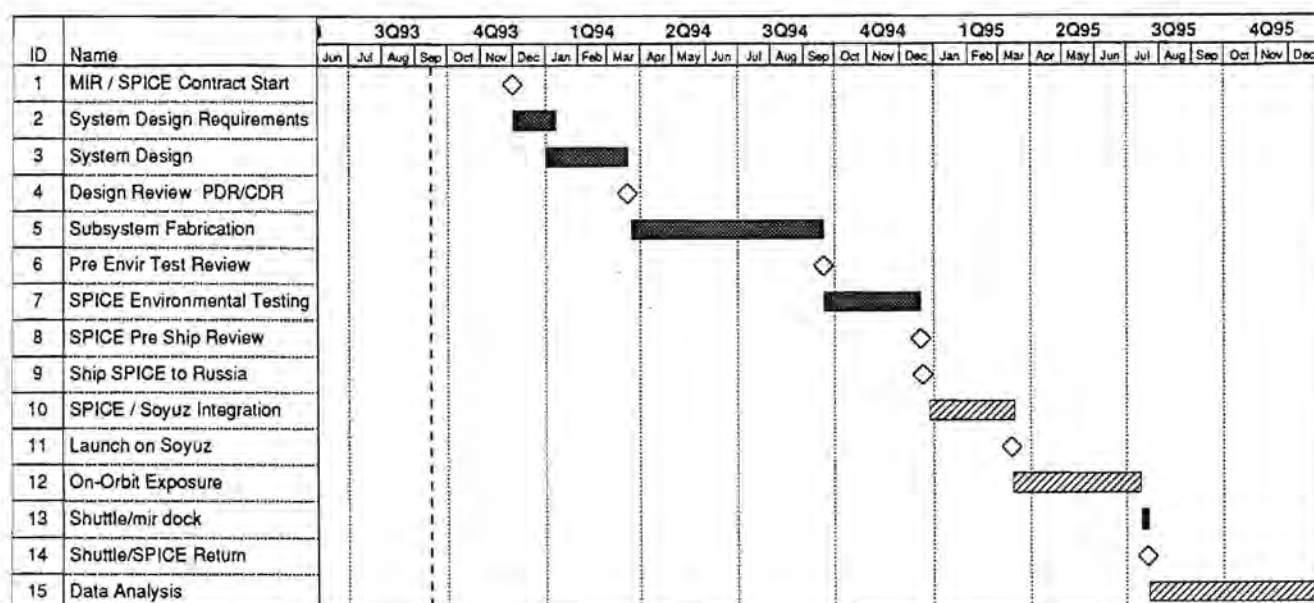


Fig. 3. Schedule of SPICE program.

available since it use requires an international agreement and (2) the Russians have very little down-payload capability in their space station transportation infrastructure. Pluses are that MIR can readily accommodate SPICE, and the Russians at the technical level appear very willing to work together to make it happen [7].

EURECA had a very successful first flight lasting a year from June 1992 to July 1993. Unfortunately, due to funding shortfall, the German government in the spring of 1993 declared that the second and third flights would be shelved. The situation has not changed officially, but the community is hopeful that a second flight will be reestablished for flight in 1995 or 1996. SPICE was originally accepted by EURECA for its second flight.

The space shuttle could be used as an orbital platform for SPICE if the science community is willing to accept collection periods of a week to two weeks integrated over many flights to obtain the total exposure time of three to six months. A major issue is the potential of not obtaining an acceptable cross-sectional sample of the space particulates and storage of the instrument between flights with assured integrity that the particulate samples already collected will not be compromised. A potential solution to the storage issue is to harvest the aerogel after each flight, but this introduces another issue, that of additional volume of material handling both for harvest and replacement. Also, the hardware will require cleaning before new aerogel and new sensors are integrated into the instrument, and system testing will have to be performed. This will add cost.

**Future Tasks:** As already stated and inferred, the science requirements are substantially defined and an instrument can be designed and fabricated to meet the requirements outlined in this paper. Once the instrument is designed and fabrication begins, it will be costly and probably impossible to accommodate running changes to meet changing requirements while maintaining schedule; thus, it will be imperative for the science community to provide precise requirements/specifications for organic and other contaminants (is it ppb or sub-ppb or ppt?) and also requirements/specifi-

cations for sensor parameters (time of impact, location of impact, trajectory, etc., and required measurement accuracies) and their priorities.

**References:** [1] Swenson B. L. (1992) *SAIC Report No. 92/1008, Vol. II*. [2] Mendez D., this volume. [3] Timeband Capture Cell Experiment (TICCE) on EURECA 1, Principal Investigator J. A. M. McDonnell, University of Kent (UK). [4] Tsou P. et al. (1988) *LPS XXIV*. [5] Barrett R. A. et al. (1992) *Proc. LPS, Vol. 22*, 203-212. [6] Voss H. D. et al. (1993) NASA Small Instrument Workshop. [7] MIR Space Station Symposium (private communications with L. A. Gorshkov), Herndon, VA, July 27-28, 1993.

**CHARGE COLLECTION DURING HYPERVELOCITY PENETRATIONS OF THIN FOILS.** R. Peterson, 3738 Arnold Drive, Houston TX 77005, USA.

The following represents trajectory sensor development work for the space-station-based Cosmic Dust Collection Facility (CDCF). This facility-class payload was to expose some 7 m<sup>2</sup> of NASA-provided general-user instruments in addition to three instruments provided by formally selected principal investigators. The preferred trajectory sensor for this general-user instrument envisioned the detection of impact-triggered plasma for both velocity measurement and location instruments.

Space station developments in late 1992/early 1993 lead to cancellation of this potential flight project, for both technical and fiscal reasons. This precipitated termination of all plasma detection work at JSC on behalf of CDCF's general-user instrument.

The following comprises three informal reports that summarize the CDCF efforts regarding plasma sensing for trajectory determinations. The reports were initially written for internal CDCF use and were not widely distributed. Because no formal publications are envisioned at present, the three reports are included in full in this document. They not only demonstrate that substantial progress was



accomplished in the development of plasma trajectory sensors during 1990–1992, but the results are hopefully of interest and use to others who may continue these developments. The chronological sequence of these three reports is reversed, with the first containing the latest information.

**Charge Collection Near the Hypervelocity Penetration of Thin Foils—Efforts to Develop a Velocity Detector for CDCF:** This report describes recent experiments using a light gas gun to test a prototype two-plane thin-foil velocity detector. The goal was to determine its capabilities in measuring projectile velocity and the location of the penetration of each foil. Figure 1 shows that each foil plane is identical, having a set of X and Y charge collection wires (the Y wires spaced 2 mm behind the X wires to prevent contact). The wires are spaced 1 cm apart and the first wire plane is 1 cm behind the foil. The two foil planes are separated by 30 cm. In most of the tests reported here, the wires were biased +40 V with respect to the 0.8- $\mu$ m-thick Al foil. All projectiles are 1/8-in-diameter glass spheres (1 mm spheres are just now being successfully launched again with this experiment in the target chamber). The projectile velocity is 6 km/s unless otherwise stated (see Fig. 3). Most data have been taken using 125- $\mu$ m-diameter W collection wires, although one graph shows the results of varying wire diameter from 50 to 1000  $\mu$ m (Fig. 2).

Before inserting the two-plane prototype, a single plane of vertical wires was used (with the same 1-cm geometry) to get preliminary data on the spatial resolution properties of this scheme. Typically, the current to six wires was recorded, along with the current to the penetrated foil and the output of a photodiode looking at the input side of the foil. The currents were indicated by the voltage across a 50-ohm load and were recorded on a set of four Tek 2232 2-channel digital oscilloscopes. Records contained 4096 samples (8 bits deep) taken at 0.2- $\mu$ s intervals.

This single, vertical wire plane was used for many shots to determine approximately what spatial resolution is possible. It was already known that the plasma/debris cloud produced behind the foil can be quite wide. Figure 2 shows a plot of charge collected from the wires vs. the distance from the wire to the foil penetration (measured perpendicularly from the path). The charge was obtained by numerical integration of the current signals. Figure 2 indicates that the location of the penetration can be located within approximately 1 cm. This implies that the resolution can be improved by decreasing the distance from the wires to the foil (which would also require more wires). The larger-area wires collect more charge, presumably because they intercept more of the foil debris, which

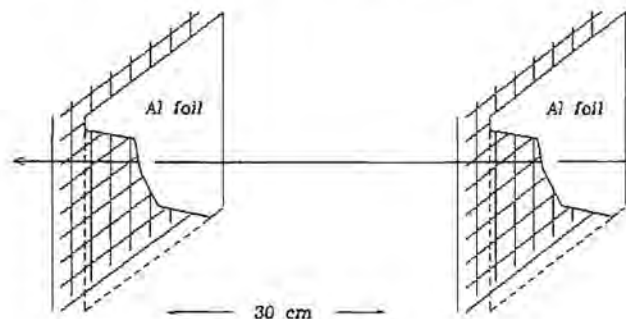


Fig. 1.

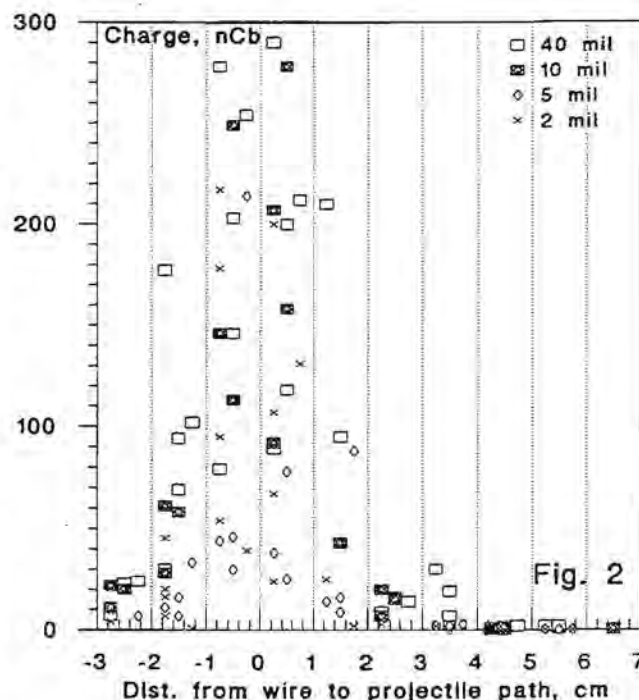


Fig. 2. Charge to variously sized wires biased +40 V, 1 cm behind 0.8- $\mu$ m Al foil penetrated by 1/8-in glass sphere. Velocity: 6 km/s (CHGPLT).

creates local plasma upon impact. The larger wire would also collect more charge from the original projectile/foil plasma as it sweeps through the region of the wires. The relative contribution from each of these two sources of charge is unknown. Figure 4 shows a typical event where wires farther from the projectile path collect charge at later times. The velocity of the debris/plasma is near the projectile velocity (6 km/s here). A careful look at Fig. 4 shows tiny signals due to the impact "flash" that are almost simultaneous with the photometer signal. These flash signals (more clearly seen with smaller particles in accelerators) would be great for timing, but much less useful for spatial information. Figure 3 shows similar data as in Fig. 2, but here the vertical scale is logarithmic and the variations in projectile velocity are highlighted.

Next, the two-foil-plane system was put in the target chamber. In order to test a simplified data gathering scheme, an analog multiplexer (MUX) and its associated timing circuitry was installed near the frame, one for each of the two-foil planes. Figure 5 shows a schematic of the integrators and the multiplexer, including all timers and comparators. The integrators were of standard design, the same as the very-low-noise designs used in the electrostatic accelerator tests. One change had to be made; the 1/8-in projectile produced currents to the wires on the order of 200 ma, greatly in excess of the current handling capability of integrated circuit amplifiers (20 ma maximum). The current had to be shunted and the current read as a voltage, which was then integrated. Figure 6 gives the modifications. Projectiles 1 mm and below can be dealt with using the standard integrator in Fig. 5.

A 16-channel MUX chip (DG506) was used so each of the 8 wire signals was applied to two inputs and the MUX timing provided 16 outputs when triggered. This yields two samples of each integrator output at times separated by 25  $\mu$ s. A simple short burst of charge

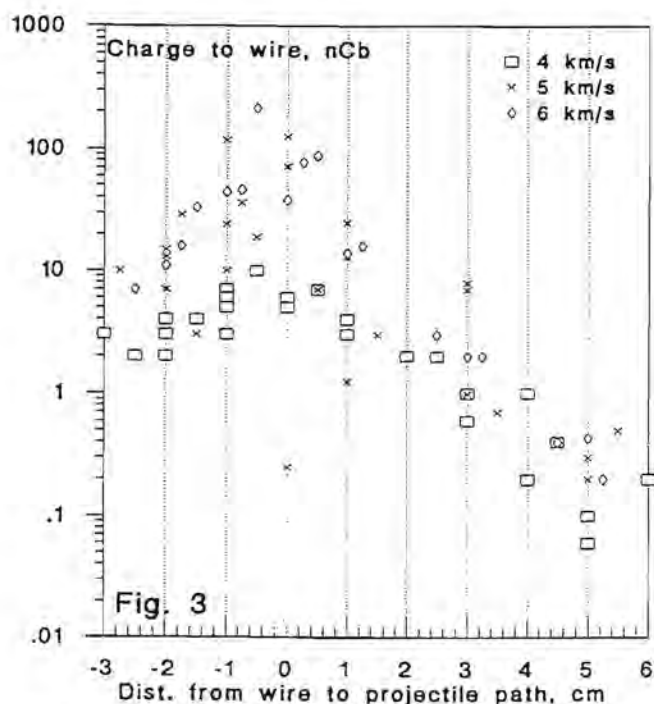


Fig. 3. Charge to 2-mm wires biased +40 V, 1 cm behind 0.8  $\mu$ m Al foil penetrated by 1/8-in glass sphere. Velocities as shown (456CHRG).

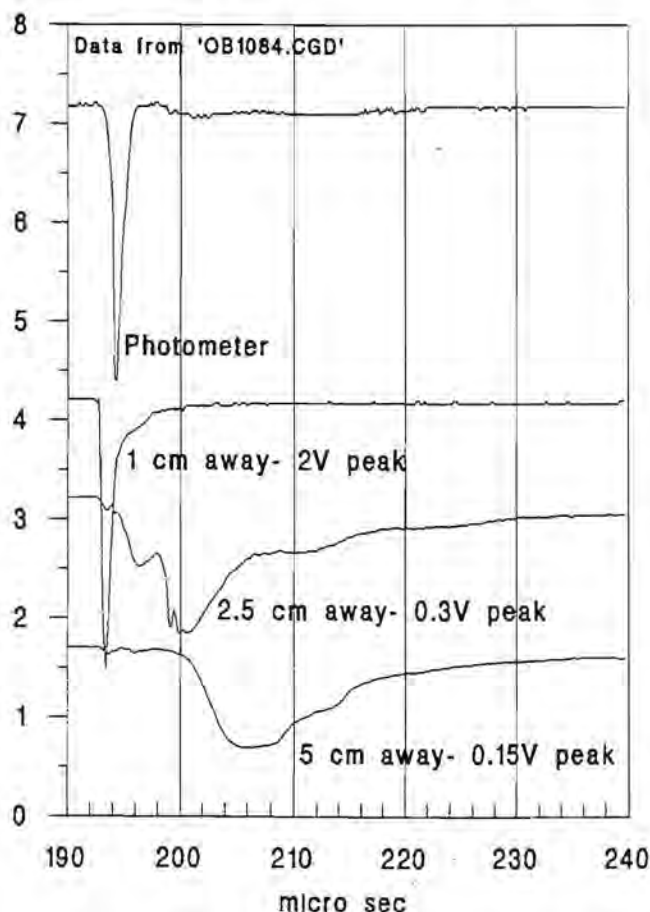


Fig. 4. Current to wires behind foil lag as distance to impact increases.

would be indicated by the two integrator samples being equal (seldom the case). Each foil plane had its own independent MUX and its output was recorded separately. The operation of the MUX system can best be understood by referring to Fig. 7 where the two signals at the bottom show the front and rear multiplexer outputs. The first positive-going signal is a timing mark inserted from the comparator, which triggers the timing circuit ("inserts time mark" labeled in Fig. 5). These timing marks are marked with dark arrows in Fig. 7. Note that the interval between these two MUX time marks is about 53  $\mu$ s, giving a little less than 6 km/s velocity over the 300-mm span between the foils. The MUX timing delays 10  $\mu$ s and then outputs channel 1 (wire #1), which is marked with the light arrows (the 8 channels are cycled through twice). The projectile struck very closely in the center between wires 2 and 3 and one can see that these two signals dominate the output. Essentially the same result is seen in the rear MUX except that the wire 3 charge is comparatively less than that of wire 2. The last two channels (7 and 8) are horizontal wires and will not be discussed farther. The front MUX shows the second data cycle with significantly greater signal than the first cycle. This appears to result from low levels of charge arriving during the 25  $\mu$ s between the two samples. For some reason, the rear MUX shows very little change between samples (more often than not, it drifts upward like the front MUX). The charge collected at the rear wires was consistently larger than that collected at the front and averaged a factor of 7 higher (in Fig. 7 the integrators driving the rear MUX had one-half the gain of the front; the rear charge is approximately 6 times larger than the front). Also note in Fig. 7 that the

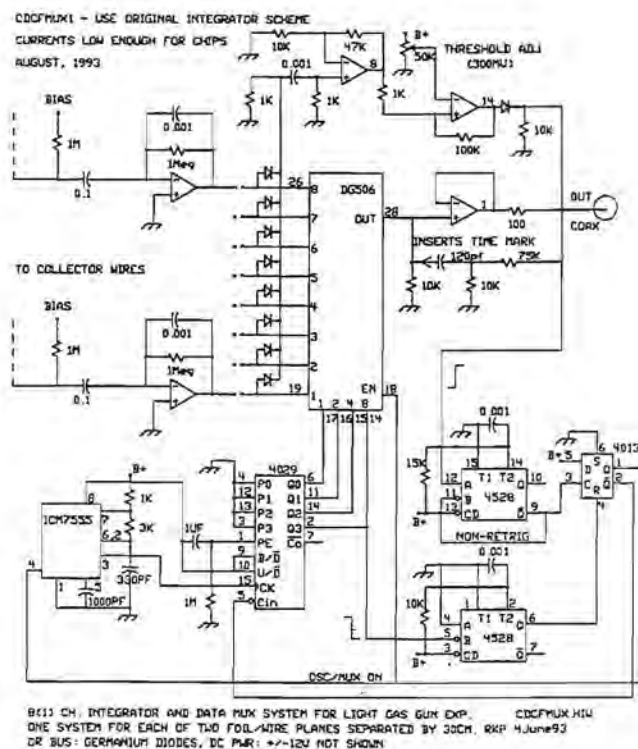


Fig. 5. Use of 1-mm projectiles drops peak currents below 20 ma where standard amplifiers can operate. Current integrator is used as in earlier dust accelerator experiments.

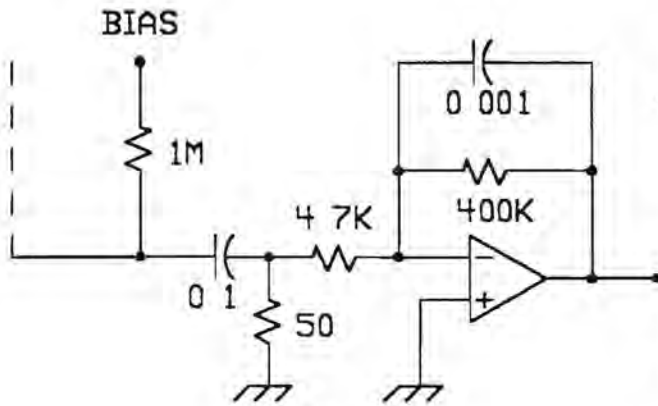


Fig. 6.

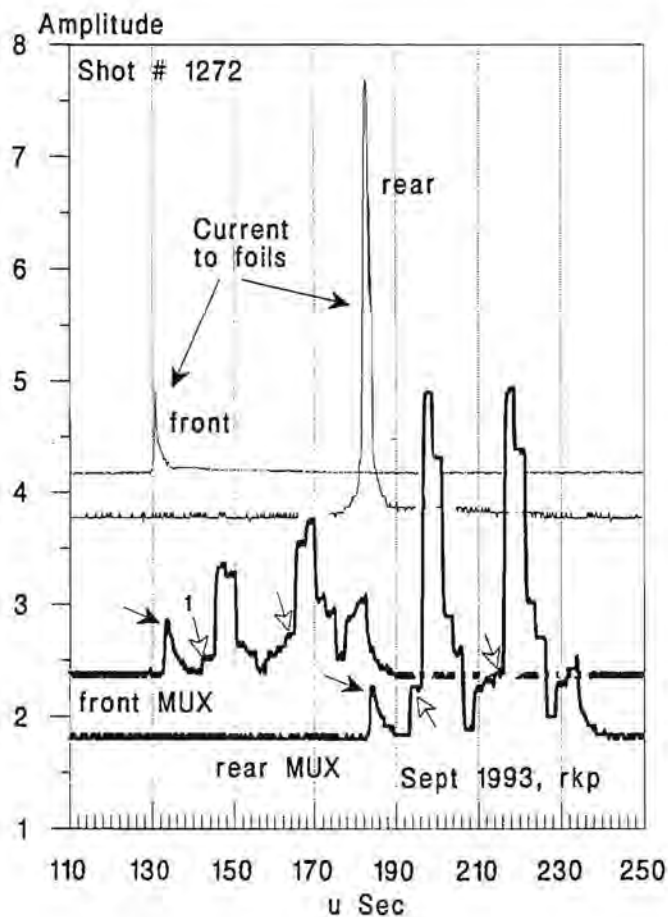


Fig. 7.

current to the rear foil is significantly larger than that seen at the front (top two traces). Since the geometry of the two planes is the same, the only known difference is that the projectile has been "excited" by penetrating the first foil. This initial shock apparently causes the second foil to produce a larger debris/plasma cloud. Witness plates show that the projectile is significantly more frac-

tured after penetrating the second 0.8- $\mu$ m-thick foil at 6 km/s. The spatial resolution obtained in the MUX experiments appears the same as seen in earlier non-MUX data (Figs. 2 and 3) and can be summarized as being roughly equal to the wire spacing  $s$ , when the wire plane is distance  $s$  behind the foil.

Figure 8 shows a comparison of the projectile velocities measured from the MUX traces vs. the average of the velocities obtained from the fixed gun instrumentation prior to projectile entry into the target chamber (several LED arrays occulted by the projectile). For some reason, the MUX velocities are 1–2% greater than the reference values. The source of this discrepancy has not been tracked down.

**Summary:** Experiments have been done using projectiles approximately 1–2 orders of magnitude smaller than the CDCF size range (dust accelerators: particles 0.1 to 1.0  $\mu$ m diameter iron spheres, 30 down to 3 km/s) and using projectiles near 2 orders of magnitude larger (light gas gun: 50- to 3200- $\mu$ m-diameter glass spheres at 5 to 6 km/s).

The following is a summary of the properties of signals seen by biased collection wires behind a penetrated foil.

1. Signal-to-biased wire has initial UV flash, followed by slower component (signal front traveling close to projectile velocity) with higher amplitude, which is due to charge from the expanding debris/

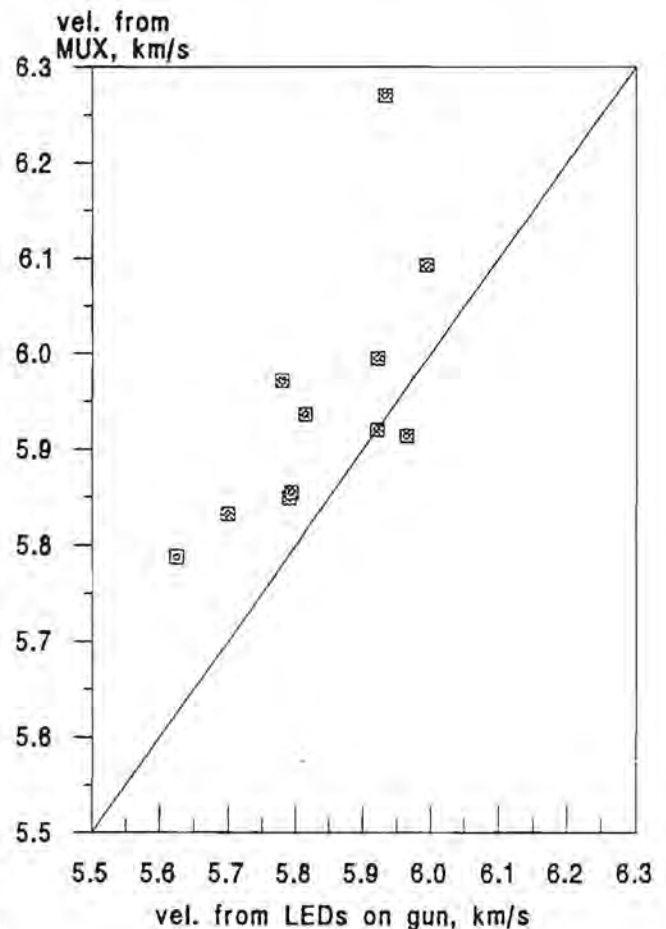


Fig. 8.



plasma cloud. The flash component is much more pronounced at high velocities (seen in dust accelerator experiments).

2. Charge collected at rear of foil scales with the mass of the exploded foil and velocity to the fourth power. At 6 km/s (a velocity used at both particle size extremes) collected charge/unit foil mass is approximately 50 Cb/kg with iron projectiles (near 1  $\mu\text{m}$  diameter) and about 6 Cb/kg with glass (1000–3000  $\mu\text{m}$  diameter) into Al foil targets. One big difference is that the projectile diameter/foil thickness ratio varies from about 10 to 3000 for the small and large projectile experiments respectively.

3. Collected charge is not a steep function of bias voltage. Signals increased very little at biases above 20 V.

4. A simple data system that measures the total collected charge from a crossed wire array behind a thin foil (data from light gas gun with large glass projectiles at 6 km/s) has the following properties: (1) Spatial resolution is approximately equal to wire spacing when wire is one wire spacing behind the foil; (2) resolution of the time of flight between two foil planes is approximately 0.2  $\mu\text{s}$ .

**Signals to Biased Wires Adjacent to a Thin Foil Penetrated by a Hypervelocity Particle:** These experiments began by using biased planar grid structures on both entrance and exit sides of the target foil. This required only two signal channels and maximized the charge collected. However, the only practicable collector scheme envisioned for CDCF uses thin wires suspended behind the target foil, two perpendicular sets of wires generating the location of a particle penetration. The first experiments using wires were done at LANL and a second (and largely unsuccessful) experiment was done at Concordia. This paper summarizes the results of the latest wire collector tests at Heidelberg, done since the December 1991 report (referred to here as HB3).

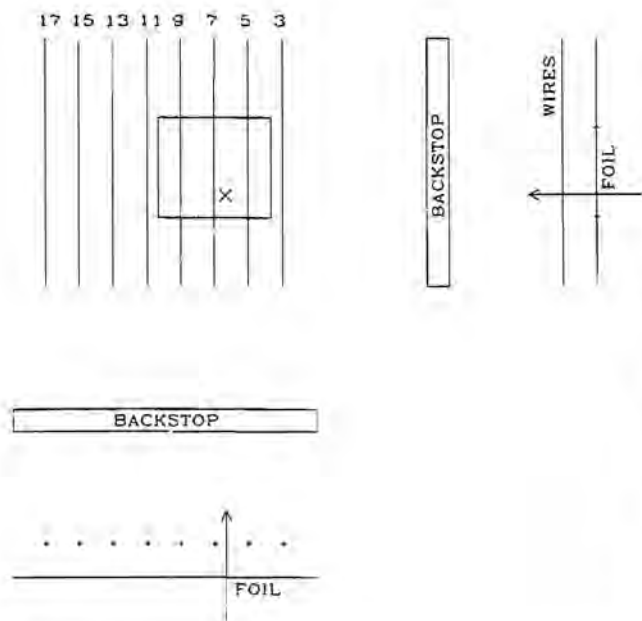


**Fig. 9.** HB3 foil and collector wire layout. Wires are 10 mm behind foil and 10 mm apart. Backstop is 44 mm behind foil. Foil is imbedded in metal plane to provide relatively constant E field in collection region.

Two Tektronix 2232 digital oscilloscopes were used to record the signals from four biased wire collectors placed behind an Al target foil. Data records varied from a total of 20–50  $\mu\text{s}$ , sampled at 25 and 10 megasamples per second respectively. Foil thicknesses of 200, 500, and 1000 Å were used. In these tests, 450 particle events were recorded and stored on floppy disks for later analysis.

The signal amplifiers are Amptek A-250 powered by  $\pm 6$  VDC batteries mounted onto the experiment frame inside the vacuum, no more than 5 cm from the end of the collector wires (stray capacitance was minimal, yielding lower ultimate noise level). The integrating amplifiers used 1 pf feedback and their gain was tested *in situ* to be such that 1 V out corresponded to a charge of  $10^{-12}$  coulomb.

The experiment arrangement is shown schematically in Fig. 9. Eight 125- $\mu\text{m}$ -diameter W wires labeled with odd integers 3 through 17 are 10 mm apart and 10 mm behind the target foil. Three different sets of four of these wires were used to provide the data signals from each penetration event. For the data presented here, the wires were biased at +190 V wrt the foil (ground). A solid Al “backstop” (same potential as foil) was 44 mm behind the foil. Since this backstop could not be avoided, it was used as a timing device to check the velocity figures obtained from the accelerator operator.

One phenomenon seen in previous tests was of particular interest (see Fig. 28): a sharp signal occurring almost instantaneously at all collectors at a time coinciding with the particle penetration of the foil (the “flash”). Much effort has been made to be sure that this signal is not an electronic artifact—it appears to be real. Because of the travel time differences to the various wires, it seemed that these signals could not be the result of charge from a plasma drawn to the wires by electric fields. A highly self-shielded plasma could pass through the electric fields from the wires closest to the penetration and then provide charge to a remote wire after the plasma density dropped, allowing the local fields to penetrate. This process would require a very measurable time delay—which is not seen. Therefore, in this series of experiments the apparatus was designed so that wires could be spaced a great distance from the penetration event to see just how far away the flash can be detected. If this flash signal amplitude does not drop as the distance is increased, it must be a spurious signal. The most distant collector wire in the HB3 tests is about 7 cm from the foil penetration (thus the maximum aspect ratio here is 7; the largest ratio in earlier experiments was about 2).

Figure 10 shows HB3 shot 260 where the particle struck the foil somewhere between wires 3 and 5. These are the signals one might expect if the world were as it should be: the charge collected at the wire closest to the impact is large, and the other wires collect progressively lower charge as one moves away from the impact (see Fig. 9 to review the wire locations). Unfortunately, things are not so simple, and shot 260 is the only one (in HB3 data) found with these simple characteristics. Figure 11 shows #184 where, again, the event occurs near wire 3. The wire 3 signal does not have the fast-rising leading edge—the “flash” as seen on wires 7 and 9—but does attain higher amplitude (the larger signal beginning at around 10  $\mu\text{s}$  into the record is due to the plasma ejected when the particle hits the solid Al backplate). The flash signal is apparently the same one seen in the LANL experiments and here it appears larger at the wire 3 cm away from the impact (wire 9)! This apparent increase in signal as one moves away from the event is what prompted placing wires much farther from the foil impact area. Figure 12, shot 236, was done with the same set of collection wires as Fig. 11, but here we see that the flash signal is much lower at wire 9 (the most distant from

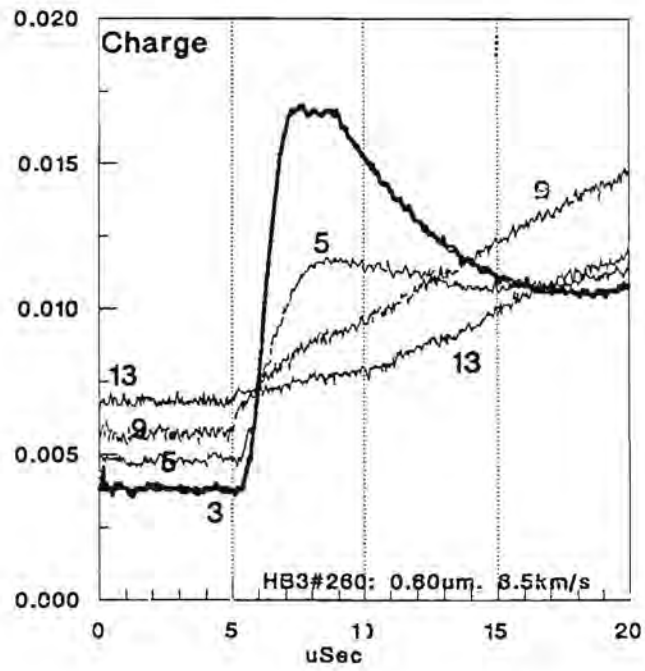


Fig. 10.

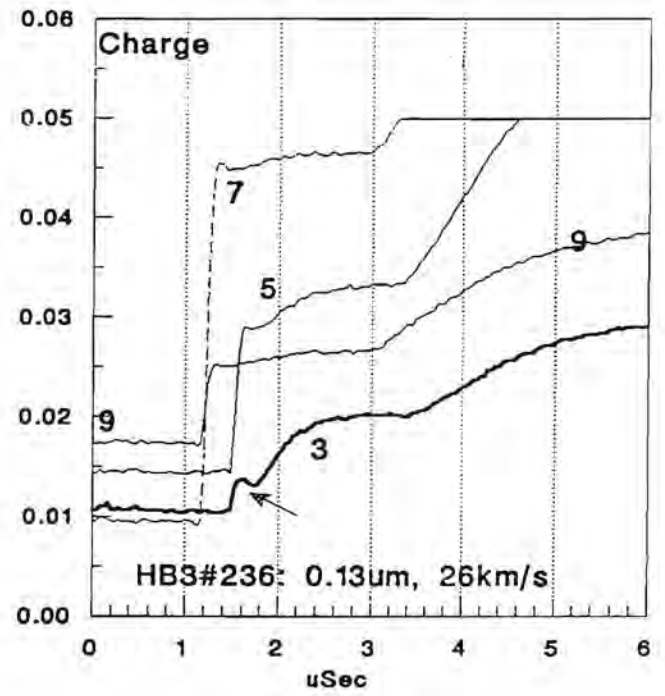


Fig. 12.

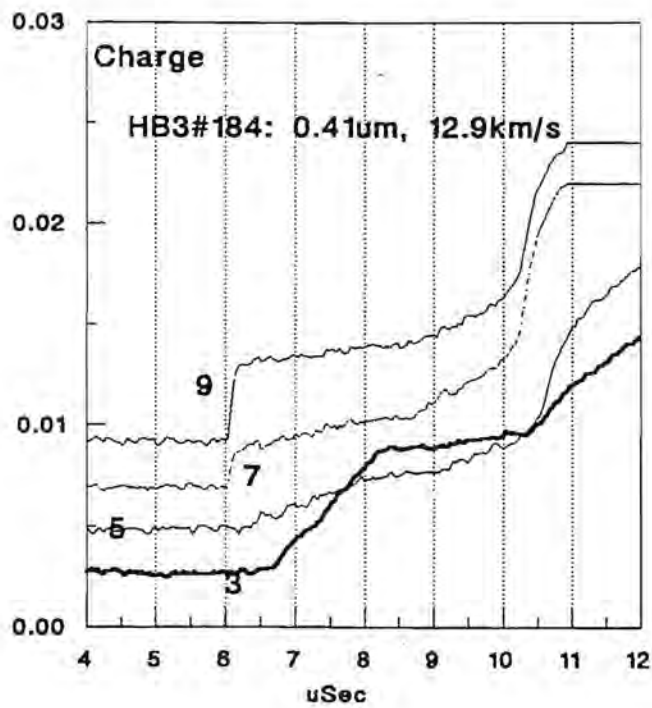


Fig. 11.

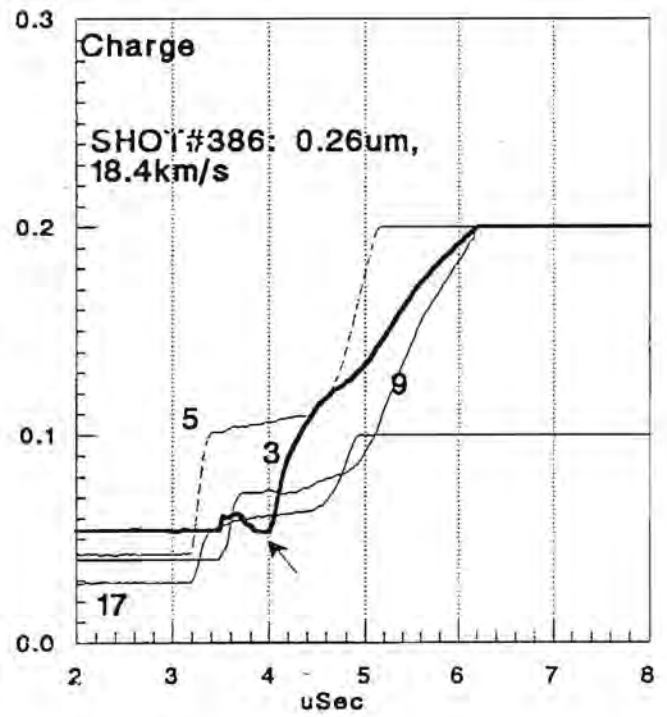


Fig. 13.

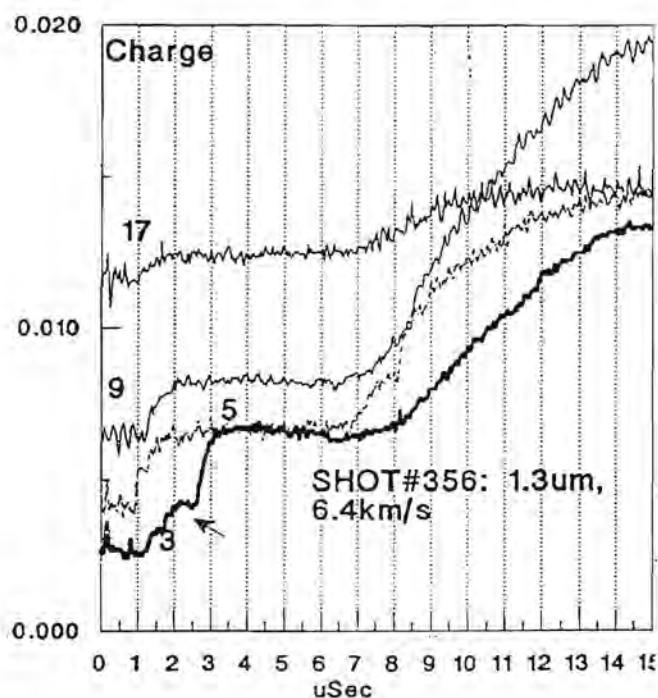


Fig. 14.

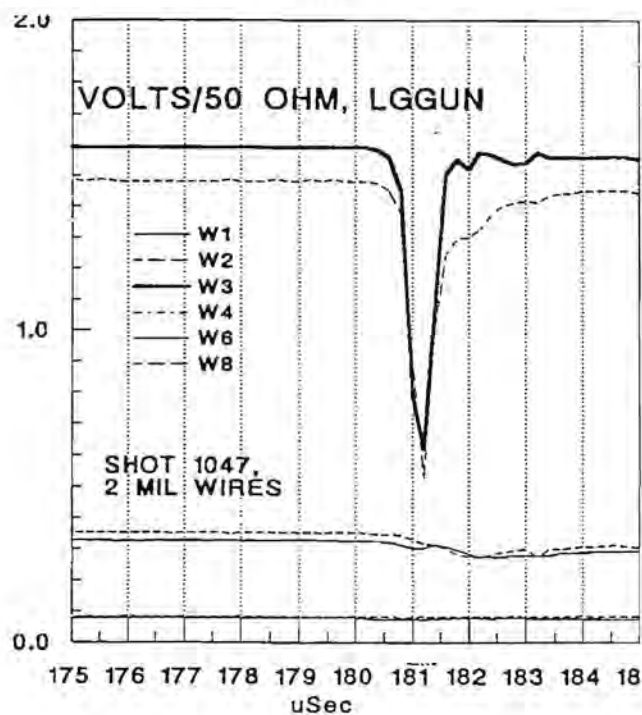


Fig. 15.

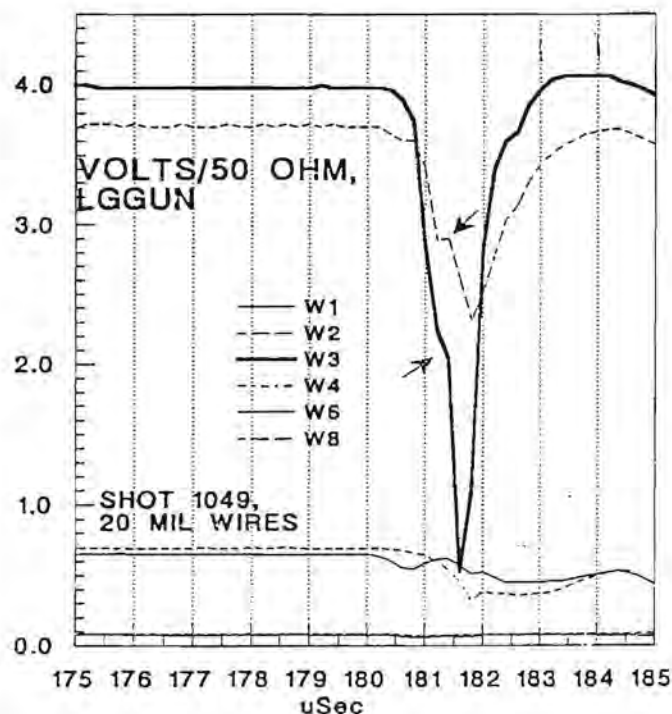


Fig. 16.

the penetration) compared to its closer neighbor, wire 7. The arrow in Fig. 12 points out a feature seen in many shots: a dip of varying amplitude followed by a slow rise. The start of the rise occurs approximately at the time the particle passes the wire. The particle in shot 236 travels  $26 \text{ mm}/\mu\text{s}$  and therefore it takes  $0.38 \mu\text{s}$  to travel the 10 mm to the wire from the foil. This time delay is more easily seen in shot 386 of Fig. 13 (some signals saturated) and in shot 356 of Fig. 14, shots at 18 and  $6.4 \text{ km/s}$  respectively. The most simple interpretation of this is that the debris cloud from the foil and/or particle intercepts the wire, generating local plasma. The gradual rise before hitting the wire is charge collected from the foil penetration plasma. Preliminary data from the JSC light gas gun is consistent with this picture, and is presented next.

**Foil/wire experiments in the light gas gun.** Figures 15 and 16 show data from a  $1/8$ -in diameter glass sphere penetrating  $0.8\text{-}\mu\text{m}$ -thick Al foil in the light gas gun at JSC. Wires 10 mm apart and 10 mm behind an Al foil are biased at  $+40 \text{ V}$ . Thus the collection geometry is very similar to that shown in Fig. 9. All shots are very close to  $6 \text{ km/s}$ . The only significant difference in the two shots is that shot 1047 is done with 2-mm-diameter W wire while shot 1049 (Fig. 16) used 20-mm wires. (Note that here we do not integrate the current collected; it is simply displayed as a voltage across the 50-ohm load. HB3 signals were integrated and displayed as charge.) The arrow in shot 1049 locates a small hump that may begin the signal due to debris hitting the 20-mm-diameter collection wire. Shot 1047, with the much smaller 2-mm-diameter collection wires, does not seem to show this effect. This appears to support the debris hypothesis mentioned earlier.

The most important feature of these light gas gun data is that the location of the particle penetration seems to be easily located and the signals not very difficult to interpret. The signals from wires fall quickly as they are located farther from the penetration event. The



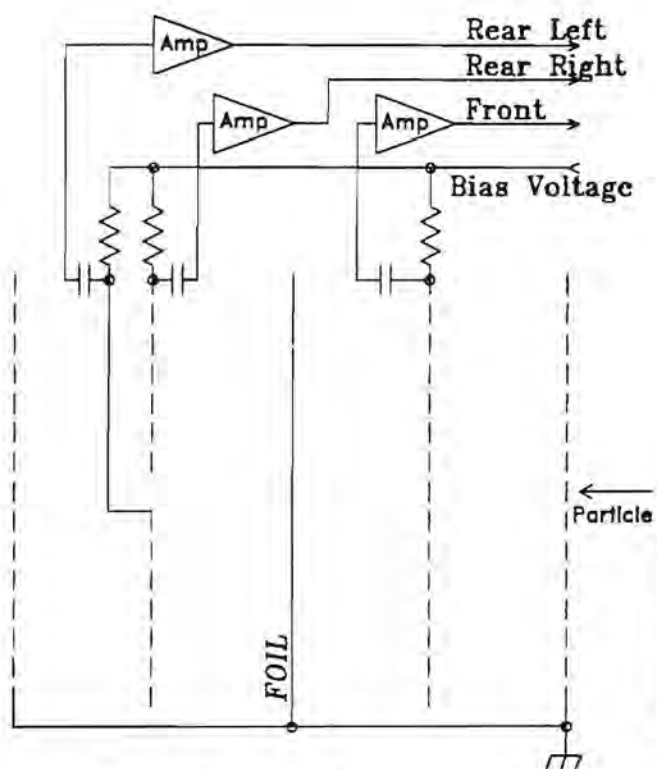


Fig. 17. Heidelberg experiment.

leading edge of the signals is a bit slower than that corresponding to the microparticles from the electrostatic accelerators, but it is on the same order of magnitude (hundreds of nanoseconds). Most of the previous light gas gun data have been with large ring collectors. Efforts are now concentrated toward the CDCF wire configuration.

**Charge Collected by a Biased Probe near the Hypervelocity Penetration of Thin Foil Experiments to Develop a Vector Velocity Detector for the Cosmic Dust Collection Facility (CDCF):** This report summarizes tests done in three locations.

*Experiments at Max-Planck-Institut (MPI), Heidelberg, 1990.* Figure 17 is a schematic of the experiment. Charge from plasma produced in the hypervelocity penetration of an Al foil is collected at positively biased grids on either side of the foil. The particles used are iron spheres ranging from 0.1 to  $\sim 2 \mu\text{m}$  in diameter at velocities from 20 down to 5 km/s. The collectors were normally biased at +40 V (experiment showed that the signals became constant at bias voltages above about +20 V). Two signals were acquired from either the front and rear collectors or the two side-by-side collectors on the rear (in the front/rear mode, the rear signal was the sum from the two collectors). Charge amplifiers in use were the same as used for the charge-sense stations on the accelerator path and had noise levels of around 10–16 Cb rms. Data were acquired and recorded on a two-channel Tektronix 2232 digital oscilloscope. No download capability was available, so 26 interesting traces were stored in the internal scope memory and later downloaded at JSC. Three of these data traces are shown in this report.

The experimental apparatus used was similar to that used in April 1989 at MPI, but it allowed the foil and collector elements to be moved (the earlier model had fixed spacings). Most data were taken using the minimum 7-mm spacing; the earlier experiment was conducted at the fixed 3-mm spacing, which could not be reproduced

Shot #77 (J), 5km/s

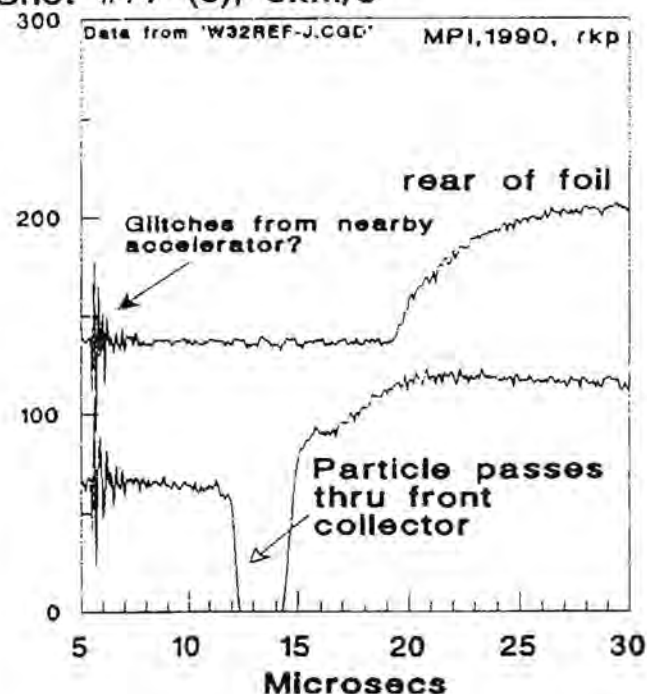


Fig. 18.

Shot #95 (K), 12km/s

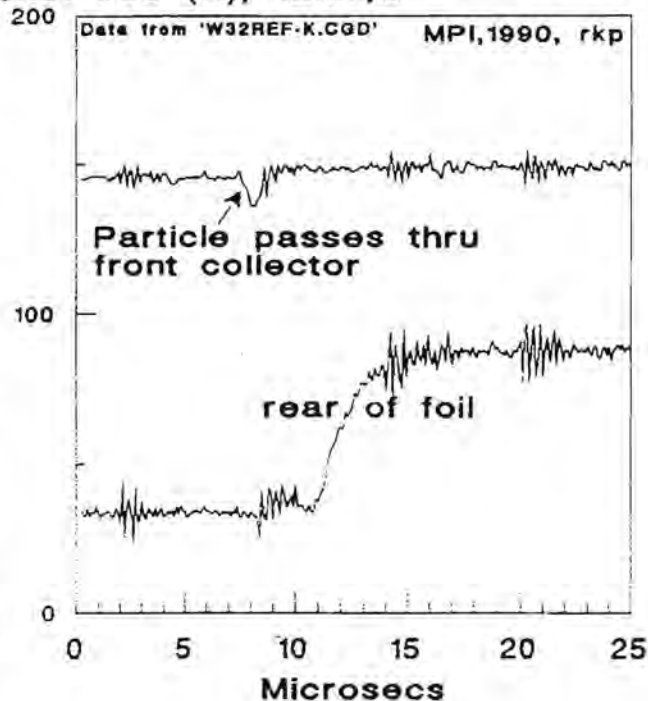


Fig. 19.

## Shot #100 (L), 16km/s

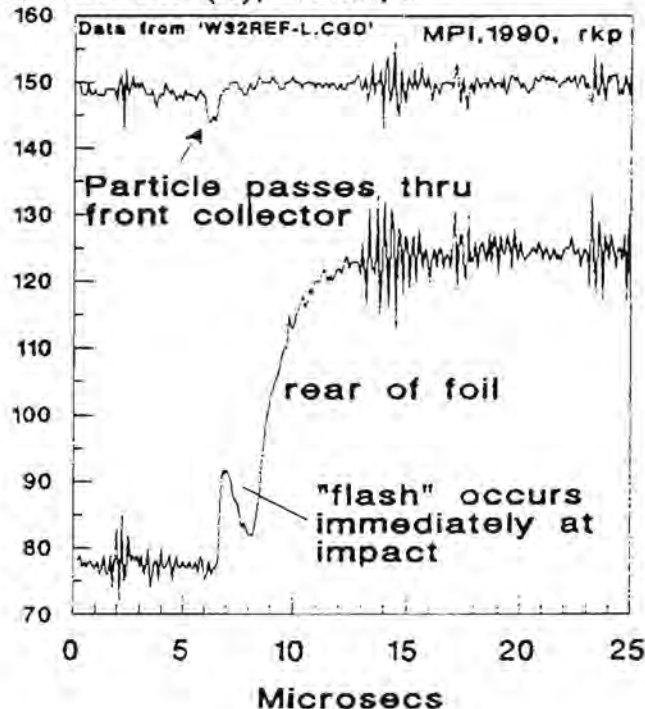


Fig. 20.

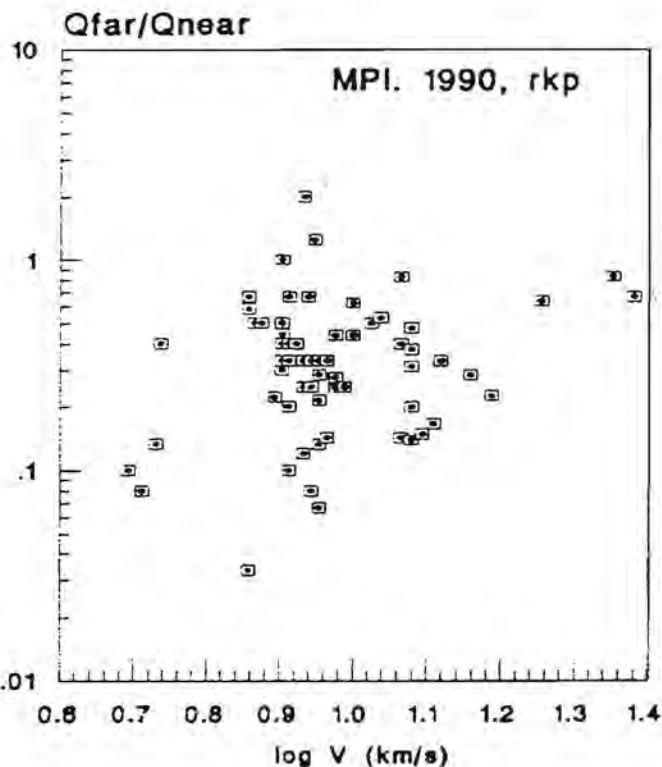


Fig. 22.

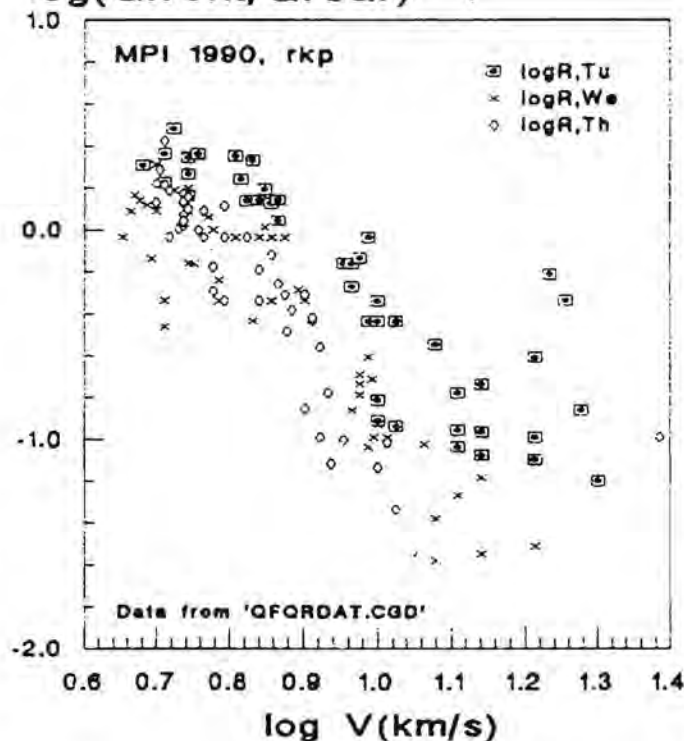
 $\log(Q_{\text{front}}/Q_{\text{rear}})$ 

Fig. 21.

on this trial. The new apparatus allowed arbitrary biasing of all elements, but this capability was not used.

Figure 18 shows a typical 5-km/s shot. The large negative spike is the charged particle passing through the front collector grid. The particle strikes the foil at almost exactly 15  $\mu\text{s}$  into the trace. The front charge signal consists of an initial fast component, followed by a slower, larger component. It is almost 5  $\mu\text{s}$  after foil impact that the rear signal begins to rise; it is of one component and it is quite slow. In this shot, the rear collector is 13 mm from the foil and the rear screen grid is 7 mm behind the collector.

A 12-km/s event is shown in Figure 19. The front signal is smaller (see Fig. 21 for a summary of the front/back ratio vs. velocity) and the charged particle is barely visible passing through the front collector grid. The rear signal still has two components but the early component is barely visible above the noise. The delay of the slow rear component is about 2  $\mu\text{s}$  (this delay appears to be related to velocity!). Figure 20 is a 16-km/s shot. Here the early signal on the rear is easily visible. The negative slope of the early signal implies either that positive ions are being collected at this point or that the surface charge on the plasma ball has reversed from negative to positive (the integrating amplifier inverts). The physical explanation of this "flash" signal is not known.

All these complex and very slow signals indicate that a velocity resolution of 1% (in a 30-cm path length) could be problematic. Speaking of resolution, Fig. 22 displays data that may indicate a limit to the spatial resolution capabilities of a foil/plasma velocity detector. In a test very similar to that done on the front of the foil in April 1989, the two rear collectors were used. The coplanar collector grids were 7 mm behind the foil and the particle beam center was

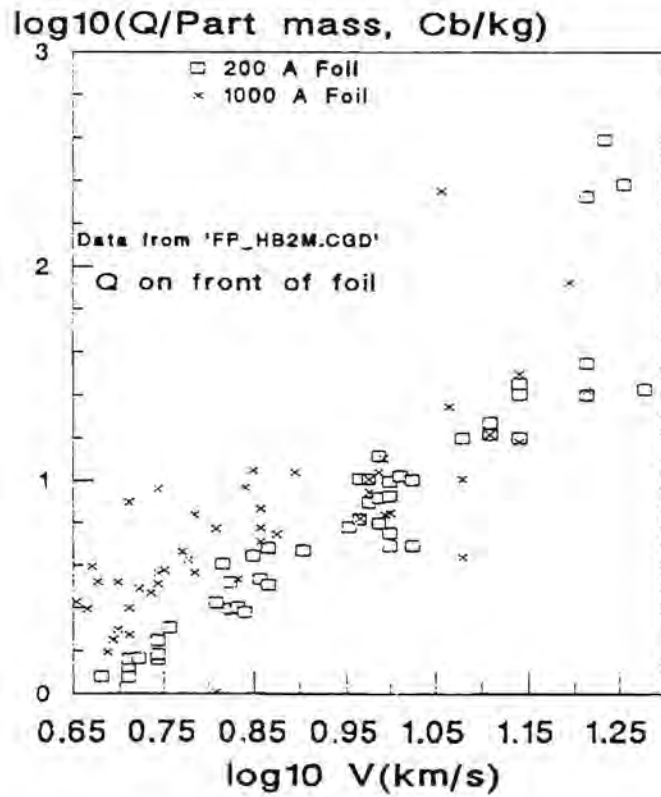


Fig. 23.

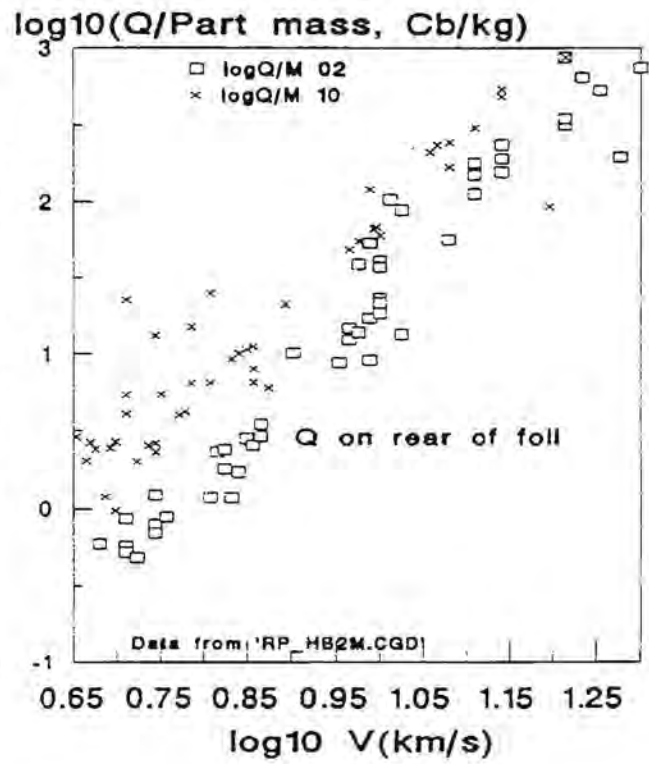


Fig. 25.

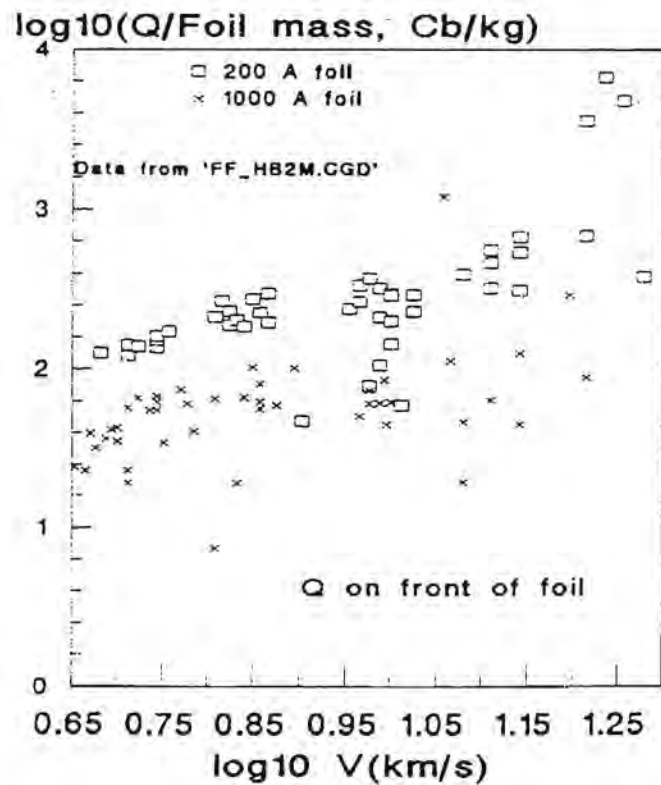


Fig. 24.

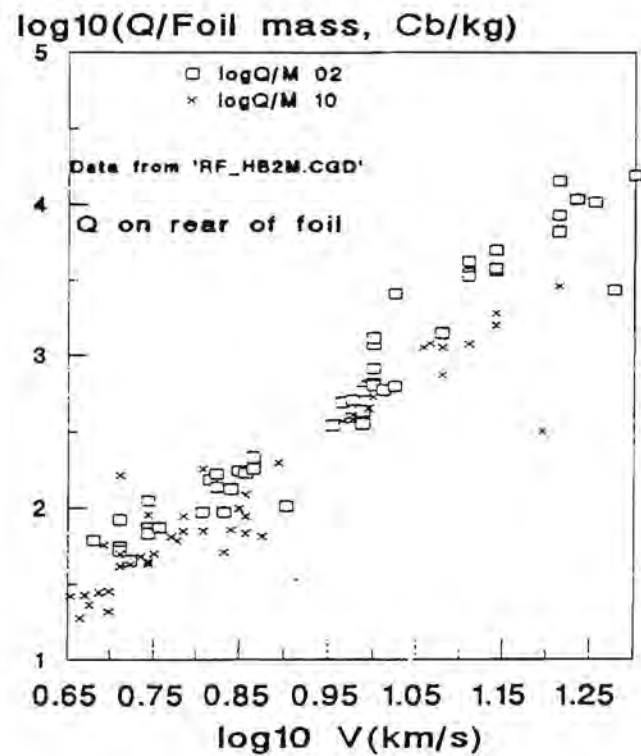


Fig. 26.



moved to a point 7 mm to one side of the gap between the two grids. The two signals recorded are appropriately named "far" and "near" and the ratio of the two is plotted vs. particle velocity in Fig. 22. No extra occulting aperture was placed in the beam path so the expected beam diameter of 3 mm allows a good deal of variation in the impact point; this may have contributed to the great scatter in the data of Fig. 22. Despite the scatter, it seems clear that, at high velocities, the charge is available over a wide area and that the ultimate spatial resolution is less than that available at low velocities.

Four graphs show details of charge collected on the front (Figs. 23 and 24) and the rear (Figs. 25 and 26) of the foil. Figure 23 shows the front charge per unit mass of the particle vs. velocity for both 0.1- and 0.02- $\mu\text{m}$ -thick foils (T). The 0.1- $\mu\text{m}$  data seem to lie above the data for the thinner foil at low velocities, but the two merge above 10 km/s. Figure 24 is the same except that the vertical axis is now charge per unit mass of the foil biscuit cut out by the particle (assumed to have the same diameter as the particle, D). Now the 0.02- $\mu\text{m}$  data lie above the 0.1- $\mu\text{m}$  data. One would expect the front charge to scale with particle mass ( $D^3$ ) in the cratering regime (when D is near T) and to scale with foil mass ( $D^2$ —see below) when  $D > T$ . D is approaching T for the 0.1- $\mu\text{m}$  foil at high velocities, but I still don't have any interesting interpretation of these data.

The rear data appear to have a simple interpretation. Figure 25 (corresponding to Fig. 23 on the front) shows that the charge/particle mass through the 0.1- $\mu\text{m}$  foil is about 5 times larger than that for the 0.02- $\mu\text{m}$  foil. Figure 26 shows that this difference disappears when charge/foil mass is plotted. Note that the velocity dependence of the charge signals on the front and rear are quite different. The front goes approximately as  $V^2$  and the rear as approximately  $V^4$ .

*Experiments at Los Alamos (LANL) in late 1990.* A special fixture was built to allow the experiment frame to be mounted in the target chamber of the dust accelerator at the LANL Ion Beam Facility (this fixture had to be abandoned after the experiments because of tritium contamination from the 5-MeV accelerator). This accelerator provides Fe particles at voltages to 5 million V and thus could provide slightly larger particles at any given velocity. The primary difference between these tests and the experiments at MPI is the use of wires for charge collectors rather than electromesh grids. Wires are thought to be the only practical method of covering the large foil area used with CDCF. These wires, being spaced at intervals many times the wire diameter, do not provide as large average electric field for charge collection as do planar grids biased at the same voltage. The initial tests had two wires in front and two in the rear of the test foil. The charge collected by the wires on front and back corresponded well to that collected by the grids at MPI, even at rather low bias voltages of 20 V. Apparently, only very low electric fields are required to collect whatever charge is available. Since charge collection at the exit side of the foil seems most desirable, the front was abandoned and four vertical wire collectors were placed at the rear. The 0.5-mm-diameter wires were 5 mm apart and 7 mm behind the foil.

Figure 27 shows the setup. The charge amplifiers were Amptek 250-A battery-powered units provided by the accelerator group. The amplifiers were mounted on the main flange, 10 in away from the actual collector wires. The coaxial connections added about 15 pf stray capacitance and raised the output noise level to about  $10^{-16}$  Cb rms, still a factor of 2 or 3 below that at MPI. For some unexpected reason, the pulse noise environment was very quiet; this allowed much more detail to be recorded. Two Tektronix 2232 digital

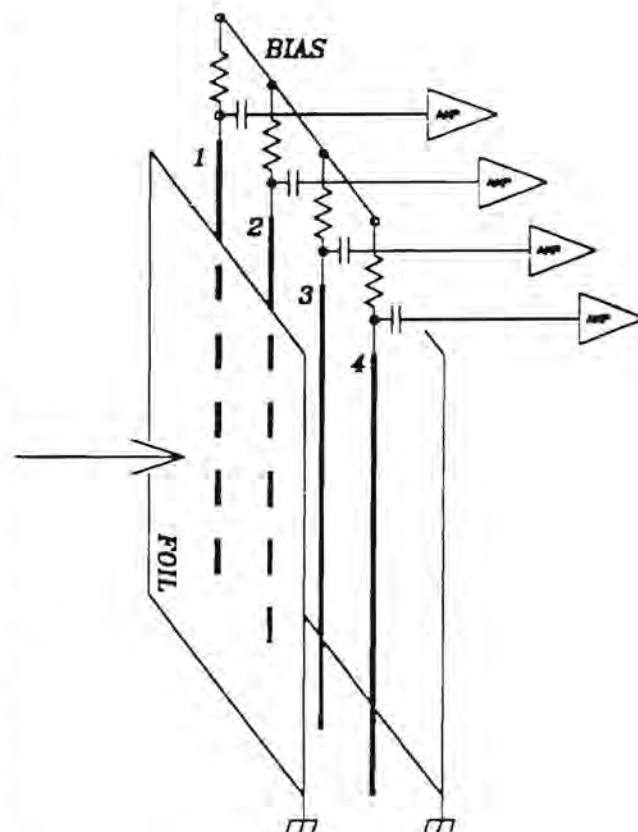


Fig. 27. LANL principal configuration.

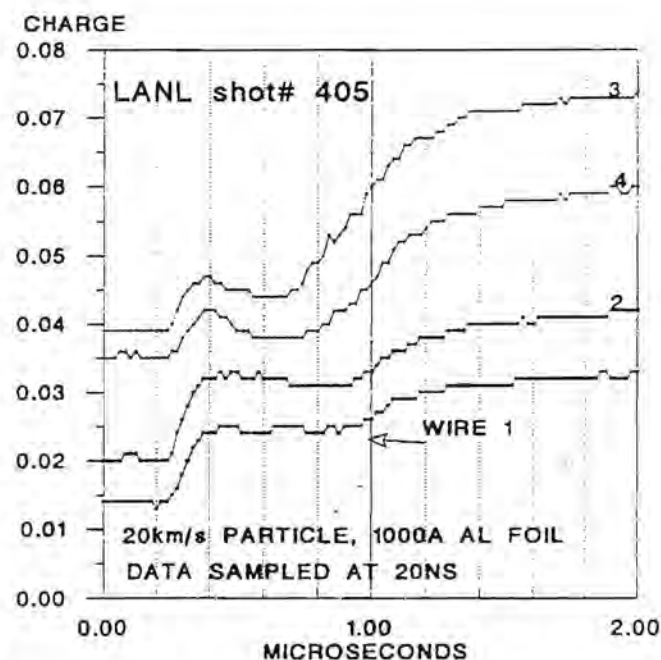


Fig. 28.

storage scopes were available, allowing four traces to be sampled and stored. The data files were downloaded to a hard disk after each shot. For most shots, signals in a 10- $\mu$ s interval were recorded (the timing window was difficult to set; very small intervals could result in most events being missed). The "flash" phenomenon, seen at MPI, was easily seen and this time was studied in much more detail. Figure 28 shows a 20-km/s shot seen in a 2- $\mu$ s window with samples every 20 ns. The particle hits near wire #3 of the array of four wires. Each wire picks up a rather strong flash signal, but the wires nearest the penetration have a much larger component arriving much later. The flash signal dips (see Fig. 20) near the impact, but apparently dips less as the charge is collected farther from the penetration. One wonders what happens as the collection point is moved even farther away—does the flash signal ever disappear? This two-component event will make it difficult to do both timing and measure total charge (giving a clue to the size of the particle). The flash component is perfect for exact timing, but it is smaller than the slow component and carries little information as to the particle size or the location of the penetration event. The slow component contains the size and location information, but is far too slow for any use in timing.

**Experiments using the two-stage light gas gun.** Although the light gas gun is limited to velocities below 7 km/s, it can provide very large projectiles up to several millimeters in diameter. Recently, the gun has been made to work in the "shotgun" mode, providing particles as small as 50  $\mu$ m. This is ideal for the size range envisioned for CDCF (10–100  $\mu$ m). Another feature of the light gas gun that is unavailable with electrostatic accelerators is that it can shoot nonmetallic projectiles. Glass is used to simulate the chemistry of cosmic dust.

Figure 29 shows the arrangement used in recent plasma experiments in the gun. Three 1/8-in diameter copper rings, 2 inches in diameter, are spaced at 1-in intervals behind the target foil. The foil is biased at ground (0V) and the three rings are biased in positive 20-V steps so that the electric field between the rings is relatively

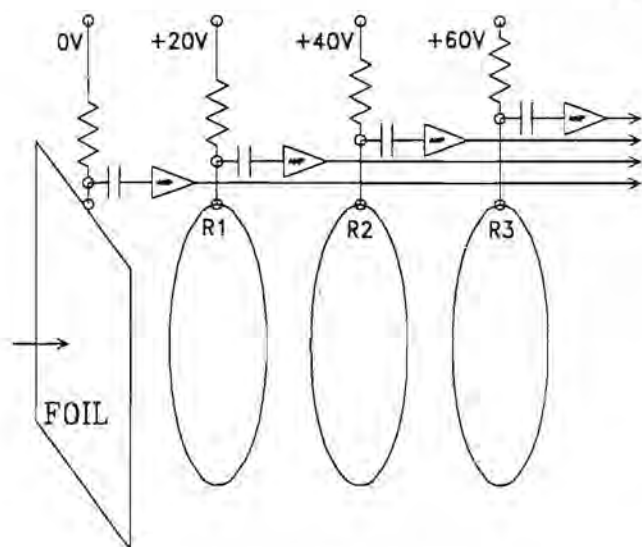


Fig. 29. Ring collectors used in the light gas gun at JSC.

uniform and consistent in sign. Plasma between any two rings will provide ions to the left and electrons to the ring on the right. Figure 30 shows signals from these electrodes obtained from a shot using a 25- $\mu$ m-thick Al foil, penetrated by a 1/8-in glass sphere projectile. The earliest signal is the ion signal from the foil itself. This signal is the total from both sides of the foil (signals from positively biased rings on the front of the foil are not shown here) and the sharp rise occurs within a small fraction of a microsecond of impact. The ring signals are shown with arrows and the sequence is as follows: First, a negative signal as the plasma ball approaches the ring from the left. Then, as the plasma passes through the ring (and the ring now becomes the negative electrode), the signal turns positive. This sequence repeats except that the last ring never collects positive charge since it is the most positive electrode in the area. Note that as the first ring signal becomes positive, the second ring goes negative; as the second goes positive, the third goes negative. The early negative signal on the third ring is apparently due to a small jet of plasma hitting a connection wire on this shot.

The relatively weak negative signal from the first ring may be due to the fact that the plasma is very dense in its first few microseconds of life; the plasma is well shielded and the electric field can only attract a small charge from its small surface. As the ball expands, its surface area grows and its density drops quickly—the debye length becomes greater and the electric field is able to penetrate deeper into the plasma. The larger signals seen later are consistent with this simple picture.

The light gas gun experiments are the only ones to date that allow study of the time development of the plasma. We hope to get further information on just how long the plasma can last. CDCF plans to use two plasma detection planes; these studies can give

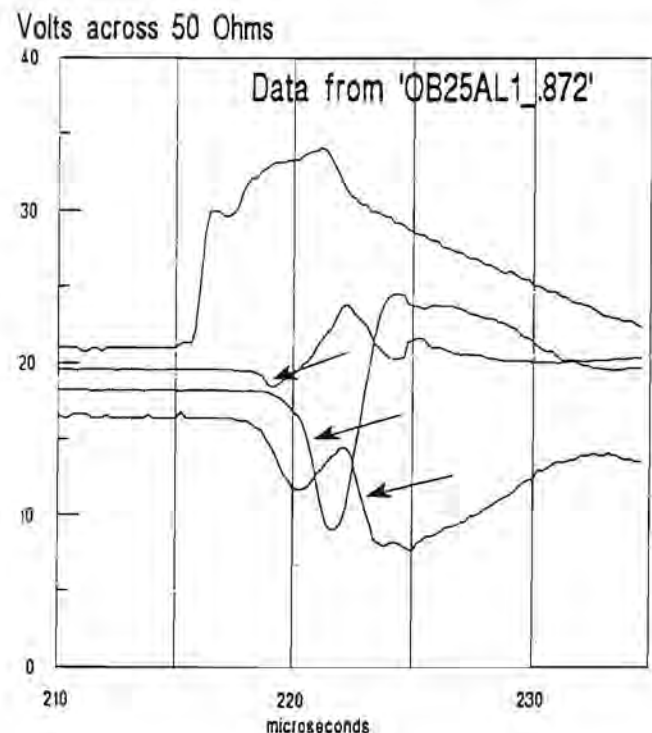


Fig. 30.

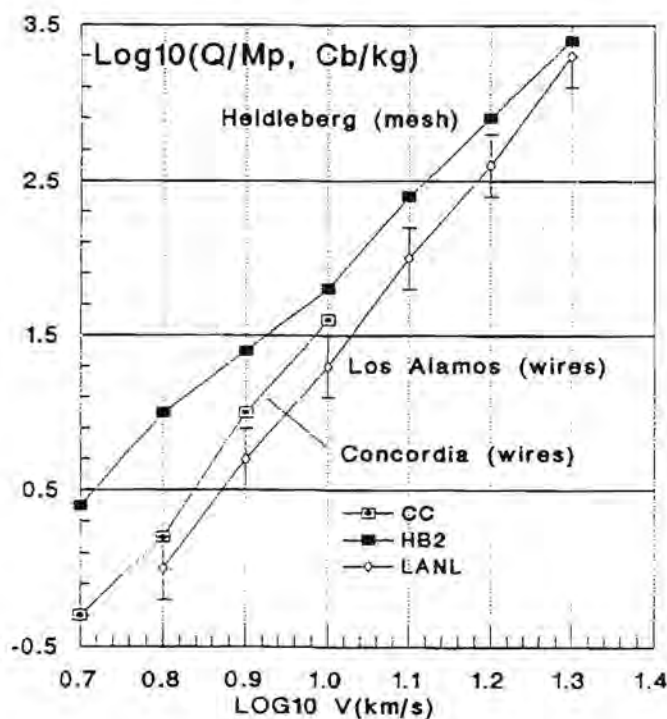


Fig. 31.

clues as to whether the first plane could cause problems for the second one downstream.

**Experiments at Concordia College, Moorhead, Minnesota.** The Concordia microparticle accelerator was used to provide sub-micrometer Fe sphere projectiles at velocities up to 10 km/s. Parallel W collector wires, 125  $\mu\text{m}$  in diameter, were placed behind a 1000-Å Al foil. The wires were 1 cm apart, 1 cm from the foil, and biased up to +200 V. Four adjacent wires were sensed with Amptek A250 charge amplifiers (mounted in the vacuum, within centimeters of the wire ends). Although the amplifier noise was quite low, the ambient noise level was very high and the very small flash signatures could not be seen. However, it was apparent that the wide spacing allowed the primary signals from only two adjacent wires to be seen (the LANL tests with wires at closer spacing showed a much wider pattern; see Fig. 28). It was found that wire diameter is not a significant factor. Figure 31 shows that the charge per unit projectile mass is consistent with that seen at LANL. The mesh collector system used at Heidelberg is a more efficient collector at low velocities, but merges with the wire data above 10 km/s. All data in Fig. 31 represent charge collected on the exit side of the penetrated foil.

**Acknowledgments:** Access to the dust accelerators at MPI, Heidelberg, and Los Alamos National Laboratory, including many useful discussions with E. Grün and G. Strandling, is gratefully acknowledged. The JSC light gas gun experiments were supported by F. Cardenas, W. Davidson, J. Haynes, and J. Winkler of Lockheed ESC, Houston. Many exchanges with F. Hörz, D. Grounds, and S. Auer contributed and shaped the course of this study.

**SCIENTIFIC OBJECTIVES OF THE PRIMITIVE BODY SAMPLE RETURN MISSIONS—AN APPROACH FROM THE LIGHT-INDUCED EFFECT ON WATER VAPOR.** M. Shimizu, ISAS, Sagami-hara-shi, Kanagawa 229, Japan.

Water is undoubtedly one of the most crucial components of the solar nebula for determining planetary composition: Planets were formed from the accretion of the dust particles in the nebula, and the redox state of Fe in the particles can be determined by the reaction of Fe with water vapor diffused into the interior of the particle in the early stage of solar system formation.

It has been discussed from various observations that the cores of Mercury, Venus, and the Earth might be metallic Fe, although the core of the Earth may be somewhat oxidized by the high pressure and temperature reaction of liquid Fe with perovskite at the boundary of the mantle and the core [1], whereas the core of Mars may be highly oxidized, as suggested by its low density.

Isotopic anomalies of various elements have frequently been observed in the solar system (in planetary atmospheres and in meteorites) and some of them can be attributed to the injection of exotic particles formed in other stars into the solar nebula. Hydrogen and D anomalies in planetary atmospheres were frequently believed to correlate with the differential escape of H and D from the exospheres of Venus and Mars, although no one knows the primordial D/H ratios before thermal escape. However, an explanation of the decrease of the observed D/H ratios with distance from the Sun was attempted by considering the light-induced drift effect [2] to displace  $\text{H}_2^{16}\text{O}$  alone to the outside in the solar nebula.

An O isotopic anomaly was observed in the carbonaceous meteorites: the ratio of  $^{17}\text{O}$  and/or  $^{18}\text{O}/^{16}\text{O}$  in the meteorites deviated from those of tap water on Earth to increase  $^{16}\text{O}$  with distance from the Sun [3]. The phenomenon could be explained by the contamination of the solar nebula from the injection of exotic materials containing pure  $^{16}\text{O}$  alone of the supernova, but the tendency of the increase could also be interpreted in terms of the light-induced effect, since  $\text{H}_2^{16}\text{O}$  alone would be moved outside, as well as the variation of the redox state of Fe in the cores of the terrestrial planets.

The light-induced effect was first advocated by Gel'mukhanov and Shalagin [4] and its photomechanical parameters were measured by Bloemink et al. [2] to suggest that transport distance of  $\text{H}_2\text{O}$  during the solar nebula phase would be  $3.5 \times 10^7$  m, 3 times the diameter of Venus, by assuming 2500 K black-body radiation from the protosolar envelope. The effect is isotopically selective, additive, and uses particle momentum instead of light momentum. Therefore the effect could cumulatively be rather strong, although it is based on the very weak gravitational redshift of the infrared radiation. However, the estimated distance is too small, since the absence of water on Venus would soon be filled by water in the vicinity of Venus at the solar side. The transported distance should be at least of the order of 0.1 AU.

We speculate that the proto-Sun would be the infrared laser star, whose radiation was strong enough to cause the above three phenomena (in the same direction): Fe oxidization, and H and O anomalies. Millimeter emission from water vapor due to light pumping was observed by irradiation of large ultraviolet flux [5]. Laser effects were also detected at wavelengths of 28 and 33  $\mu\text{m}$  [6]. Although direct observation of water laser in the near-infrared region in the laboratory is not yet available, we may expect that the proto-Sun was a strong infrared laser star, pumped by violent



molecular collisions in its envelope caused by turbulence from the interior (ultraviolet radiation would also contribute to pumping). We hope to test it by the observation of T Tauri stars by using the ISO spacecraft in the near future. The analysis of O anomalies of the returned sample from the primitive bodies in the solar system is interesting for this purpose, too.

**References:** [1] Knittle E. and Jeanloz R. (1991) *Science*, 251, 1438. [2] Bloemink H. I. et al. (1993) *Phys. Rev. Lett.*, 70, 742. [3] Clayton R. N. (1976) *EPSL*, 30, 10. [4] Gel'mukhanov F. Kh. and Shalagin A. M. (1979) *JETP Lett.*, 29, 711. [5] Gebbie H. A. and Apsley N. (1988) *Infrared Phys.*, 28, 337. [6] Gebbie H. A. (1964) *Nature* 201, 250, 202, 169.

**PENETRATION OF MULTIPLE THIN FILMS IN MICROMETEORITE CAPTURE CELLS.** C. G. Simon<sup>1,2</sup>, <sup>1</sup>McDonnell Center for the Space Sciences, Washington University, St. Louis MO 63130, USA, <sup>2</sup>Present address: Institute for Space Science and Technology, 1810 NW 6th Street, Gainesville FL 32609, USA.

As part of a continuing effort to develop cosmic dust detectors/collectors for use in space, we performed a series of hypervelocity impact experiments on combined sensor/capture-cell assemblies using 10–200- $\mu$ m-diameter glass projectiles and olivine crystals at velocities of 0.9–14.4 km/s. The design objective of the space-flight instrument is to measure the trajectories of individual particles with sufficient accuracy to permit identification of their parent bodies and to capture enough impactor material to allow chemical and isotopic analyses of samples returned to Earth. Three different multiple-film small-particle capture cell designs (0.1–100- $\mu$ m-thick Al foils with ~10, 100, and 1800  $\mu$ m spacing) were evaluated for their ability to capture impactor fragments and residue. Their performances were compared to two other types of capture cells, foil covered Ge crystals, and 0.50 and 0.120 g/cm<sup>3</sup> aerogels. All capture cells were tested behind multifilm (1.4–6.0- $\mu$ m-thick) polyvinylidene fluoride (PVDF) velocity/trajectory sensor devices. Several tests were also done without the PVDF sensors for comparison.

All capture cells collected significant amounts of impactor debris behind the PVDF sensors from nominal 100- $\mu$ m-diameter glass projectiles and olivine crystals that struck the sensor at velocities up to 6.4 km/s. At velocities >8 km/s little or no debris penetrated the second PVDF film. Results were inconclusive for velocities between 6.5 and 8 km/s. Plasma detector results showed identifiable impactor residue on Al foils for velocities up to 8.7 km/s and impact tracks with apparent debris imbedded in the aerogels for velocities up to 12.7 km/s. Maximum foil penetration of glass spheres and olivine crystals were the same, but more particulate debris was associated with olivine crystal impacts vs. glass impacts. Capture cells with 100- $\mu$ m and 1.8-mm foil spacing had similar total (cumulative) foil-penetration values, which decreased with increasing velocity. Aerogels are identified as a capture cell media that warrants further investigation. The Al multifoil capture cell with 100- $\mu$ m net spacers is identified as the most effective of the other designs and offers the advantages of compact structure, low secondary ejecta from impacts, and easy recovery of impactor debris for analysis.

**Summary:** The results of this study were reported by Simon [1] in a comprehensive report in which the morphology of impacts and impactor residues in various types of capture cells after passage

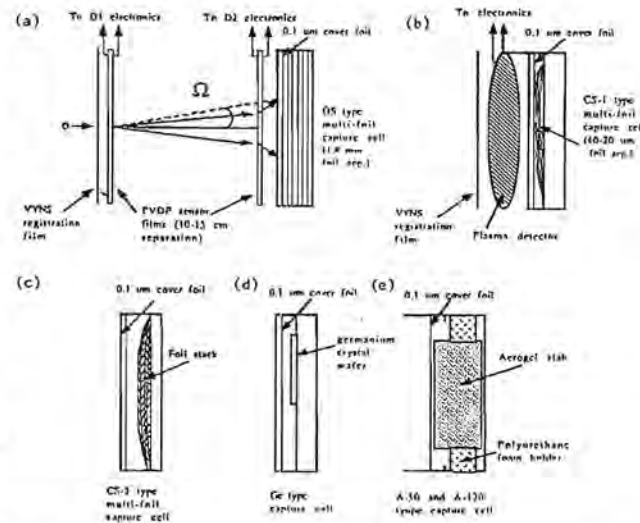


**Fig. 1.** Five capture cell designs. (a) "OS" multifoil capture cell, 1.8-mm foil spacing, showing position of two-film PVDF trajectory/velocity sensor, VYNS registration film, and effective debris dispersion angle ( $\Omega$ ); (b) "CS-1" multifoil capture cell, 10–20  $\mu$ m foil spacing, showing position of wire grid plasma detector; (c) "CS-1" multifoil capture cell with 100- $\mu$ m-thick dacron net spacers; (d) "Ge" capture cell with cover foil; (e) aerogel capture cell with Al cover foil.

through two PVDF sensor films is discussed. Impactor fragments in selected capture cells from impacts at velocities up to 6.4 km/s were identified using scanning electron microscopy with energy dispersive spectroscopy (SEM/EDS).

The five types of capture cells evaluated are shown in Figs. 1a–e. All cells used the same type of  $2.3 \times (10 \times 10)$  cm Al cassette holder to mount the target assemblies. Four of the five capture cell designs were based on flight hardware onboard the Solar Maximum satellite or the Long Duration Exposure Facility (LDEF). The successful recovery of impactor residue in the multilayer thermal blankets retrieved from Solar Max [2,3] led to the choice of Al foil multilayer "blanket" type capture cells with either 100- $\mu$ m-thick dacron net spacers, or no spacers, between thin (3–8  $\mu$ m) Al foils mounted on a 25- $\mu$ m-thick Al support foil. These were labeled "closed stacks" (CS) because the edges of the top foils were taped to the support foil, forming a thin (~2-mm-thick), closed capture cell. Another multifoil design incorporating Al films from 0.1 to 100  $\mu$ m thick with an interfoil spacing of 1.8 mm was based on the capture cell design flown by McDonnell et al. [4], which also employed multiple foils with spacing of several millimeters. Typical foil stacks in our study had a 0.1- or 0.3- $\mu$ m foil on top for event registration, followed by one to four 1.0- and/or 3.0- $\mu$ m foils, which were then followed by several 8- $\mu$ m foils and one or two 25- $\mu$ m and 100- $\mu$ m foils. These cells were labeled "open stack" (OS) because the individual frame-mounted foils were loaded into the slotted cassette holder and the sides remained open. The effect of foil thickness order was investigated by varying the number and order of the 3- and 8- $\mu$ m foils. (Foil thicknesses  $\leq 3 \mu$ m were made by physical vapor deposition of Al on Ni support grids. Other foils were high-purity, cold-rolled Al.)

A fourth capture cell design was based on our own foil-covered (200- $\mu\text{m}$  spacing) Ge crystal wafer capture cell that also flew on the LDEF [5-7]. A metal-coated, 2- $\mu\text{m}$ -thick Mylar film used in the original design to cover 0.5-mm-thick Ge crystals was replaced by either a 0.1- or 1.0- $\mu\text{m}$ -thick Al foil in this series of experiments. All the capture cell surfaces in these four designs could be accessed easily and inserted directly into analytical instruments such as optical and scanning electron microscopes (SEM) and secondary ion mass spectrometers (SIMS) without pretreatment of the impacted area. The fifth capture cell design consisted of an aerogel slab behind a 1- $\mu\text{m}$  Al foil.

A two-stage thin-film PVDF particle trajectory/velocity sensor developed and tested by our co-investigators at the University of Chicago was evaluated with the five types of capture cells. Tuzzolino [8,9] has reported results of the velocity/trajectory detector portion of the current study. The sensors function by detecting penetrations in the dipole-aligned polymer. The two-film PVDF sensors caused increasing fragmentation of particles at increasing velocities, but only dispersed the major fragments a maximum of  $\sim 5^\circ$  between the initial point of impact on the first sensor film and the points of impact on the first capture cell foil (Fig. 2). The thinnest sensor films ( $\sim 2\ \mu\text{m}$ ) caused somewhat less disruption and spread of impactor material than the two thicker types of sensor films (4.5 and 6  $\mu\text{m}$ ). For glass particles  $< 100\ \mu\text{m}$  in diameter impacting at velocities  $> 8\ \text{km/s}$ , severe fragmentation occurred and little or no impactor debris was found in the capture cells.

The effects of intermixing capture cell and impactor materials were minimized by using high-purity Al and Ge target materials. Impact areas on Al foils were cut out using a 2.5-cm-diameter ring mount for SEM analysis. Germanium crystal wafers were inserted directly into the instrument. This is a significant advantage since samples are available for immediate analysis upon return from orbit. The major disadvantage to these types of capture cells is the

high specific shock imparted to the small particles, especially into the Ge target, which results in the loss of most structural information and may cause chemical, and possibly isotopic, fractionation, as well as intermixing capture cell materials with projectile material.

X-ray maps of Na, Mg, Si, and Ca concentrations were recorded at 300 $\times$  magnification over selected impact areas around penetration holes and craters. This allowed identification of  $\sim 2\text{-}\mu\text{m}$  size particles that had higher than background concentrations of any or all of these elements. Processing of the X-ray maps allowed identification of glass and olivine projectile debris and relative element abundances. This technique was extremely useful in identifying debris deposits and segregating them from target debris and artifacts. It was apparent throughout the SEM/EDS analyses that debris morphology alone could not be used to accurately distinguish impactor debris from target debris.

All impactors fragmented during the multiple-shock impact events experienced multifilm sensor/capture-cell assemblies. Significant amounts of impactor debris, more than sufficient for chemical and isotopic analyses, in the form of melted and embedded globs and spatters and partial melt rims around holes and craters in most foils, were observed for impacts at velocities  $\leq 6.4\ \text{km/s}$ . At velocities  $> 8\ \text{km/s}$  little or no debris penetrated the second PVDF film. Results were inconclusive for velocities between 6.5 and 8 km/s. Plasma detector results showed identifiable impactor residue on Al foils for velocities up to 8.7 km/s. More particulate debris was associated with olivine crystal impacts vs. glass impacts. The maximum cumulative foil penetration was not significantly different for foils spaced 1800 or 100  $\mu\text{m}$  apart, but was approximately twice as great for foils spaced 10-20  $\mu\text{m}$  apart (Fig. 3).

The only verified intact capture of impactors in this study was observed in A-120 and A-50 cells behind the plasma detector at velocities  $\leq 3.5\ \text{km/s}$ . Intact capture of similar size particles and/or large fragments at velocities up to 7 km/s has been reported by Tsou et al. [10-12] and Zolensky et al. [13,14], and indeed there appeared to be well-defined particles at the end of aerogel tracks at velocities up to 12.7 km/s in our experiments. Six shots were performed on PVDF/aerogel assemblies in this study, but results were inconclusive due to the difficulty in identifying small glass and olivine fragments in the aerogel matrix. Colored projectiles could mitigate this problem in future studies.

Of the five capture cell designs tested in conjunction with two-film PVDF velocity/trajectory sensors, the multifilm cell with 100- $\mu\text{m}$  dacron net spacers appears to be the best. This design has the advantages of compact structure, low secondary ejecta from impacts, and easy recovery of impactor debris for analysis. The dacron net spacers confined the spread of the impactor debris cloud without increasing total foil penetration and resulted in both front and back side deposition of debris. Analysis of samples was straightforward since impact features on capture cell foils could be easily mounted in metal rings for instrumental analyses of both surfaces. The use of Al foils and dacron nets in a flight instrument would limit the ability to detect Al and C in manmade debris particles and in natural particles, and would likely be replaced by a cosmologically rare metal such as Au.

Foil-covered Ge wafer targets behind PVDF sensors also retained significant impactor debris at tested velocities up to 5.5 km/s, but offered no advantages over multifilm cells and are appreciably more expensive to produce and somewhat more difficult to package. Also, the advantage of having a pure Ge matrix for debris analysis

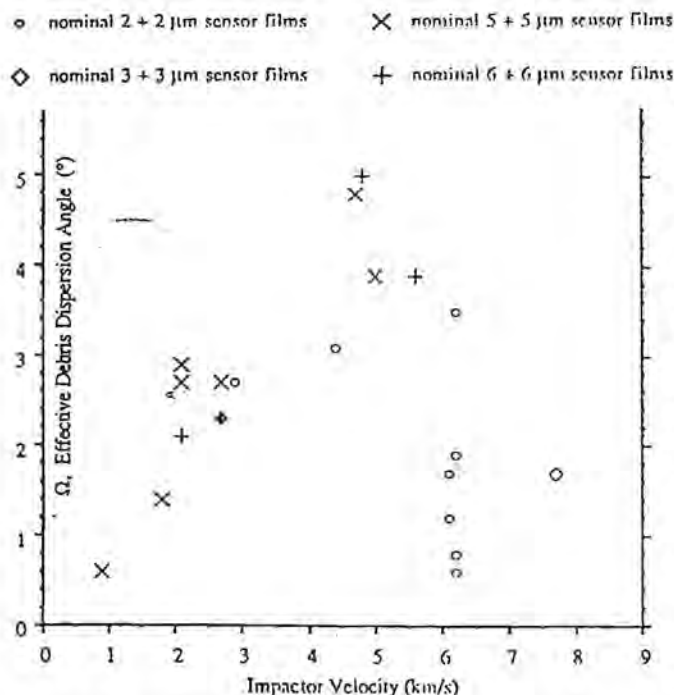


Fig. 2. Plot of impactor debris dispersion angle,  $\Omega$ , vs. velocity.

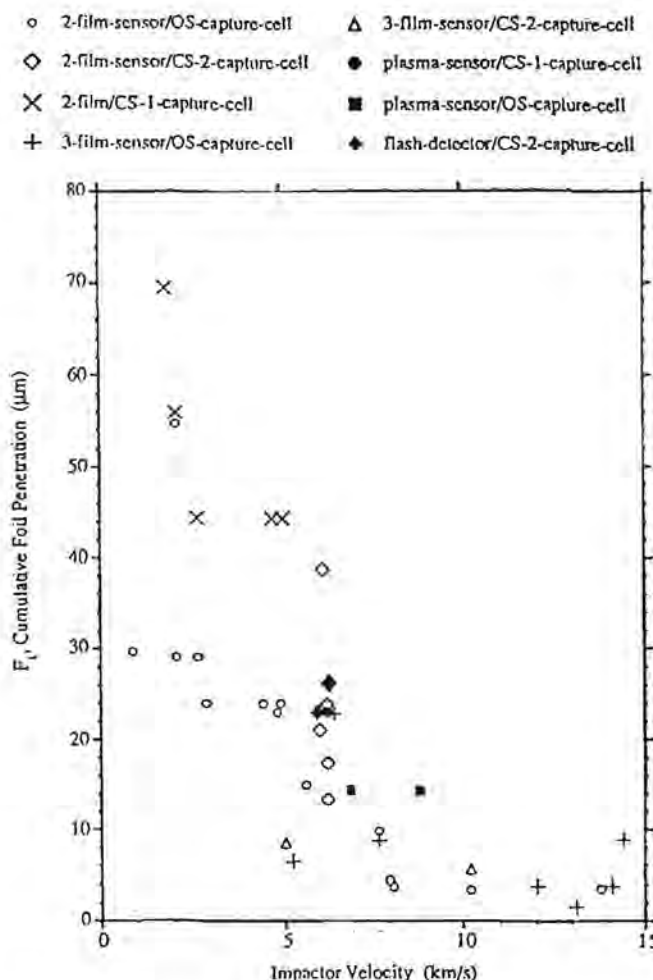


Fig. 3. Plot of cumulative foil penetration,  $F_p$ , vs. velocity. Impactors ranged in size from 10 to 200  $\mu\text{m}$ .

is countered to some extent in this design by the presence of the sensor films and Al registration film ahead of the Ge surface.

Evaluation of 50 and 120  $\text{mg}/\text{cm}^3$  aerogel targets behind PVDF sensors was inconclusive due to the limited number of tests, but initial results indicated that small impactor fragments would be difficult to locate and recover. Packaging of the friable material also needs further development. The aerogels performed well behind a simple plasma detector, and intact nominal 100- $\mu\text{m}$  glass projectiles were recovered from low-velocity impacts (<3.5 km/s). There were visual indications that significant impactor debris may have survived impacts into aerogels at velocities up to 12.7 km/s (behind a plasma sensor), but these tentative results were not verified. Metal or colored ceramic/glass projectiles should be used in future impact tests with aerogels to enhance impactor debris identification. The superior capture characteristics of the aerogels justifies further testing of these capture cell candidates in conjunction with the PVDF sensors. A standard method of containment and mounting and better microparticle location techniques need to be developed for the friable aerogel materials.

**Acknowledgments:** The author would like to thank the many collaborators involved in this study: A. Tuzzolino, E. LaRue, and G.

Drag from the Laboratory for Astrophysics and Space Research at the Enrico Fermi Institute, University of Chicago, for making this combined dust calibration series possible, and for their efforts in correlating impact events; J. Williams and R. Cordi at the Los Alamos National Laboratory for the production of the custom series of frame-mounted high-purity Al foils; M. Zolensky of the Johnson Space Center and P. Tsou of the Jet Propulsion Laboratory for supplying aerogel targets; E. Igenbergs and his staff of plasma gun operators, M. Rott, W. Reschauer, W. Frisch, A. Jean-Jacques, and K. Graf, at the Technical University of Munich for the many successful hypervelocity shots and their technical assistance in providing and operating the plasma detector system; F. Hörz and his light gas gun staff, F. Cardenas, W. Davidson, and G. Haynes, at the Johnson Space Center, also for many successful hypervelocity shots and velocity detector operation; Z. Wang and W. Cantrell at the McDonnell Center for the Space Sciences, Washington University, for SEM/EDS analyses and for assistance with the preparation of this manuscript respectively; and R. M. Walker for the original concept of combining the PVDF detectors and meteoroid capture cells and for his valued assistance in experimental design, execution, and interpretation of data. Funding for this study was provided under NASA grant NAGW-1603.

**References:** [1] Simon C. G. (1993) *J. Impact Eng.*, 14, 683–694. [2] Schramm L. S. et al. (1986) *LPS XVII*, 769–770. [3] Warren J. L. et al. (1989) *Proc. LPSC 19th*, 641–657. [4] McDonnell J. A. M. et al. (1990) 28th COSPAR Meeting, The Hague. [5] Jessberger E. et al. (1985) *LPS XVI*, 400–401. [6] Fechtig H. et al. (1987) in *Properties and Interaction of Interplanetary Dust* (R. Giese and P. Lamy, eds.), 121–126, Reidel. [7] Amari S. et al. (1991) *NASA CP-3134*, 503–516. [8] Tuzzolino A. J. (1991) *Nucl. Instr. Meth.*, A301, 558–567. [9] Tuzzolino A. J. (1992) *Nucl. Instr. Meth.*, A316, 223–237. [10] Tsou P. et al. (1988) *LPS XIX*, 1205–1206. [11] Tsou P. et al. (1989) *LPS XX*, 1132–1133. [12] Tsou P. et al. (1990) *LPS XI*, 1264–1265. [13] Zolensky M. E. et al. (1989) *LPS XX*, 1251–1252. [14] Zolensky M. E. et al. (1990) *LPS XXI*, 1381–1382.

#### ASSESSMENT OF VELOCITY/TRAJECTORY MEASUREMENT TECHNOLOGIES DURING A PARTICLE CAPTURE EVENT.

W. G. Tanner<sup>1</sup>, C. R. Maag<sup>2</sup>, W. M. Alexander<sup>1</sup>, and S. Stephenson<sup>1</sup>, <sup>1</sup>Baylor University Space Science Laboratory, Waco TX 76798 USA, <sup>2</sup>Science Applications International Corporation, Glendora CA 91740, USA.

The creation of the system composed of specific components described in several presentations of this workshop [1–3] has been conducted in a manner that will produce an integrated package for flight on EURECA 2 as COMRADE [4], on SOCCER, and on LDEF II. The function of each component of the integrated package has been described in general [1] and in detail [2,3], but one other component to be described in detail, i.e., ultra-thin-film time-of-flight determination, may be mated with any capture package envisioned.

The authors have been involved for many years in the development and application of thin-film sensors to detect a hypervelocity penetration by a dust grain. The major electronic circuit design has been conducted over the span of several decades, but the utilization



of ultrathin metallic films as charge generation media has only recently reached an acceptable level. Since the penetration event of a hypervelocity dust grain will be dominated by the material strength and thickness of the target surface, the most efficient sensor would be that for which both parameters have been minimized. The minimization of density and material strength is most appropriate for intact capture; therefore, results of the variation of that parameter will be discussed in other papers [cf. 2].

The primary parameter of a thin metallic film that has been systematically altered in this investigation was the film thickness while holding constant film density, i.e.,  $\rho = 2.70 \text{ g/cm}^3$  (2024 Al). Recently the thickness of the films has been made sufficiently small to assure perforation, and only partial fragmentation of the dust grain while providing a significant charge liberation media. Numerous experiments have shown the repeatability of penetrations and perforations with minimal fragmentation of the projectile. That the projectiles have both been simulated in the laboratory and through computer simulations allows for the repeated variation of parameters of the hypervelocity interaction.

Through this research an optimized thin-film sensor has been produced that presents a sufficient amount of matter to detect the charge liberated during perforation while providing a significant support structure for the survivability of the sensor. Combinations of thin-film substances, thicknesses, and support structures have been tested in the laboratory, on many STS flights, and during an 11-month orbital flight onboard the EURECA spacecraft. The experience gained will be utilized to develop the velocity/trajectory system for the SOCCER-like Comet Coma Sample Return (CCSR) mission.

**Background:** Since the early 1960s, the means to measure the time of flight (TOF) of a dust grain within a mechanical detection array has existed, first in the laboratory and then in space experiments. Laboratory hypervelocity dust particle accelerators have used electrostatic detection of charge on accelerated particles for TOF and particle mass determinations. These laboratory studies have led to the development of ultra-thin-film sensors that have been used for TOF measurements in dust particle space experiments. The prototypes for such devices were ultra-thin-film capacitors that were used in the OGO series of satellites [5].

The main goal of the experimental work to be described is the development of the capability to determine the velocity vector or trajectory of a dust grain traversing an integrated dust detection array. The results of these studies have shown that the capability of detecting the charge liberated by hypervelocity dust grains with diameters in the micrometer range can be detected. Based on these results, detection systems have been designed to provide a precise analysis of the physical and dynamic properties of micrometer and submicrometer dust grains, viz., Fig. 1, design verification unit (DVU). Through unique combinations of *in situ* detection systems, direct measurements of particle surface charge, velocity, momentum, kinetic energy, and trajectory have been achieved. From these measurements, the remaining physical parameters of mass, size, and density can be determined.

The heritage for the measurements providing trajectory determination is based on a long line of successful dust particle experiments. However, laboratory research efforts have been accomplished during the past decade using (1) data provided from sensing the specific charge on a dust grain traversing an experiment array designed to accurately determine the path of the grain within the

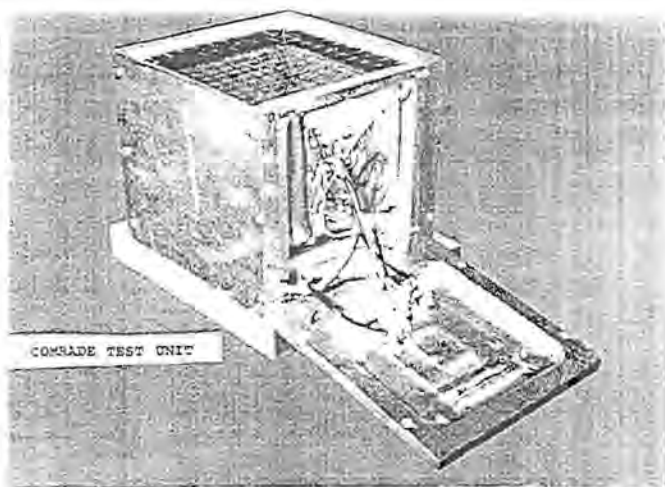


Fig. 1. Design Verification Unit (DVU), which tests the electrostatic sensor, thin-film plasma sensor, and foam capture system in the dust accelerator at University of Kent at Canterbury, Unit for Space Science (UKC-USS).

array and (2) data provided from plasma generated by a dust grain passing through very thin films within an experiment array designed to accurately determine the path of the grain within the array. The first method is used when the particle velocities within the array are low, i.e., between 10 and 100 m/s. The second method is used for particle velocities greater than 2 km/s. Recent laboratory studies have also been conducted to measure the charge present during a hypervelocity impact event.

The presence of an intense light flash upon impact has suggested that ionization of the impact site material as well as the impactor has occurred. The impact flash phenomenon has been studied extensively by several groups over the last three decades and has been attributed to the "jetting" of material near the impact site, e.g., shaped charge explosion. Luminous matter created near the impact site has also been seen to produce a spontaneous magnetic field along the axis of the impactor. Even though a complete understanding of the event still eludes researchers, the collection of charge liberated during the event has been well documented. It is that collected charge that can be utilized to establish time of flight and, consequently, the velocity vector of the penetrating particle. The assessment of the efficiency of a dust grain to penetrate a specific thickness of thin film has been conducted by both theoretical and experimental means.

The principal theoretical approach has been to perform calculations using a hydrodynamic computer code CTH [6]. This tool provides a computational laboratory where hypervelocity impacts may be controlled and observed. The complete perforation of a thin film will create a significant amount of data depicting the event. The most useful utilization of the modeled event has been the determination of the hole size generated by the penetrating dust grain. Provision must be made for the most crucial parameter controlling the simulation, i.e., time to maximum expansion of the penetration hole. That time must be commensurate with the expansion of the shock front and the rarefaction wave. Pressure, density, and temperature in the film must also be tracked to assess the progression of the energy in the material. Of equal interest is the strain rate, which signals the relaxation of the material following the passage of the shock front through the material. Once the strain rate has

reduced in value near the walls of an impact site, a commensurate decrease is seen in the other extensive variables of the interaction, and thus confirms that the progression of the crater's diameter has been halted. Penetration mechanics suggests that the more the diameter of the impactor exceeds the thin-film thickness, the less will be the erosion of the projectile during passage through the film. Thus,  $D_p/T_f$  must be maximized in order that the fragmentation of the dust grain may be minimized.

**Penetration Mechanics:** Hydrodynamic computer programs have benefited greatly from the data provided by many experiments designed to assess the effects of high-shock conditions present in materials. Principally, the "hydrocode" calculations possess equations of state that describe both the elastic-plastic and the phase transition with melt of the high-shock regime. For several years research has been underway to assess the association between specific thermodynamic properties of materials and the process of fragmentation, i.e., the catastrophic failure of materials.

The primary description of the event has evolved from the study of the very-early-stage creation of ejecta spray patterns liberated from the semi-infinite target via hypervelocity impact and the subsequent shock wave disruption of the target and projectile material. The formation of ejecta patterns seen in experimental work was utilized to test the validity of a hydrodynamic computer code designed to track the progress of a hypervelocity cratering event. Hypervelocity impact experiments have suggested a set of preferred angles, viz., 15°, 45°, 60°, 80°, at which the ejecta spray size distribution is spread by some as-yet unexplained process. In practice most hydrocodes will reproduce results commensurate with those derived from normal and oblique semi-infinite target impacts.

Perhaps the most important results of these analyses will be tested, i.e., angles of incidence with surface controls size distribution of ejecta, by data collected via EURECA TICCE while on orbit. Upon return last June 1993 materials exposed to 11 months of LEO have yielded data of oblique impacts with a specific capture material located near impact sites to capture ejecta particles for size and velocity distribution analysis.

Using CTH, many properties of hypervelocity particle thin-film capture techniques have been theoretically analyzed. Hypervelocity perforation of thin films will fragment glass spheres that have been used to simulate interplanetary dust particles (IDPs). Upon impacting a thin film with hypervelocity, a small IDP analog will fragment if, and only if, the film thickness and the IDP analog's velocity are sufficient. Hence the coupled parameters of velocity and  $D_p/T_f$  ratio will determine the degree of fragmentation the thin film will cause in the IDP analog. With a hydrocode calculation one can investigate many different values for velocity and film thickness. The fragmentation process arises from the activation of various fragmentation sites within the nonperfect crystal. The sites that are crystal defects can be stimulated into action by a shock wave's passage through the sites, which will cleave the crystal along a defect boundary. Defects have been found to activate at a specific shock velocity and thus can be by size sensitive to high or low velocity (2–10 km/s).

CTH has been used to investigate the penetration mechanics of small particles impacting and perforating a thin film. The fragmentation of IDP analogs has been investigated to determine penetration parameters of thin films. The same analysis can be applied to the fragmentation of targets or projectiles or even secondary impacts due to ejecta sprays. Molecular dynamics (MD) computer programs can provide a means to establish the velocity distribution of the

small particles created during a fragmentation event. Utilization of MD can provide a means to describe particle fragment motions. Fragmentation events can therefore be fully characterized using MD since particles will move under Newtonian kinematics and thus articles can be employed in the interaction to develop macroscopic scaling rules.

**Passage of a Particle Through a Thin Film:** The pressure an impacting dust grain experiences during a hypervelocity impact can be sufficient to alter the state of matter of the particle. However, very short-duration high-pressure pulses can be sustained in large dust grains without fragmentation or complete phase change occurring. In this class of events the cross-sectional area of the impinging dust grain and the thickness of the target are important components of the interaction. The surface area over which a force is administered and the length of time in which the impulse is delivered define the magnitude and the duration of the pressure pulse that gives rise to a sustained shock front in the material. The duration of the shock front wave is also determined by the depth of penetration and therefore the thickness of the target,  $T_f$ . If one considers the dynamics of an impact event from the perspective of a penetrating particle, the ratio that defines the aspect ratio of the dust grain, i.e.,  $L/D_p$ , may be investigated to determine the residual length of the particle upon encounter with a thin target. In the case of a thin-film penetration event, the ratio of interest is that between the diameter of the dust grain,  $D_p$ , and the thickness of the film,  $T_f$ . It has been well documented [7] that a projectile with a high aspect ratio will penetrate to a depth defined by the following relationship

$$p = L \left( \frac{\rho_p}{\rho_t} \right)^{0.5} \quad (1)$$

The penetration depth,  $p$ , of a rod into a thin film can be equated with the film thickness,  $T_f$ , and the residual length  $L_R$  of the penetrating rod can be equated with the residual diameter of the dust grain. The change in the diameter of the dust grain can be roughly estimated to be

$$\frac{L_R}{D_p} \sim 1 - \frac{T_f}{D_p} \left( \frac{\rho_p}{\rho_t} \right)^{0.5} \quad (2)$$

In the case of a ratio of  $D_p/T_f = 30$  the residual diameter of the dust grain would be greater than 90% by this estimation. Even though the not-eroded nature of the material composing the incident dust grain can only be assessed by other measurement means, the foregoing analogy may serve as a metric for further analysis (Fig. 2).

Of particular interest in these investigations is a specific empirical form that relates penetration hole size with the diameter of the penetration hole. This experimentally derived equation for the description of the penetration relationship for Fe projectiles impacting Al films of various thicknesses was developed by Carey, McDonnell, and Dixon equation (CMD) [8]. The CMD empirical equation has been compared with the results of computer simulation of hypervelocity impacts and has been plotted for various velocities of interest for surfaces flown in LEO (Fig. 3)

$$\frac{D_h}{D_p} = 1 + 1.5 \left( \frac{T_f}{D_p} \right) v^{0.5} \left[ \frac{1}{1 + \left( \frac{T_f^2}{D_p^2} \right) v^n} \right]; \quad n = 1.02 - 4 \exp(-0.9 v^{0.9}) - 0.003(20 - v) \quad (3)$$

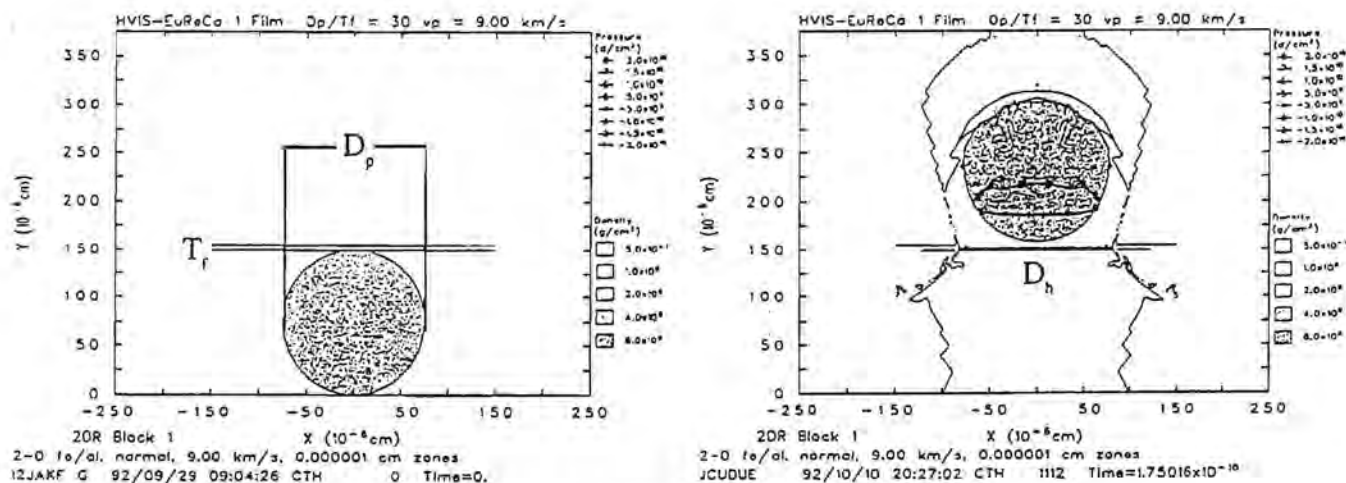


Fig. 2. CTH output to depict the measurement of a film thickness,  $T_f$ , a particle diameter,  $D_p$ , and a hole diameter,  $D_h$  for a penetration of the 500 Å EURECA/TICCE HVI Al thin film at a velocity of 9 km/s.

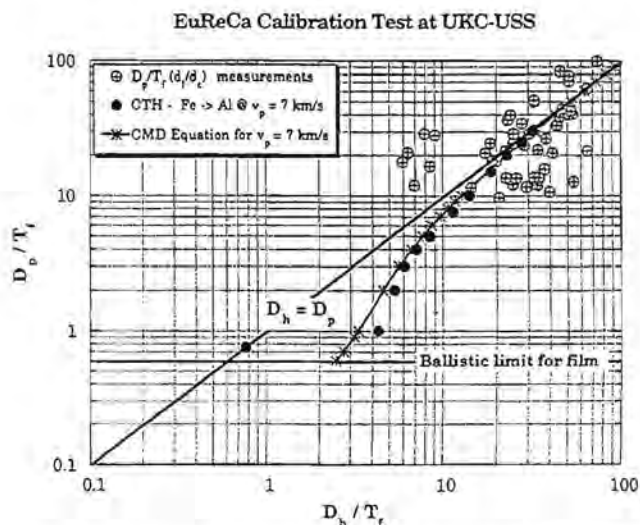


Fig. 3. Comparison of experimental penetration data with CMD and CTH data for EURECA/TICCE HVI 500 Å Al thin film.

**Experimental Results:** Results of both two-dimensional and three-dimensional computer simulations of the hypervelocity impact events that penetrate the STS and the EURECA 1 thin films will be reported. A relationship between the particle diameter,  $D_p$ , and the diameter,  $D_h$ , of the hole created in a 500-Å Al thin film ( $T_f$ ) and micropore foam ( $T_m$ ) for relevant particle and target parameters will be derived and will be compared with empirical equations. That relationship will be used to analyze *in situ* data of the thin-film experiments flown in LEO, and to determine the size distribution of grains that penetrate the thin films and are captured intact in the micropore foam [9].

Thin-film perforation events liberate a substantial quantity of charge that can be collected near the impact site. The collection sites can be so subdivided that a location in a plane can be established

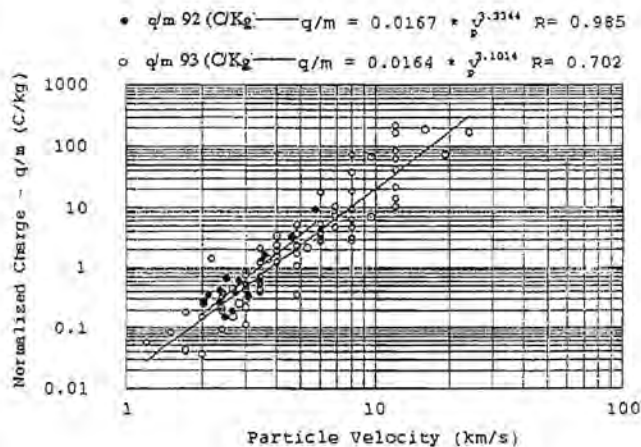


Fig. 4. Thin-film charge collection data obtained during hypervelocity penetration of a 250 Å Al thin film at the University of Kent at Canterbury during the summer of 1992 and spring of 1992.

with high accuracy. However, in order to provide the highest confidence for the survival of a dust grain while penetrating a thin film, the thickness and the density of the material composing the film should be minimized. The magnitude of charge liberated by a thin-film perforation has been assumed to be a strong function of the film thickness. The use of thinner films would thus imply a degradation in the position accuracy, especially for the very smallest dust grains ( $dp \leq 0.1 \mu\text{m}$ ). The preliminary results of experiments conducted at the University of Kent at Canterbury, Unit for Space Science (UKC-USS), indicate that the charge yield by perforation of a 250-Å Al film (Fig. 4) is commensurate with a 500-Å film (Fig. 5).

Further testing has provided data for particle velocities approaching 40 km/s. Each of the thin-film perforation events shown above were verified by a charge collection immediately in front of



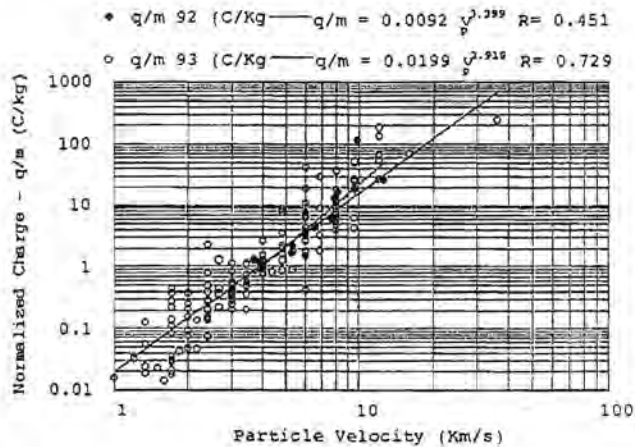


Fig. 5. Thin-film charge collection data obtained during hypervelocity penetration of a 500 Å Al thin film at the University of Kent at Canterbury during the summer of 1992 and spring of 1992.

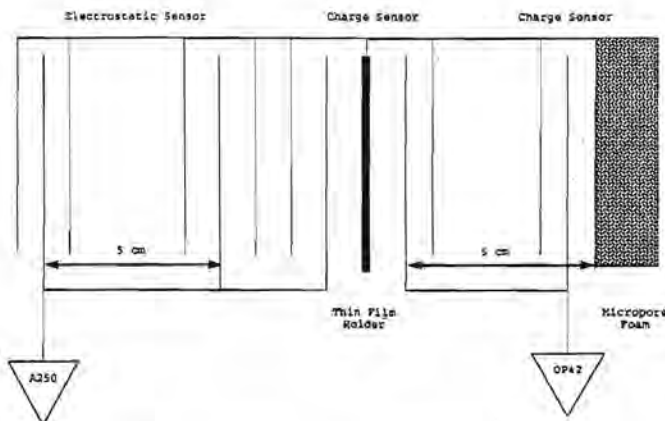


Fig. 6. Diagram depicting the configuration of the system used to collect the data shown in the previous two graphs.

an underdense foam intact capture cell situated 5 cm behind the thin film. The coincidence of all sensors recorded the time of flight, electrostatic charge, thin-film perforation, and impact charge liberation.

Charge liberation events due to hypervelocity impacts that have penetrated an ultrathin film (Al 250-Å and 500-Å) are captured in an underdense foam. Figure 6 illustrates the configuration for the experiment. Figure 7, a representative trace downloaded from the LeCroy scope during the experimental activity, can be interpreted as follows: Each point (10,000 points per division) represents  $5.00 \times 10^{-9}$  s of time. Given that the separation distance between the two electrostatic charge sensors is 5 cm, the velocity of the dust grain is 3.3 km/s. The amplitude of each pulse in the electrostatic region measures the inherent charge on the dust grain. The velocity of the dust grain allows the determination of the mass of an assumed sphere. Efficient charge collection immediately in front of the thin film is the result of a focusing potential of -45 V on the grid wires.

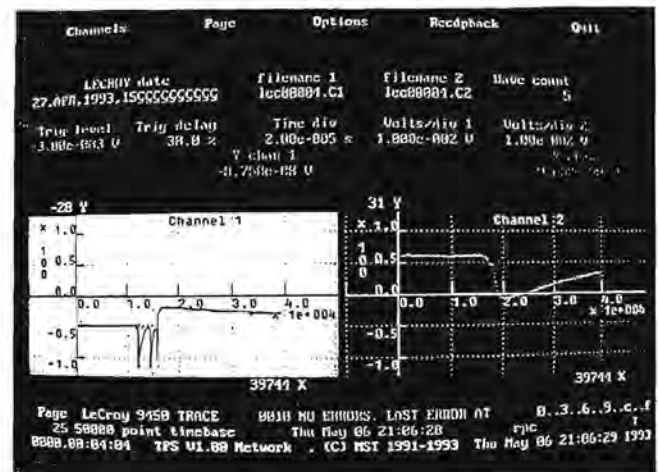


Fig. 7. Captured data represent the detection of an induced electrostatic charge from the approaching charged particle, the charge liberated when the particle penetrates a 250 Å or 500 Å Al thin film and the charge liberated when the particle is captured in a micropore polyfoam. Signals downloaded from LeCroy oscilloscope using software package developed by R. Miller of UKC-USS.

The charge collected reflects a jet initiation event and thus will be most pronounced on the front side of the thin film. Charge collected behind the thin film is much more diffuse and thus is broader in time. It should be apparent that the impact into foam liberates charge in excess of the charge measured at the rear of the film. A time of flight between the thin-film perforation and the foam impact can be analyzed to determine a change in the velocity of the perforating dust grain. Charge liberated from the C-containing material is evidenced by the excess of charge on the charge collection grid immediately in front of the foam.

**Conclusion:** The proposed ultra-thin-film experiment has been tested in the laboratory to establish the quantity of charge liberation during an intact capture event. The entire ultra-thin-film system has proved to be mechanically sound after experiencing the launch loads of the shuttle. Also, after 11 months' exposure to the LEO space environment the HVI/BUSSL 500-Å Al films exhibited no penetrations due to mechanical effects. Theoretical calculations have facilitated the determination of the penetration efficiency of the thin-film materials selected. Subsequent laboratory studies as well as analysis of the thin-film experiment flown on EURECA have demonstrated the optimization process has produced a highly successful combination of materials. These tests constitute an initial calibration of the thin-film charge detection system that will provide data depicting the dynamics of grains that COMRADE, SOCCER, or LDEF II will collect.

**References:** [1] Alexander W. M. et al., this volume. [2] Maag C. R., this volume. [3] Heppner W., this volume. [4] Borg J. et al. (1993) *1st European Conference on Space Debris*, in press. [5] Alexander W. M. et al. (1971) *Space Research XI*, 279. [6] McGlaun J. M. et al. (1989) *Intl. J. Impact Eng.*, 10. [7] Zukas J. A., ed. (1990) *High Velocity Impact Dynamics*, Wiley. [8] Carey W. C. et al. (1985) *85th Proceedings of IAU*. [9] Tanner W. G. (1992) *Intl. J. Impact Eng.*, in press.

# NONDESTRUCTIVE TIME-OF-CAPTURE, LOCATION, AND VELOCITY SENSING IN INTACT CAPTURE. P. Tsou, Jet Propulsion Laboratory, Pasadena CA 91109, USA.

Since cometary dust, like cosmic dust, is essentially randomly distributed, knowing the time of the dust capture and the location of the capture on the collector permits the identification of the specific dust particle captured. Velocity information helps to determine the trajectory of the dust particle. Our discovery of a very suitable acoustic sensor and fruitful experimental results have led to the realization of a flight velocity sensor with intact capture underdense media [1].

Velocity sensing of hypervelocity particles was a significant field of interest from the 1960s to 1970s. Generically, velocity sensing has been approached by either of two methods: first, detecting direct plasma or light emissions [2,3] onto a solid surface, or second, performing time-of-flight by film penetration [4], or by detecting charged particles passing a static electric field [5]. Impact plasma techniques required the destruction of the particles. Multiple-film penetrations were also destructive, especially for smaller particles. There is a need for an integrated, reliable, and simple location and velocity sensor compatible to our intact capture underdense medium without contributing additional damage to the captured particle.

**Film Piezoelectric Sensor:** Acoustic sensing was used for micrometeoroid detection in the first free-world satellite, Explorer. However, traditional acoustic sensors (quartz or ceramic) have a significant mechanical mismatch with underdense media and can produce considerable microphonic noise. Kynar piezo film (polarized polyvinylidene fluoride) is free from both mechanical mismatch and significant noise problems. Kynar has a very wide frequency response from 0.005 to  $10^9$  Hz; a low acoustic impedance, which better suits underdense media; a high voltage output, 10 times higher than ceramics; good stability against oxidants and UV; and good noise immunity. This sensor film can be readily made as large surface areas permitting large-scale integration with standard photo printing techniques for intricate patterns and electrical contacts.

**Capture Experiments with Kynar:** We have performed experiments with Kynar on the two promising underdense capture media, polymer foam and silica aerogel [6]. Tests have ranged from 200 m/s to 6 km/s with solid 50–75- $\mu$ m glass and 1.6–3.2-mm Al projectiles. A characteristic acoustic signal from a 75- $\mu$ m glass projectile captured in aerogel at 5.5 km/s is shown in Fig. 1. The distinct delays among sensors at different distances from the impact point can be seen clearly. The arrival times of the signal at sensors are linear up to 10-cm separation from sensor to impact point. From the delay times at different sensors, the location of the specific particle in the capture medium can be determined.

The peak amplitude of the acoustic signal in the time domain has been related to a function of the speed of the projectile. Acoustic experts suggest proper frequency filtering of the acoustic signal will clarify the relationship between the energy/momentum of the projectile and acoustic signal characteristics such as rise time and amplitude. Figure 2 shows a normalized response of two Kynar sensors on the same polyethylene foam with respect to initial projectile speed.

A most troublesome aspect of acoustic sensing is microphonic noise. Spectrum analyses of signals generated by hypervelocity

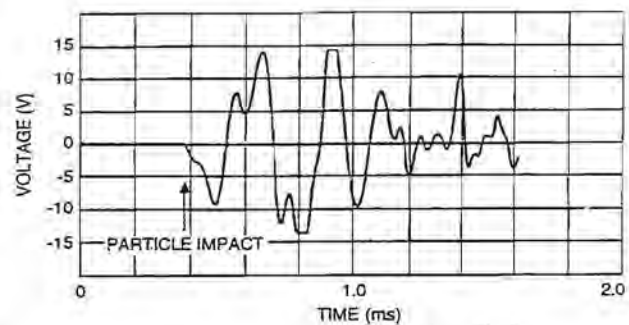


Fig. 1. Typical acoustic sensor impact signal.

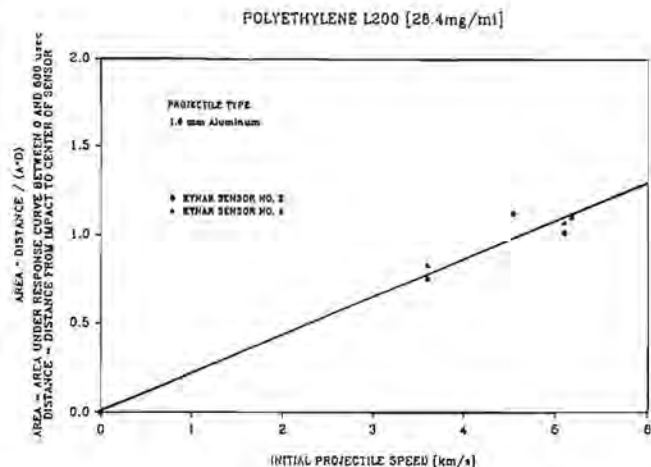


Fig. 2. Sensor response vs. speed of projectile.

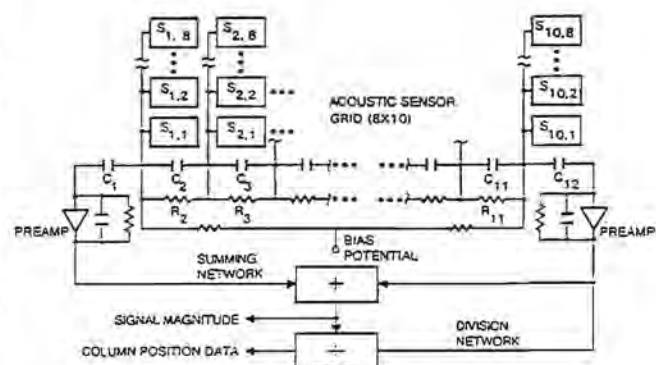


Fig. 3. Acoustic sensing schematic.

impact into underdense foam revealed a small characteristic bandwidth. This allows the Kynar sensor to be mounted to the foam directly without coupling to surrounding structures that could produce microphonics. Kynar is not prone to microphonic noise as shown by one experiment where a sensor was not attached to the underdense medium and left in suspension. No signal was picked up by the sensor from either the launch of the two-state light gas gun or the mechanical reverberation of the target tank.

Both the time of capture and capture location can be derived from an array of Kynar sensors. A schematic of this  $10 \times 8$  grid system is shown in Fig. 3. The second component of the velocity vector, direction, is obtained by measuring the particle penetration track. This track direction can be measured to better than 1%. This accomplishment makes available a very simple and integrated non-destructive velocity sensor with intact capture underdense media.

**Applications:** For the SOCCER mission, this nondestructive sensor provides a real-time signal of dust captures as well as temporal and spatial distributions of captured dust. The dust velocity is expected to be all normal to the collection surface. For Earth-orbital cosmic dust collection, this nondestructive sensor can provide a mark indicating the orientation of the collector at the time of capture for a specific particle. With postflight track morphology analysis, the particles' trajectory can be ascertained, which allows the association of the dust's parent sources.

**References:** [1] Tsou P. et al. (1989) *LPS XX*, 1134. [2] Frichtenicht J. F. (1965) *NASA Contrib. No. NASW-936*. [3] Eichorn G. (1975) *Planet. Space Sci.*, 23, 1514. [4] Berg O. E. et al. (1969) *Rev. Sci. Instr.*, 40, 333. [5] Auer S. et al. (1968) *EPSL*, 4, 178.

**THE PHYSICS OF INTACT CAPTURE.** P. Tsou<sup>1</sup>, D. J. Griffiths<sup>2</sup>, and A. L. Albee<sup>3</sup>, <sup>1</sup>Jet Propulsion Laboratory, Pasadena CA 91109, USA, <sup>2</sup>Oregon State University, Corvallis OR 97331, USA, <sup>3</sup>California Institute of Technology, Pasadena CA 91109, USA.

The ability to capture projectiles intact at hypervelocities in underdense media opens a new area of study in physics. Underdense material behaves markedly different than solid, liquid, or gas upon hypervelocity impact. This new phenomenon enables applications in science that would either not be possible or would be very costly by other means. This phenomenon has been fully demonstrated in the laboratory [1] and validated in space [2]. Even more interesting is the fact that this hypervelocity intact capture was accomplished passively. A better understanding of the physics of intact capture will lead to improvements in intact capture. A collection of physical observations of this phenomenon is presented here.

**Introduction:** Since it was accepted at one time that a projectile going faster than a speeding bullet could not be captured intact, it was believed that the only way to stop such a particle, especially at higher hypervelocities, would be to convert the particle into gas and capture the vaporized condensates, i.e., the atomization process. Capturing and studying a cosmic dust particle or any hypervelocity object by atomization is not unlike first reducing the object to atoms, and then reconstructing the object from the gas condensates. This approach proved to be very difficult, not unique, and fraught with uncertainties. By contrast, capturing a portion of a hypervelocity particle intact would preserve the object's "structure"

(phase, morphology, and mineralogy) and its full chemical and isotopic compositions. Reconstruction of the object would be easier and carried out with more confidence.

But how can intact capture of hypervelocity particles be possible? A gedanken experiment provided the inspiration for investigating just such a solution. Conceptually, there exists an extremely thin diaphragm that, when penetrated by a hypervelocity projectile, will not affect the integrity of the projectile. The diaphragm, being extremely thin, will absorb only a very small amount of the projectile's kinetic energy. However, after penetrating a very large number of such diaphragms at noninteracting separations, all the energy will be absorbed, leaving the projectile intact and at rest. Since the projectile has a finite initial kinetic energy, the number of diaphragms and the total separation between them may be very large, but is nevertheless finite. In actuality, the projectile need not be 100% recovered; by sacrificing a portion of the projectile, the capture can be achieved with even thicker diaphragms and fewer of them. This approach is a considerable improvement on the process of atmospheric reentry of meteorites, since we can control the diaphragms' material, thickness, and separation distance. The challenge then is one of reducing this arrangement to a practical instrument by using a good energy-absorbing material and reducing the number of diaphragms or size of the instrument required. This gedanken experiment has served as the guiding concept for designing experiments and developing practical materials to achieve intact capture.

**Physical Phenomena:** To generate physical data on intact capture, systematic and exploratory capture simulation experiments were performed with two-stage light gas guns up to 7 km/s and electrostatic accelerator up to 20 km/s. These simulation experiments consisted of launching projectiles with known mass and integrity at known speeds into capture media in a vacuum and at room temperature. The captured projectiles were then characterized by observing the morphology of the captured projectile and amounts of mass recovery. The capture media were examined for track dimensions, mass loss, and surface composition. Analysis tools used included optical microscope and scanning electron microscope.

**Recovery ratio.** One of the first obvious measures of hypervelocity intact capture is the projectile mass recovery ratio, (i.e., the ratio of the recovered projectile mass to the original mass). Extensive data on metal projectiles have been presented [3]. Figure 1 shows the recovery ratios of three different diameters of glass projectiles captured in polyethylene foam. Using an ablating re-entry vehicle type of model formulation, a good descriptive fit of the intact mass recovery ratio data has been achieved [4].

Conventional hypervelocity impact theory, working in the hydrodynamic limit, takes the target's bulk density to be the only target parameter influencing solid impact into solids. Applying this reasoning, the lowest bulk density target produces lower shock levels and lower temperature and thus should have the highest recovery; however, our data show that projectile recovery is more sensitive to media structure (cell size and wall thickness) and material thermal properties (decomposition point) than media bulk density [5].

**Penetration track.** Tracks or cavities produced deep in the underdense media and caused by hypervelocity projectile penetration are very different from craters formed in solid-to-solid impacts. The tracks left in underdense media tend to be thin and long and typically carrot-shaped. A track can be characterized in terms of



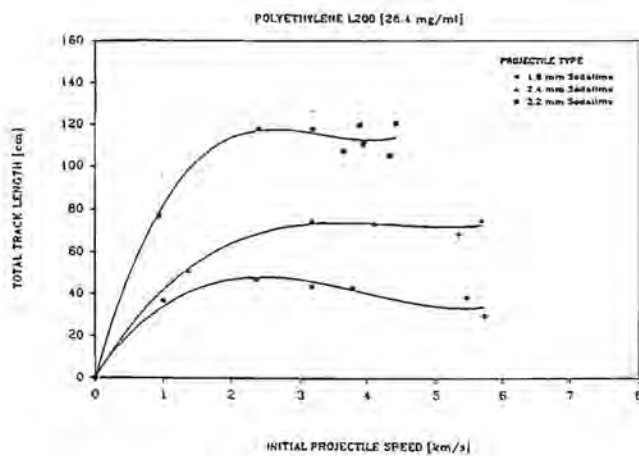


Fig. 1. Capture penetration curve.

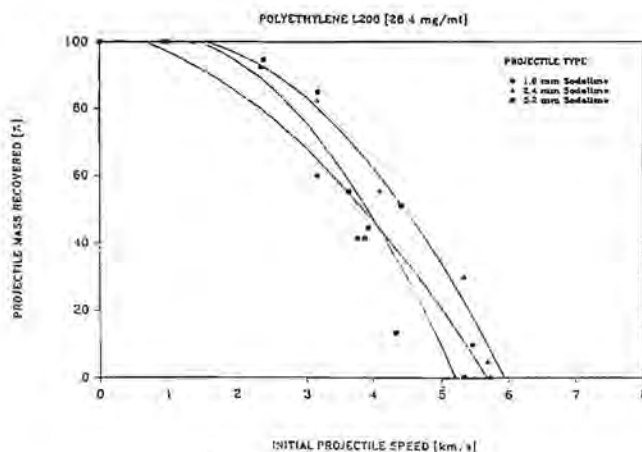


Fig. 2. Projectile recovery.

three regions: initially, the track quickly widens to a maximum, then gradually narrows, and finally bores through the medium with approximately the diameter of the projectile. The surface of the initial region tends to be rough and broken along the wall of the track cavity. Following the broken region is the transition zone, typified by smoother walls. The final region of the track shows shearing of the medium.

The penetration track lengths for the same set of experiments shown in Fig. 1 are presented in Fig. 2. Track lengths tend to be longer for lower-density media if the media structures are similar. The total track-length-to-projectile-diameter ratio ranges from about 50 to 250, permitting the determination of the projectile direction error to less than  $1^\circ$ . Assuming a simple  $F = ma$  type of equation of motion and characterizing the medium erosion in three regions, a descriptive model of the total track lengths was formulated for various projectile speeds that fitted experimental data well [4].

The combined effects of mass recovery, penetration track length, and track profile as functions of the projectile initial speed are shown in Fig. 3 as one display. It can be seen that the total penetration track tends to peak in the region of 2 to 3 km/s. The general shape of the penetration track curve seems to be invariant: a steep rise (initially linear) to a peak, then a drop to a near plateau, then a

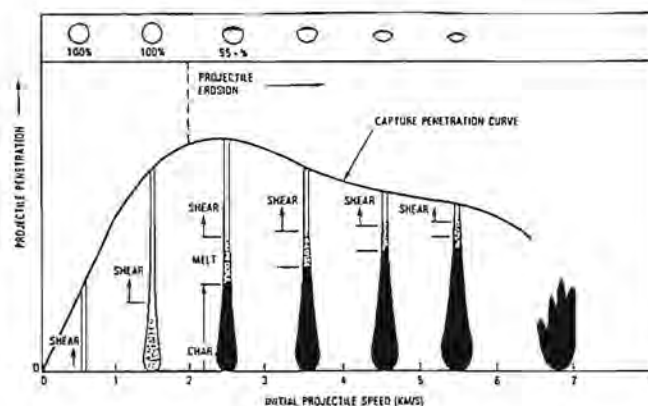


Fig. 3. Hypervelocity intact capture effects.

steep fall, and, finally, termination. A second derivative of this generic penetration track curve indicates three inflections or four regions: an all-shear region with no projectile mass loss, a media-melt region with minor projectile mass loss, a media-pyrolysis region where significant projectile mass loss begins, and, finally, a projectile disintegration region where the track is greatly enlarged and branched.

The physical mechanisms of projectile mass loss in underdense media at hypervelocities are very complex and not yet well understood. Based upon fluid dynamic formulations, drag force, and thus the peak temperature, higher mass recovery for larger projectiles is favored and is indeed indicated here. The projectile surface-to-mass ratio increases for smaller projectiles.

**Penetration track volume.** The capture medium absorbs the projectile's kinetic energy as it penetrates the medium; the manner of this energy absorption is reflected in the shape and volume of the penetration track. Since the time required to produce pyrolysis features in the media must be much greater than the projectile penetration time (about 200  $\mu$ s over a 100-cm distance for a 3.2-mm projectile), the actual shape of the track cavity must have been developed long after the projectile had come to rest. Typical track profiles for the polyethylene foam (for a 3.2-mm pyrex projectile) are shown in Fig. 4.

The volume of the track cavities correlates well with initial projectile speeds. Figure 5, using the same medium as shown in Fig. 4, plots the track volume with respect to initial projectile speed. Cavity volume is also proportional to projectile size. Since projectile velocity has two components, speed and direction, this volume-to-speed relationship provides the speed component; track orientation gives the direction. This is another valuable feature of intact capture by underdense medium: Not only is the projectile captured passively, but the projectile velocity is also recorded passively. With the knowledge of projectile velocity and given the orientation of the capture instrument, the original projectile trajectory can be calculated.

**Projectile deceleration profile.** To ascertain the manner in which the projectile loses its mass as it penetrates the underdense medium and the timing during which the loss occurs, the projectile's speed profile during capture was sought. A variety of methods to accomplish this were explored. Early success was achieved with the

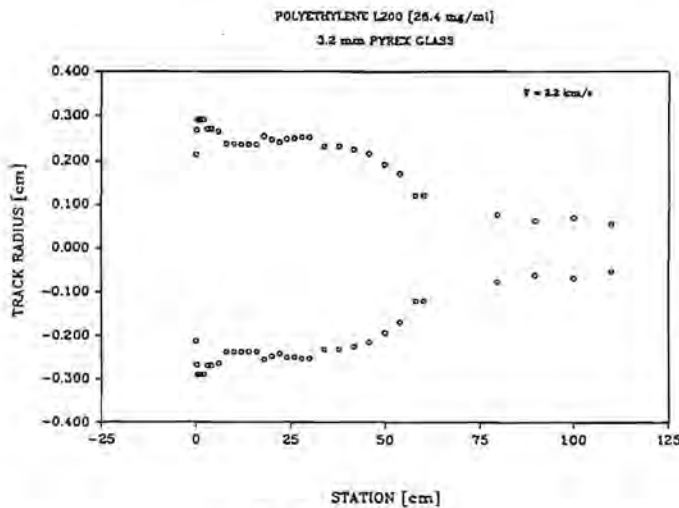


Fig. 4. Track profile.

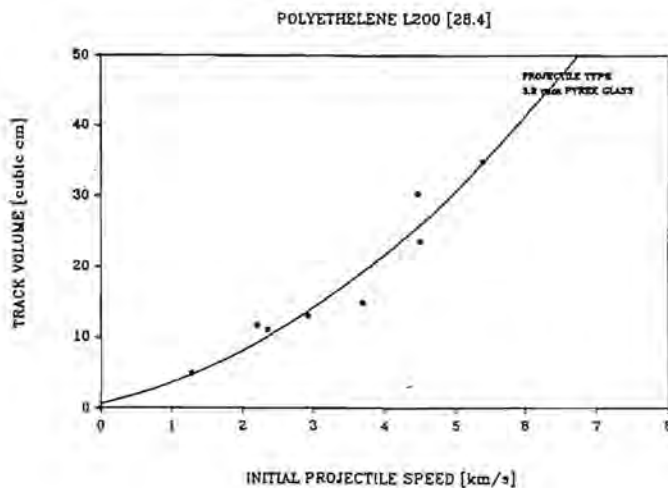


Fig. 5. Track volume.

standard and simple breakwire approach using 5- $\mu$ m-thick Cu labyrinth imprints on 25- $\mu$ m Kapton film. The breakwire was considerably stronger than the capture medium; consequently, a nondestructive motion sensor would be preferred. We adapted the magnetic pickup approach used in light gas guns to determine the passage of the projectiles. Deceleration profiles were obtained for 2.4-mm stainless steel projectiles only (the current induced on Al projectiles was not sufficient for magnetic pickup); even then, signals beyond the second station were noisy. Finally, a set of X-ray shadow graphs captured the deceleration of the projectile in four positions. As it turned out, the results from all three methods are comparable, as shown in Fig. 6.

These profiles indicate surprisingly near-linear initial deceleration. Our original hypothesis had been a much steeper exponential drop followed by slow deceleration to rest. However, this near-linear deceleration was predicted by Sandia National Laboratories' CSQII Eulerian finite-difference program for two-dimensional material response, with the underdense medium approximated by the snowplow model. This deceleration profile provides important insight into the manner of energy dissipation, useful for theoretical developments and for developing an improved intact capture medium.

*Real-time dynamics.* The real-time action and reaction between the projectile and the capture medium is immensely important to understanding the physics of the intact capture phenomenon. Since a hypervelocity intact capture event is completed in less than a fraction of a millisecond, means to provide a temporal expansion of the event are desired. Efforts to ascertain the real-time dynamic impact chemistry of the projectile and the capture media through spectroscopy [6] have proved useful in understanding dynamic impact chemistry and making temperature estimates. A wide range of wavelengths and means of spectra acquisition were examined. To determine the effectiveness of different approaches, from ultraviolet to visible have been acquired by using prisms, reflection, and transmission gratings that are then recorded by photographic and

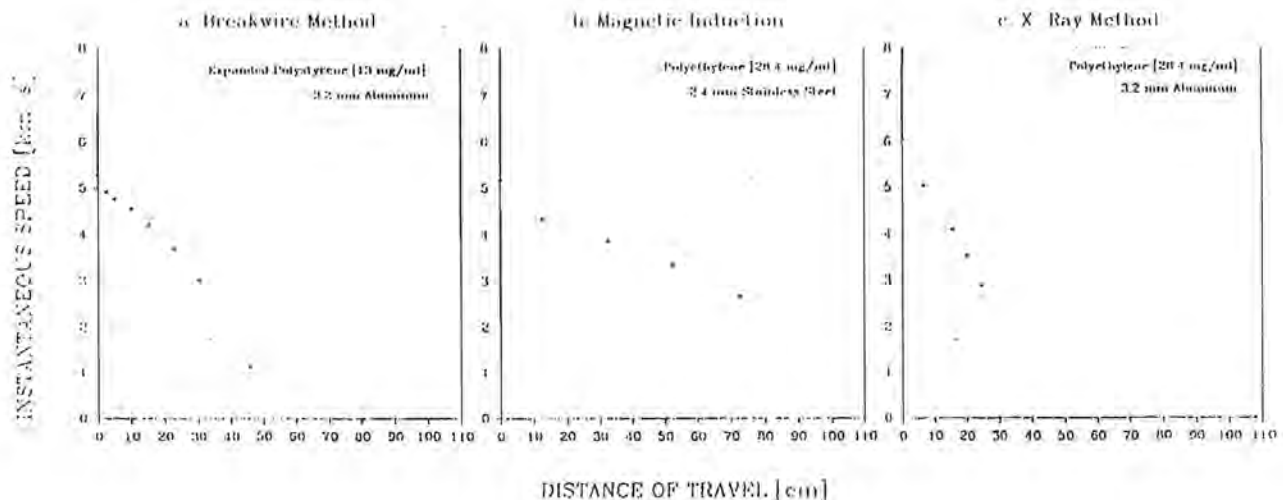


Fig. 6. Projectile deceleration profile.

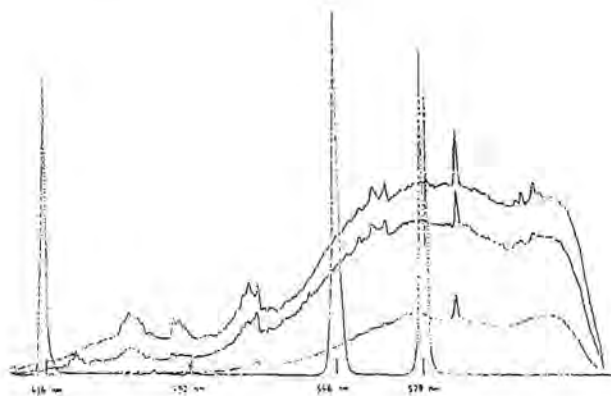


Fig. 7. Spectrum of Al into mylar.

electronic media. The first spectrum of an intact capture event is shown in Fig. 7 and was obtained from a 3.2-mm-diameter Al sphere impacting multilayers of 10- $\mu$ m mylar films with the NASA Ames reflection grating spectrograph. The black-body temperatures determined for the different polymer underdense media are in the range of 2500 to 3100 K [6].

**Momentum transfer.** A characteristic of intact capture is energy dissipation through momentum transfer by dragging the capture medium with the moving projectile. For the polymer capture medium, densely packed and melted foam would form a shell around the forward portion of the projectile. At times, the mass detached from the capture medium can be as much as the captured projectile. Fused glass is often found around the captured projectile in aerogel. This accumulation must take place after the transitional region and further protect the projectile by both momentum transfer and heat removal.

**Medium energy absorption.** One criterion that can be used to measure the overall performance of a capture medium is the percentage of the projectile's kinetic energy that medium absorbs; the unabsorbed energy produces the projectile damage. This energy absorption was crudely estimated by recording the mass of segmented foam pieces before and after a simulation experiment. Estimates of the absorbed energy were made from the loss of foam mass, the track-cavity volume, and estimated thermal constants of the capture medium and Al.

For a 3.2-mm Al projectile captured in 32-mg/ml expanded polystyrene at 6 km/s (875 J total kinetic energy), the foam's net mass loss was about 1.2 g. Using listed values of specific heat and heat of depolymerization of polystyrene of 400 J/g and 660 J/g respectively, all the total kinetic energy of the projectile can only depolymerize about 0.68 g of polystyrene. Photographs of the back ejecta substantiated this by showing substantial amounts of solid particulates. Based on measurements of the track volume, the equivalent mass loss in the track cavity was compared to the actual mass loss. This difference, about 0.6 g, should be the portion of the foam that was melted and resolidified along the track wall. Using listed polystyrene foam heat of fusion of 87 J/g, about 34% of the incoming kinetic energy would be used to melt the polystyrene. Other components of medium energy absorption, such as mechanical work, are more difficult to estimate and assumed to be relatively small.

As a check, the amount of energy absorbed by the projectile can be estimated from the measured mass loss of the projectile. Projectile mass loss can be due to vaporization, melting, or mechanical ablation. Since the shock pressure generated at 6 km/s is much too low to cause vaporization of Al, the energy absorbed by the projectile was assumed to have melted, an upperbound estimate. Using a value for Al's heat of fusion of 400 J/g and a specific heat of 9 J/g, a little more than 1% of the incoming kinetic energy contributed to the projectile mass loss. Compared to about 11% energy absorbed by the Apollo capsule in atmospheric reentry, underdense media make good intact captures.

**Summary:** The intact capture of a hypervelocity projectile would first punch a straight and narrow track through an underdense medium not much larger than its diameter in less than a millisecond covering about 100 times its diameter before coming to rest. The projectile would be in one piece, wedged at the end of the track. Some time later, as the high-energy ejecta from the medium and projectile deposited along the track wall have time to dissipate thermally, the narrow track would be enlarged into a carrot shape, as shown in Fig. 3. At the medium entry, about the first dozen cells, the projectile, and the medium would not be damaged except for a clean hole left in the medium. Beyond the entry, energetic ejecta would build up rapidly to a peak in the medium. The projectile would decelerate in a near-linear fashion before gradually coming to rest. Most of the projectile mass loss seems to occur before the point of peak diameter in the track. The actual peak shock may precede the point of track peak due to the forward motion of the ejecta.

Small cellular members in underdense media generate very low shock levels to both the projectile and medium. Underdense media readily absorb projectile energy at low thresholds, providing an efficient and low-threshold energy sink. As the aerogel capture medium is very porous, partial compaction allows another means of energy dissipation by momentum transfer. Effective capture media must have sufficient material strengths to hold medium members in place, preventing prolonged accumulation of damaging plasma, while not contributing added damage to the projectile. In all, underdense media emerge as a phase of material that decelerates and preserves a hypervelocity projectile gently and efficiently.

The signature left by an intact capture is a long, thin track in the capture medium. Low bulk density would be necessary for intact recovery; however, within a certain range, the medium's bulk density tends to affect the shape of the track more than the mass recovery. The structure of the medium, configuration, and size of cells affects mass recovery directly, both in terms of the quantity and the deformation of the recovered projectile. Other sensitive parameters are the structural and thermal properties of the capture medium.

As the density of a medium is lowered, the penetration track tends to become longer. For the same density medium, but at higher projectile speeds, the track tends to be both wider and shorter. The projectile entry hole varies with projectile speed: At low speeds, the entry hole is nearly the same diameter as the projectile; for higher speeds, the entry-hole diameter increases—reaching as much as three to four times the projectile diameter.

**References:** [1] Tsou P. et al. (1988) *LPS XIX*. [2] Tsou P. et al. (1993) *LPS XXIV*. [3] Tsou P. (1990) *Intl. J. Impact Eng.*, 10. [4] Peng S. T. J. et al. (1987) *LPI Tech. Rpt. 88-01*. [5] Tsou P. et al. (1991) *APS*. [6] Tsou P. et al. (1993) *Intl. J. Impact Eng.*, 13.



# **PVDF FLUX/MASS/VELOCITY/TRAJECTORY SYSTEMS AND THEIR APPLICATIONS IN SPACE.** A. J. Tuzzolino, Laboratory for Astrophysics and Space Research, The University of Chicago, Chicago IL 60637, USA.

The current status of the University of Chicago Polyvinylidene Fluoride (PVDF) flux/mass/velocity/trajectory instrumentation is summarized. The particle response and thermal stability characteristics of pure PVDF and PVDF copolymer sensors are described, as well as the characteristics of specially constructed two-dimensional position-sensing PVDF sensors. The performance of high-flux systems and of velocity/trajectory systems using these sensors is discussed, and the objectives and designs of a PVDF velocity/trajectory dust instrument for launch on the Advanced Research and Global Observation Satellite (ARGOS) in 1995 and of a high-flux dust instrument for launch on the Cassini spacecraft to Saturn in 1997 are summarized.

**Introduction:** For cosmic dust, the scientific importance of *in situ* particle velocity/trajectory measurements and, in particular, of particle trajectory measurement combined with compositional and isotopic information on the captured particle residue has been discussed in the literature and in various workshop reports [1-9]. In near-Earth space, where both cosmic dust and orbital debris contribute to the particulate environment, velocity/trajectory measurements permit discrimination between these two particle classes [1,3,10,11].

For regions of space where dust flux intensities may be extremely high and may coexist with backgrounds of high fluxes of charged nuclei as well as intense magnetic fields (i.e., cometary comae, planetary dust rings within magnetospheres, intense cosmic dust, or orbital debris streams), a dust instrument capable of providing particle mass spectra as well as accurate high-flux measurements in the presence of these possible backgrounds would provide important information regarding the sources, sinks, and dynamics of the dust [12].

Development of the PVDF dust sensor at the University of Chicago began in 1983 and since then the main design objectives of our PVDF technology program have addressed the two types of measurements described above, namely:

1. The ability to measure individual particle trajectories with sufficient accuracy to permit identification of their parent bodies. This, combined with chemical and isotopic analyses of the captured material in a capture cell device (and/or returned sensors), permits a direct study of the physical, chemical, and isotopic composition of matter from a known parent body.
2. The ability for accurate measurement of particle mass spectra and high dust fluxes, with immunity to possible intense backgrounds of charged nuclei (radiation belts) and/or intense magnetic fields.

In the following sections we summarize the history of this PVDF technology program, and discuss the objectives and designs of two dust instruments scheduled for launch in 1995 and 1997 that have resulted from this program.

**PVDF and PVDF Copolymer Sensors: Dust particle response.** The theory, construction, and dust particle response of pure PVDF and PVDF copolymer sensors have been described in detail in earlier reports [4-7,13]. A PVDF (or PVDF copolymer) sensor, shown in Fig. 1a, consists of a thin film of permanently polarized material. A hypervelocity dust particle impacting the

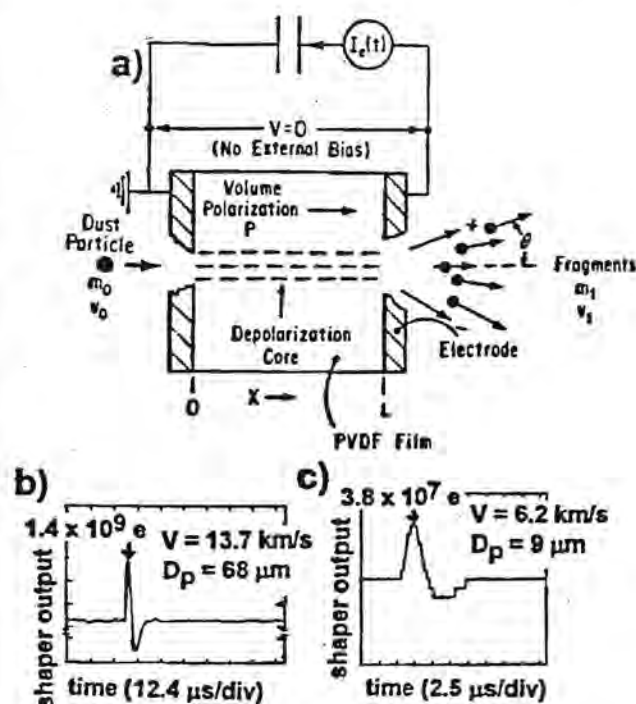


**Fig. 1.** (a) Schematic drawing of a PVDF (or PVDF copolymer) dust sensor. The sensor film, with thickness  $L$ , has a built-in volume polarization,  $P$ , as shown. (b) Example of output pulse for a 2.0- $\mu\text{m}$ -thick PVDF copolymer sensor impacted by a glass particle having velocity  $V$  and diameter  $D_p$  as indicated. (c) Example of output pulse for a 6.8- $\mu\text{m}$ -thick PVDF sensor impacted by a glass particle having velocity  $V$  and diameter  $D_p$  as indicated.

sensor produces rapid local destruction of dipoles (penetration hole), which results in a large and fast (ns range) current pulse at the input to the electronics. The output pulse amplitude, in general, depends on impacting particle mass and velocity [4-7] and is sharp in time, as illustrated in Figs. 1b,c. This fast output pulse permits a high counting rate capability for the sensor (up to  $10^4$  impacts  $\text{s}^{-1}$  with no, or small, corrections, and up to  $10^5$  impacts  $\text{s}^{-1}$  with significant but known corrections) as illustrated in Fig. 2.

The fast response of the PVDF sensor, combined with its immunity to very high background fluxes of charged nuclei and magnetic fields, made it well suited to carry out dust measurements in cometary comae, and further studies of the PVDF sensor and associated electronics led to the development of the University of Chicago Dust Counter and Mass Analyzer (DUCMA) instruments that were carried aboard the Vega 1 and Vega 2 spacecraft missions to Comet Halley [14]. The highly successful performance of the DUCMA instruments throughout the Vega 1/2 missions proved the high space reliability of PVDF sensors and their value for space dust studies [15,16].

**Electrical/thermal characteristics.** For PVDF sensors made from pure PVDF material, the dielectric constant  $\eta$  of the material is  $\eta = 12$ . For thin sensors, this high  $\eta$  results in a large detector capacitance, which degrades the rise time and amplitude at the output of a charge-sensitive preamplifier used with the sensor and also results in a large electronic noise level at the output of the linear

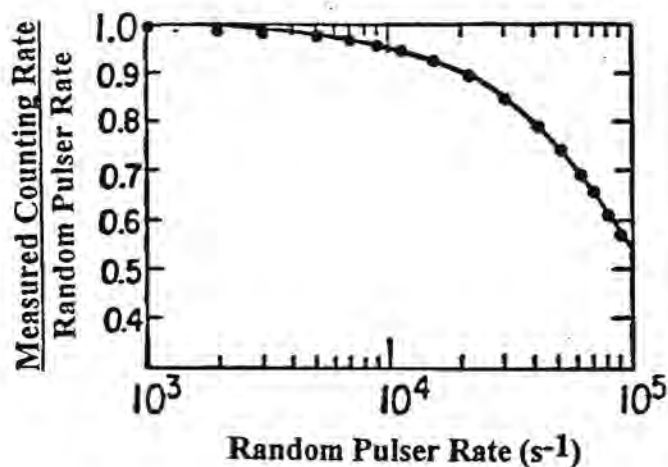


Fig. 2. An illustration of counting rate capability of PVDF sensor/electronics system. Data taken using a random electronic pulser to simulate a random particle impact rate. Up to impact rates of  $10^4 \text{ s}^{-1}$ , counting losses are  $<5\%$ .

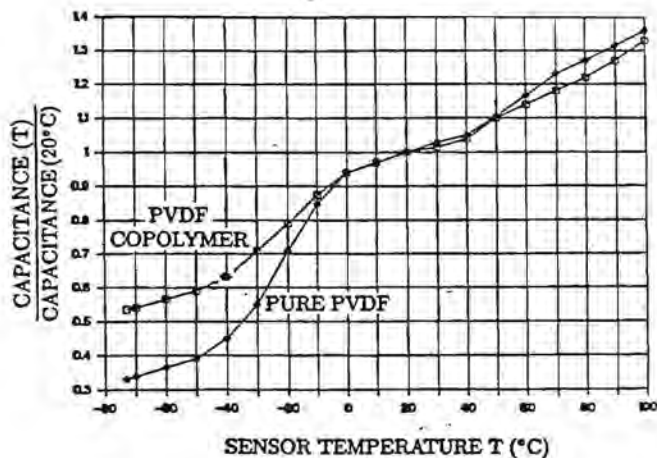


Fig. 3. Measured temperature dependence of sensor capacitance for a sensor made from pure PVDF material, and a sensor made from PVDF copolymer material.

electronics [14]. Further, the volume polarization  $P$  of pure PVDF material will degrade with time when the material is maintained at temperatures  $\geq 80^\circ\text{C}$  [17].

Recent developments in polymeric materials have led to new copolymer materials that promised to have lower  $\eta$  and improved stability of  $P$  under long-term high-temperature ( $\sim 100^\circ\text{C}$ ) exposure, and a study was undertaken to determine the possible advantages of copolymer materials over pure PVDF material. The results of these studies are included in Table 1, which summarizes the characteristics of PVDF (pure and copolymer) sensors. For the trifluoroethylene copolymer material we have studied [18], we have found this material to have distinct advantages over pure PVDF material, and have made use of this copolymer material for nearly all sensor construction over the last few years.

Although our studies have shown that copolymer sensors may be operated at temperatures up to  $\sim 100^\circ\text{C}$  for long periods of time (months) with very small ( $<5\%$ ) degradation in dust particle response, the effective sensor emissivity  $\epsilon$  and absorptivity  $\alpha$  are such that exposure of a sensor in space to solar illumination will result in sensor temperatures high enough to destroy the sensor. Since, in general, mission and instrument mounting constraints may require exposure of sensors to solar illumination for considerable periods of time, we studied different sensor-coating techniques that would restrict sensor temperatures to  $<100^\circ\text{C}$  during extended solar exposure.

TABLE 1. Characteristics of PVDF dust sensors.

- Require no operating bias voltage. Long-term stability during storage.
- Long-term high-temperature stability:
  - $P$  = polarization of sample at  $20^\circ\text{C}$  before thermal test.
  - $P'$  = polarization of sample at  $20^\circ\text{C}$  after thermal test.
  - (a) Copolymer Sensor: 21 days at  $115^\circ\text{C}$  results in  $(P-P')/P = 5.5\%$ .
  - (b) Pure PVDF Sensor: 14 days at  $115^\circ\text{C}$  results in  $(P-P')/P = 23\%$ .
- Capacitance: For sensor of given area and thickness, copolymer sensors have approximately one-half the capacitance of a pure sensor [ $\eta(\text{copolymer}) \approx 6$ ]. Also, over the temperature range  $-73^\circ\text{C}$  to  $115^\circ\text{C}$ , copolymer sensors have smaller temperature dependence of capacitance than pure sensors (Fig. 3).
- Response to dust impacts:
  - For impactors that penetrate the sensor, copolymer sensors give  $\sim 30\%$  larger signal.
- Highly radiation resistant. No measurable change in response up to  $\sim 10^7 \text{ rad}$ .
- Response to dust impacts unaffected by high background fluxes of charged particles.
- Fast detector response (few ns) enables accurate counting for high dust fluxes.
- Proven space performance on Vega 1/2 missions to Comet Halley.

The basis for our studies is illustrated in Fig. 4a, where, for our sensors (600–800-Å-thick evaporated Al contacts on the two surfaces of a thin film of PVDF material),  $\epsilon = 0.025$  and  $\alpha = 0.1$ . Assuming the deposition of a coating material having emissivity  $\epsilon'$  on that surface of the sensor that views an enclosure maintained at temperature  $T_0$ , and that the sensor is thermally insulated from its surroundings, Fig. 4b shows the calculated sensor temperature  $T$  vs. the ratio  $\epsilon' = \epsilon$  under solar exposure of the space-facing surface at 1 AU from the Sun. For an uncoated sensor ( $\epsilon' = \epsilon$ ), the sensor temperature would exceed (pure PVDF) or approach (PVDF copolymer) the melting temperature of the polymer material, i.e., the sensor would be destroyed. However, for  $\epsilon' \geq 10\epsilon$  ( $\epsilon' \geq 0.25$ ), the sensor temperature would remain  $<100^\circ\text{C}$  for enclosure temperatures  $<50^\circ\text{C}$ .

Two techniques have been developed for coating of our sensors with material having  $\epsilon' \geq 0.25$ . The first technique (developed at our laboratory) consists of applying (spray brush) a Chemglaze Z-306 coating [19] to one of the sensor surfaces, and measured emissivities  $\epsilon'$  vs. Z-306 thickness are plotted in Fig. 5 [20]. The emissivity values obtained with the Z-306 coatings are seen to be sufficiently

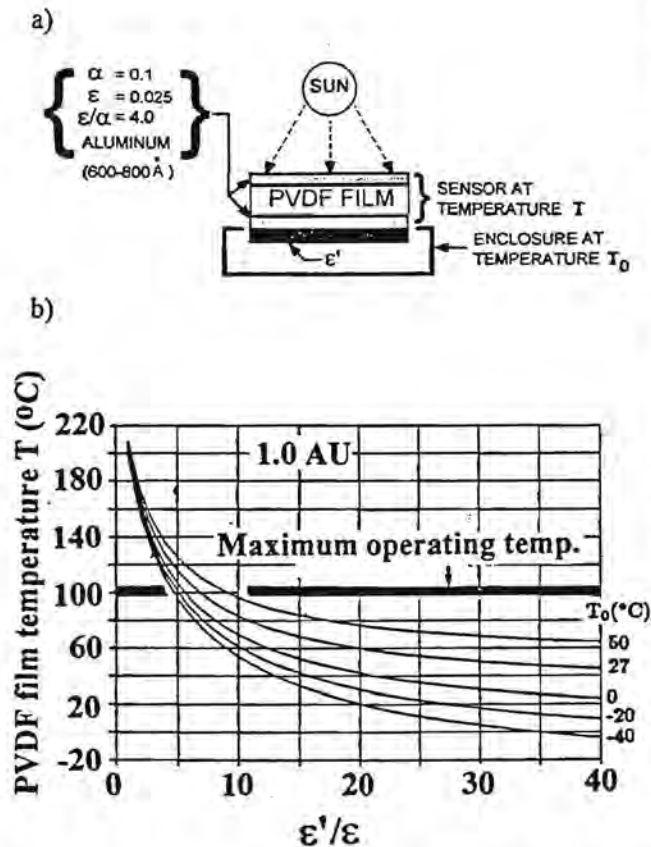


Fig. 4. (a) Model assumed for a PVDF sensor coated on one surface with material having emissivity  $\epsilon'$ . The coated surface views an enclosure maintained at temperature  $T_0$ . The space-facing sensor surface views the Sun at 1 AU distance, and the sensor (and coating) are at temperature  $T$ . The sensor is assumed to be thermally insulated from its surroundings. (b) Calculated sensor temperature vs. the ratio  $\epsilon'/\epsilon$  for the model in (a).

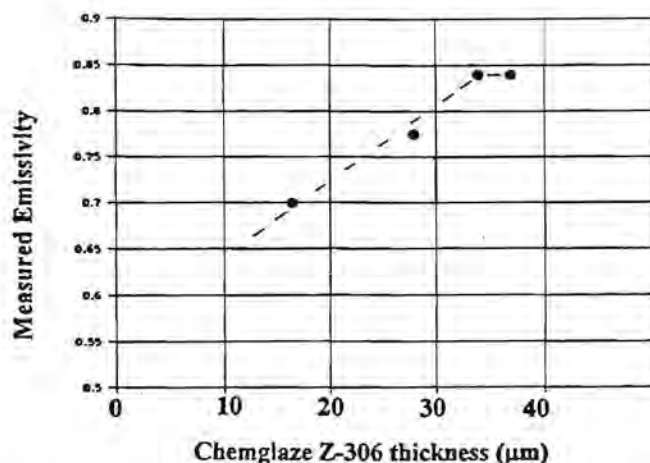


Fig. 5. Measured emissivity for a sensor surface coated with Chemglaze Z-306 vs. Chemglaze Z-306 thickness.

large as to provide a solution to the solar temperature problem for PVDF sensors. A number of sensors coated with Z-306 have been thermal/vacuum cycled over the range  $-73^{\circ}\text{C}$  to  $115^{\circ}\text{C}$  and the coatings have shown excellent adherence to the PVDF surface and complete mechanical stability.

A disadvantage to our Z-306 coating technique is that the minimum thickness coating we have achieved to date is  $\sim 17\text{ }\mu\text{m}$ . For sensors used in a system requiring particle penetration of a coated sensor with minimum particle degradation (ablation, velocity loss, fragmentation), the Z-306 coating method is not suitable at present since it would introduce considerable particle degradation [4-7].

An alternative technique that holds promise for  $\epsilon' \sim 0.4$  for a film coating on a PVDF sensor with coating thickness in the range  $1\text{--}2\text{ }\mu\text{m}$  was investigated and developed by the Aerospace Corp. [21]. Several PVDF test samples were coated (sputtering) with a  $\text{SiO}_2$  film with thickness  $1.5\text{ }\mu\text{m}$ , and measured values for  $\epsilon'$  were  $\sim 0.39$ . Although this  $\epsilon'$  value yields an acceptable solution to the sensor solar/thermal problem, and the  $\text{SiO}_2$  coating thickness ( $1.5\text{ }\mu\text{m}$ ) represents a dramatic improvement over the minimum Z-306 coating thickness ( $\sim 17\text{ }\mu\text{m}$ ), the  $\text{SiO}_2$  technique will require further study in terms of  $\text{SiO}_2$  coating adherence and stability.

**Position-sensing PVDF sensors.** Specially constructed PVDF sensors provide the capability for determination of the  $x, y$  coordinates of particle entry into the PVDF sensor. The two-dimensional position-sensing PVDF dust sensors ( $x, y$  sensors) we have developed employ resistive charge division, as shown in Fig. 6. Dust particle calibrations have shown that typical measured position errors for dust particle impacts are in the range  $\sim 1\text{--}3\text{ mm}$  for  $x$  and  $y$  [6]. In near-Earth-orbit applications, the unprotected portions of the  $x, y$  sensor surfaces would suffer from oxygen erosion effects. However, an overcoat of a thin-film oxide may provide a solution to this problem, and this possibility will be studied in the near future.

**Particle Velocity/Trajectory Measurement Using Thin PVDF Sensors:** Two thin ( $\leq 6\text{ }\mu\text{m}$  thick) sensors in a time-of-flight (TOF) arrangement may be used to determine impactor velocity. The concept is illustrated in Fig. 7a, and several dust accelerator calibrations were carried out at the Heidelberg and Munich (Germany) dust accelerator facilities to verify the concept [4-7,13], and examples of the Munich results are given in Figs. 7b-d.

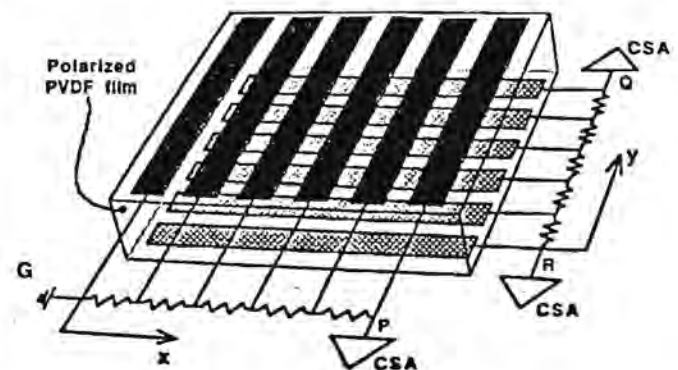


Fig. 6. A schematic illustration of a two-dimensional position-sensing PVDF dust sensor using external resistive charge division. Three signals ( $P, Q, R$ ) yield the  $x, y$  coordinates of particle impact [6].



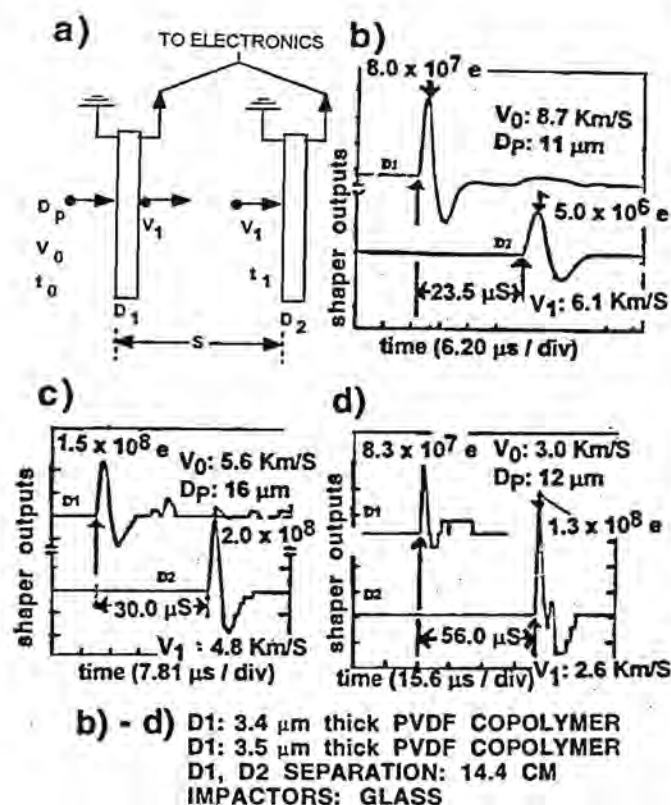


Fig. 7. (a) Illustration of particle impact velocity determination by time-of-flight. An impactor with velocity  $V_0$  and diameter  $D_p$  impacts a thin PVDF  $D_1$  sensor at time  $t_0$ , emerges from  $D_1$  with reduced velocity  $V_1$ , and impacts  $D_2$  at a later time  $t_1$ , with  $\Delta t = t_1 - t_0$ . With  $S$  known and  $\Delta t$  measured,  $V_1 = S/\Delta t$ . From the amplitude of the  $D_1$  output pulse and  $V_1$ , both  $V_0$  and  $D_p$  are determined from calibration data. (b-d) Examples of two-sensor time-of-flight data obtained during dust calibrations carried out at the Munich dust accelerator during May 1989. Indicated are the  $D_1, D_2$  sensor thicknesses, the glass impactor ( $2.5 \text{ g/cm}^3$ ) diameter  $D_p$ , and the  $D_1, D_2$  separation  $S$ .

For particle trajectory measurement, moderate trajectory accuracy ( $\sim 5^\circ$  trajectory error) may be obtained by using arrays of non-position-sensing sensors arranged in two planes of given separation. Approximate particle trajectory is determined by electronic identification of the upper and lower plane sensors penetrated by the particle [4,5]. For high trajectory accuracy ( $\sim 1^\circ$  trajectory error), two planar arrays of PVDF x,y sensors would provide this capability, although at higher electronic complexity [6].

**Combined PVDF Trajectory-Capture Cell Systems:** Following our early calibrations of thin PVDF sensors in a TOF arrangement, it became clear that a PVDF TOF telescope combined with a capture cell device would provide the additional capability of an Earth-based chemical and isotopic analysis of captured dust. The PVDF trajectory system would provide measurements of impacting particle flux, mass, velocity (by time-of-flight), and trajectory. The capture cell system would provide for capture of particle residues following penetration of the trajectory system by the impactor.

Subsequent Earth-based analyses would yield chemical and isotopic composition of the residues. Thus, the combined trajectory-capture cell instrumentation would provide the capability to measure the orbital elements of individual particles prior to capture.

Dust accelerator calibrations on combined PVDF trajectory-capture cell systems established that, for 75% of all impactors with velocities  $\leq 8 \text{ km/s}$ , thin PVDF trajectory systems satisfied the requirements of (1) velocity trajectory determination, (2) identification of the location of particle fragments in capture cells, and (3) sufficient mass following penetration of the trajectory sensors for successful capture and subsequent chemical and isotopic analysis [7,22].

**Current University of Chicago PVDF Dust Instrument Programs:** Continuing development of PVDF sensors and associated electronics has led to two current programs described below.

*The Space Dust (SPADUS) instrument for flight on the Advance Research and Global Observation Satellite (ARGOS).* A SPADUS (SPADUS) instrument designed to measure the flux, mass distribution, velocity/trajectory, and impact-time characteristics of near-Earth dust (both cosmic dust and orbital debris) is currently under development for flight on the Advanced Research and Global Observation Satellite (ARGOS), with a launch in September 1995. SPADUS is being jointly developed by groups at the University of Chicago (dust sensors and linear electronics), the Lockheed Space Sciences Laboratory (digital electronics), and the Space Sciences Division of the Naval Research Laboratory (mechanical design and construction). SPADUS will be integrated and flown by the DOD Space Test Program, with funding for the University of Chicago portion of SPADUS development provided by the Office of Naval Research and NASA.

The ARGOS objective is to demonstrate high-temperature superconductivity technology, stellar navigation and timing concepts, electric propulsion, and conduct upper atmosphere imaging and environment studies, with SPADUS providing continuous measurements of the particulate environment. The ARGOS mission and the SPADUS instrument have been described in [10,11], and the characteristics of SPADUS are summarized in Fig. 8.

*High Rate Detector (HRD) instrument for the Cassini mission to Saturn.* The High Rate Detector (HRD) instrument is currently under development as a subsystem of the Cosmic Dust Analyzer (CDA) experiment (E. Grün, MPI, CDA Principal Investigator). The CDA has been described in [12] and the goals of the CDA are to study the dust environment at Jupiter encounter, in the asteroid belt, in the saturnian system, and in interplanetary space throughout the cruise portion of the mission.

The HRD exploits the high counting rate capabilities of PVDF sensors, and is designed to measure intense dust fluxes and particle mass spectra during ring plane crossings, where fluxes are expected that may saturate the rate capability of the Dust Analyzer portion of the CDA [12]. The characteristics of the HRD are summarized in Fig. 9. Launch of the Cassini spacecraft is scheduled for November 1997.

**Future Space Applications of PVDF-based Instrumentation:** PVDF-based instruments utilizing new gate-array microcircuitry in combination with programmable microprocessors would provide low-power, lightweight, and flexible instrumentation that would be ideally suited to a number of possible future space missions. An instrument similar to SPADUS combined with arrays of capture cell devices behind the trajectory instrumentation would

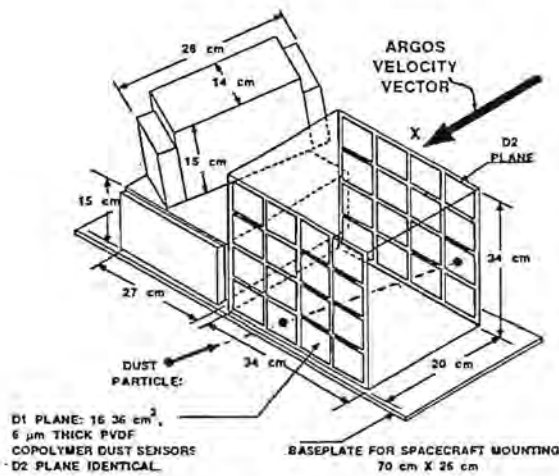


**Fig. 8.** Summary of the SPADUS instrument. Characteristics: Single sensor; 36 cm<sup>2</sup>, 6- $\mu$ m-thick PVDF copolymer; particle mass (10 km/s):  $5 \times 10^{-12}$  g ( $D_p = 2 \mu$ m) to  $1 \times 10^{-5}$  g ( $D_p = 200 \mu$ m); particle velocity: 1 to 10 km/s with 1–4% error, greater error for velocity > 10 km/s; particle trajectory: mean angular error of 7° for isotropic dust flux; sensitive area of D1 array (16 sensors): 0.058 m<sup>2</sup>; geometry factor for isotropic dust flux: (a) D1 array—0.20 m<sup>2</sup> sr, (b) D1, D2 arrays—0.04 m<sup>2</sup> sr; field of view (full cone): (a) 180° for flux, (b) 120° for trajectory; low-resolution pulse-height-analysis: 32 channels for each of 32 dust sensors; high-resolution pulse-height analysis: 2000 time points, 8 bits/point, each of four channels; estimated weight: 8 Kg; estimated power: 6.5 W.

provide important near-Earth dust measurements on an LDEF II mission or MIR. We have begun the design of a SPADUS-type instrument that would provide data comparable to that provided by SPADUS (Fig. 8), but with significantly reduced weight and power requirements (~2 kg and ~2.5 W, with no capture cells). Such an instrument would be suited for deep-space missions.

For a simpler dust instrument that would provide measurement of particle mass distribution and flux, with no velocity/trajectory information, an instrument similar to the HRD, but with a total PVDF sensing area of 1000 cm<sup>2</sup>, would provide useful dust data in a variety of space environments. Such an instrument would provide the dust data listed in Fig. 9, would weigh ~1 kg, and require ~0.4 W.

**Acknowledgments:** The author thanks J. A. Simpson, R. B. McKibben, M. Perkins, E. LaRue, and staff at the University of Chicago for their important contributions to the PVDF development program and their contributions to SPADUS and HRD development. He thanks H. Voss, R. Baraze, R. Fisher, J. Kilner, J. Mobilia, D. Chenette, and R. Vondrak at the Lockheed Space Sciences Laboratory and H. Gursky, M. Lovellette, D. Woods, and G. Fritz at the Naval Research Laboratory for their participation in SPADUS design and development, and E. Grün and the entire CDA consortium for their contributions to the interfacing of the HRD to the CDA. The University of Chicago group is grateful to R. G. Joiner for his continuing sponsorship of SPADUS and for his efforts in obtaining partial support for SPADUS development. Finally, we thank the DOD Space Test Program for providing the SPADUS flight on ARGOS, and the Aerospace Corp. and Rockwell International staff

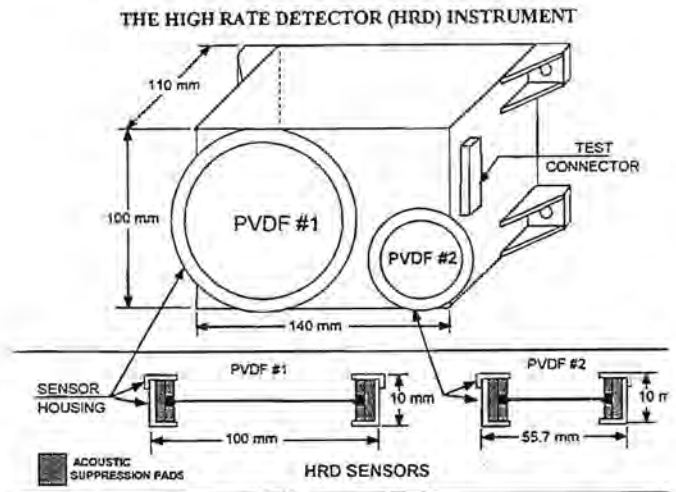


**Fig. 9.** Summary of the HRD instrument. Characteristics: Sensors: #1-50 cm<sup>2</sup>, 28- $\mu$ m-thick PVDF copolymer; #2-10 cm<sup>2</sup>, 6- $\mu$ m-thick PVDF copolymer; particle velocity: >1 km/s; thresholds: each sensor has four mass thresholds; particle mass: differential and integral flux =  $2 \times 10^{-12}$  g to  $2 \times 10^5$  g; integral flux > $2 \times 10^{-5}$  g; discrete events: recording of impact time (1 s accuracy) and threshold firings for each impact—up to  $3 \times 10^2$ /s no corrections,  $3 \times 10^2$  to 103/s, known corrections; counting rates: up to 104/s no corrections; 104 to 105/s, known corrections; data storage: microprocessor system with 60 k bytes data storage memory; flight modes: (a) normal (cruise): continuous recording of impact time, threshold firings and integral counts, (b) fast: integral counts recorded and stored each  $\Delta t$  seconds during ring-plate crossings— $\Delta t$  selectable at 0.1, 0.2, . . . , 0.9, 1.0 seconds, (c) calibrate: periodic calibration with in flight calibrator; estimated weight: 914 g; estimated power: 430 mW.

who have made integration of SPADUS into ARGOS possible. The University of Chicago effort for SPADUS is supported in part by ONR Grant N00014-91-J-1716 and NASA Grant NAGW-3078. The Lockheed SPADUS effort is supported in part by the Lockheed Independent Research Program, and the Naval Research Laboratory SPADUS effort is supported by in-house funding. The University of Chicago funding for HRD development is provided by NASA Subcontract JPL 959531.

**References:** [1] Hörz F., ed. (1986) *LPI Tech. Rpt.* 86-05. [2] Mackinnon I. D. R. and Carey W. C., eds. (1988) *LPI Tech. Rpt.* 88-01. [3] McDonnell J. A. M., ed. (1992) *Hypervelocity Impacts in Space*, Univ. of Kent at Canterbury. [4] Simpson J. A. et al. (1989) *Nucl. Instr. Meth.*, A279, 611–624. [5] Simpson J. A. and Tuzzolino A. J. (1989) *Nucl. Instr. Meth.*, A279, 625–639. [6] Tuzzolino A. J. (1991) *Nucl. Instr. Meth.*, A301, 558–567. [7] Tuzzolino A. J. (1992) *Nucl. Instr. Meth.*, A316, 223–237. [8] Jackson A. A. and Zook H. A. (1992) *Icarus*, 97, 70–84. [9] *Workshop on the Analysis of Interplanetary Dust* (1993) LPI, Houston. [10] Tuzzolino A. J. et al. (1993) *NASA CP-3194, Part 4*, 1535–1549. [11] Tuzzolino A. J. et al. (1993) *Adv. Space Res.*, 13, No. 8, 133–136. [12] Ratcliff P. R. (1992) *J. Brit. Interplanet. Soc.*, 45, 375–380. [13] Simpson J. A. and Tuzzolino A. J. (1985) *Nucl.*

*Instr. Meth.*, A236, 187–202. [14] Perkins M. A. et al. (1985) *Nucl. Instr. Meth.*, A239, 310–323. [15] Simpson J. A. et al. (1986) *Nature*, 321, 278–280. [16] Simpson J. A. et al. (1987) *Astron. Astrophys.*, 187, 742–752. [17] Furukawa T. and Wang T. T. (1988). *The Applications of Ferroelectric Polymers*, Chapman and Hall, New York. [18] Ferren R. A. (1988) *The Applications of Ferroelectric Polymers*, Chapman and Hall, New York. [19] Obtained from the Lord Corp., Erie, PA. [20] Measurements carried out at the Aerospace Corp., Los Angeles, CA. [21] K. Aitchison, Aerospace Corp., El Segundo, CA, private communication. [22] Simon C. G. (1993) *Intl. J. Impact. Eng.*, in press.

# THE USE OF SILICA AEROGEL TO COLLECT INTERPLANETARY DUST IN SPACE M. E. Zolensky<sup>1</sup>, R. A. Barrett<sup>2</sup>, and F. Hörz<sup>1</sup>, <sup>1</sup>NASA Johnson Space Center, Houston TX 77058, USA, <sup>2</sup>Lockheed Engineering and Sciences Co., Houston TX 77058, USA.

We report on impact experiments to evaluate the suitability of silica aerogel as a capture medium for interplanetary dust particles in space. The structure of silica aerogel is such that even micrometer-sized hypervelocity particles may sense it as a target of very low density; consequently shock stresses and temperatures due to impact should be minimized. We performed impact experiments in a light gas gun that employed projectiles manufactured from forsterite, pyrrhotite, and calcite. From these experiments we have developed techniques that will permit the successful extrication of interplanetary dust particles from aerogel. We note a rough correlation between increasing particle penetration lengths and decreasing aerogel density, and there is a poor correlation of track lengths with impact velocity at laboratory-attainable velocities of 5–7 km/s. We conclude that aerogel track length should not be used even as (crude) velocity indicators. Transmission electron microscope studies show the recovered particulate residues are encased in melted silica aerogel, which possibly protects the residue from some impact damage. Individual minerals within interplanetary dust are expected to exhibit differential survival, and may be vaporized, melted, dehydrated, or structurally reordered. However, some mineral grains should successfully be captured in an unmelted state at encounter velocities <8 km/s.

**Introduction:** Several proposed missions will seek to collect individual interplanetary dust or cometary particles in space. Associated capture media must be deliberately developed to minimize potential particle degradation and destruction. Upon retrieval to Earth-based laboratories the captured particles may then be characterized in detail. An outstanding technical challenge has been to develop suitable capture media permitting successful deceleration and capture of particles in a manner permitting laboratory analysis of particle residues. This capture of hypervelocity particles in the least destructive fashion depends upon the dissipation of the particle's kinetic energy. A successful capture medium must dissipate the maximum amount of energy into the target in such a manner that the fraction that is unavoidably partitioned into the impactor is kept below the specific heats of fusion and vaporization of the projectile. Deceleration by molecular collisions in a gas or by viscous drag in a liquid seems impractical for most purposes. For this reason, low-density foams or stacked-foil capture cells are being evaluated at this time (CDCF Report, 1990). The former material is the focus of

this paper, which expands on the work reported by Tsou et al. [1–3].

We report here on impact experiments using silica aerogel as a deceleration and capture medium. This material can be manufactured with a bulk density  $\ll 1 \text{ g/cm}^3$  [4], and therefore will induce low shock stresses and associated temperatures even at predicted encounter velocities of 15–20 km/s [e.g., 5,6]. It has a suitable microstructure, with irregular chains and clusters of  $\text{SiO}_4$  tetrahedra, generally <100 Å in dimension and fairly uniform distribution of associated void space [4]. The solids composing any suitable low-density, porous medium must have substantial, nonporous dimensions significantly less than the projectile diameter, otherwise the impacting particle will sense them as massive (and successive) plates, possibly even as infinite half-space targets (in the extreme case), voiding the low acoustic impedance and thus shock-stress properties of the bulk material. Aerogel meets the requirement of low bulk density at dimensional scales smaller than the expected micrometer-sized cosmic dust impactors better than most other low-density materials, and is therefore a top candidate capture medium for CDCF flight instruments from the viewpoint of shock processes.

The first projectile-recovery experiments using silica aerogels were reported by Tsou et al. [2], who successfully retrieved soda lime glass spheres and olivine grains that impacted at ~6 km/s. They also analyzed the detailed geometry and length of projectile penetration tracks, which are generally visible to the naked eye in transparent aerogels. We have expanded on the experiments performed by Tsou et al. by employing different, more realistic projectiles, such as powdered calcite, olivine, enstatite, and pyrrhotite, as well as artificial interplanetary dust analog spheres. We further tested a suite of different silica aerogel materials varying in density from 120 to 20 mg/cm<sup>3</sup>.

**Structure and Composition of Silica Aerogel:** Silica aerogel is a transparent medium that transmits most wavelengths of light, but scatters the shorter wavelengths to produce its blue color. We employed several varieties of aerogel in our experiments. The 250-mg/cm<sup>3</sup> silica aerogel was provided to us by L. Koch-Miramond, Service d'Astrophysique, Gif-Sur-Yvette, France. The 120-mg/cm<sup>3</sup> silica aerogel was produced by Henning Airglass in Staffanörp, Sweden. Still lower-density varieties of 60, 40, and 20 mg/cm<sup>3</sup> were developed and fabricated by Lawrence Hrubesh at Lawrence Livermore National Laboratory [4].

We imaged 120-mg/cc silica aerogel samples in a JEOL 2000FX TEM, at 200 kV. These samples were prepared by vacuum impregnation using the epoxy MBED-812, followed by ultramicrotomy. Imaging shows the silica aerogel consists of loosely bonded, nanometer-sized "balls" of silica. We saw no evidence of long-range structural order or large pores in this particular material.

We also investigated some of the opaque, white silica "droplets" commonly produced during impact experiments as projectiles penetrate and compress the silica aerogel; this material typically coats projectile residue. High-resolution transmission electron microscope (TEM) imaging reveals that these "droplets" actually consist of welded, 50–200-nm-sized, rounded silica grains with considerable long-range order. This probably indicates that the particle capture process (at least at laboratory impact velocities of 5–7 km/s) induces melting and subsequent crystallization (increasing long-range ordering) of the originally amorphous aerogel.

**Contaminants:** Trace-element analyses of the silica aerogel were performed by Instrumental Neutron Activation Analysis (INAA)



on two samples of silica aerogel having densities of 120-mg/c<sup>3</sup> and 60-mg/c<sup>3</sup>. The 120-mg/c<sup>3</sup> aerogel contains Fe (60 ppm), Sn (4 ppm), Br (2 ppm), Zn (0.3 ppm), Cr (0.2 ppm), Sb (10 ppm), Co (8 ppb), and Sc (60 ppt). The 60-mg/cc sample contains Rb (12 ppm), Na (3.4 ppm), Zn (0.4 ppm), Br (0.2 ppm), and Au (10 ppb). The Sn, Au, and Zn are most likely traceable to autoclave materials, and Br to the solvents used in aerogel extraction, but the source of alkalis is unknown. These data show the silica aerogel can be highly pure. Even if impacting particles were mixed with molten silica aerogel in amounts many times the particle mass, bulk trace-element analyses would not be greatly affected.

It is an important goal to develop organic-free capture media, since there is interest in the biogenic component of interplanetary dust [7]. Hrubesh and Poco [4] reported the levels of H and C contaminants within the hydrophobic silica aerogel monoliths manufactured at Lawrence Livermore National Laboratory to be approximately 1.2 and 4.5 wt% respectively. This organic contamination is due to incomplete removal of alcohol and other solvents used in its manufacture; complete removal of water and organic contaminants is difficult due to unusually large specific free surface area. Accordingly, we have evaluated the facility with which water and organic species may be removed from aerogels by heating.

In thermogravimetric analysis (TGA) of three aerogel samples (60, 120, and 250 mg/c<sup>3</sup> samples) heated in a flowing He atmosphere, the three samples lost 0.9–8.0 wt% by simple heating to approximately 900°C in the dried He carrier gas for 1.5 hr. The largest weight loss, 8.0 wt%, was noted for the 120 mg/c<sup>3</sup> aerogel sample. The 60 mg/cc sample lost only 2.3 wt%; the smallest weight loss observed was for the 250-mg/c<sup>3</sup> sample, which lost only 0.9 wt%. The TGA data indicate that to remove most volatile contaminants, aerogel must be uniformly heated to at least 600°C and remain in an environment in which significant volatiles cannot be readsorbed by the aerogel.

**Impact Experiments:** *Light gas gun.* A 5-mm light gas gun was used to accelerate projectiles of approximately 100  $\mu$ m diameter via the so-called "shot-gunning" method. This technique involves an ensemble of particles (typically about 100) being loaded into a cylindrical cavity of a four-piece sabot. These four pieces will separate radially once they exit the gun barrel, permitting the particle cloud to expand in such a manner that at least a few particles will make it to the target (typically 2–6 grains). The sabot pieces and the majority of the particulates are intercepted by a massive steel aperture located 2 m in front of the target. We know from independent experiments that sabot and actual particle velocity are identical to within 2%, and that the velocity spread among these particles that reach the target is also <2%.

*Aerogel targets.* We assembled the aerogel targets in two ways, depending on the size and shape of the aerogel monoliths at hand. The 120 mg/c<sup>3</sup> monoliths measured 2.5  $\times$  15  $\times$  15 cm each, permitting entire targets to be assembled by merely stacking pieces. In all other cases, we placed monolith cylinders (with heights and diameters of approximately 2.5 cm) of the lower-density aerogels within tight cavities excavated within monoliths of the 120 mg/c<sup>3</sup> aerogel. Based on a few initial experiments with 120 mg/cc samples that were 2.5 cm thick, pronounced spallation phenomena occurred at the rear surface, including total failure of the target if free-standing. As monolith thickness was limited to 2.5 cm, it was necessary to encase the low-density samples as described above and to back the first monolith with additional 120 mg/c<sup>3</sup> material in the rear. This

arrangement typically resulted in a composite aerogel block at least 5 cm thick that inhibited spallation at the free surface of the sample cylinder. The dimensions of the cylinders were sufficient to terminate the particle's travel, capturing the entire particle penetration track.

*Projectiles.* The projectiles consisted of irregular grains, 105–125  $\mu$ m in diameter, obtained by grinding and sieving of large, high-quality single crystals of calcite (density 2.7 g/c<sup>3</sup>), olivine (forsterite, density 3.2 g/c<sup>3</sup>), enstatite (density 3.2 g/c<sup>3</sup>), and pyrrhotite (density 4.6 g/c<sup>3</sup>). These minerals were chosen for their varying physical properties and relevance to interplanetary dust studies. The projectiles were initially accelerated separately and, later, as a 1:1:1 mixture of calcite, forsterite, and pyrrhotite. A few experiments were also made employing artificial cosmic dust analog spheres, consisting of the above minerals in an epoxy matrix. The aggregates were then carefully ground into 1-mm-diameter spheres using a small ball mill familiar to crystallographers (featuring agitation within an abrasive-lined, cylindrical container).

**Results:** Twenty-one cosmic dust impact simulation experiments were successfully performed using the two-stage light gas gun. The shots were made into the silica aerogel targets at velocities ranging from 5.1 to 7.2 km/s. Each of the impact experiments employing the large, simulated interplanetary dust spheres resulted in a crater of significant size (>1 cm) in the aerogel monolith, made largely by spallation processes. So much mass was displaced that it was very difficult to locate and extract projectile residue grains from among the ejected aerogel debris. There was no clean-cut, single penetration track caused by the main projectile mass, nor any number of distinct tracks caused by major projectile fragments. This was an unexpected result compared to that obtained by Tsou et al. [2], and our own experiments with monomineralic powders at smaller projectile scales (see below). We have not followed up on possible reasons for this difference, which either relates to dimensional scaling or to possible strength differences of the projectiles, with the epoxy binder controlling the bulk behavior of the millimeter-sized impactors.

When the 100- $\mu$ m-diameter mineral grains were shotgunned, they bore into the silica aerogel, producing gently curving penetration "tracks." Along the trunk and at the terminus of each track, small projectile residue grains were evident. We carefully measured the track lengths for each experiment. We then excavated the projectile residues at the bottom of the tracks for TEM characterization. The recovered residues from these experiments were typically highly brecciated, locally devolatilized and melted, and welded together with fractured and melted aerogel. However, crystalline domains remained in all residues. A few projectiles were found to have survived unmelted; however, all recovered mineral grains showed evidence of abrasion. The minerals successfully recovered from the shotgun experiments were forsterite and pyrrhotite. No calcite was recovered, even in experiments that employed only calcite powders. Indeed, no penetrations or other evidence of impacts were observed in the latter experiments, indicating that the calcite projectiles disintegrated in the gun barrel due to rapid acceleration and associated gravitational forces that seem to exceed the calcite's compressive and/or tensile strength.

Figure 1 shows a target of the 40 mg/c<sup>3</sup> aerogel following impact of shotgunned mineral mixture at 6.4 km/s. Approximately one dozen tracks are visible, with the longest measuring 18 mm. This track morphology was typical; the shorter tracks are due to frag-

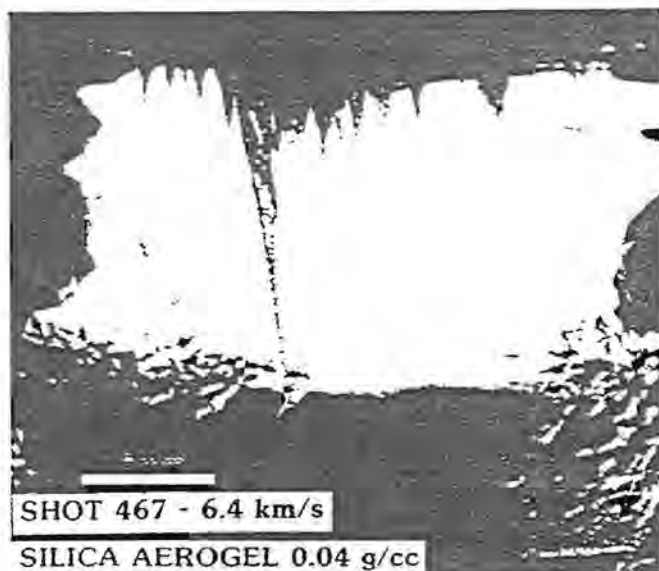


Fig. 1. Tracks in 40-mg/cc silica aerogel made by the impacts of olivine and pyrrhotite particles traveling at 6.4 km/s. The variation in track lengths observed was typical for this study and our light gas gun performance in 1989–1990, being due to projectile fragmentation and differences in projectile masses (see text); the longest track shown measures 18 mm.

mented projectiles. At higher magnifications residue particulates are apparent along the entire main track, with the largest recoverable mass lodged at the track terminus.

**Residue Extraction and Characterization:** An important purpose of this work was to develop sample preparation techniques for extracting impactor residue from silica aerogels, preparatory to performing detailed TEM characterization. To extract a residue particle, we first trimmed the aerogel from around the particle using an X-Acto blade, observing the operation under a binocular microscope, until there remained only a small amount of aerogel enclosing the particle. This aerogel block was then vacuum-impregnated with EMBED 812 low-viscosity epoxy. The impregnation with uncured epoxy served to render the aerogel completely transparent, permitting final removal of the residue particle. We then set the extracted particle into fresh EMBED 812 for curing and ultramicrotomy. Samples of aerogel examined with the TEM were prepared in the same manner.

The TEM analyses show that the recovered projectile residue grains were typically rounded, abraded, fractured, and encased within melted silica aerogel. Shots at the highest gun velocities attained and into low-density aerogels, i.e., best approximation to the expected conditions for the actual Cosmic Dust Collection Facility, were studied in greatest detail. These shots were at 6.29 and 7.18 km/s respectively and employed target densities of 40 and 20 mg/cc respectively. The projectile residues recovered from all of these shots were basically similar. A few grains of pyrrhotite were recovered, but in other cases only Fe blebs were observed, resulting probably from volatilization of S during impact.

In all cases a residue grain was present at the terminus of the projectile tracks in the aerogels. Much smaller residue grains were also observed at irregular intervals in off-shoot tracks located about

the main trunks of the tracks. We are not able to confidently determine the masses of any of these residue grains due to their small size, disrupted nature, and intimate mixing with aerogel (see below).

Crystalline olivine is the principal and most resistant phase observed in the current experiments. Figure 2 shows that the forsterite residue is fractured and mixed with melted and unmelted aerogel.

The projectile forsterite grains contain a flaky, layerlike phase similar to phyllosilicates. This phase had the composition of serpentine or forsterite, and prominent basal spacings varying from 6.3 to 9.3 Å. This description is very similar to the so-called "intermediate" phase pseudomorphs after serpentine described by Akai [8] and Zolensky et al. [9] in the course of heating experiments with serpentine from the Murchison CM chondrite (at temperatures between 400 and 600°C). We conjecture that the forsterite from our impact experiments originally contained small regions of serpentine, as is ubiquitous within most olivines. During the impact experiments this included serpentine was dehydrated and structurally transformed into the intermediate phase. Zolensky et al. [9] noted that at temperatures in excess of 600°C this intermediate phase transforms to olivine and/or pyroxene. This observation is significant since serpentine and other phyllosilicates are principal components of interplanetary dust [10].

**Penetration Track Analyses:** We have plotted the longest track lengths made by impacting forsterite as a function of target density for shots in four different aerogels, separately showing the shots at 6 and 7 km/s (Fig. 3). We note that the track lengths are much shorter for the denser aerogels. These indicate a rough negative correlation between track lengths and silica aerogel target density, which we can conclude only for these projectile velocities and target densities. We presume that the larger cells of the low-

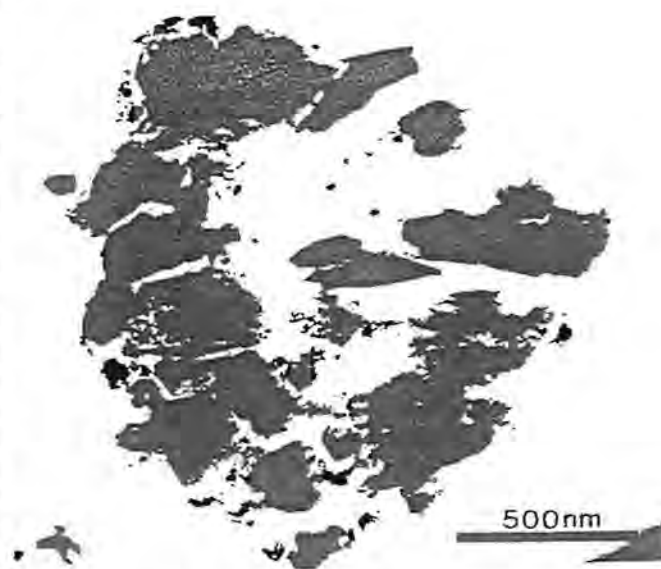


Fig. 2. TEM image of 1000-Å-thick ultramicrotomed section of a forsterite grain. The forsterite is porous, fractured (with minor chattering attributable to the ultramicrotomy process). Stippled areas are included grains of silica aerogel. The olivine grain has been severely processed by the impact experiment.

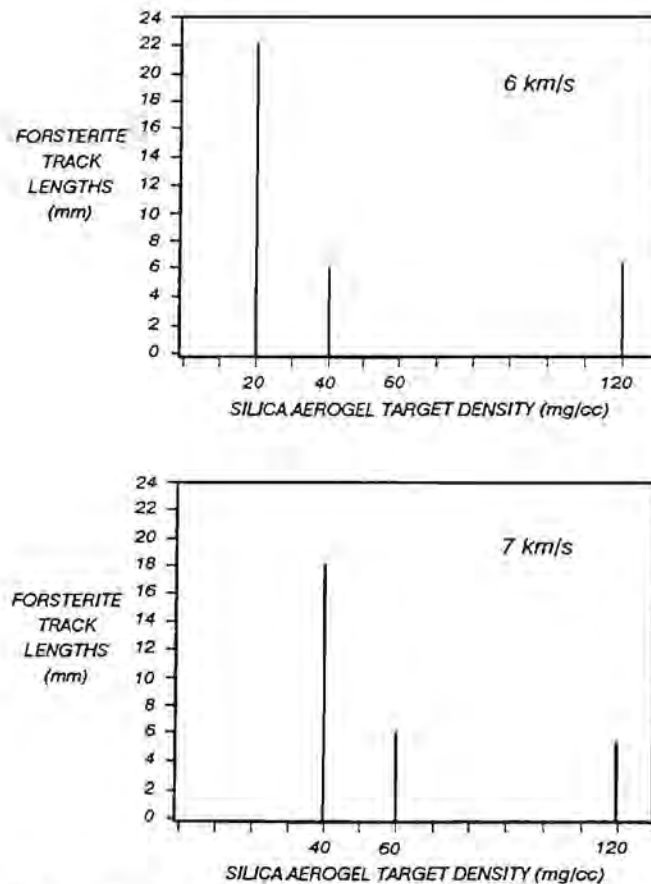
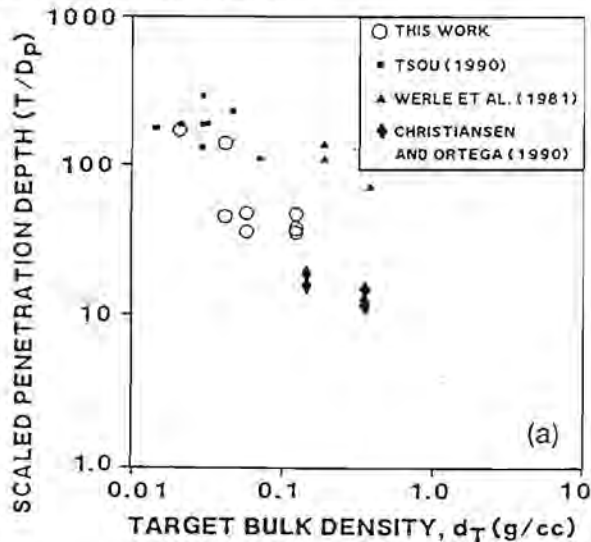


Fig. 3. Plots of maximum measured track lengths made by forsterite projectiles into silica aerogels, shown as a function of aerogel bulk density, all at 6 and 7 km/s. Measurement errors are  $\pm 0.3$  mm.



density aerogel will allow a slower deceleration of the particles. This factor is important in determining the minimum feasible density of aerogel that can be used to assure complete deceleration of the projectile within a capture cell.

The aerogel track lengths ( $T$ ) from eight impact experiments from the current study are normalized to projectile diameter ( $D_p$ ) in Fig. 4 and compared to other penetration studies in porous media of very low densities ( $\ll 1$  g/cc), such as space shuttle tiles (foamed silica [11]), diverse organic foams [1], and "Saffile," a porous alumina [12]. All these studies, however, employed metal projectiles, such as Al alloys and stainless steel. Figure 4a plots density-scaled penetration tracks lengths against target bulk density ( $d_T$ ), and Fig. 4b normalizes the widely variable density parameters for all studies, with  $d_p$  being projectile density. Where possible, only those experiments between 6 and 7 km/s are compared in Fig. 4; however, the Werle et al. data are typical for  $<5$  km/s. Clearly, absolute penetration depth is inversely proportional to target density (Fig. 4a) and increases with increasing density contrast between projectile and collection medium (Fig. 4b). A least-squares fit of the data points in Fig. 4b results in

$$d_p/d_T = 1.997 (T/D_p)^{0.975}$$

with a correlation factor of  $r^2 = 0.761$ . Clearly, factors other than density alone must be important, considering that the materials summarized in Fig. 4b range from  $Al_2O_3$  to  $SiO_2$  to diverse organic molecules. For these reasons we deemed velocity scaling of this dataset to be inappropriate (see also below). However, we note that removal of the nonsilica materials from Fig. 4b results in a greatly improved correlation.

We have compared forsterite track lengths vs. projectile velocity for shots in the 120 mg/cc aerogel, to explore the effects of impact

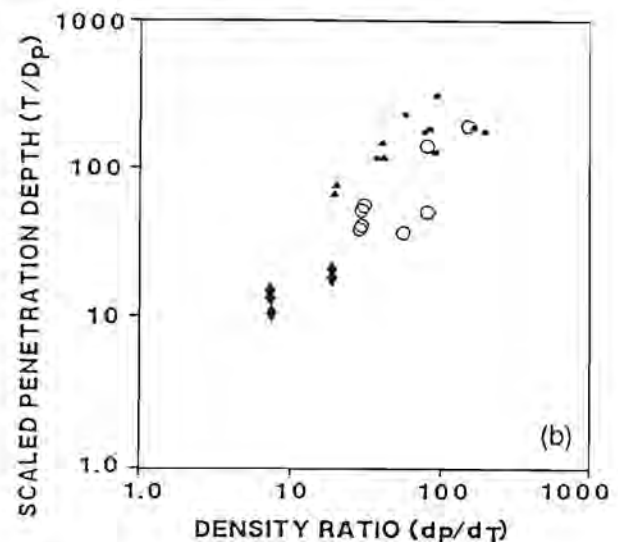


Fig. 4. Comparison of penetration track lengths in silica aerogel (this study) with those from previous experiments in porous materials of extremely low densities. Results from the current study are shown for velocities ranging 5.1 to 7.2 km/s for aerogels with densities of 20, 40, 60, and 120 mg/cc. (a) Depicts actual observations plotted against bulk density of the targets and (b) displays this same data following scaling of impactor and target densities. Some of the scatter inherent in (a) is eliminated by this normalization of density, yet substantial scatter remains. This result serves to illustrate that properties other than density and velocity must play a substantial role in determining track lengths in low-density media. The salient experimental conditions were as follows: Werle et al. [12]: steel projectiles at 0.4–7.9 km/s,  $D_p = 1.5$ –2 mm, targets were  $Al_2O_3$  (Saffile) of 180 and 340 mg/cc; Tsou [1]: Al projectiles at 0.3–6.5 km/s, diverse organic materials ranging in density from 13 to 68 mg/cc; Christiansen and Ortega [11]: diverse Al and nylon projectiles at 4.4–7.1 km/s foamed silica shuttle protective tiles of 140–350 mg/cc.



velocity at otherwise identical conditions. We conclude from this comparison that track length is not a sensitive indicator of projectile speed, for the velocities of our experiments.

Werle et al. [12] were the first to report that penetration tracks in porous alumina of 180 and 340 mg/cc are substantially deeper at 2–3 km/s than at higher velocities. Tsou [1] reports identical penetration maxima at relatively modest velocity (2–3 km/s) in porous organic media.

The fact that density scaling (Fig. 4b) does not substantially reduce the scatter observed in the raw data (Fig. 4a) is indicative that parameters other than density alone must exert a substantial role. As was suggested by Anderson and Ahrens [6], deceleration by viscous drag may dominate projectile deceleration in very-low-density targets, rather than shock-wave interactions or impact processes in general. The ubiquitous production of a molten aerogel cap at the projectile's front face may also be evidence of non-shock-related processes and forces that affect projectile deceleration in aerogel.

The above summaries and comparisons with other low-density target penetration data are merely offered here to underscore the conclusion that absolute penetration depth will have a complex relationship with projectile speed and other initial impact conditions.

**Conclusions:** We believe that low-density silica aerogel is chemically and structurally appropriate as a capture cell medium for the collection and recovery of interplanetary dust particles in space. Organic contaminants in the aerogels, unless reduced, may limit its usefulness for study of biogenic components in interplanetary dust. We have developed techniques that will permit the successful extrication of interplanetary dust particles from aerogel capture cells.

We note a rough negative correlation between the particle track lengths and the silica aerogel target density, a trend consistent with other experiments into foamed targets. There is only a poor correlation of track lengths with impact velocity at 5–7 km/s. Accord-

ingly, we conclude that (at the velocities and aerogel densities germane to this study) aerogel track lengths should not be used as velocity indicators; this conclusion seems to be corroborated by previous studies as well.

TEM studies show the recovered particulate residues from silica aerogel capture cells are encased in melted silica aerogel. The aerogel appears to melt on impact and forms a plug, possibly protecting the impactor from excessive damage. From our experiments simulating cosmic dust impacts, we conclude that individual minerals of cosmic dust are expected to exhibit differential survival. The minerals may be vaporized or melted, as in the case of S volatilizing from pyrrhotite. They may be dehydrated and structurally reordered as for the pseudomorphous "intermediate" phase observed after serpentine. Finally, relatively pristine mineral grains should actually be captured, as for our forsterite, although this is demonstrated only at modest encounter velocities (<8 km/s). The "intact" capture of entire complex projectiles, however, seems impractical at laboratory impact speeds.

**Acknowledgments:** We acknowledge L. Hrubesh for his development of the very-low-density silica aerogels used in this study. F. Cardenas, W. Davidson, and G. Haynes ably performed the light gas gun shots.

**References:** [1] Tsou P. (1990) *Intl. J. Impact Eng.*, 10, 615–627. [2] Tsou P. et al. (1990) *LPS XXI*, 1264–1265. [3] Tsou P. et al. (1989) *LPS XX*, 1132–1133. [4] Hrubesh L. W. and Poco J. F. (1990) *Contract Rept. #T-1143RAM2*, LLNL, 12 pp. [5] Hörz F. et al. (1986) *LPI Tech. Rpt. 86-05*, 58–60. [6] Anderson W. and Ahrens T. J. (1988) *LPI Tech. Rpt. 88-01*, 21–22. [7] CDCF Report (1990) *NASA TM-102160*, 28 pp. [8] Akai J. (1990) *14th Symp. Antarctic Meteorites*, 22–23. [9] Zolensky M. E. et al. (1993) *GCA*, 57, 3123–3148. [10] Zolensky M. E. and Lindstrom D. J. (1992) *LPS XXII*. [11] Christiansen E. and Ortega J. (1990) *AIAA Space Prog. Tech. Conf., Abstracts*, AIAA 90-3666, 13. [12] Werle V. et al. (1981) *Proc. LPSC 12th*, 1641–1647.

# List of Workshop Participants

---

## W. M. Alexander

*Space Science Laboratory  
Department of Physics  
Box 97266  
Baylor University  
Waco TX 76798-7266  
Phone: 817-755-3405  
Fax: 817-755-3409*

## Bill Anderson

*Mail Stop 252-21  
California Institute of Technology  
Pasadena CA 91125  
Phone: 818-395-2986*

## Siegfried Auer

*1906 Paris Court  
A & M  
Bowie MD 20716  
Phone: 301-249-7715  
Fax: 301-249-7715*

## Ruth Barrett

*Mail Code C23  
Lockheed Engineering and Sciences Co.  
2400 NASA Road 1  
Houston TX 77058  
Phone: 713-483-5017  
Fax: 713-483-5347  
E-mail: [sn@mroate-barrett](mailto:sn@mroate-barrett)*

## Don Brownlee

*Department of Astronomy  
Physics Hall  
University of Washington  
Seattle WA 98195  
Phone: 206-543-8575  
Fax: 206-685-0403  
E-mail: [brownlee@astro.washington.edu](mailto:brownlee@astro.washington.edu)*

## Mark J. Burchell

*Unit for Space Sciences  
Physics Lab  
University of Kent  
Canterbury Kent CT2 7NR  
UK  
Phone: 0227-764000 x3248  
Fax: 0227-762616  
E-mail: [mjb6@ukc.ac.uk](mailto:mjb6@ukc.ac.uk)*

## Donald S. Burnett

*Mail Stop 170-25  
Geology Division  
California Institute of Technology  
Pasadena CA 91125  
Phone: 818-395-6117  
Fax: 818-568-0935  
E-mail: [burnett@legs.gps.caltech.edu](mailto:burnett@legs.gps.caltech.edu)*

## Mark J. Cintala

*Mail Code SN4  
NASA Johnson Space Center  
Houston TX 77058  
Phone: 713-483-5032*

## Joe Davis

*16-739  
Laboratory of Molecular Structures  
Massachusetts Institute of Technology  
77 Massachusetts Avenue  
Cambridge MA 02139  
Phone: 617-253-4710  
Fax: 617-253-8699  
E-mail: [joedavis@rich.mit.edu](mailto:joedavis@rich.mit.edu)*

## Donald L. DeVincenzi

*Mail Code 245-1  
Space Science Division  
NASA Ames Research Center  
Moffett Field CA 94035  
Phone: 415-604-5251  
Fax: 415-604-6779  
E-mail: [dldevincenzi@nasamail.nasa.gov](mailto:dldevincenzi@nasamail.nasa.gov)*

## Stanley F. Dermott

*211 SSRB  
Department of Astronomy  
University of Florida  
Gainesville FL 32611  
Phone: 904-392-5089  
Fax: 904-392-5089  
E-mail: [dermott@astro.ufl.edu](mailto:dermott@astro.ufl.edu)*

## Tammy Dickinson

*Mail Code SLC  
NASA Headquarters  
Washington DC 20546  
Phone: 202-358-0284  
Fax: 202-358-3097  
E-mail: [tdickinson@sl.ossa.ms.hq.nasa.gov](mailto:tdickinson@sl.ossa.ms.hq.nasa.gov)*

George J. Flynn

Department of Physics  
Hudson Hall -223  
State University of New York at Plattsburgh  
Plattsburgh NY 12901  
Phone: 518-564-3156  
Fax: 518-564-3152

Mark Fonda

Mail Stop 239-12  
NASA Ames Research Center  
Moffett Field CA 94035  
Phone: 415-604-5744  
Fax: 415-604-0092

A. Fujiwara

Department of Physics  
Faculty of Science  
Kyoto University  
Kyoto  
JAPAN  
Phone: 0427-51-3911

James Gooding

Mail Code SN2  
NASA Johnson Space Center  
Houston TX 77058  
Phone: 713-483-5126  
Fax: 713-483-2911  
E-mail: gooding@sn.jsc.nasa.gov

Robert H. Hertz

Orbital Science Corp.  
2771 N. Garey Ave.  
Pomona CA 91767  
Phone: 909-593-3581

Lawrence Hrubesh

Box 808  
Lawrence Livermore National Laboratory  
Livermore CA 94550  
Phone: 415-423-1691

A. A. Jackson

Mail Code C23  
Lockheed Engineering & Sciences Co.  
2400 NASA Road 1  
Houston TX 77258  
Phone: 713-333-7679  
E-mail: SN::JACKSON

Klaus Keil

Department of Geology and Geophysics  
Planetary Geosciences Division  
University of Hawaii at Manoa  
Honolulu HI 96822  
Phone: 808-956-3898  
Fax: 808-956-6322  
E-mail: keil@baby.pgd.hawaii.edu

Don Lewis

Jet Propulsion Laboratory  
4800 Oak Grove Drive  
Pasadena CA 91109-8099  
Phone: 818-354-0840  
Fax: 818-358-4950  
E-mail: dwlewis@nasamail.nasa.gov

David J. Lindstrom

Mail Code SN4  
NASA Johnson Space Center  
Houston TX 77058  
Phone: 713-483-5135  
Fax: 713-483-5347  
E-mail: dlindstrom@snmail.jsc.nasa.gov

Jer-Chyi Liou

Mail Code SN3  
NASA Johnson Space Center  
Houston TX 77058  
Phone: 713-244-5975  
Fax: 713-483-5276  
E-mail: liou@snmail.jsc.nasa.gov

Carl R. Maag

T&M Engineering  
6831 Sherwood Drive  
Laverne CA 91750  
Phone: 909-596-3235

David J. Mendez

Lockheed Missiles and Space Co.  
3251 Hanover Street  
Palo Alto CA 94304  
Phone: 408-743-2080

Marc-Oliver Mewes

Atomic and Molecular Physics  
Room 25-249  
Massachusetts Institute of Technology  
77 Massachusetts Ave.  
Cambridge MA 02139  
Phone: 617-253-4178  
Fax: 617-253-4876  
E-mail: mom@athena.mit.edu

Michael A. Meyer

Mail Code SLC  
Exobiology Program  
Solar System Exploration Division  
NASA Headquarters  
Washington DC 20546  
Phone: 202-358-0307  
Fax: 202-358-3097  
E-mail: mmeyer@sl.ms.oss.hq.nasa.gov



Kenji Nishioka

Mail Stop 239-12  
SETI Institute  
NASA Ames Research Center  
Moffett Field CA 94035-1000  
Phone: 415-604-0103  
Fax: 415-604-0092  
E-mail: kenji\_nishioka.sss\_mail@qmgate.arc.nasa.

William Niu

Orbital Science Corp.  
2771 N. Garey Avenue  
Pomona CA 91767  
Phone: 909-593-3581

Rob Peterson

3738 Arnold  
Houston TX 77005  
Phone: 213-666-7644

H. A. Roeder

Orbital Science Corp.  
2771 N. Garey Ave.  
Pomona CA 91767  
Phone: 909-593-3581  
Fax: 909-593-2843

James T. Ryder

Lockheed  
1110 Lockheed Way  
Sunnyvale CA  
Phone: 415-424-2171

T. H. See

Mail Code C23  
NASA Johnson Space Center  
2400 NASA Road 1  
Houston TX 77058  
Fax: 713-483-5347

Mikio Shimizu

Institute of Space and Astronautical Science  
3-1-1, Yoshinodai, Sagami-hara-Shi  
Kanagawa Pref. 229  
JAPAN  
Phone: 427-51-3911 x2529  
Fax: 427-59-4237

Charles Simon

Institute of Space Sciences and Technology  
1810 NW 6th Street  
Gainesville FL 32609-8590  
Phone: 904-371-4778  
Fax: 904-372-5042  
E-mail: bjc@ufl.edu

Stepheni Stephenson

Space Science Laboratory  
Department of Physics  
Baylor University  
P.O. Box 97303  
Waco TX 76798  
Phone: 817-755-3879  
Fax: 817-755-3878

William G. Tanner

Space Science Laboratory  
Department of Physics  
Baylor University  
P.O. Box 97303  
Waco TX 76798-7303  
Phone: 817-755-3404  
Fax: 817-755-3878  
E-mail: tanner@baylor.edu

Lawrence A. Taylor

Department of Geological Sciences  
University of Tennessee  
Knoxville TN 37996-1410  
Phone: 615-974-6013  
Fax: 615-974-2368  
E-mail: lataylor@utkvm.utk.edu

Kathie Thomas

Mail Code C23  
Lockheed Engineering and Sciences Co.  
Houston TX 77058  
Phone: 713-483-5029

Peter Tsou

Mail Stop 183-501  
Jet Propulsion Laboratory  
4800 Oak Grove Drive  
Pasadena CA 91109  
Phone: 818-354-8094  
Fax: 818-354-0966

Anthony Tuzzolino

University of Chicago  
933 E. 56th Street  
Chicago IL 60637  
Phone: 312-702-7798  
Fax: 312-702-6645

K. T. Uesugi

Institute of Space and Astrophysical Science  
3-1-1 Yoshinodai  
Sagami-hara  
Kanagawa 229  
JAPAN  
Fax: 81-427-59-4241  
E-mail: 1ono@isasmacl.newslan.isas.ac.jp

Robert M. Walker

*Department of Physics  
Washington University  
Campus Box 1105  
One Brookings Drive  
St. Louis MO 63130  
Phone: 314-935-6225  
Fax: 314-935-4083  
E-mail: [rmw@howdy.wustl.edu](mailto:rmw@howdy.wustl.edu)*

Jack Warren

*Lockheed Engineering and Sciences Co.  
2400 NASA Road 1  
Houston TX 77058  
Phone: 713-483-5122*

Jerry Winkler

*Mail Code C23  
Lockheed Engineering and Sciences Co.  
2400 NASA Road 1  
Houston TX 77058  
Phone: 713-483-5096*

Michael Zolensky

*Mail Code SN2  
NASA Johnson Space Center  
Houston TX 77058  
Phone: 713-483-5128*

Herbert A. Zook

*Mail Code SN3  
NASA Johnson Space Center  
Houston TX 77058  
Phone: 713-483-5058  
Fax: 713-483-5276  
E-mail: [SN::ZOOK](mailto:SN::ZOOK)*